

UNIVERSITA' DEGLI STUDI DI PARMA

Dottorato di Ricerca in Scienze Chimiche

Ciclo XXVII (2012-2014)

INORGANIC AND HYBRID INORGANIC-ORGANIC SYSTEMS FOR CONSERVATIVE TREATMENTS OF STONE AND WOOD MATERIALS

Coordinatore:

Chiar.mo Prof. Roberto Cammi

Tutors:

Chiar.mo Prof. Giovanni Predieri

Chiar.mo Prof. Angelo Montenero

Chiar.mo Prof. Pier Paolo Lottici

Dottoranda: Laura Bergamonti

2015

Alle persone che amo

CONTENTS

List of Acronyms	vii
Table captions	ix
Figure captions	xi
INTRODUCTION AND AIM OF THE WORK	1
PART A: Synthesis and characterization of amidoamines as model molecules for polyamidoamines	
A.1 - INTRODUCTION	3
A.1.1 - Amidoamines	3
A.1.1.1 - The Aza-Michael Addition reaction	3
A.2 – EXPERIMENTAL	4
A. 2.1 - Materials	4
A. 2.2 – Synthesis	4
A. 2.2.1 – AADEtA	4
A. 2.2.2 - AAEtA	5
A. 2.2.3 - MBADEtA	5
A. 2.3 – Characterization	5
A. 2.3.1 - Electrospray ionisation mass spectrometry (ESI-MS)	5
A. 2.3.2 - Nuclear magnetic resonance (NMR): ¹ H-NMR, ¹³ C-NMR	5
A. 2.3.3 - Fourier Transform Infrared Spectroscopy (FT-IR)	5
A. 2.3.4 - μ-Raman Spectroscopy	5
A. 3 - RESULTS AND DISCUSSION	6
A. 3.1 – Characterization	7
A. 3.1.1 - Pure reagents	7
A. 3.1.1.1 – Acrylamide	7
A. 3.1.1.1.1 - ¹ H-NMR and ¹³ C{ ¹ H}-NMR	7
A. 3.1.1.1.2 - Vibrational spectroscopies: FTIR and Raman	8
A. 3.1.1.1.3 - Raman spectra of “neat acrylamide” and in water solution	10
A. 3.1.1.2 - N,N'-methylenebisacrylamide (MBA)	12
A. 3.1.1.2.1 - NMR	12
A. 3.1.1.2.2 - Vibrational spectroscopies: FTIR and Raman	13
A. 3.1.1.2.3 - Raman spectra of N,N'-methylenbisacrylamide crystals	14
A. 3.1.1.3 - Ethanolamine (EtA), Diethanolamine (DEtA)	16
A. 3.1.1.3.1 - NMR	16

A. 3.1.1.3.2 - Vibrational spectroscopies: FTIR and Raman	17
A. 3.1.2 - Molecules	19
A. 3.1.2.1 – AADEtA	19
A. 3.1.2.1.1 – ESI-MS	19
A. 3.1.2.1.2 – NMR	20
A. 3.1.2.1.3 – FTIR	21
A. 3.1.2.1.4 - Raman and reaction kinetics	22
A. 3.1.2.2 – AAEtA	24
A. 3.1.2.2.1 - ESI-MS	25
A. 3.1.2.2.2 – NMR	25
A. 3.1.2.2.3 – FTIR	26
A. 3.1.2.2.4 – Raman	27
A. 3.1.2.3 – MBADEtA	28
A. 3.1.2.3.1 - ESI-MS	28
A. 3.1.2.3.2 – NMR	28
A. 3.1.2.3.3 – FTIR	29
A. 3.1.2.3.4 – Raman	30
A. 4 – CONCLUSIONS	32
A. 5 – REFERENCES	33
PART B: Functionalized polyamidoamines (PAA) as wood preservatives against fungi and termites	
B. 1 – INTRODUCTION	37
B. 1.1 - Wood structure and properties	38
B. 1.2 - Wood degradation	41
B. 1.2.1 - Abiotic degradation	41
B. 1.2.2 - Biotic degradation: Fungi, termites	42
B. 1.3 - Protective treatments	45
B 1.3.1 – Polyamidoamines	46
B. 2 – EXPERIMENTAL	50
B. 2.1 - Materials	50
B. 2.2 - Synthesis of protective formulations	52
B. 2.2.1 - Synthesis of Polyamidoamine with alcoholic functionality (PAAOH)	52
B. 2.2.1.1 - PAAOH	52
B. 2.2.1.2 - PAAOH NO solvent	52

B. 2.2.2 - Synthesis of Polyamidoamine with siloxane functionality: SiPAA and SiPAAOH	53
B. 2.3 - PAA characterization	53
B. 2.3.1 - Solid State NMR Spectroscopy (SS-NMR): ¹³ C-NMR, ²⁹ Si-NMR	54
B. 2.3.2 - Differential scanning calorimetry (DSC)	54
B. 2.4 - Wood samples	54
B. 2.5 - Wood treatments	55
B. 2.5.1 - Polymer application by dip coating (type 1)	56
B. 2.5.2 - Polymer application by impregnation (type 2a and 2b)	56
B. 2.6 - Characterization of treated wood	57
B. 2.6.1 - Scanning Electron Microscopy - SEM/EDS micro-analysis	57
B. 2.6.2 - Environmental Scanning Electron Microscopy (ESEM)	58
B. 2.6.3 - Colorimetric measurements	59
B. 2.7 - Accelerated aging test UNI EN 84 (1997)	58
B. 2.8 - Efficacy tests against biological attack	58
B. 2.8.1 - Brown rot and white rot fungi: <i>C. puteana</i> , <i>T. versicolor</i> , <i>P. placenta</i>	58
B. 2.8.1.1 - Accelerated test against <i>C. puteana</i> in mini-block samples	59
B. 2.8.1.2 - Standard test according to UNI EN 113 (1996)	61
B. 2.8.2 - Efficacy test of the treatments against termites: laboratory no-choice test	62
B. 3 - RESULTS AND DISCUSSION	64
B. 3.1 - Characterization of protective treatments	64
B. 3.1.1 - Polyamidoamine with hydroxyl functionality: PAAOH	64
B. 3.1.1.1 - ESI-MS	64
B. 3.1.1.2 - NMR	67
B. 3.1.1.3 - Vibrational spectroscopies: FTIR and Raman	70
B. 3.1.1.4 - Differential scanning calorimetry (DSC)	74
B. 3.1.2 - Polyamidoamine with siloxane functionality: SiPAA	76
B. 3.1.2.1 - NMR	76
B. 3.1.2.2 - Vibrational spectroscopies: FTIR and Raman	79
B. 3.2 - Characterization of treated wood	81
B. 3.2.1 - ESEM	82
B. 3.2.2 - ¹³ C and ²⁹ Si CP/MAS solid state NMR	84
B. 3.2.3 - FT-Raman	85
B. 3.2.4 - Colour changes	87

B. 3.3 - Efficacy tests against biological attack	88
B. 3.3.1 - Brown rot and white rot fungi: <i>C. puteana</i> , <i>T. versicolor</i> , <i>P. placenta</i>	88
B. 3.3.1.1 - Accelerated test against <i>C. puteana</i> in mini-block samples	88
B. 3.3.1.2 - Standard test according to UNI EN 113 (1996)	93
B. 3.3.2 - Efficacy test of treatments against termites: laboratory no-choice test	95
B. 3.3.2.1 - Subterranean termites - <i>Reticulitermes lucifugus</i>	95
B. 3.3.2.2 - Dry-wood termites - <i>Kaloterme flavicollis</i>	98
B. 4 – CONCLUSIONS	101
B. 5 – REFERENCES	102
PART C: TiO₂ by sol-gel in acid and basic environments: characterization and photocatalytic activity for calcarenites stone protection	
C. 1 – INTRODUCTION	109
C. 1.1 - TiO₂ and its photocatalytic activity	110
C. 1.2 - Stone materials	111
C. 2 – EXPERIMENTAL	112
C. 2.1 - Materials and syntheses of TiO₂	112
C. 2.2 - Stones samples	113
C. 2.3 - Characterization of TiO₂ sols	114
C. 2.3.1 - XRD measurements	114
C. 2.3.2 - μ -Raman spectroscopy	114
C. 2.3.3 – TEM	114
C. 2.3.4 - DLS and ELS	115
C. 2.3.5 - Photocatalytic activity of the nanosols	115
C. 2.4 - Characterization of TiO₂-based coatings on calcarenite stones	116
C. 2.4.1 - The stone samples: petrographic analysis	116
C. 2.4.2 - ESEM and SEM-EDS	116
C. 2.4.3 - Chromatic changes	117
C. 2.4.4 - Self-cleaning tests on the stone	117
C. 2.4.5 - Water absorption by capillarity	117
C. 2.4.6 - Salt crystallization	118
C. 3 - RESULTS AND DISCUSSION	118
C. 3.1 - The TiO₂ sols and powders	118
C. 3.1.1 – Syntheses	118
C. 3.1.2 – XRD	119
C. 3.1.3 - μ -Raman	121

C. 3.1.4 – TEM	123
C. 3.1.5 - DLS – ELS	125
C. 3.1.6 - Photocatalytic activity of the sols	127
C.3.2 - Coatings applied to the calcarenite stones	133
C. 3.2.1 - Modica and Comiso stones (Pietra di Modica e Pietra di Comiso)	133
C. 3.2.1.1 - Stone treatments	133
C. 3.2.1.2 - Petrographic analysis	133
C. 3.2.1.3 - SEM-EDS	134
C. 3.2.1.4 - μ -Raman	136
C. 3.2.1.5 - Colour changes	138
C. 3.2.1.6 - Photocatalytic activity	138
C. 3.2.1.7 - Water absorption by capillarity	140
C. 3.2.1.8 - Salt crystallization test	142
C. 3.2.2 - Lecce stone (Pietra di Lecce)	142
C. 3.2.2.1 - Stone treatment	142
C. 3.2.2.2 - Petrographic analysis	143
C. 3.2.2.3 - Electron microscopy and EDS	143
C. 3.2.2.4 - Chromatic changes	145
C. 3.2.2.5 - Photocatalytic activity of the coatings	146
C. 3.2.2.6 - Capillarity absorption	147
C. 3.2.3 - Noto stone (Pietra di Noto)	148
C. 3.2.3.1 - Petrographic analysis	148
C. 3.2.3.2 - Synthesis and application of the coatings	149
C. 3.2.3.3 - SEM and EDS spectra	149
C. 3.2.3.4 - Chromatic changes	151
C. 3.2.3.5 - Capillarity absorption	151
C. 3.2.3.6 - Salt crystallization	151
C. 3.2.3.7 - Photocatalytic activity of the coatings	154
C. 4 – CONCLUSIONS	155
C. 5 – REFERENCES	156
CONCLUSIONS	166
ACKNOWLEDGEMENTS	168
PUBLICATIONS	169

LIST OF ACRONYMS

AA	Acrylamide
AADEtA	Acrylamine+Diethanolamine
AAEtA	Acrylamine+Ethanolamine
AC	Absorption Coefficient
APTES	γ -Aminopropyltriethoxysilane
CP/MAS	Cross Polarization/Magic Angle Spinning
DEtA	Diethanolamine
DLS	Dynamic Light Scattering
DOC	Degree of Condensation
DSC	Differential Scanning Calorimetry
ELS	Electrophoretic Light Scattering
ESEM	Environmental Scanning Electron Microscopy
ESI-MS	Electrospray Ionisation - Mass Spectrometry
EtA	Ethanolamine
EtOH	Ethanol
FT-IR	Fourier Transform Infrared Spectroscopy
FT-Raman	Fourier Transform Raman Spectroscopy
FWHM	Full Width at Half-Maximum
HAADF	High Angle Annular Dark Field
HRTEM	High Resolution Transmission Electron Microscopy
IEP	Iso-Electric Point
LM	Leached Mass
MB	Methylene Blue
MBA	N,N'-Methylenebisacrylamide
MBADEtA	N,N'-Methylenebisacrylamide + Diethanolamine
MC	Moisture Content
MeO	Methyl Orange
MeOH	Methanol
ML	Mass Loss
μ -Raman	Micro-Raman Spectroscopy
NMR	Nuclear Magnetic Resonance
PAA	Polyamidoamines
PAAOH	Polyamidoamine with Hydroxyl Functionality
RCI	Relative Capillarity Index
RH	Relative Humidity
RT	Room Temperature
SEM/EDS	Scanning Electron Microscope
SiPAA	Polyamidoamine with Siloxane Functionality
SiPAAOH	Polyamidoamine with Hydroxyl and Siloxane Functionality
SS-NMR	Solid State NMR Spectroscopy
STEM	Scanning Transmission Electron Microscopy
TEM	Transmission Electron Microscopy
TiAcAc	Titania Sol + Acetic Acid
TiAcAu	Titania Sol + Acetic Acid + Gold Nanoparticles

TiAcN	Titania Sol+ Acetic + Nitric Acid
TiAcNNa	Titania Sol+ Acetic + Nitric Acid + Sodium Hydroxide
TiMaA	Titania Sol + Malonic Acid + Triethylamine
TiMaAN	Titania Sol + Malonic Acid + Triethylamine + Nitric Acid
WPG	Weight Percent Gain
XRD	X-Ray Diffraction
ΔE^*	Total Color Difference

Table captions

Table A.1 - Vibrational bands (FTIR and Raman) of acrylamide.

Table A.2 - MBA frequencies.

Table A.3 - Vibrational modes in DEtA and EtA.

Table B.1 - Structural formula and chemical/physical properties of each reagent and used in the polymer synthesis.

Table B.2 - Synthesized polymers with the acronyms and description of the reaction conditions.

Table B.3 - Polyamidoamines functionalized with EtA and APTES.

Table B.4 - Wood samples used in efficacy tests against fungi and termites.

Table B.5 - Screening tests made on Pinus sylvestris L. mini-block samples treated with different PAAs.

Table B.6 - Minimum mass loss for each fungus species, as required by EN 113.

Table B.7 - Description of samples and termites species used in efficacy test UNI EN 118.

Table B.8 - ¹³C-NMR chemical shifts and related assignments.

Table B.9 - ²⁹Si NMR chemical shifts and related assignments (spectra in Fig. B.32).

Table B.10 - ¹³C NMR chemical shifts and related assignments.

Table B.11 - Colorimetric changes for the different treatments of the Pinus Sylvestris wood.

Table B.12 - Max humidity before impregnation and weight percent gain (WPG₁) values after impregnation of pinewood samples treated with different sol-gel solutions, used in accelerated efficacy tests against C. puteana.

Table B.13 - Weight Percent Gain, leached formulation, mass loss due to exposure to C. puteana and moisture content of the treated sample.

Table B.14 - Weight Percent Gain, mass loss due to exposure to C. puteana and moisture content of the treated sample.

Table B.15 - Weight Percent Gain, mass loss due to exposure to C. puteana and moisture content of samples treated with PAAOH and SiPAA by fast dipping, in Augeo191 SL.

Table B.16 - Mass loss ML, mass loss corrected due to exposure to C. puteana ML and moisture content MC of treated samples.*

Table B.17 - WPG₁ and standard deviation of PAAs obtained from nine samples.

Table B.18 - Efficacy test on pinus sylvestris sample treated with SiPAA and SiPAAOH in methanol and Augeo against C. puteana and P. placenta.

Table B.19 - Weight Percent Gain of the treated sample (WPG_1) and of leached mass (WPG_2) with respect to untreated mass and the leached formulation (LF).

Table B.20 - Samples used to evaluate the fungi virulence.

*Table B.21- Results of the no-choice test for *Reticulitermes lucifugus*. Av = average; sd = standard deviation.*

*Table B.22 - Results of the no-choice test for *Kalotermes flavicollis*. Av = average; sd = standard deviation.*

Table B.23 - Treated wood resistance according to NORMAL EN 350-1:199.

.....

Table C.1- The synthesized sols.

Table C.2 - The stone samples investigated.

Table C.3 - Proportion ($\pm 5\%$) of anatase and brookite and crystallite sizes (± 0.5 nm) in TiO_2 powders from the sols.

Table C.4 - pH and Zeta potential of the nano-sols.

Table C.5 - Zeroth-order rate constant k_0 (min^{-1}) for the photodegradation of the sols, from the linear fits to the curves in Fig. C.15.

Table C.6 - Colorimetric data (mean values) of the Modica and Comiso stone samples before and after the application of the TiO_2 TiAcN coatings.

Table C.7 - Water absorption coefficient (AC) in $\text{kg}/(\text{m}^2\text{s}^{1/2})$ by capillarity, estimated in the first hour and relative capillarity index (RCI) on the whole duration of the test.

Table C.8 - Colorimetric data of the "pietra di Lecce" samples before and after the application of the coatings.

Table C.9 - Water absorption coefficient (AC) in $\text{kg}/(\text{m}^2\text{s}^{1/2})$ calculated in the first five minutes and relative capillarity index (RCI) on the whole duration of the test.

Table C.10 - The synthesized sols.

Table C.11 - Colorimetric parameters of the uncoated and coated stone.

Table C.12 - Water absorption coefficient (AC) in $\text{kg}/(\text{m}^2\text{s}^{1/2})$ calculated in the first 30 minutes and relative capillarity index (RCI) on the whole duration of the test.

Figure captions

Fig. A.1 - Scheme of the Michael addition reaction.

Fig. A.2 - Reaction scheme of AA with EtA and DEtA.

Fig. A.3 - Reaction scheme of MBA with DEtA.

Fig. A.4 - ^1H -NMR of acrylamide in DMSO- d_6 .

Fig. A.5 - $^{13}\text{C}\{^1\text{H}\}$ -NMR of acrylamide in DMSO- d_6 .

Fig. A.6 - FTIR (a) and Raman (b) spectra of acrylamide. The insert shows a detail of amide I, vinyl group and amide II absorption bands.

Fig. A.7 - Raman spectra at 298 K in solid acrylamide (a) and in acrylamide aqueous solution (b).

Fig. A.8 - The Raman spectra in the 1500-1750 cm^{-1} spectral region of solid acrylamide (a) and acrylamide in water solution (b).

Fig. A.9 - The MBA molecule.

Fig. A.10 - ^1H NMR of MBA in DMSO- d_6 .

Fig. A.11 - $^{13}\text{C}\{^1\text{H}\}$ -NMR spectrum of MBA.

Fig. A.12 - FTIR (a) and Raman (b) spectra of crystalline (neat, solid) MBA.

Fig. A.13 – a) Needle crystals of MBA; b) Raman spectra of MBA crystals at different orientations (V, H) and polarizations (PP, OP). The inset shows non polarized spectrum at low frequencies down to 20 cm^{-1} .

Fig. A.14 - FTIR and Raman spectra of ethanolamine (EtA).

Fig. A.15 - FTIR (a) and Raman spectra (b) of Diethanolamine (DEtA).

Fig. A.16 - ESI-MS spectrum of AADEtA (acrylamide+diethanolamine).

Fig. A.17 - ^1H -NMR of AADEtA (acrylamide-diethanolamine) synthesized in water at 55 °C for 4h. The arrows indicate the signals from the protons shown in the inset.

Fig. A.18 - $^{13}\text{C}\{^1\text{H}\}$ -NMR of AADEtA.

Fig. A.19 - FTIR spectrum of AADEtA molecule, synthesized in water, compared with that of acrylamide (a); detail of the amide group in AADEtA and in acrylamide (b).

Fig. A.20 - Raman spectra of AADEtA and acrylamide in water solution (a); detail of the amide region (1750-1500 cm^{-1}).

Fig. A.21 - Sequence of Raman spectra during acrylamide and diethanolamine reaction.

Fig. A.22 - Time evolution of the normalized area of the C=C stretching band (a). Plot of the reciprocal of the data in the first two hours and linear fit. The inverse of the slope is the half life of the reaction.

Fig. A.23 - ESI-MS of the AADEtA obtained in water at 55 °C for 4h.

Fig. A.24 - ^1H -NMR spectrum in DMSO- d_6 of the AAEtA product.

Fig. A.25 - $^{13}\text{C}\{^1\text{H}\}$ -NMR spectrum of AAEtA.

Fig. A.26 - FTIR spectra of AAEtA and of pure reagents.

Fig. A.27 - Raman spectrum of AAEtA obtained in water at 55 °C for 8 hours.

Fig. A.28 - ESI-MS spectrum of MBADEtA.

Fig. A.29 - ^1H -NMR spectrum of MBADEtA.

Fig. A.30 - $^{13}\text{C}\{^1\text{H}\}$ -NMR spectrum of MBADEtA.

Fig. A.31 - FTIR spectra of MBADEtA, MBA and DEtA.

Fig. A.32 - Raman spectra of MBADEtA after 4 h and 24 h reaction times, in water at 298 K.

Fig. A.33 - Raman spectra taken during the addition reaction MBA+DEtA.

.....

Fig. B.1 - Hierarchical structure of wood (from [www.forestplatform.org/Tobias Kohnke](http://www.forestplatform.org/Tobias_Kohnke)).

Fig. B.2 - Scheme of the transversal section of a stem, showing the distinctive parts of its macro structure (<http://kids.britannica.com/elementary/art-66141>).

Fig. B.3 - Schematic representation of wood. Softwood: 1. tracheids, 2. ray parenchyma, 3. Resinous canals. Hardwood: 1. latewood: 2. spring wood, 3. ray parenchyma, 4. vessels, 5 axial parenchyma (www.sfera-group.it).

Fig. B.4 - Schematic representation of the cell wall structure: primary wall, the secondary wall and middle lamella. S1, S2, S3 are the different sub-layers of the secondary wall [B8].

Fig. B.5 - The white rot fungus *Trametes versicolor* (L.:Fr.) Pilat.

Fig. B.6 - The brown rot fungus *Coniophora puteana* (Shum.:Fr) P. Karsten

Fig. B.7 - *Reticulitermes lucifugus* worker (left) and soldier (right).

Fig. B.8 - *Kalotermes flavicollis* royal brown and yellow-cream "false workers" (left) and soldier (right).

Fig. B.9 - Reaction scheme of polyaddition of prim-monoamine (a) and sec-diamine (b) to bisacrylamide. R = H, aliphatic or aromatic substituent.

Fig. B.10 - Reaction scheme of polyaddition of N,N'-methylenebisacrylamide (MBA) and ethanolamine (EtA).

Fig. B.11 - Reaction scheme of polyaddition of N,N'-methylenebisacrylamide and 3-aminopropyltriethoxysilane.

Fig. B.12 - The three principal axes of wood with respect to grain direction and growth rings.

Fig. B.13 - (a) Impregnation system (vacuum/nitrogen), type 2a; (b) Impregnation chamber (vacuum/atmospheric pressure), type 2b [CNR-IVALSA].

Fig. B.14 - Screening tests: preparation of mini-specimens at the end of the test.

Fig. B.15 - Testing procedure for *Reticulitermes lucifugus*.

Fig. B.16 - Testing procedure for *Kalotermes flavicollis*.

Fig. B.17 - ESI-MS spectrum of PAAOH obtained with water as solvent. Comparison between two mixing modes: EtA slowly added into MBA solution (a) or MBA slowly added into EtA (b).

Fig. B.18 - Reaction scheme of PAAOH.

Fig. B.19 - $^1\text{H-NMR}$ (D_2O) of PAAOH.

Fig. B.20 - $^{13}\text{C-NMR}$ spectrum of PAAOHns at 25 °C (a) and after heating at 55 °C (b).

Fig. B.21 - $^{13}\text{C-NMR}$ of the polymers PAAOH b (ethanol) and PAAOH d (methanol). The direction of the polymerization is indicated according to the conditions of synthesis.

Fig. B.22 - FTIR spectra of PAAOH in water (a), ethanol (b) and methanol (d) compared with that of MBA. On the right are shown details of the spectral regions 3500÷2500 cm^{-1} (top) and 1700÷1400 cm^{-1} (bottom).

Fig. B.23 - Raman spectrum of PAAOH synthesized without solvent and of the pure reagents.

Fig. B.24 - Raman spectra: comparison between PAAOH in different solvents and 1-2-3 mixing modes (a); Raman spectra of PAAOH in C=O and C=C region (b).

Fig. B.25 - Time evolution of the Raman spectra on PAAOH at 55 °C.

Fig. B.26 - Raman spectra of PAAOHns taken at different temperatures.

Fig. B.27 - DSC of *N,N'*-methylenebisacrylamide (MBA): heating up to decomposition (a); one scan up to fusion (b); two repeated scans until fusion (c).

Fig. B.28 - DSC of PAAOH b1 and PAAOH b2: one scan up to 300 °C.

Fig. B.29 - DSC of PAAOH b2 after heat treatment.

Fig. B.30 - $^{13}\text{C-NMR}$ of SiPAA (MBA:APTES=1:1) polymer.

Fig. B.31 - $^{13}\text{C-NMR}$ spectra of SiPAAOH with different EtA/APTES ratios.

Fig. B.32 - $^{29}\text{Si-NMR}$ spectra: comparison between SiPAAOH polymers synthesized at different EA/APTES ratios.

Fig. B.33 - FTIR spectra of SiPAA b2 and SiPAAOH b2, 1:0.5:0.5.

Fig. B.34 - Raman spectrum of SiPAA in ethanol (MBA:APTES = 1:1).

Fig. B.35 - Raman spectra of pure reagents and polymers SiPAA .

Fig. B.36 - (a) ESEM image along the cross section of a wood sample treated with SiPAAOH in Augeo by dip coating; (b) EDS microanalysis in the two areas indicated.

Fig. B.37 - EDS microanalysis results for %Si, with respect to O_2 , along the whole thickness of the SiPAA treated sample compared to the untreated sample.

Fig. B.38 - EDS microanalysis results for %Si, with respect to O_2 , along the whole thickness of the SiPAAOH treated sample compared to the untreated sample.

Fig. B.39 - ^{13}C CP/MAS NMR spectrum of SiPAA-impregnated wood.

Fig. B.40 - ^{29}Si CP/MAS solid NMR spectrum of SiPAA treated wood.

Fig. B.41 - a) FT-Raman of *Pinus Sylvestris* wood, untreated. b) Detail of the spectrum in the 1800-700 cm^{-1} range.

Fig. B.42 - FT-Raman of untreated and SiPAA treated wood.

Fig. B.43 – SiPAA - Left, fungus *C. puteana*, sample 911 (treated) and 40 (control). Center: *T. versicolor*, samples 867 (treated) and 54 (control). Right: *P. placenta*, samples 940 (treated) and 53 (control).

Fig. B.44 – SiPAAOH - Left: *C. puteana*, samples 954 (treated) and 63 (control). Center: *T. versicolor*, samples 941 (treated) and 70 (control). Right: *P. placenta*, samples 804 (treated) and 66 (control).

Fig. B.45 – PAAOH - Left: *C. puteana*, samples F17 (treated) and C15 (control). Center: *T. versicolor*, samples F11 (treated) and C11 (control). Right: *P. placenta*, samples F08 (treated) and C8 (control).

Fig. B.46 - Reference samples for the virulence of *C. puteana*.

Fig. B.47 - *Reticulitermes lucifugus*. Visual examination of the attack degree.

Fig. B.48 - (a) Level of attack; mass loss of the samples after the attack (b) and survival of the colonies (c, d).

Fig. B.49 - *Kalotermes flavicollis*. Visual examination of the attack degree.

Fig. B.50 - (a) Level of attack; mass loss of the samples after the attack (b) and survival of the colonies (c, d).

.....
Fig. C.1 - The chemical structure of methyl orange (MeO) and Methylene blue (MB).

Fig. C.2 - XRD patterns of the nanocrystalline titania powders obtained from the nanosols: A and B indicate anatase and brookite reflections, respectively.

Fig. C.3 - XRD pattern of the TiAcNNa powder showing the NaNO_3 reflections. The small feature (*) at about 22.38° could not be indexed.

Fig. C.4 - Fit of the main anatase and brookite diffraction peaks to determine the brookite content.

Fig. C.5 - Raman spectra of TiO_2 powders: the wavenumbers of the anatase peaks are indicated. Asterisks indicate some brookite features. In spectrum of TiAcNNa, the peaks of “nitratine” are indicated by N.

Fig. C.6 - a) HRTEM image of TiAcN; b) Fourier Transform of a): the reflections named A and B are originated from the regions in a) marked with the same letter.

Fig. C.7 - a) Bright field zero-loss TEM typical image of the TiMaA sample with the diffraction pattern taken from the same region as inset; b) HRTEM image where isolated anatase titania particles are clearly identified.

Fig. C.8 - (a) Large area HAADF - STEM image (essentially Z-contrast) of TiAcAu powder. Gold particles are visible over agglomeration of TiO₂ nanoparticles. (b) TEM image in bright field mode of an Au particle in TiAcAu, revealing the very fine grain of TiO₂ particles on the background.

Fig. C.9 - (a) Ring diffraction pattern from TiO₂ nanoparticles in a 100x100 nm² region in TiAcAu. (b) Intensity profile of the diffraction pattern. The crystalline phase is anatase (A). The feature (B) at about 3.5 nm⁻¹ is due to brookite.

Fig. C.10 - Particle size distribution for TiAcN (full line) and TiMaA (dashed line) sols.

Fig. C.11 - Influence of pH on the zeta potential for the TiAcN and TiMaA sols.

Fig. C.12 - Methyl orange photo-catalytic degradation measured by the decrease of the dye absorbance at different UV irradiation time.

Fig. C.13 - Methylene blue photo-catalytic degradation measured by the decrease of the dye absorbance at different UV irradiation time.

Fig. C.14 - UV/Vis absorption spectra of: MB water solution (3x10⁻⁵M), TiMaA sols with different concentrations of MB (MB/TiMaA) and pure TiMaA sol (9.22x10⁻³M).

Fig. C.15 - Photodegradation rate under UV irradiation: a) MeO and b) MB without and with TiAcAc, TiAcN and TiMaA catalysts.

Fig. C.16 - Polarizing optical microscope images of thin sections of Comiso (a) and Modica (b) stones.

Fig. C.17 - SiO₂ pretreated Comiso stone: the EDS spectra refers to the a and b areas indicated on the SEM image.

Fig. C.18 - TiO₂ (TiAcN) coated Modica stone: a low amount of Ti is visible down to 500 μm. The EDS spectra refers to the areas a (left) and b (right) indicated on the SEM image.

Fig. C.19 - SiO₂/TiO₂ pretreated Comiso stone. The EDS spectrum was taken from the surface of the sample. The Ti features are indicated.

Fig. C.20 - Raman spectrum on Modica stone treated with SiO₂/TiO₂. C=calcite from the bulk limestone. SiO₂ does not give an observable spectrum.

Fig. C.21 - Microscopic image (a) and Raman map (b), on the area indicated, of the distribution of anatase/brookite nanocrystals obtained through the (smoothed) intensity map of the blue-shifted main anatase/brookite Raman peak at ~ 15 cm⁻¹. The map has been acquired with 100x magnification on an 8x8 array.

Fig. C.22 - Normalized chromatic changes ΔC (chroma) of the MeO stained (0.001 M) Comiso (a) and Modica (b) stone samples, as a function of the irradiation time with the UV source. The comparison between untreated and $\text{SiO}_2/\text{TiO}_2$ or TiO_2 coated surfaces is reported.

Fig. C.23 - Normalized chromatic changes ΔC (chroma) of the MeO stained (0.1 M) Comiso (a) and Modica (b) stone samples, as a function of the irradiation time with the UV source. The comparison between untreated and $\text{SiO}_2/\text{TiO}_2$ or TiO_2 coated surfaces is reported.

Fig. C.24 - Capillarity water absorption curves (in kg/m^2) of Comiso and Modica stone samples before and after the application of TiO_2 and $\text{SiO}_2/\text{TiO}_2$ coatings.

Fig. C.25 - Percentage mass difference during the 15 crystallization cycles of Comiso (a) and Modica (b) stones.

Fig. C.26 - Polarizing optical microscope images of thin sections of "pietra di Lecce". The characteristic fossils of Lecce stone, planctonic foraminifera (*Globigerinoides sp* and *Globorotalia sp*) and calcareous nanofossils, are detectable.

Fig. C.27 - (a-b) ESEM images of TiAcN film after five applications: extended microcracks and cavities and radial microcracks in the form of "flowers" are evident. (c) and (d) EDS spectra taken within a microcrack and on the continuous film between the microcracks, respectively.

Fig. C.28 - (a) ESEM image of the TiAcAu film (three applications) with large microcracks. (b) EDS spectrum within a microcrack of the TiAcAu film; (c) EDS spectrum between the microcracks.

Fig. C.29 - (a) EDS map of Ti distribution on the "pietra di Lecce" surface coated with three applications of TiAcAc nanosol; (d) EDS map of the Ti depth distribution for the TiAcAc coating.

Fig. C.30 - Normalized chroma changes ΔC of the MeO stained Lecce stone samples, as a function of the irradiation time with the UV source. The comparison between untreated and different TiO_2 coated surfaces is reported.

Fig. C.31 - Capillarity absorption Q_i (in kg/m^2 units) plotted as a function of the square root of time (in seconds) of Lecce stone samples before and after the application of TiAcAc, TiAcAu, TiAcN and TiAcNa coatings.

Fig. C.32 - Polarizing optical microscope images of thin sections of Pietra di Noto, where micro- and macrofossils are easily identified: a) Foraminifera; b) Echinoidea

Fig. C.33 - SEM images (350x) and EDS maps of Ti on the pietra di Noto surface coated with three applications of TiAcN and TiMaA nanosols. a) Uncoated pietra di Noto surface; b) TiAcN coating; c) Ti distribution for TiAcN coating; d) TiMaA coating; e) Ti distribution for TiMaA coating.

Fig. C.34 - Capillarity absorption curves Q_i vs $t^{1/2}$ for non-treated (NT), TiAcN and TiMaA coated samples.

Fig. C.35 -Mass-loss percentage vs. salt crystallization cycles for untreated and treated pietra di Noto.

Fig. C.36 - Raman spectra of pietra di Noto, untreated (NT), coated with TiMaA, and after the crystallization test (CT). Thenardite spectrum is reported for comparison.

Fig. C.37 - Photocatalytic activity vs. time of the TiMaA and TiAcN coatings on Methylene Blue and Methyl Orange dyes, measured by chromatic changes ΔC of the stained stone.

INTRODUCTION AND AIM OF THE WORK

Since the beginning of civilization, wood and natural stone accompanied the human great "revolutions", being materials used to express creativity and technological capabilities. Wood and stone were employed in the construction of buildings, for the manufacture of objects, tools and utensils or for the creation of works of art. In the conservation of the cultural heritage, therefore, it is natural that these two materials have received particular attention.

The conservation problems related to these two materials are obviously very different. Wood is an organic and heterogeneous material whose degradation is mainly due to the action of biodeteriogens. Stone is an inorganic material: its degradation is mainly due to the combined action of weather and pollutants that trigger mechanisms for physical and chemical degradation.

The first action to be taken, for the conservation and protection of our cultural heritage, is to prevent the conditions that lead to the deterioration of the work of art.

In the case of lignocellulosic materials, conservation is essentially the prevention of the attack by xilophagous organisms. For stone materials, protection of the artifacts is carried out with coatings that prevent the deterioration process.

The present research has therefore focused on the synthesis, characterization and application of inorganic and hybrid organic-inorganic systems for conservative treatments of stone and wood. The wood preservative synthesized and tested for biocidal activity is a polyamidoamine functionalized with hydroxyl and siloxane groups, while the coating applied on the stones is a water based TiO₂ nanosol with photocatalytic and self-cleaning properties.

The work is divided into three parts:

In PART A is reported the synthesis of amidoamines by Michael addition reaction between an α,β -unsaturated amide (2-propenamamide or N,N'-methylenebisacrylamide) and an amine (ethanolamine or diethanolamine). Their synthesis is a simple system for the study of polyamidoamines.

The characterization of the starting reagents and the products of addition was made by means of different techniques (ESI-MS, NMR, FTIR and Raman spectroscopy) in order to define the best reaction conditions.

In PART B are investigated organic and hybrid inorganic-organic polyamidoamines for wood protection, functionalized with OH or siloxane groups or both. Polymers were applied on wood samples and their efficacy against fungi and termites has been verified according to UNI EN. The interaction with the substrate, the depth of penetration and the color changes induced by the treatment were also investigated.

PART C is devoted to the synthesis and characterization of sol-gel TiO₂ based coatings for the photocatalytic self-cleaning of stone material. Coatings at different pH were applied to biocalcarenites typical of southern Italy (Comiso, Modica, Noto and Lecce stones) used in the Baroque period of interest for cultural heritage. The effectiveness of the photocatalytic sols was verified by evidence of degradation of dyes under UV-Vis irradiation. In accordance with the rules on cultural heritage, the harmlessness of coating towards the substrate has been investigated.

PART A

Synthesis and characterization of amidoamines as model molecules for polyamidoamines

A.1 - INTRODUCTION

Polyamidoamines (PAA) can be synthesized by polyaddition of aliphatic primary amines or secondary diamines to bisacrylamides. One of the main advantages of PAAs is their versatility, due to the possibility of functionalization, which allows building complex molecular architectures by relatively simple synthetic procedures [A1-2]. Polyamidoamines obtained via polyaddition of MBA with primary amines used for the protection of lignocellulose materials against biological attack will be presented in the next chapter.

Single molecules of amidoamines were then produced in order to obtain the characterization of a small, relatively simple system, that can be considered as precursor of polyamidoamines, and mimic the physical-chemical properties of the corresponding polymers. The starting reagents were also investigated to understand the reaction mechanism.

A.1.1 - Amidoamines

The amidoamines are β -amino carbonyl compounds obtained by addition of primary or secondary amines to mono/bis-acrylamides. The β -amino functionality is a segment of important natural and synthetic products. These compounds and their derivatives, such as β -aminoamides, are versatile intermediate molecules for the synthesis of nitrogen-containing products: antibiotics, β -amino alcohols, optically active amino acids, products with a wide range of biological activities or pharmacological properties [A3-11]. A convenient way to introduce an amine function is the 1,4-addition of nitrogen nucleophile to α,β -unsaturated carbonyl-containing compounds, also called aza-Michael addition [A12-13]. The reaction is carried out in polar solvents at room temperature very efficiently with or without catalyst. Significant rate acceleration of this reaction is observed in water compared to organic solvents [A14-15].

The Michael reaction is a "Green Chemistry" method. The development of simple and environmental friendly processes to obtain organic compounds is currently receiving considerable attention [A16].

A. 1.1.1 - The Aza-Michael addition reaction

The Michael addition reaction, usually known "conjugate addition", has received a great attention as a polymer synthesis strategy for tailored macromolecular architectures [A17] and has been employed in the synthesis of linear [A2], graft, hyperbranched [A18], dendritic and crosslinked [A19] polymers such as hydrogels [A20], thermosetting resins and coatings [A21].

The Michael addition, named for Arthur Michael, is a simple reaction between nucleophiles (Michael donor) and activated electrophilic olefins (Michael acceptor). The reaction scheme is shown in Fig. A.1. A wide variety of functional groups possess sufficient nucleophilicity to behave as Michael donors (amines, thiols and phosphines) or even more as Michael acceptors (acrylates, acrylamides, cyanoacrylates, vinyl sulfones, vinyl ketones, vinyl phosphonates, vinyl pyridines, azo compounds, α,β -unsaturated aldehydes, β -keto-acetylenes and acetylene esters) [A22].

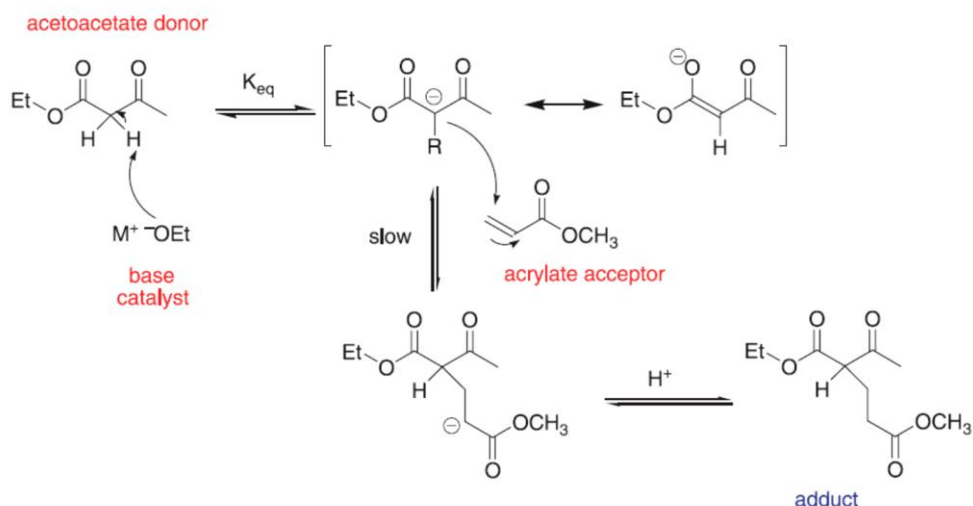


Fig. A.1 - Scheme of the Michael addition reaction [A17].

Originally, the reaction was carried out mostly with carbon nucleophiles, and then other nucleophiles have been used, like N (aza-Michael) and S (thia-Michael), to design C-N and C-S bond, respectively [A23]. The conjugate addition of nitrogen nucleophiles represents an especially interesting variant, since the resulting β -amino carbonyl compounds, including β -amino acids [A24] and β -lactams [A25], are both pharmacologically and synthetically of great importance. The reaction is implemented under mild conditions enabling the preparation of a wide range of polymers in environments in which other polymerization mechanisms would not operate such as in biological applications. The reaction proceeds rapidly at room temperature, provides low cure times, involves less toxic precursors and is characterized by the absence of volatile byproducts [A25]. The aza-Michael, in particular, can be performed in water without any catalyst at room temperature. The increase of the reaction rate in water with respect to other solvents was explained by H-bonding of H₂O to the amine and carbonyl group of α,β -unsaturated compounds [A16].

A. 2 - EXPERIMENTAL

A. 2.1 - Materials

N,N'-methylenebisacrylamide (99%), ethanolamine (98%), diethanolamine (99.5%) were purchased from Sigma-Aldrich, acrylamide (98%) from Fluka.

A. 2.2 - Synthesis

To verify the influence of synthesis conditions (steric hindrance, solvent, reaction time and temperature) on the aza-Michael reaction rate, acrylamide (AA) or N,N'-methylenebisacrylamide (MBA) with diethanolamine-DEtA (*sec*-amine) and acrylamide with ethanolamine-EtA (*prim*-amin) were added in different solvents (water and ethanol), at two temperatures (RT and 55 °C) and at different reaction times (4h, 12h, 48h).

The molecules obtained by Michael addition are henceforth named AADEtA (AA+ DEtA), AAEtA (AA+EtA) and MBADEtA (MBA+DEtA).

A. 2.2.1 – AADEtA

Acrylamide, dissolved in the solvent (water or ethanol), and *sec*-amine in equi-molar ratio, were mixed into a bottom round flask, equipped with magnetic stirrer. The mixture was stirred for 4h, 8h

and 48h at room temperature or at 55 °C. The clear and yellow pale solutions were dried in *vacuo* and analyzed by ESI-MS, NMR, FT-IR and Raman spectroscopies.

A. 2.2.2 – AAEtA

The adduct between N,N-methylenebisacrylamide and ethanolamine, in molar ratio 1:2, was obtained by adding dropwise a water or alcoholic solution of EtA to a solution (in the same solvent) of MBA. The reaction mixture was stirred at room temperature (or 55°C) for 4h (8h or 48h) and then the solvent was evaporated in *vacuum* to give the crude product (yield 97%) as an amber-yellow viscous liquid.

A. 2.2.3 - MBADEtA

The addition product between acrylamide (AA) and diethanolamine (DEtA), in molar ratio 2:1, was obtained with the same procedure described above. The final product is a pale yellow solution.

A. 2.3 - Characterization

The model amidoamine molecules have been characterized with a variety of experimental techniques: Electrospray Ionization Mass Spectrometry (ESI-MS), Nuclear Magnetic Resonance (NMR), Attenuated Total Reflection (ATR)/Fourier Transform Infrared (FTIR) and Raman and spectroscopies.

A. 2.3.1- Electrospray ionization mass spectrometry (ESI-MS)

Electrospray ionization mass spectrometry (ESI-MS) was recorded using Thermo Scientific™ LTQ XL Linear Ion Trap Mass Spectrometer (Ion spray voltage 4 (kV); capillary temperature, 200 °C; sheath gas flow rate 5 (arb.)). Samples were solubilized in methanol. Flow injection analysis was done in positive ionization mode and in full scan mode across the 50.00-250.00 m/z range.

A. 2.3.2 - Nuclear magnetic resonance (NMR): ¹H-NMR, ¹³C-NMR

NMR spectra were acquired with BRUKER AVANCE 300 and BRUKER AVANCE 400 NMR spectrometers. The instruments use a 5 mm multinuclear probe (¹H, ¹³C), for high resolution with actively shielded gradient along the z-axis, equipped for automatic tuning and matching. The samples were dissolved in deuterated solvents: D₂O, DMSO-d₆, CDCl₃. For the determination of the chemical shift, data were compared with those in the literature.

A. 2.3.3 - Fourier Transform Infrared Spectroscopy (FT-IR)

The Fourier-Transform Infrared (FT-IR) spectroscopy investigations were carried out on the product obtained by drying the solutions of the Michael reactions. Spectra were collected with a Thermo-Nicolet Nexus spectrometer equipped with a Thermo Smart Orbit ATR diamond accessory. The spectral resolution was 4 cm⁻¹, operating in the 4.000-400 cm⁻¹ range. Data were elaborated with OMNIC software.

A. 2.3.4 - μ-Raman Spectroscopy

Non-polarized Raman spectra on the samples were recorded at 632.8 nm in a nearly backscattered geometry with a Horiba - Jobin Yvon LabRam micro-spectrometer (300 mm focal length

spectrograph) equipped with an integrated Olympus BX40 microscope provided with x10-x50-x100 objectives. The spectral resolution was about 1.5 cm^{-1} .

The Rayleigh radiation was blocked by an edge filter and the backscattered Raman light was dispersed by an 1800 grooves/mm holographic grating on a Peltier cooled CCD, consisting of an array of 1024/256 pixels. The entrance slit width was fixed at $100 \mu\text{m}$. The laser power was adjusted by means of density filters to avoid uncontrolled thermal effects. The power on the sample was always less than 1 mW.

Spectra were collected using both x100 and long working distance x50 microscope objectives. Typical exposures were 10-60 s, with 5-9 repetitions. The system was regularly calibrated using the 520.6 cm^{-1} Raman band of silicon or by means of reference emission lines of Ne or by Cd light sources. The data analysis was performed by LabSpec built-in software.

A. 3 - RESULTS AND DISCUSSION

The reaction schemes examined are reported below (Fig. A.2, A.3).

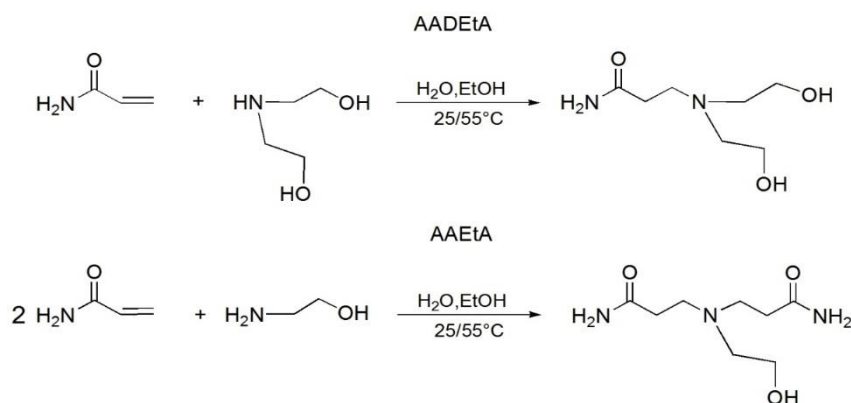


Fig. A.2 - Reaction scheme of AA with EtA and DEtA.

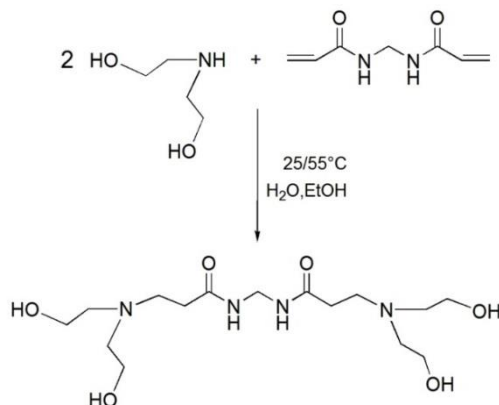


Fig. A.3 - Reaction scheme of MBA with DEtA.

After a series of experiments, it was established that an excellent yield of the Michael adduct can be achieved by reacting a mixture of acrylamide and diethanolamine in water at 55°C for 4h, without catalyst. Because of the strong nucleophilicity of the nitrogen atom of amines, base catalysts are often unnecessary in aza-Michael reaction. The reaction tends to follow second-order kinetics based on the concentration of the olefin acceptor and of the amine [A17].

The AA+EtA and MBA+DEtA reactions required much longer times (12-48 hours). Primary amines can react with two equivalents of acceptor to form tertiary amines while bisacrylamide requires two equivalents of donor. The second addition affects the kinetics of the reaction, especially as the concentration of the secondary amine increases [A17].

In general, the reactions were very clean and high yielding. All the reactions in water were quite fast, compared to the reactions in ethanol. Water plays an important role by forming hydrogen bonds with the carbonyl group, and consequently accelerating the addition step [A15].

To better characterize the reaction products, ^1H -NMR and $^{13}\text{C}\{^1\text{H}\}$ -NMR, Raman and Infrared spectra of the pure reagents were firstly recorded.

A. 3.1 - Characterization

A. 3.1.1 - Pure reagents

A. 3.1.1.1 – Acrylamide

A. 3.1.1.1.1 - ^1H -NMR and $^{13}\text{C}\{^1\text{H}\}$ -NMR

In Figure A.4 and A.5 are shown the ^1H -NMR and $^{13}\text{C}\{^1\text{H}\}$ -NMR spectra of acrylamide in $\text{DMSO}-d_6$, respectively.

The ^1H -NMR spectrum of acrylamide consists of two broad signals downfield (7.5 and 7.1 ppm) due to the proton of NH_2 and of signals due to the vinyl protons at slightly higher fields. Amides have an important resonance contribution that confers considerable double bond character between the carbon atom of the carbonyl and the amide nitrogen. This limits rotation about the carbon nitrogen bond, and this makes the two amide protons different. The protons of terminal vinyl group are labeled as shown in the insert in Fig. A.4. Protons H(a), H(b) and H(c) are non-equivalent and there is a small interaction between them. This interaction is due to the effect that the proton spin has on the bonding electrons. Protons H(b) and H(c) are attached to the same atom, and have a small value of J . Proton H(a) interacts with both H(b) and H(c): its orientation with respect to H(b) is trans and yields a higher coupling constant while its cis interaction with H(c) yields a lower coupling constant [A26]. The signals due to vinyl protons consist therefore of three doublets of doublets (insert in Fig. A.4): δ 6.19 (a) (J_{ab} 14.7 Hz; J_{ac} 9.9 Hz), δ 6.07 (b) (J_{ab} 14.7 Hz, J_{bc} 2.6 Hz) and δ 5.59 (c) (J_{bc} 2.6 Hz, J_{ac} 9.9 Hz).

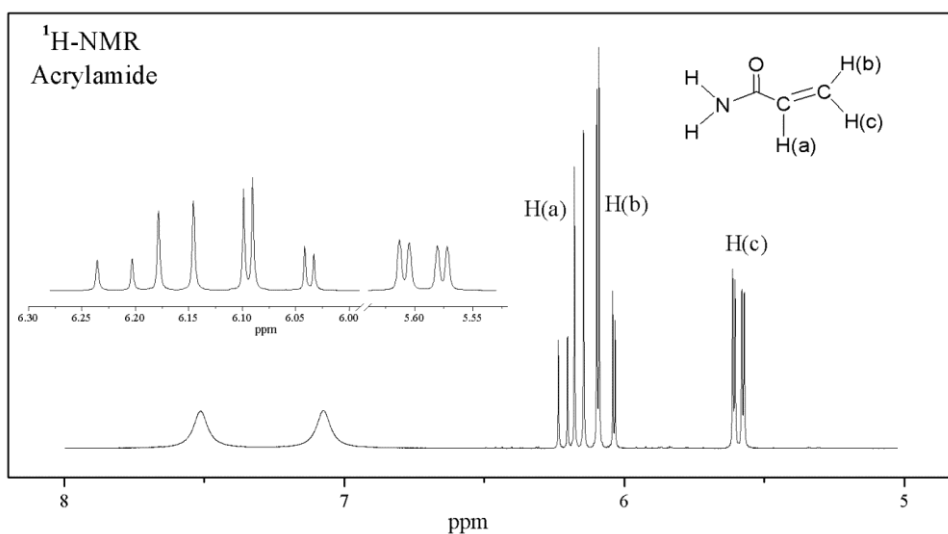


Fig. A.4 - ^1H -NMR of acrylamide in $\text{DMSO}-d_6$.

The $^{13}\text{C}\{^1\text{H}\}$ -NMR spectra are generally easier to interpret than in ^1H -NMR. In the $^{13}\text{C}\{^1\text{H}\}$ -NMR spectrum (Fig. A.5) the signal due to the carbonyl carbon atom is at 167 ppm (1) and those due to the carbon atoms of the vinyl moiety are at 132 ppm (3) and at 126 ppm (2). The peak (3), corresponding to the methine carbon atom, is shifted downfield due to its proximity to the electron withdrawing carbonyl group [A26].

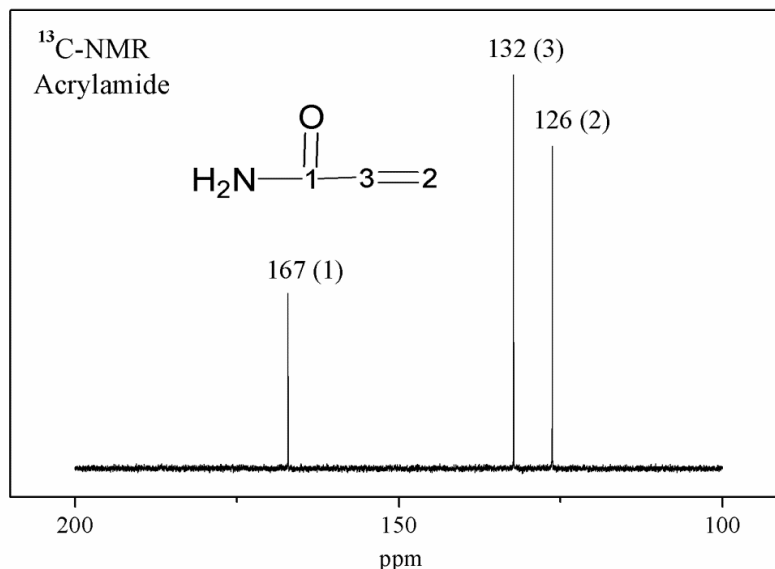


Fig. A.5 - $^{13}\text{C}\{^1\text{H}\}$ -NMR of acrylamide in $\text{DMSO}-d_6$.

A. 3.1.1.1.2 - Vibrational spectroscopies: FTIR and Raman

As regards the Raman and IR spectra of amides, all show a medium-strong carbonyl absorption band, known as the amide I band, NH stretching bands (two in primary amide only one in secondary amide) and a strong NH deformation band, named amide II¹. Their position depends on the degree of hydrogen bonding and on the physical state of the compound.

The C=O absorption of amides occurs at lower wavenumber than "normal" carbonyl absorption due to the resonance effect [A27]. Primary amides in the solid phase, in general, show a strong amide I band at about 1650 cm^{-1} and a sharp amide II absorption band in the range $1655 - 1620\text{ cm}^{-1}$ with an intensity of one-half to one-third of amide I. In solution, the amide II band appears at lower wavenumbers, $1620 - 1590\text{ cm}^{-1}$, and usually is separated from the amide I band.

In the α,β -unsaturated amides, the carbonyl absorption band moves to higher wavenumbers (1665 cm^{-1}) due to the inductive effect -I of the double bond. This effect reduces the length of the C=O bond and thus increases its force constant and the absorption frequency [A28].

The FTIR and Raman spectra of solid acrylamide are shown in Fig. A.6. The NH and CH stretching vibrations can be observed in the region at high wavenumbers. In particular, the two bands, strong in the FTIR absorption spectrum and weak in the Raman spectrum, at 3339 cm^{-1} and 3159 cm^{-1} are assigned to the antisymmetric and symmetric stretching modes of the NH_2 group, respectively. On the other hand, the bands between ≈ 3000 and 3120 cm^{-1} , strong in the Raman spectrum and very weak in FTIR, are due to the stretching modes of the terminal vinyl groups ($\nu_{\text{as}}(=\text{CH}_2)$ at 3105 cm^{-1} , $\nu_{\text{s}}(=\text{CH}_2)$ at 3009 cm^{-1} , $\nu(=\text{CH})$ at 3031 cm^{-1} [A29-30]).

¹ The amide II is due to the coupling of NH bending and CN stretching vibrations

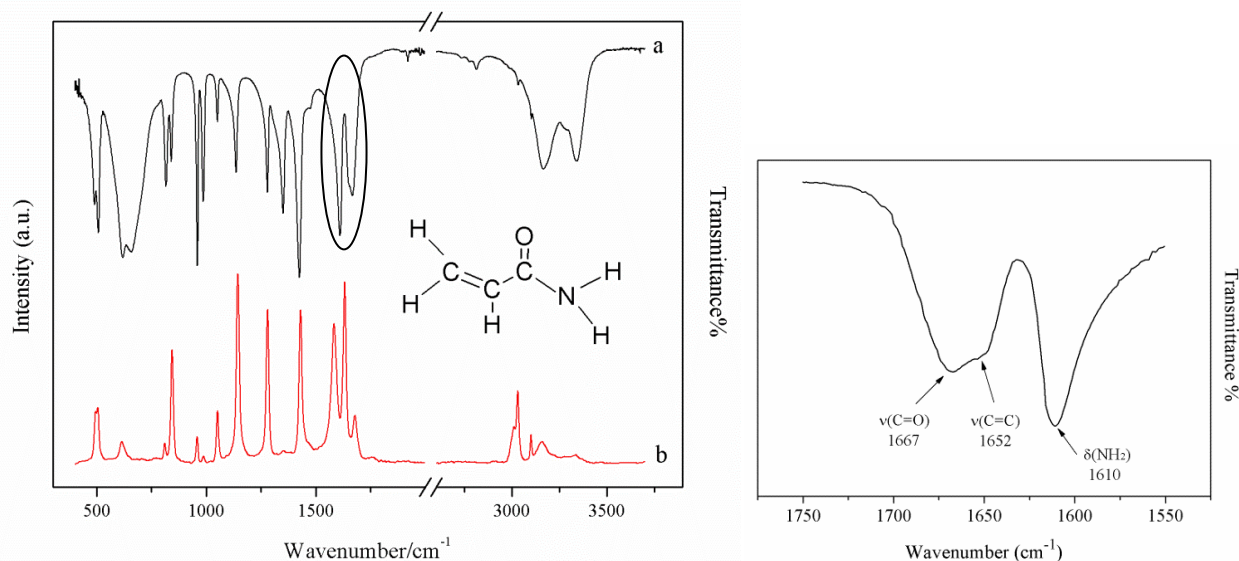


Fig. A.6 - FTIR (a) and Raman (b) spectra of acrylamide. The insert shows a detail of amide I, vinyl group and amide II absorption bands.

The vibrational bands of amide group ($\text{H}_2\text{NC}=\text{O}$) are found in the $1700\text{--}1550\text{ cm}^{-1}$ spectral region. The amide I and amide II bands are very strong both in FTIR and in Raman spectra. In the FTIR spectrum, the Amide I band is at 1667 cm^{-1} and the amide II band at 1610 cm^{-1} . This asymmetric amide II band is apparently due to a superposition of two bands. Jonathan [A31], in a solution of acrylamide in chloroform, found two bands at 1618 and 1592 cm^{-1} . The Raman vibrational frequencies of amide group are shifted with respect to FTIR. The amide I is centered at 1681 cm^{-1} and the amide II band at 1583 cm^{-1} . The strong band in the Raman spectra at 1633 cm^{-1} , between the two amide bands, is due to the stretching vibration of double bond ($\nu(\text{C}=\text{C})$). In the FTIR spectrum the $\nu(\text{C}=\text{C})$ band is visible only as a shoulder on the low-frequency side of the $\nu(\text{C}=\text{O})$ absorption band. The absorption band of the alkene bond in conjugation with the carbonyl group is located at lower wavenumbers (about 30 cm^{-1}) than that of an isolated $\text{C}=\text{C}$ bond and its intensity is greater [A27]. The remaining deformation modes of NH_2 , i.e. $\rho(\text{NH}_2)$, $\omega(\text{NH}_2)$ and $\tau(\text{NH}_2)$, are assigned to the Raman bands at 1143 [A33], 811 and 708 cm^{-1} and to the IR absorption bands at 1137 [A33], 816 cm^{-1} (or 843 cm^{-1} [A31]) and 618 cm^{-1} [A31-32]. The other strong bands are due to bending vibrations of vinyl CHs and to skeletal vibrations of C-C and C-N. The strong bands at 1424 cm^{-1} and at 1351 cm^{-1} in FTIR spectrum are attributed to $\delta(\text{CH}_2)$ and $\delta(\text{CH}) + \nu(\text{CN})$ according to Ref. A30) respectively. In the Raman spectrum, the $\delta(\text{CH}_2)$ band is very strong and centered at 1430 cm^{-1} , while the $\rho(\text{CH})$ band at 1351 cm^{-1} is very weak. The stretching vibration of C-N (named amide III)² is present with strong intensity in the Raman spectrum and medium intensity in IR at 1281 cm^{-1} . The out of plane deformation vibrations of vinyl group are located at 1051 cm^{-1} ($\rho(\text{CH}_2)$), 958 cm^{-1} ($\omega(\text{CH}_2)$) and at 843 cm^{-1} ($\omega(\text{CH})$) [A32] (811 cm^{-1} (R) and 816 cm^{-1} IR [A31]). In Table A.1 are summarized the bands observed in Raman and IR spectra of acrylamide.

² Very complex band resulting from mixtures of several atomic displacements

Table A.1 - Vibrational bands (FTIR and Raman) of acrylamide.

IR		Raman			Assignment	Notes
Ref. [A32]	observed	Ref. [A32]	observed	observed		
Solid		Solid		Solution		
3358w	3339ms	3342w	3339br	3355m	$\nu_{as}(\text{NH}_2)$	
3180w	-	3163vs	3189vw	3278ms	$\nu_{as}(\text{NH}_2)$	
	3159ms	-	3159m	3204ms	$\nu_s(\text{NH}_2)$	
3105vs	3101w	3103w	3105ms	3106ms	$\nu_{as}(\text{CH}_2)$	
3030ms	3033w	3030ms	3031s	3035s	$\nu_s(\text{CH})$	
3011w	-	-	3009m	3004ms	$\nu_s(\text{CH}_2) + \nu(\text{CH})$	
1675w	1667s	1685ms	1681m	1668ms	Amide I $\nu(\text{C}=\text{O})$	
1650w	1652	1639vs	1633vs	1629vs	$\nu(\text{C}=\text{C})$	
1612ms	1610s	1595vs	1583vs	1599vs	Amide II	$\delta(\text{NH}_2) + \nu(\text{CN})$ doublet [A31]
1430vs	1424vs	1432vs	1430vs	1433vs	$\delta(\text{CH}_2)$	
1353s	1351s	1350w	1351w	1338vw	$\rho(\text{CH})$	$\delta(\text{CN})$ [A28,A33]
1282s	1281m	1280s	1281m	1283vs	Amide III	$\nu(\text{CN}) + \delta(\text{NH}_2)$
1138 s	1137m	1149s	1143vs	1125s	$\rho(\text{NH}_2)$	
1053s	1051mw	1052s	1051ms	1052m	$\rho(\text{CH}_2)$	
991s	985s	990	985w	972mw	$\nu(\text{C}-\text{C})$	[A31,A33]
963vs	958vs	963w	958ms		$\omega(\text{CH}_2)$	
831m	843m	831s	843s	835w	$\omega(\text{CH})$	$\omega(\text{NH}_2)$ [A31,A33]
816m	816ms	816m	811mw		$\omega(\text{NH}_2)$	$\omega(\text{CH})$ [A31,A33]
708w		708	708vw		$\tau(\text{NH}_2)$	
660w	660s	665w			$\tau(\text{CH}_2)$	
626w	618s	626s	613mw	620m	$\delta(\text{CN})$	$\tau(\text{NH}_2)$ [A31,A33]
510vs	503s	-	507ms	514sh	$\delta(\text{O}=\text{C}-\text{N})$	
		490m	496 ms	494m	$\tau(\text{C}=\text{O})$	

ν = stretching; δ = bending; ρ = rocking; ω = wagging; τ = twisting

A. 3.1.1.1.3 - Raman spectra of “neat acrylamide” and in water solution

Fig. A.7 displays the Raman spectra obtained for solid acrylamide and for acrylamide in water solution, at 298 K. As reported by Duarte et al. [A33], ab initio calculations of the conformation of neat acrylamide dimers and their vibrational spectra indicate that the monomers exist in two stable conformations *trans* and *cis* conformers, even if at 298 K the most stable and populated form is the *trans* conformer (91%). Due to the presence of $-\text{NH}_2$ and $-\text{C}=\text{O}$ groups in both the *trans* and *cis* conformers of acrylamide, a considerable amount of intermolecular hydrogen bonding is expected to occur [A34]. Thanks to mutual interaction of two acrylamide *trans* conformers, dimers may be obtained. The stability of dimers is assured by intermolecular hydrogen bonds involving the $\text{C}=\text{O}$ (proton acceptor) and NH_2 (proton donor) groups of opposite monomers [A33]. Solid-state acrylamide exists generally in the hydrogen-bonded dimeric form and also in trimeric form.

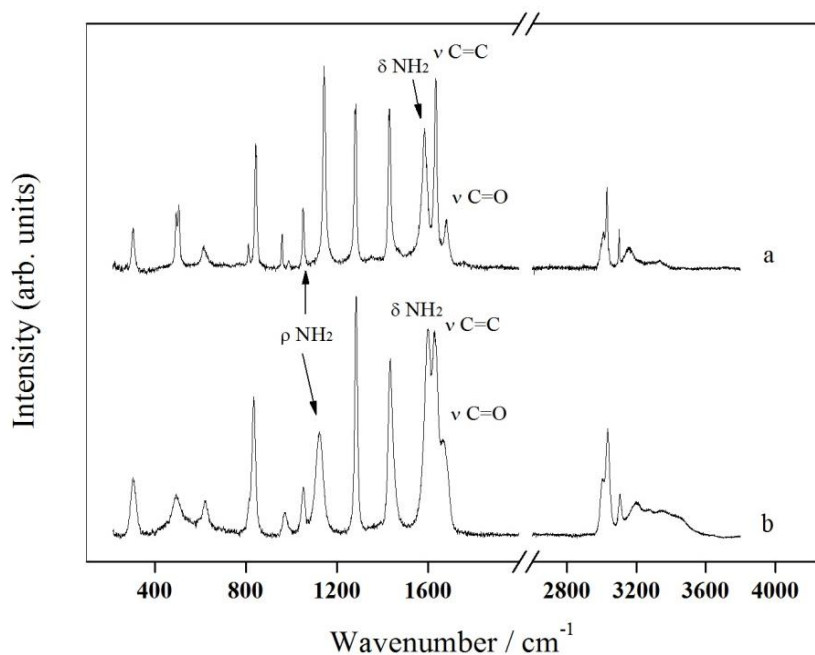


Fig. A.7 - Raman spectra at 298 K in solid acrylamide (a) and in acrylamide aqueous solution (b).

As expected, the most relevant changes between the spectra of solid acrylamide and in water solution occur in the NH_2 stretching, amide I (stretching $\text{C}=\text{O}$) and amide II (NH_2 deformation) regions. The main vibrational bands of solid acrylamide are discussed above (par. A. 3.1.1.1). In the spectrum of acrylamide in water solution 0.2M, the NH_2 stretching band shift to higher wavenumbers (3355 and 3204 cm^{-1}) as well as $\delta(\text{NH}_2)$ (1599 cm^{-1} , $\approx 16\text{ cm}^{-1}$ up-shift), while the carbonyl stretching band is found at 1668 cm^{-1} , down-shifted by $\approx 13\text{ cm}^{-1}$. No significant change is observed for the $\nu(\text{C}=\text{C})$ band. In addition to the shifts described, a general broadening of the $\nu(\text{C}=\text{O})$ band and of deformation band $\delta(\text{NH}_2)$ is evident.

In Fig. A.8 are compared the Raman spectra of acrylamide, in solid form and in water solution, in the spectral region $1550\text{-}1700\text{ cm}^{-1}$, where the major changes are observed.

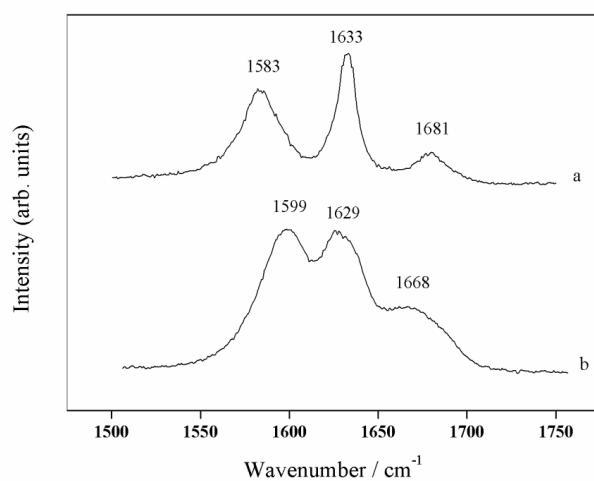


Fig. A.8 - The Raman spectra in the $1500\text{-}1750\text{ cm}^{-1}$ spectral region of solid acrylamide (a) and acrylamide in water solution (b).

A. 3.1.1.2 - N,N'-methylenebisacrylamide (MBA)

N,N'-methylenebisacrylamide (MBA, $C_7H_{10}N_2O_2$, Fig. A.9) is a bifunctional amide largely used as a cross-linking agent during the formation of polyacrylamide and as a building block for the synthesis of polyamidoamines by addition reaction with primary amines. Despite its wide use in many areas, the knowledge of the crystal structure of MBA is still missing, due to the difficulties to obtain good quality crystals, and the vibrational dynamics properties have received little attention.

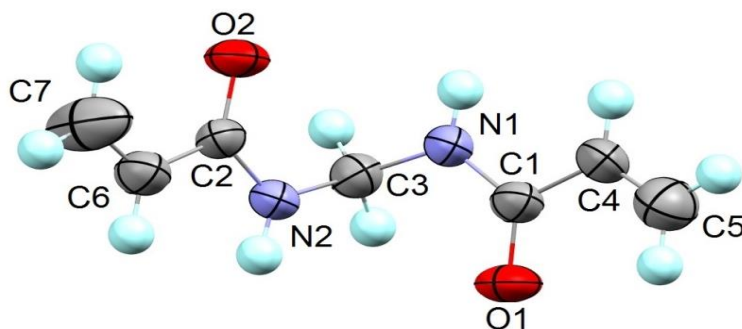


Fig. A.9 - The MBA molecule.

A. 3.1.1.2.1 - NMR

Fig. A.10 shows the 1H -NMR spectrum of MBA. The triplet signal at δ 4.54(e) is attributed to methylene bridge protons (J 5.9; $-NHCH_2NH$). Amidic protons give a triplet not well defined at δ 8.75(d) ($-NHCH_2NH$). Signals due to vinyl protons are at δ 6.25 (a) (J 9.9), $\delta = 6.13$ (c) (J 14.9) and $\delta = 5.63$ (b) (J 9.7). With respect to 1H -NMR spectrum of pure acrylamide, the doublets due to coupling of vinyl protons are not resolved.

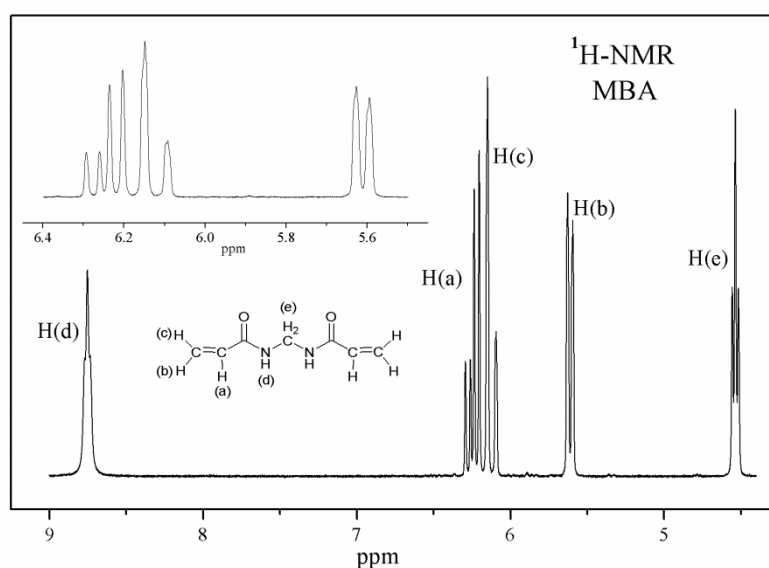


Fig. A.10 - 1HNMR of MBA in $DMSO-d_6$.

The $^{13}\text{C}\{^1\text{H}\}$ -NMR spectrum of MBA (Fig. A.11) shows the signal due to the carbonyl carbon (1) at 165.5 ppm and of the two vinyl carbons at 131.7 ppm (3) and δ 126.6 (2). The carbon of the aliphatic CH_2 , bridge between the two NH groups, resonates at $\delta = 43.9$ ppm.

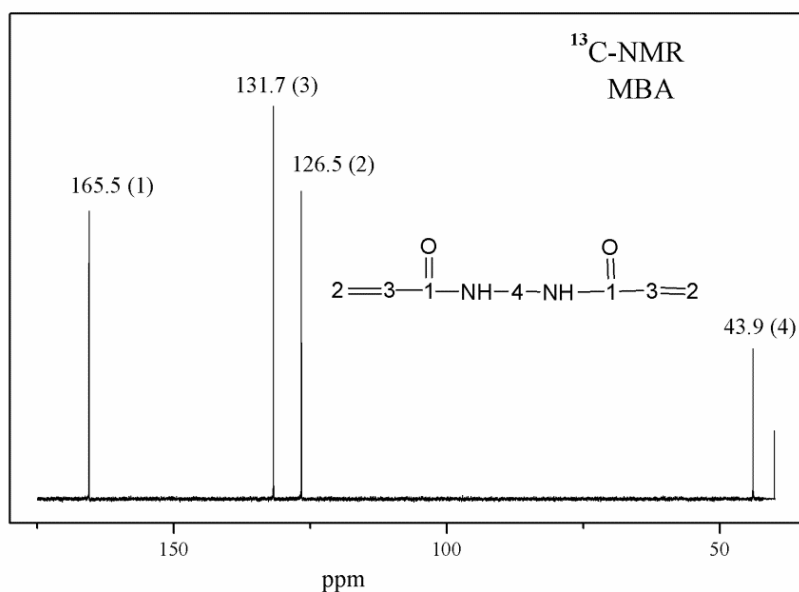


Fig. A.11 - $^{13}\text{C}\{^1\text{H}\}$ -NMR spectrum of MBA.

A. 3.1.1.2.2 - Vibrational spectroscopies: FTIR and Raman

In Fig. A.12 the FTIR and Raman spectra of MBA commercial powder are compared.

The strong infrared band centered at 3308 cm^{-1} and the weak band at 3304 cm^{-1} in Raman are assigned to $\nu(\text{NH})$. The amide I and amide II bands are strong in IR (1659 cm^{-1} and 1545 cm^{-1}) and medium-weak in Raman (1659 cm^{-1} and 1541 cm^{-1}). The band observed both in IR and Raman at 1306 cm^{-1} is attributed to C-N stretching (Amide III). The other significant bands in the IR and Raman spectra are related to stretching and deformation vibration of terminal vinyl groups. The antisymmetric stretching $\nu_a(=\text{CH}_2)$ at 3067 cm^{-1} IR and at 3057 cm^{-1} in Raman; the weak band at 3005 cm^{-1} (R) is due to symmetric stretching $\nu_s(=\text{CH}_2)$. The $\nu(=\text{CH})$ stretching vibration, weak in IR at 3037 cm^{-1} , gives medium-strong Raman counterpart at 3035 cm^{-1} [A35]. The m/s band at 3103 cm^{-1} in the Raman spectrum is attributed to the first overtone of NH scissoring (at 1541) enhanced by Fermi resonance interaction with the CH_2 stretching. The double bond stretching mode $\nu(\text{C}=\text{C})$ is strong both in IR and Raman, observed at 1626 cm^{-1} and 1631 cm^{-1} , respectively. The IR and Raman bands at 1435 cm^{-1} , 1073 cm^{-1} and 910 cm^{-1} may be assigned to $=\text{CH}_2$ scissoring rocking and wagging deformation modes, respectively [A35], and those at 1306 cm^{-1} , 993 cm^{-1} , 685 cm^{-1} to $=\text{CH}$ rocking, trans-wagging and cis-wagging, respectively [A35]. Frequencies and vibrational assignment of the main functional groups in MBA are resumed in Table A.2. The assignments are made according to [A35-A36].

As far as we know, only one paper reports the Raman spectrum of MBA [A36] and a calculation by a valence force field for some vibrational modes, assuming a planar structure for MBA (C_s point group).

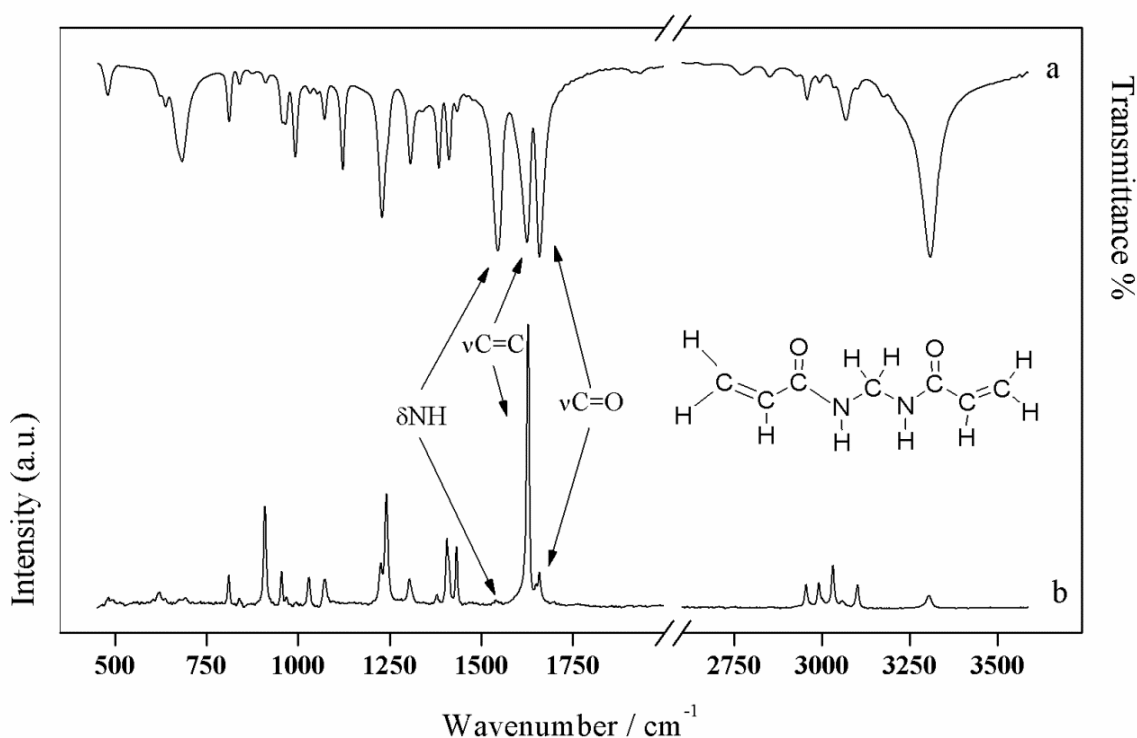


Fig. A.12 - FTIR (a) and Raman (b) spectra of crystalline (neat, solid) MBA.

A. 3.1.1.2.3 - Raman spectra of N,N'-methylenebisacrylamide crystals

MBA crystals were obtained in the form of elongated needles (Fig. A.13a) by slow evaporation of water solutions [A37]. Their structure was determined by single crystal X-ray diffraction assisted by a crystal structure prediction analysis applied on preliminary low quality powder diffraction data. The crystal structure is monoclinic, space group $C2/c$. The b axis is along the growth direction. Details on the structure determination will be published elsewhere.

The primitive unit cell of MBA crystals contains $Z=4$ formula units. The factor group analysis for $C2/c$ (C_{2h}^6) gives 252 vibrational modes at the Γ -point corresponding to $63A_g + 63B_g + 63A_u + 63B_u$ symmetry species. The A_g and B_g modes are Raman active, whereas the u -modes are only IR-active.

Here are reported (Fig. A.13b) micro-Raman spectra taken at RT with 632.8 nm excitation light on single needle-like crystals of MBA, taken at different orientations of the crystals (V = incident light polarization along the b -axis, H = incident light polarization perpendicular to the b -axis) and at parallel (PP) and crossed (OP) incident/scattered light polarizations. The scattering geometries evidence both A_g and B_g symmetry vibrational modes. A complete normal coordinate analysis and calculation of the Raman tensors and intensities of the active modes by ab-initio DFT methods are in progress.

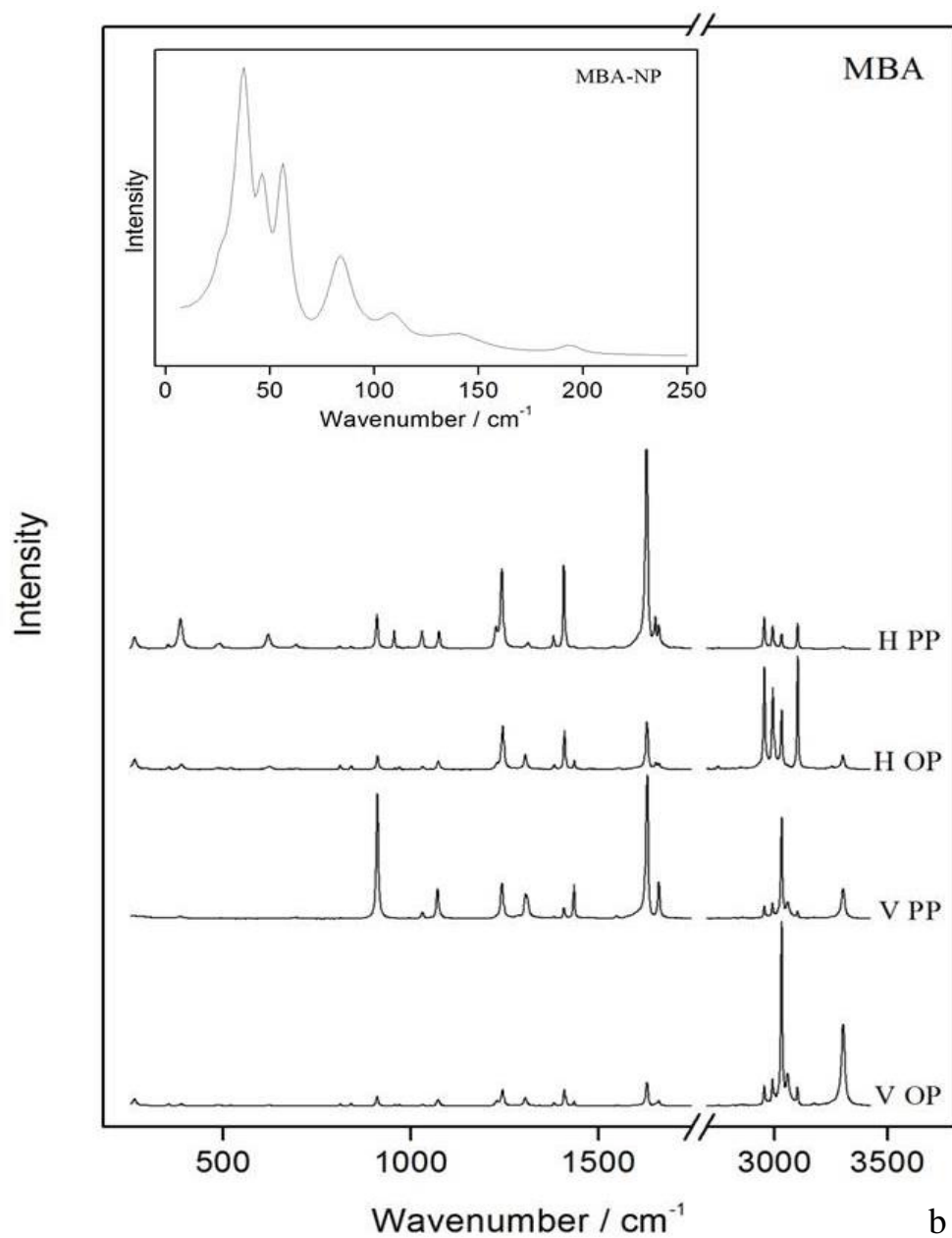
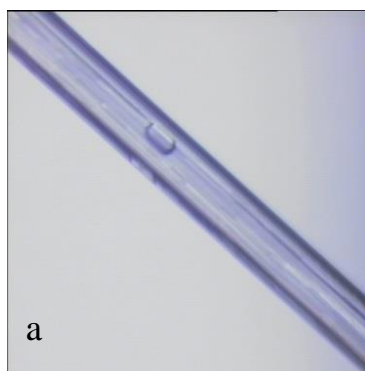


Fig. A.13 – a) Needle crystals of MBA; b) Raman spectra of MBA crystals at different orientations (V, H) and polarizations (PP, OP). The inset shows non polarized spectrum at low frequencies down to 20 cm^{-1} .

Table A.2 - MBA frequencies.

IR		Raman		Assignment	Notes
Ref. [A36]	observed	Ref. [A36]	observed		
	Solid		Solid		
3308s	3308s	3308s	3304m/s	v(N-H)	
3105vs			3103ms	$v_{as}(C_{\beta}H_2)+2 \times 1541$	Fermi resonance /amide II [A35]
3060s	3067ms		3057ms	$v_s(C_{\beta}H_2)$	
3030ms	3037w	3030ms	3035s	$v(C_{\alpha}H)$	[A35]
	2991w		2995ms		
2943s	2952ms	2957ms	2958ms	$v_{as}(C'H_2)$	
			2937m	$vs(C'H_2)$	
2845ms	2844m		2851m	$v(C_{\alpha}H)$	
1650vs	1659s	1662ms	1659m	Amide I $v(C=O)$	
1620vs	1626s	1635vs	1631vs	$v(C=C)$	
1535vs	1545s		1541w	Amide II	
1428ms	1435vs	1441s	1435vs	$\delta(C_{\beta}H_2)$	
1405s	1410s	1415	1409m	$\delta(C'H_2)$	
1380vs	1383s		1381w	$\omega(C'H_2)$	
1301vs	1306s	1311	1306 ms	Amide III	$\rho(C_{\alpha}H)$ [A35]
1138 s	1120m	1149s	1143s	$\rho(C'H)$	[A35]
1070s	1073s	1078ms	1073mw	$\delta(C_{\alpha}H)$	$\rho(C_{\beta}H_2)$ [A35]
987vs	993s		993w	$\rho(C_{\beta}H_2)$	trans $\omega(C_{\alpha}H)$ [A35]
965vs	967s	963w	968w	$v(C-C_{\alpha})$	
955vs	958vs	-	958m	$v(NC)$	
	910		910s	$\omega(NC')$	$\omega(C_{\beta}H_2)$ [A35]
831m	840m	831s	843w	$\tau(C'H_2)$	
816m	810s	816m	811mw	$\omega(NH_2)$	
	685m		685m		cis $\omega(C_{\alpha}H)$ [A35]
660w	666s	665w	670s	$\delta(O=C-N)$	
627w	618s	-	622w	$\delta(O=C-N)$	
510vs	512w	-	517w	$\delta(C_{\beta}=C_{\alpha}-C)$	
485s	478s	-	494w	$\delta(C_{\beta}=C_{\alpha}-C)$	

v = stretching; δ = bending; ρ = rocking; ω = wagging; τ = twisting

A. 3.1.1.3 - Ethanolamine (EtA), Diethanolamine (DEtA)

A. 3.1.1.3.1 - NMR

NMR analysis was performed by dissolving the reagent in DMSO- d_6 .

The 1H -NMR and $^{13}C\{^1H\}$ -NMR spectra of amines used in the synthesis of amidoamines are dominated by the signals due to the protons in the aliphatic chains.

Ethanolamine: δ_H 3.34 (2H, t, J 6.0 Hz, NCH_2CH_2OH) and 2.54 (2H, t, J 6.0 Hz, NCH_2CH_2OH); δ_C 63.87 corresponds to the carbon C(1) linked to alcoholic groups and $\delta_C = 44.55$ to the carbon C(2) linked to amine nitrogen.

Diethanolamine: δ_H 4.47 (1H, br, NCH_2CH_2OH), 3.45 (2H, t, J 5.9 Hz, NCH_2CH_2OH) and 2.56 (2H, t, J 5.9 Hz, NCH_2CH_2OH); δ_C 60.67 corresponds to the carbon C(1) linked to alcoholic groups and $\delta_C = 57.89$ to the carbon C(2) linked to amine nitrogen.

A. 3.1.1.3.2 - Vibrational spectroscopies: FTIR and Raman

The characteristic vibrational frequencies of amines, in FTIR and Raman spectra, arise from the NH_2 and NH group. The stretching of the NH_2 and NH group appears in the same region as OH stretching bands, at slightly lower frequency. In primary amines (RNH_2), there are two bands in this region, corresponding to the asymmetrical and the symmetrical NH_2 stretching modes. Secondary amines show only a single weak stretching band in the $3300\text{-}3200\text{ cm}^{-1}$ region, having only one N-H bond. The NH_2 bending vibration is observed in primary amines whereas the secondary amines usually do not show the NH bending band.

The strong and broad band due to N-H_2 and NH wagging mode is detected for both amines in the region $910\text{-}665\text{ cm}^{-1}$. As expected, the H -bonding leads to a reduction of stretching frequencies (OH , NH_2 , NH), an increase in NH_2 bending frequency and a broadening of the spectral bands. Normally in FTIR spectra the OH stretching bands are stronger than the NH_2 and NH stretching ones, while in Raman spectra the reverse is true [A35].

The IR and Raman spectra of ethanolamine (EtA) and diethanolamine (DEtA) are reported in Fig. A.14 and A.15, respectively.

In ethanolamine (Fig. A.14) the $\nu(\text{OH})$, $\nu_{\text{as}}(\text{NH}_2)$ and $\nu_{\text{s}}(\text{NH}_2)$ vibrations are found at 3356 , 3294 and 3172 cm^{-1} (at wavenumbers slightly higher in Raman), typical values for intermolecular H -bonded hydroxyl and amine groups, red-shifted with respect to the free molecules [A38]. The shoulder on the low wavenumber side of the $\nu_{\text{s}}(\text{NH}_2)$, in IR spectrum, is due to the first overtone of the NH_2 scissoring improved by Fermi resonance interaction with the NH_2 symmetric stretching [A35]. At 1599 cm^{-1} a medium/strong (IR), medium/weak (R) band is found, assigned to the NH_2 scissoring vibration. The NH_2 wagging is attributed to the strong band at 873 cm^{-1} in the IR and Raman spectra. The 1106 and 965 cm^{-1} bands are associated to the C-N stretching mode. The strong band at 1078 cm^{-1} is due to the out of phase CO stretching mode. The OH in-plane bending is coupled to the adjacent CH_2 wagging and gives rise to some bands in the $1400\text{-}1200\text{ cm}^{-1}$ region.

Fig. A.15 displays the IR (a) and Raman (b) spectra of DEtA. Fig. A.15 displays the IR (a) and Raman (b) spectra of DEtA. The broad OH stretching band at $\sim 3400\text{ cm}^{-1}$ appears superimposed on the clear NH stretching band at $\sim 3300\text{ cm}^{-1}$ while the shoulder on the low wavenumber side of the ν_{NH} , in the IR spectrum ($\sim 3180\text{ cm}^{-1}$), is a combination band. The $\nu_{\text{as}}(\text{C-N-C})$ and $\nu_{\text{s}}(\text{C-N-C})$ are found at 1125 cm^{-1} and 863 cm^{-1} , respectively. In the CH stretching region the strong bands in the $2820\text{-}2950\text{ cm}^{-1}$ range may be assigned to the antisymmetric and symmetric $\nu(\text{CH}_2)$ modes of the methylene groups. In the region $1500\text{-}1200\text{ cm}^{-1}$ there are strong bands due to the scissoring and wagging of CH_2 whereas the rocking vibration of the methylene groups is in the $800\text{-}650\text{ cm}^{-1}$ range. Wavenumbers and vibrational modes assignments to functional groups in diethanolamine DEtA and ethanolamine EtA are summarized in Table A.3 [A27, A35].

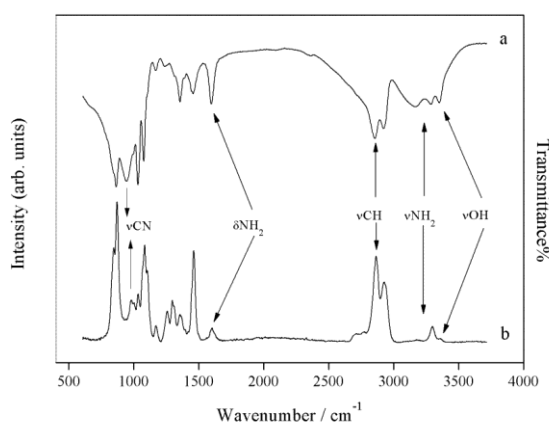


Fig. A.14 - FTIR and Raman spectra of ethanolamine (EtA).

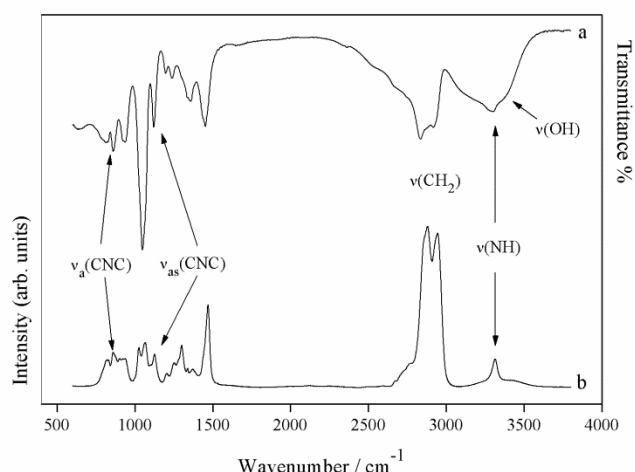


Fig. A.15 - FTIR (a) and Raman spectra (b) of Diethanolamine (DETA).

Table A.3 - Vibrational modes in DEtA and EtA.

Ethanolamine		Assignment [A38]	Diethanolamine		Assignment[A27,A35]
IR	Raman		IR	Raman	
3356ms	3359m	$\nu(\text{O-H})$	3397br	3400br	$\nu(\text{O-H})$
3294ms	3297s	$\nu_{as}(\text{NH}_2)$	3294br	3304ms	$\nu_{as}(\text{NH}_2)$
3172ms	3177w	$\nu_s(\text{NH}_2)$			
	2938sh	$\nu_{as}(\text{C}'\text{H}_2)$	2921s	2934vs	$\nu_{as}(\text{C}'\text{H}_2)$
2923vs	2926vs	$\nu_{as}(\text{C}''\text{H}_2)$		2864vs	$\nu_{as}(\text{C}''\text{H}_2)$
2855vs	2867vs	$\nu_s(\text{C}''\text{H}_2)$	2836s		$\nu_s(\text{C}''\text{H}_2)$
2826sh		$\nu_s(\text{C}'\text{H}_2)$			$\nu_s(\text{C}'\text{H}_2)$
1599ms	1599mw	$\delta(\text{NH}_2)$	1667vww		$\delta(\text{NH})$
1471sh		$\delta(\text{C}'\text{H}_2)$	1450ms	1467vs	$\delta(\text{C}'\text{H}_2)$
1457m	1462s	$\delta(\text{C}''\text{H}_2)$	1435sh		$\delta(\text{C}''\text{H}_2)$
1445sh		$\omega(\text{C}'\text{H}_2)$			
1391sh	1398vw	$\omega(\text{C}''\text{H}_2)$			
1356m	1365m	$\delta(\text{OH})$	1358m	1367	$\omega(\text{C}'\text{H}_2) + \delta(\text{OH})$
1311vw	1314sh	$\rho(\text{C}''\text{H}_2)$	1334sh	1335w	$\omega(\text{C}''\text{H}_2)$
	1297ms	$\rho(\text{C}'\text{H}) + \delta(\text{OH})$	1290sh	1298 ms	$\rho(\text{C}''\text{H}_2)$
1260sh	1260ms	$\nu(\text{CN})$ [A28]	1242w	1252mw	$\rho(\text{C}'\text{H}) + \delta(\text{OH})$
1168mw	1168mw	$\rho(\text{C}'\text{H}_2)$	1195w		
	1106s	$\nu(\text{CN})$	1125ms	1125s	$\nu_{as}(\text{CN})$
1076vs	1078s	$\nu(\text{CO})$	1051s	1064m	$\nu(\text{CO})$
1031vs	1033m	$\rho(\text{NH})$			
965s	965mw	$\nu(\text{CN})$			
942m	945mw	$\nu(\text{CC})$	940m	922br	$\nu(\text{CN}) + \nu(\text{CC}) + \nu(\text{CO})$
			919m		$\nu(\text{CN}) + \nu(\text{CC}) + \nu(\text{CO})$
864ms	873s	$\omega(\text{NH}_2)$	863m	863m	$\nu_s(\text{CN})$
835sh	846m	$\tau(\text{C}''\text{H}_2)$	824br	823mw	$\rho(\text{C}'\text{H}_2)$
					$\tau(\text{C}''\text{H}_2)$

A. 3.1.2 - Molecules

To verify the progress of the reactions, the analysis was performed through ESI-MS, NMR, FTIR and Raman spectroscopies. In the following sections, the characterization by different techniques of the individual amidoamine molecules synthesized by reacting *prim*- and *sec*-amine with acrylamide and bisacrylamide, according to aza-Michael addition, is presented. The aza-Michael addition is a simple nucleophile addition to activated electrophilic olefins. Ethanolamine (EtA), diethanolamine (DEtA) as nucleophiles and prop-2-enamide (acrylamide, AA) and N,N'-methylenebisacrylamide (MBA) as electrophiles were chosen for the present study. In particular, the changes in the characteristic vibrational peaks involving the CC double bond of amides ($\nu(=CH_2)$, $\nu(=CH)$) and $\nu(C=C)$ are investigated. During the addition reaction, the amine nitrogen attaches to β -unsaturated carbon of the carbonyl amide group and the double bond of acrylamide disappears, becoming a single bond: the vibrational bands associated with the vinyl group should reduce and eventually disappear.

A. 3.1.2.1 – AADEtA

The 3-[bis(2-idroxyethyl)amino]propanamide (named in this work AADEtA), obtained by reaction between acrylamide and diethanolamine, is the first molecule model designed to export the new knowledge of a simple reaction to improve the synthesis of the polyamidoamines. For this molecule, a study of reaction kinetics using Raman spectroscopy was also attempted.

The reaction mixture was stirred at room temperature for 5 h and then the solvent was evaporated in vacuo to give the crude product, (Yield: 99%) as a viscous liquid honey-like; elemental analysis found: C, 46.98; H, 9.21; N, 15.81 %; $C_7H_{16}N_2O_3$ requires C, 47.72; H, 9.15; N, 15.90%].

A. 3.1.2.1.1 - ESI-MS

Fig. A.16 shows the mass spectrum of AADEtA molecule synthesized using H_2O as solvent, at 55 °C for 4h. The signal with the highest intensity at m/z 177.24 is due to molecular peak $[M+H]^+$. At a lower intensity the ions m/z 199.19 and 248.21, corresponding to sodium adduct $[M+Na]^+$ and to acrylamide-adduct. The mass spectrum also indicates a fragment ion at m/z 118.78 due to mass loss of an amide group.

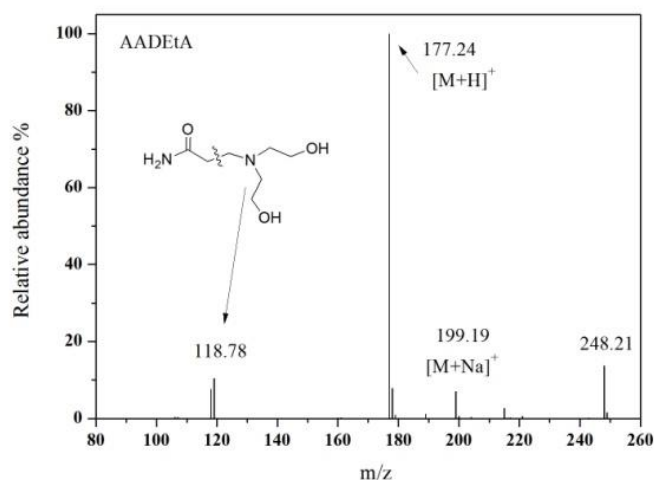


Fig. A.16 - ESI-MS spectrum of AADEtA (acrylamide+diethanolamine).

A. 3.1.2.1.2 – NMR

Figs. A.17 and A.18 show the ^1H -NMR and $^{13}\text{C}\{^1\text{H}\}$ -NMR spectra, respectively, of the reaction product AADEtA in Dimethyl sulfoxide- d_6 (DMSO- d_6).

In the ^1H -NMR spectrum (Fig. A.17) are present two broad signals, due to the proton of the amide, at low fields δ 7.45 (1H, br s, $\text{C}=\text{O}-\text{NH}_2$) and δ 6.80 (1H, br s, $\text{C}=\text{O}-\text{NH}_2$) and a broad signal at δ 4.3 due to the hydrogen atom of the alcoholic moiety (2H, br s, $\text{NCH}_2\text{CH}_2\text{OH}$). The attribution of the triplet signals to the protons has been obtained by integration of the signals: protons of the ethanolic chain at δ 3.42 (4H, t, J 6.3 Hz, $\text{NCH}_2\text{CH}_2\text{OH}$) and δ 2.51 (4H, t, J 6.3 Hz, $\text{NCH}_2\text{CH}_2\text{OH}$) and newly formed protons by the addition of amine to the double bond at δ 2.69 (2H, t, J 6.9 Hz, $\text{NCH}_2\text{CH}_2\text{CO}$) and δ 2.18 (2H, t, J 6.9 Hz, $\text{NCH}_2\text{CH}_2\text{CO}$). The vinyl protons of starting acrylamide are almost completely disappeared.

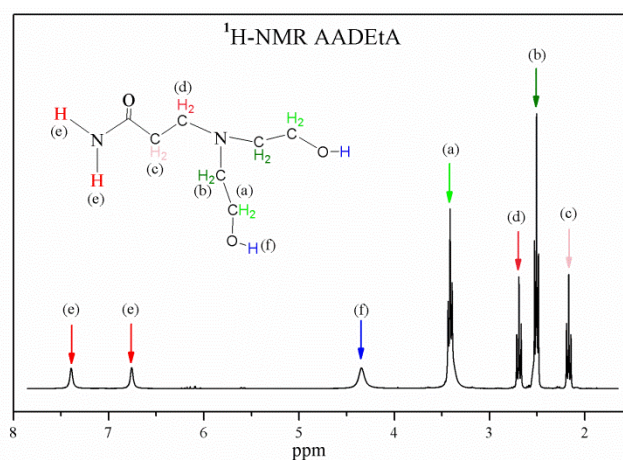


Fig. A.17 - ^1H -NMR of AADEtA (acrylamide-diethanolamine) synthesized in water at 55 °C for 4h. The arrows indicate the signals from the protons shown in the inset.

In the $^{13}\text{C}\{^1\text{H}\}$ -NMR spectrum (Fig. A.18) the signal at 175 ppm is due to the quaternary carbon atoms, with chemical shift at lower fields with respect to the acrylamide reagent (167.17 ppm). The signals of the carbon atoms resulting from the addition reaction are found at 56.56 and 33.46 ppm. Moreover, signals due to the carbon atoms of the added amine are also present (59.51 and 51.03 ppm). The multiplet at about 39.9 ppm is due to six carbon atom of DMSO- d_6 .

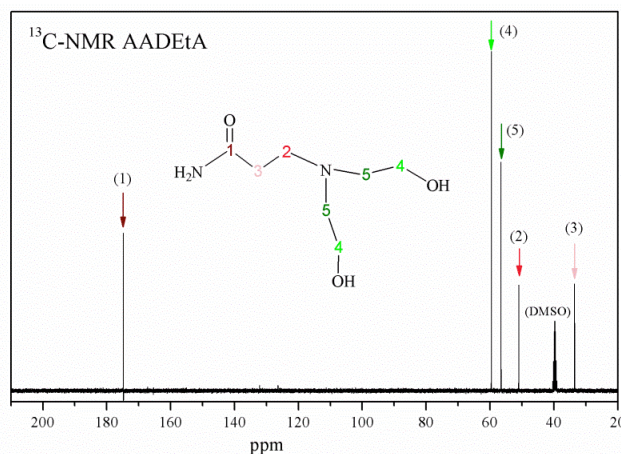


Fig. A.18 - $^{13}\text{C}\{^1\text{H}\}$ -NMR of AADEtA.

A. 3.1.2.1.3 - FTIR

In Fig. A.19a, the FTIR spectrum of the AADEtA molecule obtained in water, at 55 °C, is compared with the spectrum of acrylamide, while in Fig. A.19b it is reported a detail in the 1750-1500 cm^{-1} region.

The IR spectrum of acrylamide (Fig. A19a), as previously discussed, exhibits two intense bands due to the C=O stretching (1667 cm^{-1}) and NH_2 deformation vibrations (1610 cm^{-1}). The position of these bands depends on the occurrence of hydrogen bonds and of the double bond. The shoulder at 1642 cm^{-1} is assigned to C=C stretching. During the addition reaction, the amine nitrogen attaches to β -unsaturated carbon and the double bond of acrylamide becomes a single bond. Therefore, the vibrational bands associated with the vinyl group should reduce and eventually disappear.

Fig. A.19b shows a detail of the FTIR spectrum in the wavenumber range of the amide group for the product molecule compared to that of the starting reagent. It can be noticed that the band related to C=C stretching vibration disappears nearly completely in the product. At the same time, the band associated to $\nu(\text{C}=\text{O})$ shifts of about 10 cm^{-1} to lower frequencies and slightly increases in intensity, while the $\delta(\text{NH}_2)$ band keeps the same wavenumber but broadens and decreases in intensity.

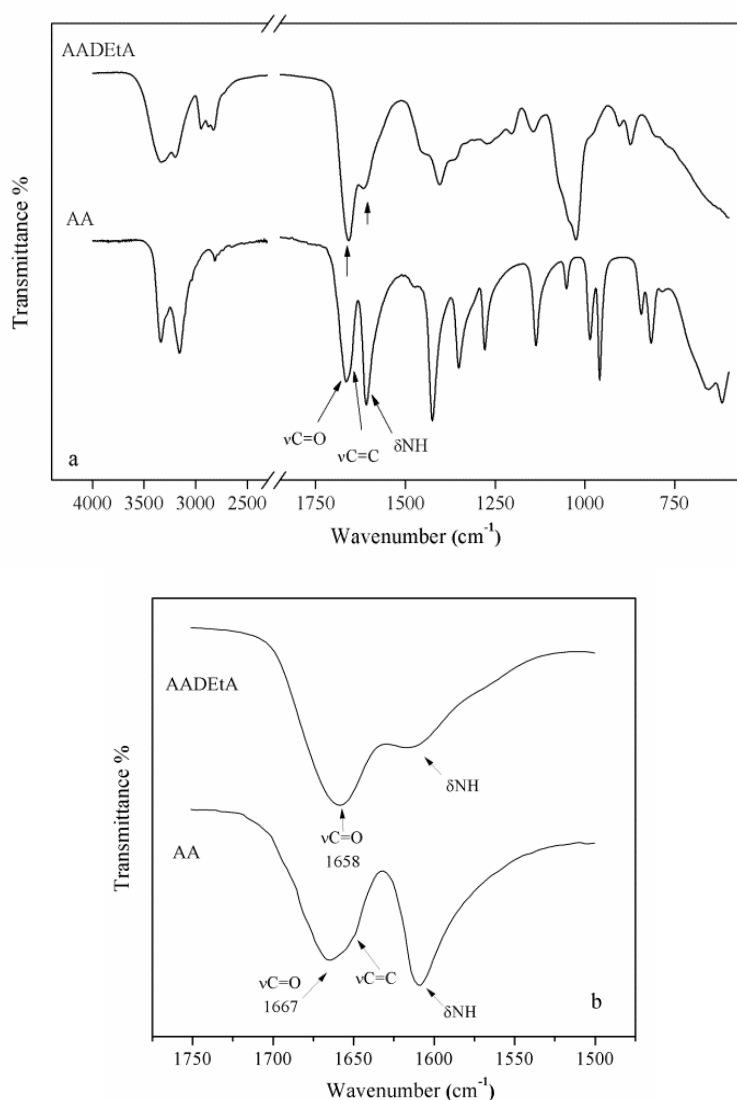


Fig. A.19 - FTIR spectrum of AADEtA molecule, synthesized in water, compared with that of acrylamide (a); detail of the amide group in AADEtA and in acrylamide (b).

A. 3.1.2.1.4 - Raman and reaction kinetics

The progress of the aza-Michael reactions between acrylamide and diethanolamine was studied through Raman spectroscopy. During the consumption of monomers, the acrylic C=C double bond is converted into a C-C single bond. The Raman spectra confirm the intensity decrease of the characteristic vibrational bands corresponding to the C=C stretching mode and to the stretching and bending modes of C-H vinyl bond. Moreover, the reaction product AADEtA is characterized by the presence of a tertiary amino-group and the intensity of the Raman band relative to C-N bond stretching vibration, newly formed, increases with the progress of the reaction.

In Fig. A.20 the Raman spectrum of AADEtA (in water at 55 °C, for 4h) compared with that of acrylamide reagent in water solution is reported. In acrylamide spectrum, the strong peak at 1627 cm^{-1} is attributed to C=C stretching, the medium peak at 1668 to amide I (C=O stretching) and the strong peak at 1601 cm^{-1} to amide II (C-N stretching and C-N-H bending) vibrations [A31, A33].

During the reaction, as the amine react and the double bond is broken, the 1627 cm^{-1} band decreases until it disappears completely. Due to the chemical environment changes, amide I band (1668 cm^{-1}) and the amide II band (1602 cm^{-1}) shift to 1663 and 1614 cm^{-1} , respectively.

The intense peak at 1433 cm^{-1} in the acrylamide spectrum, assigned to superposition of CH₂ bending mode and amide III (C-N stretching mode), after reaction is split in two bands at 1462 and 1415 cm^{-1} [A33]. Another very strong band of acrylamide is that corresponding to the vinyl C-H bending mode at 1292 cm^{-1} . This band disappears during the reaction, while a broad aliphatic C-H bending vibration in the adduct product emerges at 1309 cm^{-1} as expected when a C=C bond is broken.

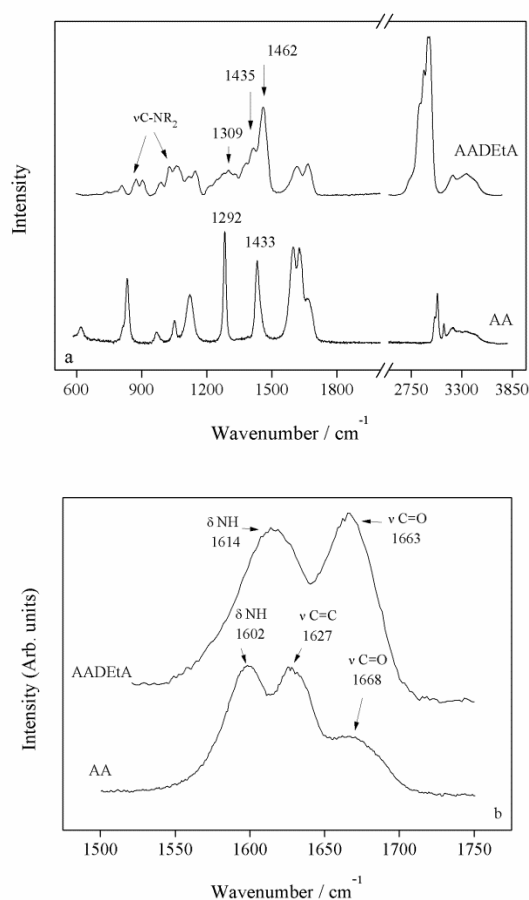


Fig. A.20 - Raman spectra of AADEtA and acrylamide in water solution (a); detail of the amide region (1750-1500 cm^{-1}).

A study of the reaction kinetics between acrylamide and diethanolamine, at a molar ratio AA:DEtA = 1:1 at room temperature, has been attempted by Raman spectroscopy, focusing on the C=C stretching band at about 1630 cm⁻¹. Fig. A.21 shows the sequence of Raman spectra taken at time intervals of 3 min during the addition reaction, in water and at RT. The intensity of the C=C stretching band gradually decreases, up to its complete disappearance, after about 5 hours.

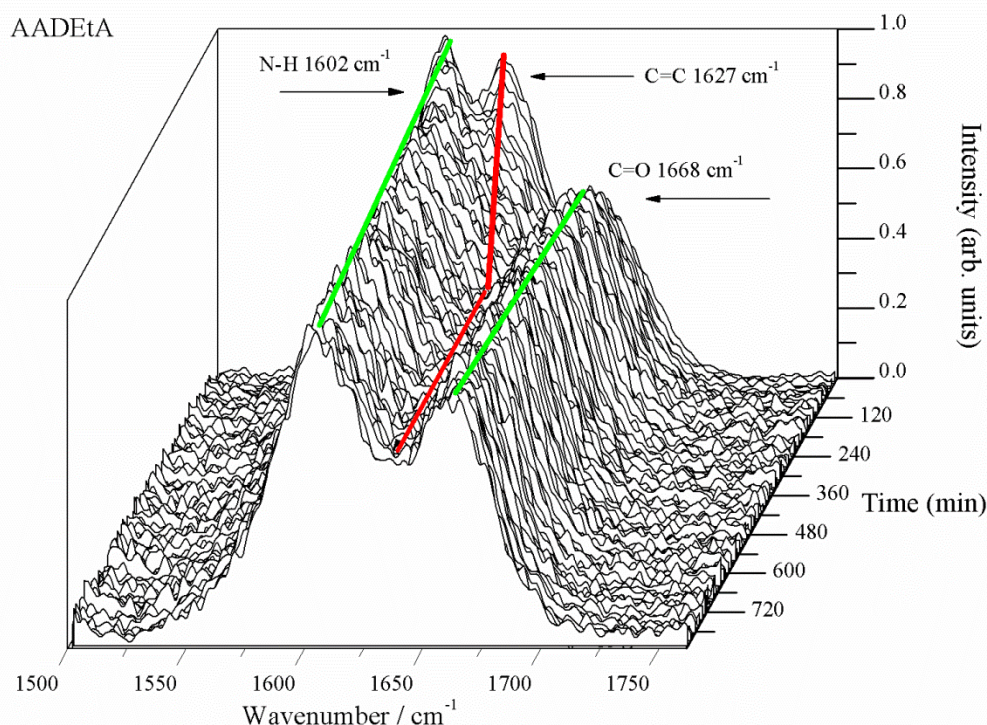


Fig. A.21 - Sequence of Raman spectra during acrylamide and diethanolamine reaction.

The intensity of the C=C band at time t has been determined through a band deconvolution procedure in the 1500-1750 cm⁻¹ range by pseudo-Voigt functions: the area of the C=C band at 1627 cm⁻¹ $A(t)$ has been taken as a measure of the band intensity. The time evolution of the ratio $A(t)/A(0)$ during reaction, is reported in Fig. A.22a. If we assume the area of the C=C band proportional to the concentration C of the acrylamide reagent, we notice that a plot of $A(0)/A(t)=C(0)/C(t)$ (i.e. of the reciprocal of the normalized concentration) as a function of time (Fig. A.22b) may be well approximated by a linear fit, at least in the first two hours. This result suggests a second order reaction $X+Y \rightarrow Z$ with $X(0)=Y(0)$, described by

$$1/X(t)=1/X(0)+k_2t \quad (A1)$$

where $X(t)$ is the concentration of the X species at time t and k_2 is the second order rate constant or

$$X(0)/X(t)=1+X(0)k_2t \quad (A2)$$

with an half-life $t_{1/2} = 1/(X(0)k_2) \sim 45$ min [A39].

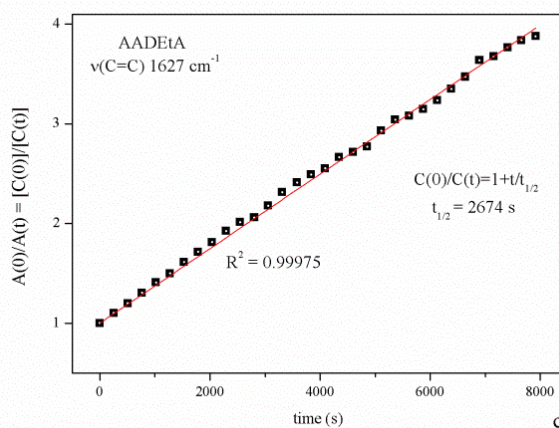
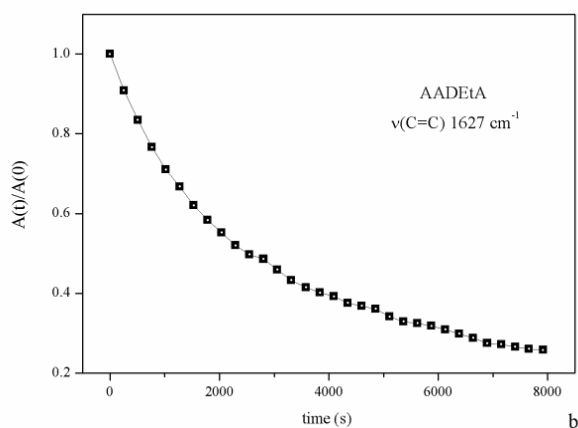
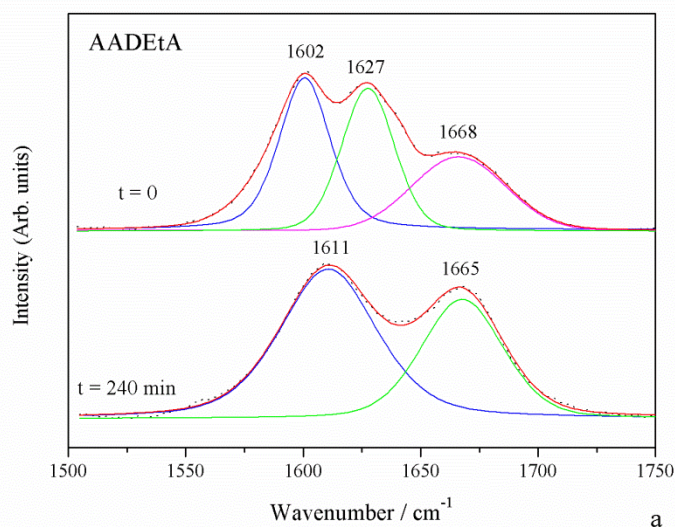


Fig. A.22 - Time evolution of the normalized area of the C=C stretching band (a). Plot of the reciprocal of the data in the first two hours and linear fit. The inverse of the slope is the half life of the reaction.

A. 3.1.2.2 - AADEtA

The AADEtA molecule is obtained by reaction between acrylamide and ethanolamine in molar ratio amide:amine = 2:1.

The ethanolamine is a primary amine used for the synthesis of polyamidoamine whose biocidal activity will be discussed in Part B. In general, the reactivity of the primary amines in addition reactions to α , β -unsaturated compounds is lower than the secondary amines [A2] Nevertheless, in the experimental conditions here used (in water at 55 °C for several hours) excellent results were obtained (yield: 98%). The product obtained after drying in vacuum looks like a white powder.

Elemental analysis gives C, 46.98; H, 9.21; N, 15.81%; $C_7H_{16}N_2O_3$ requires C, 47.72; H, 9.15; N, 15.90%.

A. 3.1.2.2.1 - ESI-MS

The mass spectrum (Fig. A.23) obtained from AAEtA is characterized by a signal produced by protonation of the amidoamine molecule $[M+H]^+$ at m/z 204.32. The formation of a sodium adduct $[M+Na]^+$ is also detected (signal at m/z 226.27).

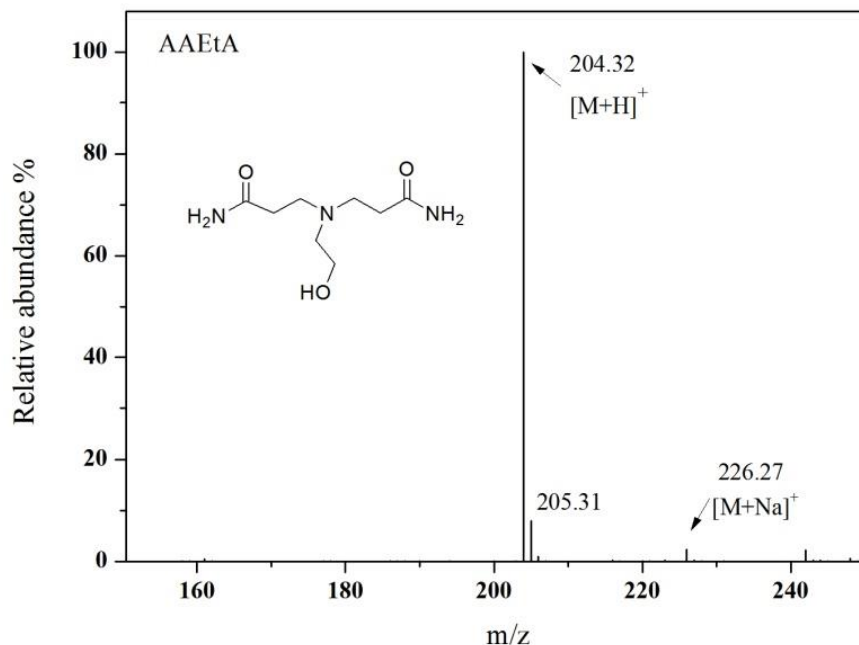


Fig. A.23 - ESI-MS of the AAEtA obtained in water at 55 °C for 4h.

A. 3.1.2.2.2 - NMR

NMR measurements confirm that the addition reaction has occurred. In Figs. A.24 and A.25 are reported the ^1H -NMR and $^{13}\text{C}\{^1\text{H}\}$ -NMR spectra, respectively, of the reaction product in dimethylsulfoxide- d_6 (DMSO- d_6).

In the ^1H -NMR spectrum (Fig. A.24) the broad signals at δ 7.40 (1H, br s, NH_2) and δ 6.81 (1H, br s, NH_2) are due to the proton atoms of the amide, while the broad signal at δ 4.5-3.5 (1H, br s, $\text{NCH}_2\text{CH}_2\text{OH}$) is due to the hydrogen atom of the alcoholic moiety. The triplet signals attributed (by integration) to the protons in the alkyl chain are found at δ 2.65 (4H, t, J 6.9 Hz, $\text{NCH}_2\text{CH}_2\text{CO}$) and δ 2.17 (4H, t, J 6.9 Hz, $\text{NCH}_2\text{CH}_2\text{CO}$) and the protons of the ethanolic chain at δ 3.43 (2H, t, J 6.0 Hz, $\text{NCH}_2\text{CH}_2\text{OH}$) and 2.46 (2H, t, J 6.0 Hz, $\text{NCH}_2\text{CH}_2\text{OH}$).

In the $^{13}\text{C}\{^1\text{H}\}$ -NMR spectrum (Fig. A.25) signals of the carbon atoms resulting from the addition reaction are identified (50.97 and 33.51 ppm) and signal due to the carbonyl carbon atoms, due to loss of the double bond, is shifted from 167.17 (pure acrylamide) at 172.68 ppm. At δ 56.49 and δ 59.51 signals due to the carbon atoms of the added amine are visible.

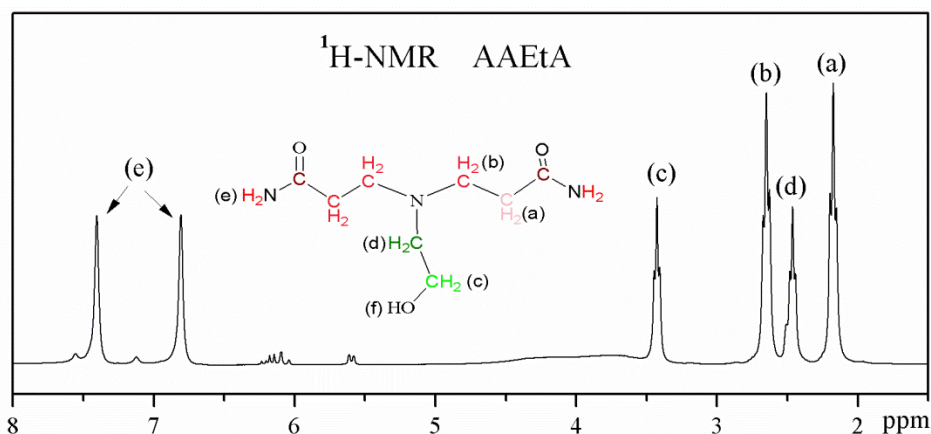


Fig. A.24 - ¹H-NMR spectrum in DMSO-d₆ of the AAEtA product.

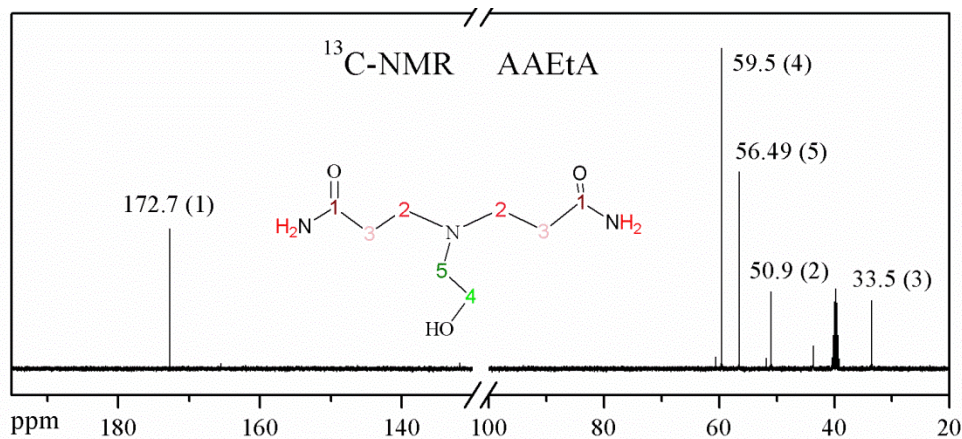


Fig. A.25 - ¹³C{¹H}-NMR spectrum of AAEtA.

A. 3.1.2.2.3 - FTIR

FTIR and Raman investigation confirmed that reaction occurred, by the identification of the functional groups of the product molecule.

The IR absorption spectrum of AAEtA, obtained by acrylamide and ethanolamine in H₂O at T=55 °C for 4h, is reported in Fig. A.26 together with the spectra of the starting molecules.

As pointed out in the discussion on the AADEtA molecule the spectral region to be observed to ensure the successful addition reaction, is that related to the amide group of acrylamide.

You can immediately see that in AAEtA the bands associated to amide I and amide II are completely changed. The amide I is shifted of ~15 cm⁻¹ and amide II of ~ 5 cm⁻¹ to lower wavenumbers with respect to the pure AA reagent. These red-shifts are due to the disappearance of the conjugated double bond. In the region of OH and NH stretching modes, the AAEtA product shows significant changes: the NH antisymmetric stretching vibration of the acrylamide broadens, due to the overlap with the OH stretching mode of ethanolamine. The ethanolamine aliphatic chain and the new methylene groups, formed following the breakup of the double bond, contribute to broad bands at ~ 2950 and 2830 cm⁻¹ (stretching) and at ~ 1430 cm⁻¹ (bending), respectively.

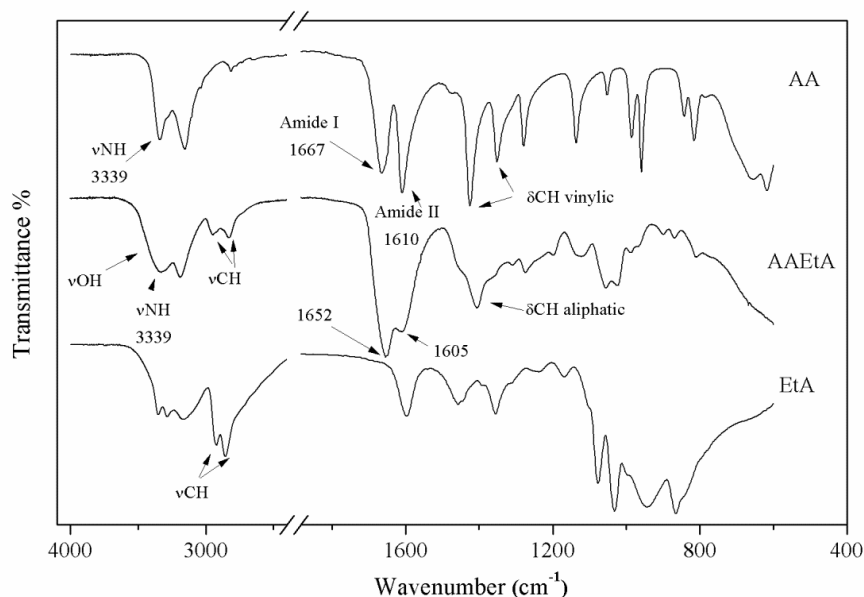


Fig. A.26 - FTIR spectra of AAEtA and of pure reagents.

A. 3.1.2.2.4 - Raman

The Raman spectrum of the reaction product AAEtA is shown in Fig. A.27. It may be noticed the disappearance of the band associated to stretching vibration of the double bond (1627 cm^{-1}) and a shift of the vibrational frequencies of the amide group at 1660 cm^{-1} and 1614 cm^{-1} for the amide I and II respectively. We can reasonably assume that this shift is due to the disappearance of the double bond as these vibrational frequencies are similar to those of the propionamide, the corresponding not-acrylic amide [A40]. At high wavenumbers, the bands associated to the vinyl CH and CH_2 stretching vibrations disappear. The strong bands in the $2950\text{--}2800\text{ cm}^{-1}$ range are associated with C-H stretching vibrations ($\nu(\text{C-H})$) deriving from the addition of ethanolamine to the double bond of acrylamide.

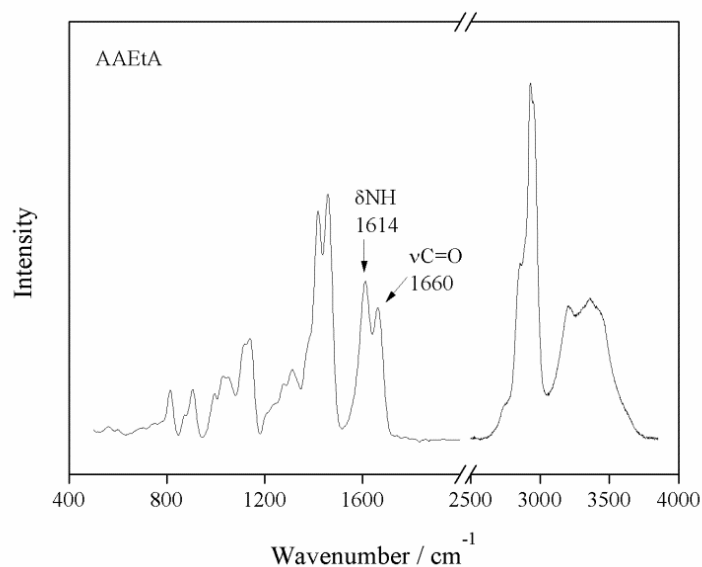


Fig. A.27 - Raman spectrum of AAEtA obtained in water at $55\text{ }^\circ\text{C}$ for 8 hours.

A. 3.1.2.3 - MBADEtA

The reaction between MBA and diethanolamine in molar ratio amide:amine=1:2 was made using water as solvent, stirring for 8 hours at 55 °C. The yield was about 97%. The product is a honey-like viscous liquid, pale yellow coloured. The results of the C, H, N elemental analysis were: C, 46.99; H, 9.01; N, 21.21% (C₈H₁₇N₃O₃ requires C, 47.28; H, 8.43; N, 20.67%).

A. 3.1.2.3.1 - ESI-MS

In Fig. A.28 is displayed the mass spectrum of the MBADEtA synthesized by MBA and diethanolamine using H₂O as solvent, at 55 °C for 4h. The highest intensity signal is due to [M+H]⁺ at m/z 365.45. At lower intensity m/z 387.30 corresponds to sodium adduct [M+Na]⁺. The signal at m/z 189.01 is consistent with the fragment ion upon loss of β-amino carbonyl group, produced in the ionization source from the [M+H]⁺ ion.

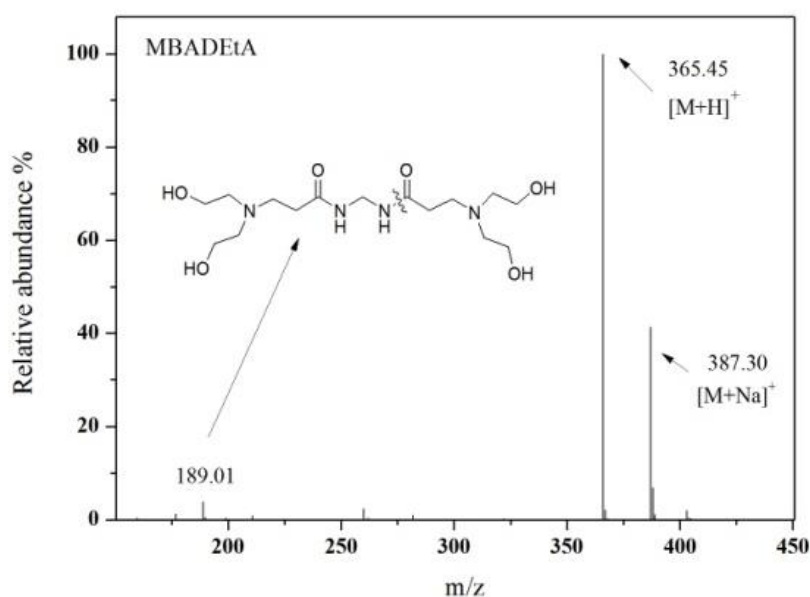


Fig. A.28 - ESI-MS spectrum of MBADEtA.

A. 3.1.2.3.2 - NMR

In Fig. A.29 is reported the ¹H-NMR spectrum obtained from MBADEtA. The triplet signal observed at δ 8.55 is due to NH amide (2H, t, *J* 6.0 Hz, CH₂NHCO) and that at 4.34 ppm is due to methylene bridge protons (2H, t, *J* 5.7 Hz, CH₂NHCO) from MBA. The aliphatic proton of ethanolic chains from diethanolamine are at 3.41 ppm (8H, t, *J* 6.0 Hz, NCH₂CH₂OH) and 2.49 ppm (8H, t, *J* 6.0 Hz, NCH₂CH₂OH). The newly formed protons by the addition of amine to double bond resonate at δ 2.69 (4H, t, *J* 6.9 Hz, NCH₂CH₂CO) and 2.20 (4H, t, *J* 6.9 Hz, NCH₂CH₂CO). A small residual in the range 6.5-5.5 ppm of vinyl protons from starting bisacrylamide is barely perceptible.

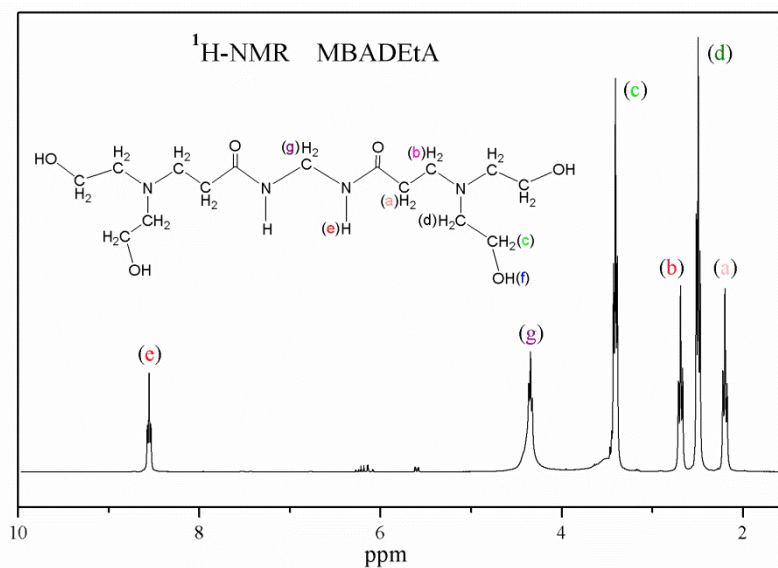


Fig. A.29 - ¹H-NMR spectrum of MBADEtA.

In the ¹³C{¹H}-NMR spectrum of the MBADEtA, shown in Fig. A.30, the signal due to the carbonyl carbon is at δ 172.7 and the carbon of the aliphatic CH₂ bridge between the two NH groups, resonates at δ 43.7. The signals of the vinyl carbons (δ 131.72 and δ 126.61 in MBA) are fully disappeared. The signals of the aliphatic carbon atoms newly formed are found at 59.5 and 33.5 ppm. The signals due to the carbon atoms of the added amine are at 56.5 and 50.9.

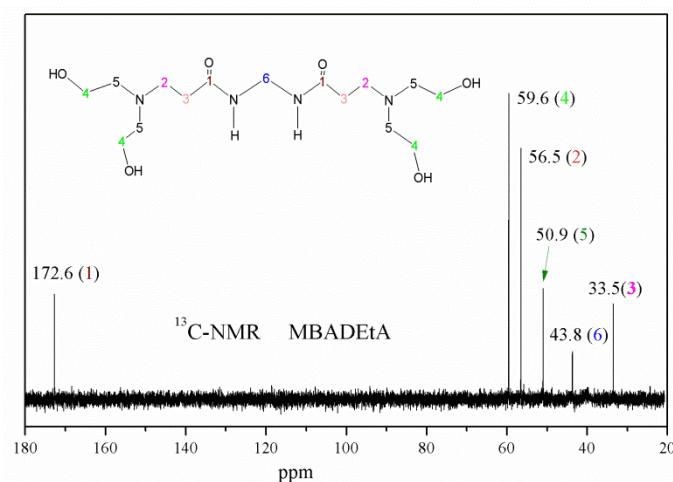


Fig. A.30 - ¹³C{¹H}-NMR spectrum of MBADEtA.

A. 3.1.2.3.3 - FTIR

Fig. A.31 shows the IR absorption spectrum of MBADEtA obtained in water at 55 °C (4h reaction time) compared with those of starting reagents. In the spectrum of the molecule, the broad band at 1638 cm⁻¹ is due to the overlapping of the bands relative to the C=O and C=C bond stretching vibrations, that were at 1657 and 1627 cm⁻¹ in pure MBA, respectively. In addition, in the high wavenumber region, one can see the peak at 3064 cm⁻¹, marked by an arrow, ascribable to ν (=CH₂) of the double bond of unreacted bisacrylamide. Looking at the region of aliphatic bond stretching (<3000 cm⁻¹), the CH₂ symmetric and antisymmetric stretching vibrations and the broad band due to

$\nu(\text{OH})$ of diethanolamine at about 3500 cm^{-1} , are clearly discernible. At about 1050 cm^{-1} is observable a broad band due to the stretching vibration of the C-O bond from the alcoholic chain of diethanolamine.

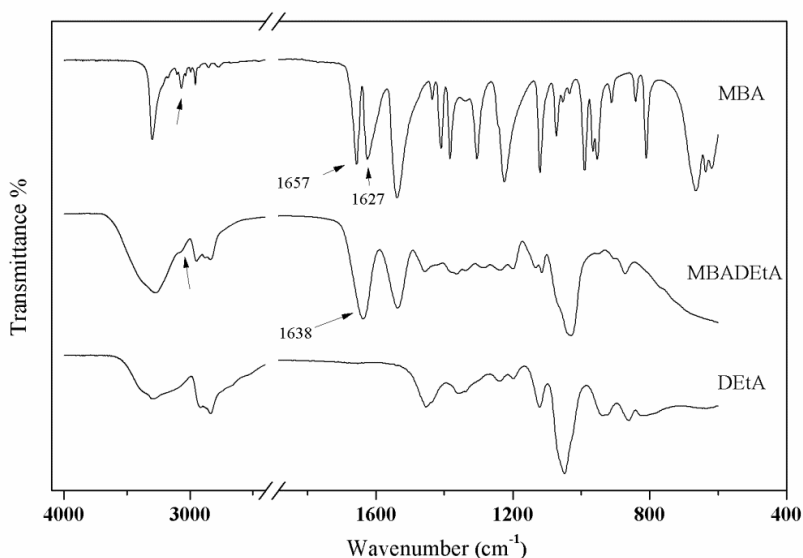


Fig. A.31 - FTIR spectra of MBADEtA, MBA and DEtA.

A. 3.1.2.3.4 - Raman

To complete the characterization of the product obtained by the adding bisacrylamide and diethanolamine, Raman spectroscopy analyses were made in different reaction conditions (water / ethanol, at ambient temperature/ $55\text{ }^{\circ}\text{C}$, 4/24h). The band corresponding to the stretching vibration of the double bond and of CH vinyl of the MBA reagent are still present after 4 h. The Raman spectra confirmed that at these synthesis conditions a small residue of the starting reagents is observed. The reaction has to be carried out for longer times, as suggested in similar studies [A2, A41]. As a comparison, Fig. A.32 shows the Raman spectra obtained for MBADEtA synthesized in water, at room temperature, for 4 and 24h of reaction. After 24 hours, the MBA bands are absent.

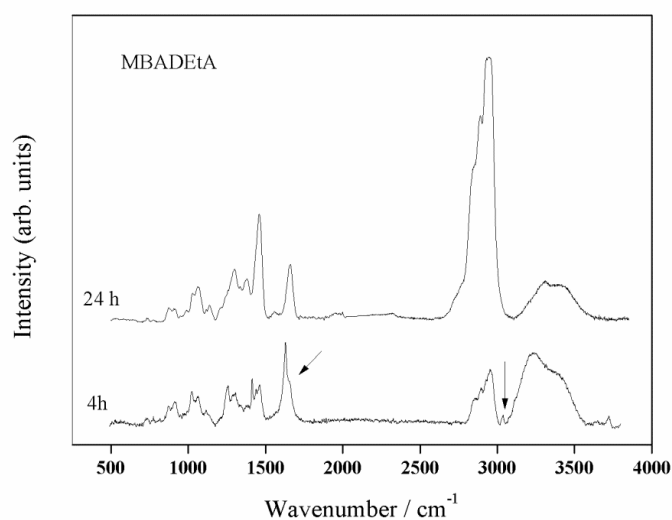


Fig. A.32 - Raman spectra of MBADEtA after 4 h and 24 h reaction times, in water at 298 K .

The reaction at 55 °C was monitored in time by Raman spectroscopy. Spectra were acquired at 30 min intervals (Fig. A.33). A decrease of the intensity of the C=C stretching modes (1629 cm⁻¹) and of vinyl CH₂ and CH bending modes at 1432 cm⁻¹ and 1243 cm⁻¹, respectively, is evident.

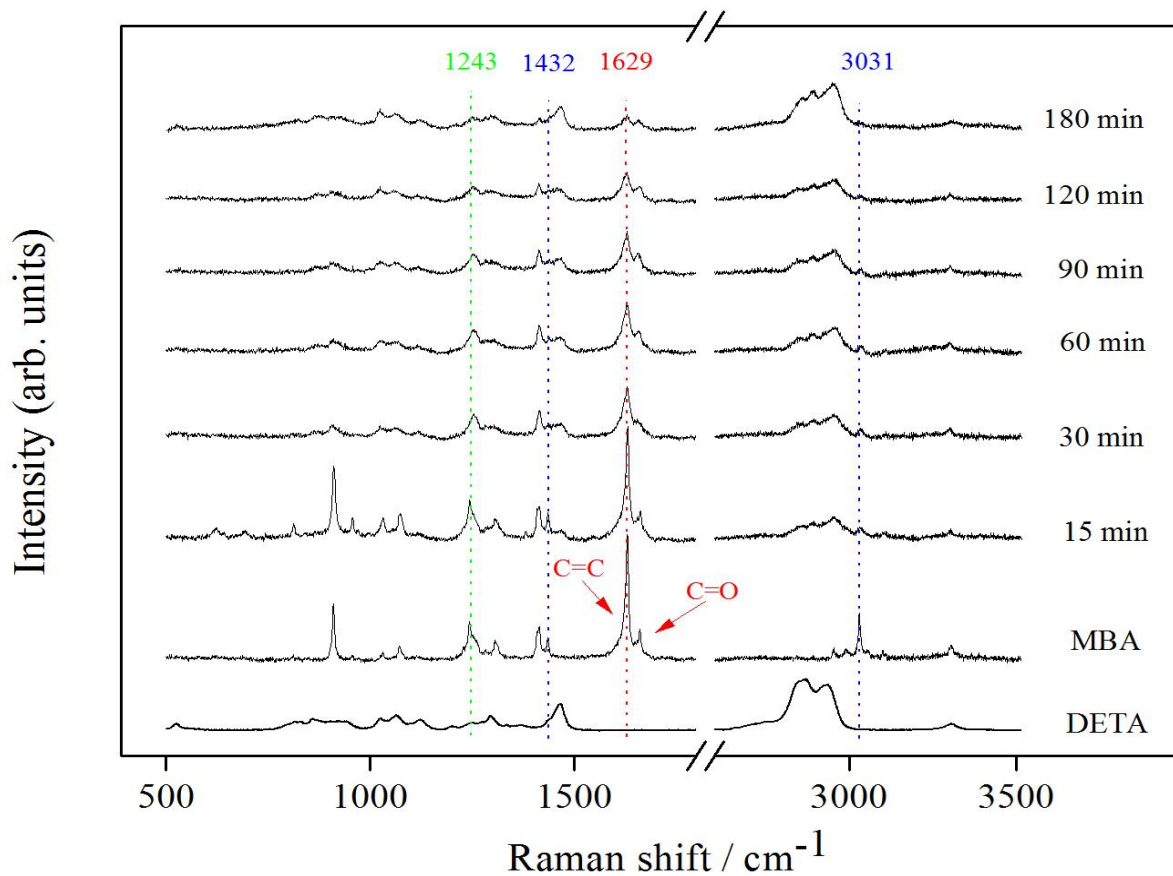


Fig. A.33 - Raman spectra taken during the addition reaction MBA+DEtA.

A. 4 – CONCLUSIONS

In this chapter small model molecules, synthesized by Michael reaction, have been studied and the best conditions for their synthesis have been verified. The Michael reaction has great importance for the synthesis of β -amino carbonyl compounds, versatile intermediates for the synthesis of biologically important natural products, antibodies and β -amino alcohols, polymers. The synthesized amidoamines serve as a model for polyamidoamine polymers, which will be studied in the next chapter.

Ethanolamine and diethanolamine have been used as Michael donors, whereas acrylamide and methylenebisacrylamide as Michael acceptor.

The characterization of these molecules was done by ESI-MS and NMR, FTIR and Raman spectroscopic techniques. The reaction was followed through the changes of the functional groups involved in the addition reaction, in particular by the disappearance of acrylamide double bond. Mass spectra have allowed to verify the formation of the adduct with no trace of the starting reagents, within the instrumental detection limits.

The addition has been achieved in high yields, in polar protic solvent (ethanol or water) without any catalyst, at room temperature or under moderate heating. Water is the better solvent for this type of reaction: the rate acceleration of the reaction is explained by H-bonding of H₂O with amine and acrylamide. The hydrogen bond with the acrylamide carbonyl oxygen, increasing the electrophilic character of the β -carbon, facilitates the attack by the nucleophile. In addition, the hydrogen bond with the H atom of amine increases the nucleophilic character of the amine N atom. Thus, through hydrogen bonding, water activates the amine and the conjugate alkene and then greatly facilitates the addition.

The reactions take place spontaneously: at room temperature they require quite a long time (several hours or even days).

In the aza-Michael reaction, secondary amines are more nucleophilic than primary amines and are therefore more reactive. However, it is worth noting that this is highly dependent on the electronic and steric environment of the amine. The diethanolamine reacts completely with acrylamide according to a second order kinetics while with MBA the reaction is very slow and the reaction kinetics has been not determined.

The reaction between ethanolamine and acrylamide needs higher temperature (about 50 °C) and longer time. The kinetics of the reaction is complex and difficult to describe.

The same procedures and techniques used for the study of amidoamines have been applied for the synthesis and characterization of polyamidoamines.

A. 5 - REFERENCES

- [A1] Franchini J., Ferruti P., *Perspectives on: Recent Advances in Poly(amidoamine)s Chemistry*. Journal of Bioactive and Compatible Polymers, 19 (2004) 221-236.
- [A2] Ferruti P., *Poly(amidoamine)s: Past, Present, and Perspectives*. Journal of Polymer Science, Part A: Polymer Chemistry 51(2013) 2319-2353
- [A3] Rao K. C., Arun Y., Easwaramoorthi K., Balachandran C., Prakasam T., Yuvaraj T. E., Perumal P. T., *Synthesis, antimicrobial and molecular docking studies of enantiomerically pure N alkylated b-amino alcohols from phenylpropanolamines*. Bioorganic & Medicinal Chemistry Letters, 24 (2014) 3057-3063.
- [A4] Busto E., Gotor-Fernandez V., Gotor V., *Hydrolases in the Stereoselective Synthesis of N-Heterocyclic Amines and Amino Acid Derivatives*. Chemical Reviews, 111 (2011) 3998-4035. DOI: 10.1021/cr100287w
- [A5] Mallakpour S., Zadehnazari A., *Advances in synthetic optically active condensation polymers - A review*. eXPRESS Polymer Letters, 5 (2011) 142-181.
- [A6] Phua P.H. Mathew S.P., White A.J.P., de Vries J.G, Blackmond D.G., Hii K.K, *Elucidating the Mechanism of the Asymmetric Aza-Michael Reaction*. Chem. Eur. J., 13 (2007)4602 - 4613.
- [A7] Davis, F. A., Yang, B., *Direct Asymmetric Synthesis of β -Amino Ketones from Sulfinimines (N-Sulfinylimines)*. Synthesis of (-)-Indolizidine 209B_ Organic Letters, 5 (2003) 5011-5014. DOI: 10.1021/ol035981+
- [A8] Murata Y., Kato N., Komatsu K., *The Reaction of Fullerene C60 with Phthalazine: The Mechanochemical Solid-State Reaction Yielding a New C60 Dimer versus the Liquid-Phase Reaction Affording an Open-Cage Fullerene*. The Journal of Organic Chemistry, 66 (2001) 7235. DOI: 10.1021/jo010496i.
- [A9] Hayashi Y., Itoh T., Ohkubo M., Ishikawa H., *Asymmetric Michael Reaction of Acetaldehyde Catalyzed by Diphenylprolinol Silyl Ether*. Angewandte Chemie International Edition, 47 (2008) 4722-4724.
- [A10] Ranucci E., Bignotti F., Paderno P. L., Ferruti P., *Modification of albumins by grafting poly(amido amine) chains*. Polymer, 36 (1995) 2989-2994.
- [A11] Bartoli G., Cimarelli C., Palmieri G., *Convenient procedure for the reduction of β -enamino ketones: synthesis of γ -amino alcohols and tetrahydro-1,3-oxazines*. Journal of the Chemical Society, Perkin Transactions 1 (1994) 537-543. DOI: 10.1039/P19940000537
- [A12] Deuri S., Katakai D., Phukan P., *Iodine catalysed aza-Michael addition of carbamates to chalcones*. Indian Journal of Chemistry, 51B (2012) 1163-1167.
- [A13] Rulev A. Y, *Aza-Michael reaction: achievements and prospects*. Russian Chemical Reviews, 80 (2011) 197. DOI: 10.1070/RC2011v080n03ABEH004162

- [A14] Tang X.-J., Yan Z.-L., Chen W.-L., Gao Y.-R., Mao S., Zhang Y.-L., Wang Y.-Q., *Aza-Michael reaction promoted by aqueous sodium carbonate solution*. Tetrahedron Letters, 54 (2013) 2669-2673
- [A15] Ranu B. C., Banerjee S., *Significant rate acceleration of the aza-Michael reaction in water*. Tetrahedron Letters, 48 (2007) 141-143
- [A16] Ballini R., *Eco-Friendly Synthesis of Fine Chemicals*, 2009, Published by The Royal Society of Chemistry, Thomas Graham House, Science Park, Milton Road, Cambridge CB4 0WF, UK
- [A17] Mather B.D., Viswanathan K., Miller K.M., Long T.E., *Michael addition reactions in macromolecular design for emerging technologies*. Progress in Polymer Science, 31 (2006) 487-531.
- [A18] Gao C., Yan D., *Hyperbranched polymers: from synthesis to applications*. Progress in Polymer Science, 29 (2004) 183-275.
- [A19] Esfand R. Tomalia D. A., *Poly(amidoamine) (PAMAM) dendrimers: from biomimicry to drug delivery and biomedical applications*. Drug Development and Therapeutics, 6 (2001) 427-436.
- [A20] Holden C.H., Tyagi P., Thakur A., Kadam R., Jadhav G., Kompella U. B., Yang H., *Polyamidoamine dendrimer hydrogel for enhanced delivery of antiglaucoma drugs*. Nanomedicine: Nanotechnology, Biology, and Medicine, 8 (2012) 776-783.
- [A21] Percot, A., Zhu, X. X., Lafleur, M. *A simple FTIR spectroscopic method for the determination of the lower critical solution temperature of N-isopropylacrylamide copolymers and related hydrogels*. Journal of Polymer Science Part B: Polymer Physics, 38 (2000) 907-915. DOI: 10.1002/(SICI)1099-0488(20000401)38:7<907::AID-POLB1>3.0.CO;2-5
- [A22] Perlmutter P., *Conjugate addition reactions in organic synthesis*, Tetrahedron organic chemistry series, Pergamon, Oxford-New York 1992
- [A23] Heravi M.M., Hajiabbasi P., *Recent advances in C-heteroatom bond forming by asymmetric Michael addition*. Mol Divers, (2014) 18:411-439. DOI: 10.1007/s11030-013-9494-2.
- [A24] Juaristi E., *Enantioselective Synthesis of α -Amino Acids*, Wiley-VCH, Weinheim, 1997.
- [A25] Enders D., Wang C., Liebich J.X., *Organocatalytic Asymmetric Aza-Michael Additions*. Chemistry European Journal, 15 (2009) 11058 - 11076. DOI: 10.1002/chem.200902236
- [A26] Brown, N. R., Frazier, C. E., *Synthesis of labeled acrylamide and N-methylolacrylamide (NMA): ^{15}N -acrylamide, ^{13}C -NMA, ^{15}N -NMA, and ^{13}C , ^{15}N -NMA*. Journal of Labelled Compounds and Radiopharmaceuticals, 48 (2005) 1031-1039. DOI: 10.1002/jlcr.1015.
- [A27] Socrates G., *Infrared and Raman Characteristic Group Frequencies*. Tables and Charts. Third Edition (2001) John Wiley & Sons, Ltd.
- [A28] Nyquist, R. A., Putzig, C. L. and Leugers, M. A., *Handbook of Infrared and Raman Spectra of Inorganic Compounds and Organic Salts*. Academic Press, San Diego, CA, USA, 1997

- [A29] Sharma B. B., Murli C., Sharma S.M., *Hydrogen bonds and polymerization in acrylamide under pressure*. Journal of Raman Spectroscopy, 44 (2013) 785-790.
- [A30] Gupta M. K., Bansil R., *Laser Raman spectroscopy of polyacrylamide*. Journal of Polymer Science: Polymer Physics Edition, 19 (1981) 353-360.
- [A31] Jonathan N., *The Infrared and Raman Spectra and Structure of Acrylamide*. Journal of Molecular Spectroscopy 6 (1961) 205-214
- [A32] Sundaraganesan N., Puviarasan N., Mohan S., *Vibrational spectra, assignments and normal coordinate calculation of acrylamide*. Talanta. 54 (2001) 233-41.
- [A33] Duarte A.S.R., A.M.A da Costa, Amado A.M., *On the conformation of neat acrylamide dimers—a study by ab initio calculations and vibrational spectroscopy*. Journal of Molecular Structure: THEOCHEM, 723 (2005) 63-68.
- [A34] Singh S., Srivastava S.K., Singh D. K., *Hydrogen bonding patterns in different acrylamide-water clusters: microsolvation probed by micro Raman spectroscopy and DFT calculations*. RSC Adv., 4 (2014) 1761
- [A35] Colthup N. B., Daly L. H., Wiberley S. E., *Introduction to Infrared and Raman Spectroscopy*, 3d. ed., Academic, New York, 1990.
- [A36] Reddy B.V., Rao G.R., *Vibrational spectra and modified valence force field for N,N'-methylenebisacrylamide*. Indian J.Pure Appl Phys, 46 (2008) 611-616
- [A37] Graiff C., Pontiroli D., Bergamonti L., Cavallari C., Lottici P.P., Predieri G., *Structural Investigation of N,N'-methylenebisacrylamide via X-ray Diffraction Assisted by Crystal Structure Prediction*, Journal of Applied Crystallography, 2015 – in press
- [A38] Silva C.F.P., Silva, C. F., Duarte, M. L. T., Fausto R., *A concerted SCF-MO ab initio and vibrational spectroscopic study of the conformational isomerism in 2-aminoethanol*. Journal of Molecular Structure, 482-483 (1999) 591-599
- [A39] Schwolow S., Heikenwälder B., Abahmane L., Kockmann N., Röder T., *Kinetic and Scale-up Investigations of a Michael Addition in Microreactors*. Org. Process Res. Dev., 18 (2014) 1535–1544.
- [A40] Beer, M., Kessler, H. B.; Sutherland, G. B. B. M. *Spectra of Homologous Series of Monosubstituted Amides*. The Journal of Chemical Physics, 29 (1958) 1097-1104. <<http://hdl.handle.net/2027.42/70627>>
- [A41] Ferruti P., Marchisio M.A., Duncan R., *Poly(amido-amine)s: Biomedical Applications*. Macromol. Rapid Commun, 23 (2002) 332-355.

PART B

Functionalized polyamidoamines (PAA) as wood preservatives against fungi and termites

The present work aims to achieve novel preventive treatments for the preservation of wood against fungi and termites with broad spectrum of action, low effective concentration, low environmental impact and good fixation into the wood.

Polyamidoamine (PAA) polymers functionalized by hydroxyl and siloxane groups are tested for the protection of lignocellulosic materials against biotic degradation. The polyamidoamines are synthesized by nucleophile addition of primary amines (ethanolamine) to bisacrylamide (N,N'-methylenebisacrylamide, MBA) in water or alcohol.

To obtain the siloxane network linked to amidoamine polymers, APTES precursor was made to react directly with MBA by a sol-gel process in situ. The process generates hybrid inorganic-organic silica network penetrating the wood cell walls.

The improvement of wood biological resistance due to the presence of amino-groups and amino-functional silanes groups against fungal growth in wood has been reported in literature [B6-7, B33]. Various methods of treatment, ranging from immersion to impregnation under vacuum, have been implemented. Modified wood by hybrid organic-inorganic sols was exposed to attack by decay-fungi (*Coniophora puteana*, *Trametes versicolor*, *Poria placenta*) and termites (*Reticulitermes lucifugus*, *Kaloterms flavicollis*). For each treatment, the interaction and diffusion into the wood structure and the preservative efficacy were evaluated.

B. 1 - INTRODUCTION

Wood is one of the oldest materials used by humans in a large variety of artifacts, due to its particular aesthetic characteristics and mechanical properties, and especially in view of the fact that it is a resource readily available. Wood has been used for thousands of years as a building material and architectural woodworks, for shipbuilding, furnishings, musical instruments and in the artistic field for realization of carvings and church furniture, sculptures, paintings.

Wood is still widely used especially in the building sector thanks to its physical-mechanical properties (tensile strength and compressive elastic modulus, low density, insulating properties) and for its aesthetic properties.

Wood is an organic, hygroscopic and anisotropic material and for its organic nature has some disadvantages: unprotected wood by the long-term impact of oxygen, light and water under atmospheric conditions can warp, split, rot and decay. Moreover, wood is a source of nutrients for microorganisms, fungi and insects, leading to its complete biological destruction.

To improve wood biological durability, dimensional stability, hardness and UV-stability, many treatments have been attempted. Most of the commonly employed strategies for protecting wood involve drying, coating and/or impregnation. A large variety of compounds has been tested for wood modification, including anhydrides, carboxylic acids, isocyanates, aldehydes, alkyl chlorides, lactones, nitriles and epoxides [B1-2].

As regards the improvement of the wood durability, the European Union recently banned most of the products developed in the chemical industry in 19th century, because of their high toxicity. They were mainly phenolic compounds and polychlorine, arsenic or chromium salts and/or copper salts, easily leachable and diffusible in the environment.

This research is focused on developing new wood preservatives, harmless and eco-friendly, for increasing resistance to fungal and termite decay.

The treatments tested are the polyamidoamines, a class of bio/eco-compatible *tert*-amino polymers that, due to their basicity and chemical reactivity, are able to interact with biological macromolecules present in organisms. The polyamidoamines are used as carrier for biologically active substances and as complexing agents of heavy metal ions [B3-5]. The tertiary amines are known for their antibacterial activity [B6-7]. The organic water-soluble polyamidoamines and organic-inorganic hybrid coating based on hydroxyl and siloxane functionalized polyamidoamines were tested for their biocidal activity against fungi and termites.

B. 1.1 - Wood structure and properties

Wood is a complex biological structure, a composite of many chemistries and cell types acting together to serve the needs of a living plant. It is a porous and fibrous structural tissue found in the stems and roots of trees and woody plants belonging to the Spermatophyta subdivisions of gymnosperms (conifers) and angiosperms (deciduous trees). The term softwood is used to describe wood from gymnosperms (mostly conifers), and hardwoods are woods that come from angiosperms (flowering plants) [B8].

Wood structure can be examined at decreasing scales (Fig. B.1):

- Tree stem macro structure
- Timber microscopic structure
- Cellular structure
- Wood cell ultrastructure and wall chemistry



Fig. B.1 - Hierarchical structure of wood (www.forestplatform.org /Tobias Köhnke).

- Tree stem macro structure

Looking at the cross section of a tree stem several observations can be made [B9]. The trunk is composed of various materials present in concentric bands. From the outside of the tree to the inside, they are outer bark, inner bark, vascular cambium, sapwood, heartwood, and the pith (Fig. B.2):

- **outer bark** provides mechanical protection to the softer inner bark against damage from parasites and helps to limit evaporative water;
- **inner bark** or phloem, is the tissue through which sugars produced by photosynthesis are translocated from the leaves to the roots;
- **vascular cambium** is the layer between the bark and the wood that produces both these tissues each year: phloem cells toward the outside and xylem cells toward the central axis of the stem;

- **sapwood** is the younger, active, “living” wood; its principal functions are to conduct water (or sap) from the roots to the leaves and to store up the reserves;
- **heartwood** (*duramen*) is the stem central area; it is formed by dead cells whose function is of mechanical support to the stem;
- **pith** at the very center of the trunk is the remnant of the early growth of the trunk, before wood was formed.

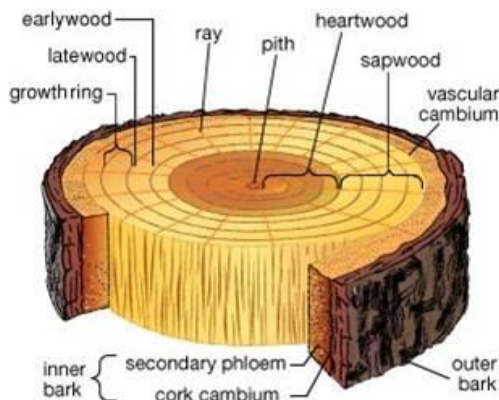


Fig. B.2 - Scheme of the transversal section of a stem, showing the distinctive parts of its macro structure (<http://kids.britannica.com/elementary/art-66141>).

All the tissues comprised between the cambium and the stem central axe are called “wood”. In a cross-section, stem shows growth rings, that in the temperate species correspond to the annual activity of the cambium and are due to the alternate production of cells with large lumen (“spring wood”) and cells shorter with thicker walls (“summer wood” or “latewood”). Medullary rays, perpendicular to the growth rings and allowing the radial transmission of sap and storing up the reserves of carbohydrates and mineral salts, are also visible in many tree species.

The process of sapwood transformation in heartwood is known as *duramification*. In many species, heartwood often appears darker due to oxidation of phenolic compounds. Heartwood has the same strength as sapwood but has greater natural resistance to biological attack, thanks to toxic compounds mostly deposited in the cells during its formation and also because of its lower permeability to water and oxygen.

Chemical preservative treatments are performed on sapwood because of its lower natural durability and higher impregnation properties.

- *Timber microscopic structure*

Wood has a porous, heterogeneous and anisotropic structure.

Hardwoods and softwoods can be distinguished microscopically by distribution and dimension of the pores, visible in the stem transversal section (Fig. B.3). Softwood, called *omoxilo*, consists for 90 to 95% of volume of *tracheids*, having both the functions of raw sap conduction and support.

Hardwood is called *eteroxilo* because of the difference between vessels, with the functions of raw sap conduction, and fibers, responsible for mechanical resistance [B8].

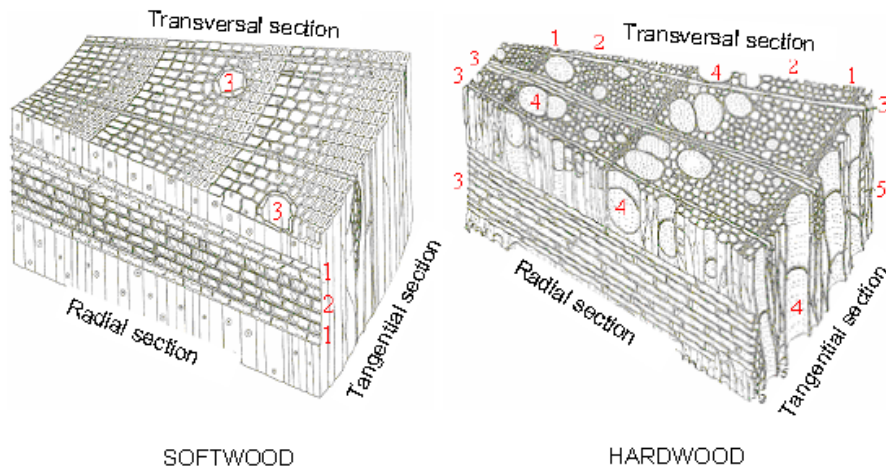


Fig. B.3 - Schematic representation of wood. Softwood: 1. tracheids, 2. ray parenchyma, 3. Resinous canals. Hardwood: 1. latewood: 2. spring wood, 3. ray parenchyma, 4. vessels, 5 axial parenchyma (www.sfera-group.it).

- Cellular structure

The wood cells are formed by the cell wall and by the internal cell lumen that is a void space. The cell wall has a complex structure, composed of several layers (Fig. B.4). Moving from the lumen we can distinguish: the secondary wall, mainly composed of cellulose microfibrils arranged in three sub-layers (S1, S2, S3); the primary wall, constituted principally of pectine and lignin and the middle lamella, rich in pectin compounds and especially in lignin (70%), is the cementing layer between adjacent cells.

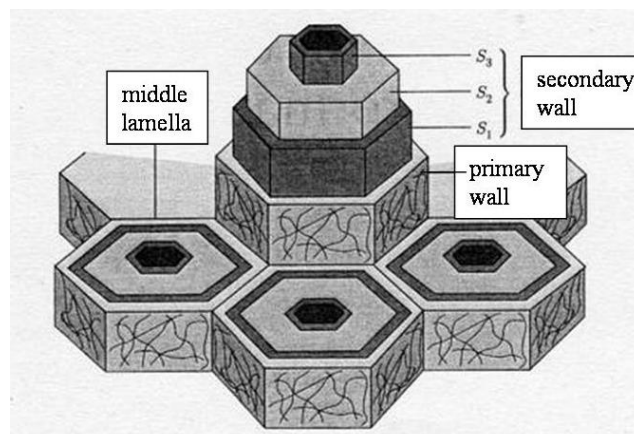


Fig. B.4 - Schematic representation of the cell wall structure: primary wall, the secondary wall and middle lamella. S1, S2, S3 are the different sub-layers of the secondary wall [B8].

- Wood cell ultrastructure and wall chemistry

The major chemical components in wood cell walls are cellulose (between 40 to 55% of the total cell wall mass), hemicellulose (approximately 25-40%) and lignin (18-33%). Proteins (<10 %) and compounds of lower molecular weight (extractable, mineral salts) (<1 %) can also be present [B10]. Cellulose can be described as a long string-like molecule with high tensile strength. The microfibrils of the cellulose molecules are collected into even longer, stronger thread-like macromolecules. Cellulose is a linear polymer formed by the sequence of cellobiose obtained by reaction from two D-anhydroglucopyranose molecules, linked by beta 1-4 glycosidic linkages.

Adjacent cellulose chains are held together by hydrogen bonds. The degree of polymerization (the number of glucose units per cellulose molecule) ranges between 8000 and 10000, depending on the tree species.

Hemicellulose links the lignin and cellulose into a unified whole in each layer of the cell wall: the less-ordered cellulose is linked to hemicellulose molecules through hydrogen bonds; hemicellulose is then linked to lignin molecules through covalent bonds.

Hemicellulose are relatively short, branched heteropolymers, whose monosaccharide components are D-glucose, D-xylose (often acetylated in position 2 or 3), L-rhamnose, D-mannose, L-arabinose, D-galactose as well as the uronic acid of glucose and galactose, depending mainly on the tree species, wood tissue and cell wall layer. The monosaccharide units are linked, by 1-3, 1-6 and 1-4 glycosidic bonds, to form polymers having a degree of polymerization usually lower than 200.

Lignin is present as an encrusting substance and contributes to give compressive strength. It is a complex aromatic three-dimensional polymer of phenylpropanic alcohols: p-coumaryl alcohol [4-(3-hydroxy-1-propenyl)phenol], coniferyl alcohol [4-(3-hydroxypropenyl)-2-methoxyphenol] and sinapyl alcohol [4-(3-hydroxypropenyl)-2,6-dimethoxy-phenol]. The major difference in the chemical structure of these monomers is the presence or absence of methoxyl (-OCH₃) groups at the 3 and 5 positions of the aromatic ring. The lignin structure depends on the vegetal species of wood.

Substances with low molecular weight, also called extractives represent only in a small percentage of wood cell walls (1.2% of dry mass for hardwood, from 3.5% to 10% for softwood, the extractives influence colour, hygroscopicity, smell and resistance. In some species, they are toxic and play a role against the attack by bacteria, fungi and termites.

B. 1.2 - Wood degradation

Despite its matrix of cellulose, hemicellulose, and lignin, which gives wood significant strength properties and a marked resistance to chemical and microbial attack, a variety of organisms and processes are capable of degrading wood. The agents causing the deterioration and destruction of wood fall into two categories: Biotic (biological) and abiotic (non-biological). Biotic agents include decay and mold fungi, bacteria and insects. Abiotic agents include sun, wind, water, certain chemicals and fire.

B. 1.2.1 - Abiotic degradation

When wood is exposed to outdoor climate, a complex combination of chemical and physical factors contribute to its weathering. The chemical reactions involved lead to the degradation of both cellulose (and hemicellulose) and lignin.

Water is one of the main factors of wood degradation. Especially when wood is used outdoors, temperature and humidity variations cause changes of wood moisture content until new equilibrium conditions are reached. Shrinking and swelling occur as the wood changes moisture content in response to changes in the relative humidity of the atmosphere, i.e., when the air is humid, wood absorbs moisture and swells; when the air is dry, wood loses moisture and shrinks [B11-12].

Sun radiations can even cause wood degradation. The UV component of sunlight, which acts in combination with moisture, temperature, and oxidative agents such as oxygen and/or ozone, depolymerize lignin and cellulose [B13-14].

Wood easily catches fire. Wood consists of organic compounds that are composed mainly of carbon and hydrogen. They can combine with oxygen and burn.

B. 1.2.2 - Biotic degradation: Fungi, xilophagous insects

The main causes of degradation of wood are represented by biological agents, especially fungi and xylophages insects. These organisms cause aesthetic and/or mechanical decay.

The term “natural durability” is used to express intrinsic resistance of a wood species to defined xilophagous organisms. It is generally referred to the duramen and depends on chemical and physical characteristics of wood, such as density, nitrogen and starch content, lignin quantity and type and especially the presence of extractives.

- *Fungi*

Fungi are eukaryotic and carbon-heterotrophic (free from chlorophyll) organisms with chitin in the cell walls, reproduce asexually and/or sexually by non-flagellate spores; they can be unicellular or pluricellular, but the unicellular forms have a minor part to play in the colonization and decay of wood. Pluricellular fungi are filamentous: they are formed by hyphal filaments and the wood is colonized through the apical growth of hyphae.

Wood-decay fungi can develop in the wood only if certain environmental conditions are satisfied: moisture, temperature, pH, light (wood moisture content of about 20-30% and atmospheric temperature ranging from about 10°C to 40°C). Wood-stain fungi are highly pH sensitive, they usually grow best in slightly acidic substrates but Basidiomycetes have an optimum range of 4-6 [B15]. Also light is known to influence enzyme regulation in fungi [B16].

Taxonomically, the fungal species responsible for wood decay belong to the subdivisions of Ascomycotina, Basidiomycotina and Deuteromycotina; as concerns decay modalities, wood-decay fungi can be classified according to the type of decay that they cause. The best-known types are white rot and brown rot.

- *White Rot Fungi*

White rot is caused by basidiomycetes and some genera of ascomycetes. They are capable to break down all major wood components (cellulose, hemicelluloses and lignin) more or less simultaneously. Fungi colonize the wood via ray parenchyma and vessels or resin canals (in softwoods) and grow principally in the wood cell lumen [B15]. Wood affected by white rot normally does not crack across the grain and will only shrink and collapse when is severely degraded. White rot fungus commonly causes rotting of the wood that becomes moist, soft and spongy, or stringy and to appear white bleached. The strength of the infested wood decreases gradually until it becomes spongy to the touch and stringy when broken.

In Fig. B.5 is shown the white rot fungus *Trametes versicolor* (L. Fr.) Pilat., the Basidiomycetes that is used for test of the biocidal activity efficacy in this work.



Fig. B.5 – (a) The white rot fungus *Trametes versicolor* (L.:Fr.) Pilat;
(b) White rot decay.

- *Brown Rot Fungi*

Brown rot is caused by Basidiomycetes, which metabolize the cellulose and hemicelluloses of the woody cell wall by non-enzymatic and enzymatic action, but leave the lignin almost unaltered. Brown rot fungi colonize wood via the rays and spread in the longitudinal tissue through pits and by means of microhyphae. They grow inside the cell lumina and there in close contact with the tertiary wall. The cellulolytic enzymes penetrate through the relatively resistant tertiary wall (high lignin content) and diffuse into the secondary wall, where they degrade the carbohydrates completely. Due to the rapid cellulose de-polymerization, the dimensional stability and mechanical properties particularly decreases [B15]. Wood affected by brown rot is usually dry and fragile, readily crumbles into cubes because of longitudinal and transverse cracks (tending to crack across the grain). Infected wood may be greatly weakened, even before any external evidence of decay can be seen. Brown rot is generally more serious than white rot. Old infestations of brown rot, which have dried out, will turn to powder when crushed. They are often labeled as "dry rot." Most brown-rot fungi affect conifers and usually are uniformly distributed over the substrate. The brown rot fungus *Coniophora puteana* (Shum:Fr) P. Karsten is reported in Fig. B.6.

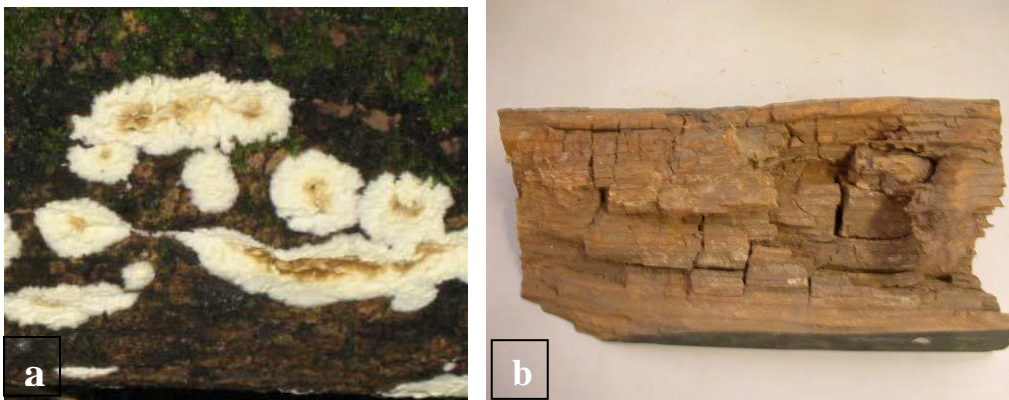


Fig. B.6 – (a) The brown rot fungus *Coniophora puteana* (Shum.:Fr) P. Karsten; (b) Brown rot decay.

- *Termites*

Termites (*Dictyoptera* Order, *Isoptera* Suborder) are social insects that live in colonies of thousands/millions of individuals, with different individuals specialized to perform different tasks and functions (castes). The regal caste (king and queen) includes the only individuals of the colony that can reproduce; the caste of workers (both male and female) is composed of individuals who are concerned with the construction and maintenance of the nest, to find and assimilate food, to feed and take care of all the comrades; the caste of soldiers (both male and female) is responsible for the defense of the colony from predators (like ants) and competitors.

Termites feed on a variety of materials containing cellulose and to digest their food and supplement nitrogen sources are closely tied to the symbiont community hosted in their gut (consisting of flagellate protists and anaerobic bacteria). The formation of new colonies is borne by the winged individuals (only individuals to complete post-embryonic development) that, after the swarming flight from the nests of origin, will constitute the future pairs of regal founders [B17].

Termites are the most dangerous pests of wood, especially the structural one, in many areas of the world.

In Europe, the most represented species belong to the *Rhinotermitidae* and *Kalotermitidae* families, having different biology and manner of infestation of wood substrates.

Fam. *Rhinotermitidae*, to which belong different species of the genus *Reticulitermes*, including *R. lucifugus* (Fig. B.7), comprises some of the most important agents of structural damages in urban

areas. They are "underground" termites, with colonies of several thousand to a few million individuals and nests within and near the ground requiring high humidity. These termites reach the sources of food through underground tunnels.



Fig. B.7 - *Reticulitermes lucifugus* worker (left) and soldier (right) [B17].

From the nest, the wood is reached through existing cavities in the walls or through tunnels built by the workers, even on exposed surfaces, with a mixture of saliva, dirt and excrements (called trenches, or "Tubes"). The walkways protect termites from light and air and maintain contact with the moist soil. When they attack the wood, the galleries of the subterranean termites, parallel to the fiber direction, are always covered by excrements that, being rich in moisture, clot and stick in the point where they are released. The droppings are mixed with soil and saliva, and this compound is used to build the cells in which the workers crowd, occupying the free spaces following the attack of wood or paper, constituting the so-called replacing wood (or paper).

Fam. *Kalotermitidae*, to which belong *Kalotermes flavicollis* (Fig. B. 8) and *Cryptotermes brevis*, are the so-called "dry wood termites" for their habit of building epigeal nests of dry wood; these termites form colonies of several hundred - a few thousand individuals, do not require moisture or direct contact with the ground, normally attack dead wood in forest areas but can occasionally infest wood objects and timber structures in conditions of low humidity. In this Family the tasks of workers are carried out by so-called "pseudergati" (= false workers). The galleries made within the wood appear clean and the droppings (fecal pellets), in the shape of barrels with hexagonal section, are deposited by gravity at the lowest points of the tunnels (e.g. at floor level).



Fig. B.8 - *Kalotermes flavicollis* royal brown and yellow-cream "false workers" (left) and soldier (right) [B17].

Given the nature extremely cryptic and elusive (termites avoid light and free air) and, at least for underground species, the subterranean habits, these insects are able to establish their colonies without being discovered, so that often their presence is eventually detected when the damage is substantial and irreparable. The wood is eaten from the inside, leaving no trace of superficial holes or sawdust, as happens for xylophagous beetles. The wood surface is never affected, so you can make an estimate of the damage only removing it [B17].

For these features, termite control is extremely difficult to take, because of the inherent difficulties to locate and reach infested sites, to verify the effectiveness of the treatment, to completely eradicate the colonies: in fact, the reproductive biology of these insects is such that if one or both members of the royal couple are missing, neotenic replacing king or queen are formed that guarantee the continuity of the reproduction of the same colony.

B. 1.3 - Protective treatments

Most of the commonly employed strategies for protecting wood involve drying, coating and or impregnation.

Coating provides protection to wood used both indoors and outdoors. Wood coatings are generally classed as either film-forming or penetrating. Film-forming treatments, such as paints, contain pigments that screen wood from solar radiation and, because they form a barrier over the wood surface, they also prevent surface wetting and erosion. Coating prevents rapid uptake and loss of moisture and reduces shrinking and swelling that can lead to surface cracking and other problems. Nevertheless their main drawback is the loss of adhesion during weathering due to failure of the underlying wood. Deteriorating paint film actually increases the decay hazard. Cracked paint allows moisture to come into contact with wood surface, and poses a barrier to rapid and completes re-drying [B18].

Penetrating treatments typically contain a hydrophobic component such as waxes, natural oils or resins. The formation of a hydrophobic coating raises the contact angle of the treated wood preventing water from being readily taken up by the surface or sub-surface capillaries. This reduces moisture absorption and imparts a certain degree of dimensional stability to wood [B19]. Additives are often added to coating products to enhance wood stability to solar radiation. For examples, stains containing pigments partially obscure the wood surface, and hence reduce the amount of light reaching the wood [B20]. Flame retardant additives used in the past are: chlorinated and brominated biphenyls and diphenyls, carrying high environmental and health risks; boric acid, soluble zinc, phosphorous and metal salts, whose main disadvantage is the low leaching resistance when in contact with water [B21]. The addition of fungicides to coating provides some protection against development of decay and molds [B22].

Wood Preservation from biotic decay

Wood preservation includes physical or chemical treatments with the aim of inhibiting the activity and viability of wood-degrading organisms (remedial treatments) or applied on wood in order to prevent biological attack (preventive treatments).

In 1998 the European Directive on the Biocidal Products (98/8/EC) listed different biocidal product types including, among them, wood preservatives (Product Type 8). The Biocidal Products Directive BPD 98/8/EC (1998) came into force in September 2006 and approximately 50% of biocides for wood preservation were removed from the market due to their toxicity for human body and for the environment. The list of banned biocidal products is reported in the Official Journal of the European Union, Commission Regulation (EC) No 1451/2007 of 4 December 2007.

Alkylammonium compounds, especially quaternary and tertiary amine salts, are general biocides that inhibit the cell respiratory activity and affect the semi-permeable membrane causing leakage of cell constituents. Tertiary amines and tertiary amine salts are thought to inhibit extra-cellular hydrolytic enzymes. They are also used as bactericides and surfactants; the efficacy of the addition

of inorganic copper to quaternary ammonium compounds against wood decay fungi and termites has been proved [B6-7]. Chemical wood preservatives are divided into two groups: Water-borne, oil-borne chemicals and organic solvent-based preservatives.

The formulation of water based preservatives usually consists of a main biocide, sometimes a secondary biocide and other additives (fixatives, water repellents). Copper compounds have been used as fungicides over a century and copper sulphate or other salts have been applied against fungi causing decay in wood but they are scarcely resistant to water leaching [B22-26]. About 75% of wood that is commercially treated today is treated with waterborne salts, and chromates, copper, arsenate, sometimes zinc and silver [B27-28] are the compounds used in treating for the greatest volume of wood [B29]. Ammonium compounds and boric acid/borates are also used as active principles [B30]. The main disadvantages are that wood may swell and that many salt treatments are not chemically fixed in wood and will leach.

The creosote and pentachlorophenol are oil-borne preservatives that provide general protection against decay causing fungi, termites, marine borer and other insects. They are effective protecting wood in direct ground contact [B31]. Oil based or oil borne preservatives are generally used for treating of wood used outdoors in industrial applications such as ties, piling and poles.

Organic solvent preservatives consist of biocidal compounds dissolved in a volatile or non-volatile non-polar organic solvent. The main solvent carriers used in the past, and now banned were heavy fuel oil, kerosene, petrol and white spirit. Waxes, varnishes and vegetal oils, largely diffused as wood finishing treatments in the past, are now still in use [B19, B32].

Modification of wood by sol-gel process for preservative purpose

To eliminate, or at least limit the abiotic and biotic decays of the constituents of wood, it is possible chemically modify the structure of lignocellulosic polymers. Wood modification can change important properties of the wood including biological durability, dimensional stability, hardness and UV-stability [B13]. Controlling the moisture content of the wood is a very effective way to protect timber [B2]. Wood properties can be improved by chemical modifications, generally obtained by covalently bonding chemicals to the polymeric constituents of wood [B33]. The most effective technologies used are heat treatment, treatments with silica, silicones and silanes and treatments with chitosans [B34-37]. Silane monomers can easily penetrate into the cell wall of wood, polymerize in situ and thus reduce the leaching during outdoor use [B34-35]. Wood treated with alkoxysilane shows improved cell wall bulking, dimensional stability, moisture uptake and durability [B38]. The application of silica by sol-gels onto wood surface, improve the durability of the wood and introduce antisoiling properties [B39]. The siloxane materials can polymerize onto the cell walls and can strongly influence the biotic resistance of the wood by modifying its physical-chemical characteristics [B33]. Wood results less recognizable by biodeteriogens as a substrate adequate for their development. In addition, these treatments could reduce the moisture sorption properties, hence limiting biological attacks and enhancing natural durability [B40]. A wide range of organosilicons as protective agents against basidiomycetes attack are used in outdoor applications and good efficacy results were obtained [B41]. The use of trialkoxysilane leads to the formation of inorganic-organic hybrid materials containing organic functions with desired properties. Inorganic sols may be applied with addition of a broad range of organic or inorganic additives [B42].

B. 1.3.1 - Polyamidoamines

The tert-amino polymers are an important class of polymers containing tertiary amino groups, either aliphatic and cycloaliphatic, as structural units [B43].

Since the first half of the twentieth century examples of polyaddition of active hydrogen atoms from different functional groups (-SH, -NH, -OH etc.) to double or triple bond carbon-carbon or carbon-nitrogen are known [B44-47]. The first polymers obtained by aza-Michael polyaddition of primary

or secondary amines to C=C double bond activated by adjacent electron-withdrawing groups, named polyamidoamines (PAAs), date from around the sixties of twentieth century [B48-50]. The tertiary polyamines and their N-oxides are mainly used in pharmacology as soluble drug carriers [B51-52], as anti-heparinic [B53] and thanks to their basicity and chemical reactivity may interact with a number of biological macromolecular substances present in living organisms [B4-5, B54].

Tert-amino polymers can be grouped into three main classes based on the tert-amino group position [B43]: (a) Polymers having amino groups situated in the main chain. - This type is synthesized by polyaddition of mono- or diamines (or aminoacids) to a compound having two vinyl double bonds activated by adjacent electron attracting groups. The functional groups (hydroxyl groups, carboxyl, etc.) linked to amines, which do not interfere with the process of polyaddition, may be considered as side substituents. (b) Polymers in which the amino-group is bound to the main chain as side group. - These polymers are characterized by an alternating disposition of the co-units along the chain. (c) Polymers in which the amino groups are situated upon other groups as constituent of side chains. - These polymers, partially stereo-regular, could be synthesized using anionic catalysts at low temperatures.

Polyamidoamines (PAAs) are a family of water-soluble, biomimetic, and biodegradable tertiary amino polymers characterized by amidic and *tert*-aminic groups regularly distributed along the macromolecular chain [B5, B43]. They are obtained by stepwise Michael-type polyaddition of primary amines and secondary diamines to bisacrylamide (Fig. B.9). PAAs are generally soluble in water, in alcohol and chloroform and insoluble in aliphatic hydrocarbon and are often very hygroscopic [B55]. The amidoamine polymers can be linear or crosslinked. To obtain linear PAA *prim*-monoamines and *sec*-diamines are used, while to obtain crosslinked insoluble resins *prim*-diamine are employed [B55]. In the early eighties of the nineteenth century great success has achieved a family of hyperbranched polymers, initialed PAMAM, extensively studied and modified for biotechnological applications [B56-59] PAMAM are different from crosslinked PAAs, because in their dendrimer-like backbone each amide group (a) is preceded and followed by an amine group (b) and viceversa, having a ... a ... b ... a ... b ... sequence, while the sequence of the two groups in the PAA chains is ... a ... a ... b ... a ... a ... b ... or ... a ... a ... b ... b ... a ... a ... b ... b ... depending if *prim*-amines or bis-*sec*-amines have been employed in their synthesis, respectively [B55].

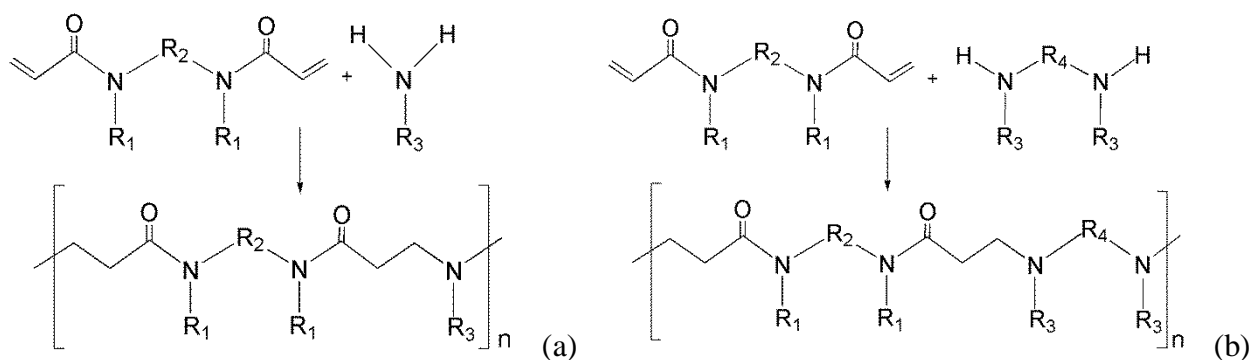


Fig. B.9 - Reaction scheme of polyaddition of *prim*-monoamine (a) and *sec*-diamine (b) to bisacrylamide. R = H, aliphatic or aromatic substituent.

The addition mechanism of the amine to the double bond is a 1-4 nucleophilic addition to α,β unsaturated carbonyl compound: the nitrogen is bound to the carbon β of the activating group, while hydrogen migrates on the carbon in α , with an ionic mechanism [B55]. Polyaddition takes place in absence of secondary reaction and does not require acid or basic catalysts. The solvent has a great influence on the reaction rate: the reaction is faster using polar solvents with respect to non-polar solvents. To accelerate the reaction and obtain products with high molecular weight is necessary to use protic solvents [B48]. Michael polyaddition is best made in aqueous media, or alternatively,

alcohols. An excellent substitute of water is the ethylene glycol. When there are problems of solubility of the reagents, methanol, ethanol, N-methyl-N, N-di-2-hydroxyethyl amine and benzyl alcohol can also be used. The aprotic solvents are not suitable as reaction media [B55]. Manfredi et al. [B60] have performed a comparative study on the kinetics of the polyaddition of 2-methylpiperazine and 2,5-dimethylpiperazine with 1,4-bisacryloylpiperazine, in protic and aprotic solvents. In the protic solvents, the polyaddition proceeded through a two-step mechanism, each step involving one of the two different *sec*-amine groups following pseudo-second-order kinetics. In dimethylformamide, the polyaddition proceeded through third-order kinetics.

Most PAAs have a weight-average molar mass (M_w) and number-average molar mass (M_n) in the range 5000-30000 and 10000-50000 respectively. To obtain high molecular weight PAAs the choice of solvent, monomer concentration, monomer steric hindrance, reaction temperature are central. As regards concentration, higher is better, whereas as regards steric hindrance, lower is better [B43, B55].

The preferred reaction temperature to obtain products of high molecular weight and fast polymerization rate is between 15 °C and 60 °C. At higher temperatures, about 90-100 °C in water, the molecular weight rapidly reaches a maximum and then decreases with time. This behavior can be explained by the contemporary occurrence of hydrolysis of the amide bond [B43]. *Ceteris paribus*, the molecular weight of the polymers depends on the molar ratio of the two monomers (high molecular weight is obtained with equimolar ratio of the monomers).

Another factor that affects the polymerization degree of amidoamines is the double bond reactivity. It changes according to characteristics of the activating group and decreases in the following order:

-CN> -CONR₂≥ --COOR> -COOH≥ -COONa. For the same activating group a decrease of reactivity is observed when an alkyl substituent on carbon α is introduced [B48].

PAA solutions are clear and slightly viscous and after drying take a fibrous appearance. Most of the PAAs are completely soluble in water and alcohols and insoluble in aliphatic hydrocarbon solvents; some may be soluble in other organic solvents (CHCl₃, DMSO). In organic solvents or aqueous media, the intrinsic viscosity usually is in the range 0.15 - 1 dl/g. [B43, B55].

Due to their regular structure, the polyamidoamines can crystallize, although usually are rubber-like or honey-like at room temperature. Many PAAs are partially crystalline in the solid state. A few of them crystallize spontaneously while in some cases, in particular for PAAs derived from primary amines, crystallization must be induced by solvent treatment [B43]. In PAAs where cyclic structures are present, i.e. bisacryloylpiperazine/piperazine, the crystallization is observed during polymerization. In crosslinked PAAs, for low to moderate crosslink density, usually there are crystalline domains, involving the linear chain segments between the crosslink points. These domains are stable in aqueous systems and act as reinforcing fillers, significantly increasing the mechanical strength of the resultant hydrogels [B61]. Melting point (MP) and thermal stability of PAAs depend on crosslinking and crystallinity degree. In poor crystalline polymers, the MP is between 80-120 °C and thermal stability of is quite low and most cases at about 140 °C -170 °C starts the polymer decomposition. At high crystallinity degree, MP is around 200 °C and in PAAs where cyclic structures are present MP is over 270 °C, with decomposition [B43, B61].

The basicity constants of PAAs are related to the type of amine and bisacrylamide used in the synthesis. The PAAs are medium-weak bases. All amino groups in the main chain are ionizable and, with good approximation, the number of "real" basicity constant is equivalent to the amino group numbers in the repetitive unit as if each unit was an isolated molecule [B62-64]. This behavior is probably attributable to the high charge-sheltering efficiency of the two amide groups interposed and the relatively long distance between the ionizable groups belonging to different units, combined with the linear conformation of PAAs in solution [B62]. Protonation restricts the conformational freedom of the macromolecule which acquires a rigid structure. The first protonation leads to the formation of strong hydrogen bonds between "onium" ions and carbonyl groups belonging to the same monomeric unit and when the first protonation is complete the polymer tends to assume a rigid structure. With a second protonation, by the electrostatic repulsion

between the positively charged onium ions belonging to the same unit, there is a further increase in the rigidity of the structure and an increase of the intrinsic viscosity [B62].

The polyamidoamines that have a tertiary amino group in the main chain do not undergo the second stage of protonation and therefore have a greater conformational freedom [B55].

Many PAAs may form coordination complexes with some heavy metal ions (Cu^{2+} , Ni^{2+} , Co^{2+}). Also the metal complexation, similarly to protonation, leads to stiffening of the PAA conformation in solution. To act as a complexing agent, at least two amine nitrogen atoms per unit are required, not belonging to a cyclic structure and not separated by more than three carbon atoms [B65].

In the synthesis of PAAs from the two monomers in stoichiometric ratio, the terminal groups of the chain can be a secondary amine or acrylamide [B43]. Replacing one of the two monomers with other functional groups, crosslinked PAAs with different chemical and mechanical properties may be obtained [B55, B66-69].

The crosslinked polyamidoamines can easily be obtained:

- replacing amines with primary diamines which, having four mobile hydrogens, behave as tetra-functional monomers
- increasing the number of double bonds present, replacing, for example, the amine monomer with unsaturated amines, which may be activated through the process of post-radical polymerization.
- replacing the amine monomer with siloxane groups capable of forming Si-O-Si reticulation.

In this way, water-insoluble gels are obtained having mechanical properties applicable in various fields. The crosslinked PAAs have good chemical resistance to water hydrolytic degradation and a good capability of metal ion complexation.

Of particular interest are the inorganic-organic hybrid polyamidoamines functionalized with hydrophilic and siloxane groups. The inorganic component of these materials can be obtained by sol-gel using alkoxides of silicon or other metals as precursors. In the case of hybrid organic-siloxane polymers the main advantage is the stability towards hydrolysis of the Si-C bond that binds covalently the organic substituents to the inorganic matrix.

The class of hybrid polyamidoamines functionalized with alcohol and siloxane groups is compatible with organic polymeric materials. What can be achieved is a hybrid coating in which the organic phase gives flexibility characteristics, while the consolidating properties are given by the stability of the Si-O-Si bond of the siloxane precursor, capable of polymerizing within the medium, by means of the sol-gel process. Furthermore, the presence of alcohol groups can give the polymer affinity with materials containing hydroxyl groups (such as lignocellulosic material) through the formation of hydrogen bond [B70].

B. 2 - EXPERIMENTAL

B. 2.1 - Materials

Reagents and solvents N,N'-methylenebisacrylamide (MBA), 2-aminoethanol (EtA), γ -aminopropyltriethoxysilane (APTES), methanol, ethanol were purchased from Sigma-Aldrich. The 2,2-dimethyl-4-hydroxymethyl-1,3-dioxolane (Augeo SL191) solvent was provided by Renner Italia spa, Bologna. All reagents were used as received without further purification. In Table B.1 are summarized the structural formulae and some chemical and physical properties of each reagent.

In order to find the best reaction conditions, several syntheses of polymers, by varying the reaction conditions (solvent, mixing mode of the reagents, temperature), were attempted. In Table B.2 are summarized the synthesized polymers with the acronyms and a short description of the reaction conditions. All synthesized products were characterized by ESI-MS, NMR, FTIR and Raman spectroscopy and DSC.

Table B.2 - Structural formula and chemical/physical properties of each reagent and solvent used in the polymer synthesis.

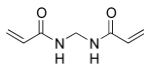

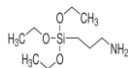
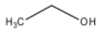
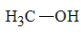
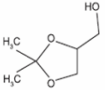
Structural Formula	Reagents and solvents	MW (g/mol)	Density (g/cm ³) 25°C	MP (°C)	BP (°C)	Water solubility (mg/l) 25°C	Purity %
	N,N'-methylenebisacrylamide (MBA)	154.17	1.24	300	-	2x10 ⁴	99
	2-Aminoethanol (EtA)	61.08	1.02	-70	171	complete	98
	3-Aminopropyltriethoxysilane (APTES)	221.37	0.95	98	213	7.6x10 ⁵	97
	Ethanol (EtOH)	46.07	0.79	-114.3	78.4	complete	96
	Methanol (MeOH)	32.04	0.79	-98	65	complete	99
	2,2-dimethyl-4-hydroxymethyl-1,3-dioxolane (Augeo SL191)	132	1.07	-26.4	191	complete	97

Table B.2 - Synthesized polymers with the acronyms and description of the reaction conditions.

Sample	Molar ratio	Solvent	Mixing condition			
PAAOH b1	MBA:EtA=1:1	Ethanol	MBA not completely dissolved	EtA slowly dropwise into MBA		
PAAOH b2						
PAAOH b3						
PAAOH d1		Methanol		EtA slowly dropwise into MBA		
PAAOH d2						
PAAOH d3					MBA slowly dropwise into EtA	
PAAOH e2	MBA:EtA=1:1	Augeo	MBA completely dissolved	EtA slowly dropwise into MBA		
SiPAA b2	MBA:APTES=1:1	Ethanol				
SiPAA d2		Methanol				
SiPAA e2		Augeo SL 191				
SiPAA a2		Water				
SiPAAOH a2	MBA:EtA:APTES=1:0.5:0.5					
SiPAAOHa2	MBA:EtA:APTES=1:0.6:0.4					
SiPAAOH a2	MBA:EtA:APTES=1:0.7:0.3					
SiPAAOH a2	MBA:EtA:APTES=1:0.8:0.2					
SiPAAOH a2	MBA:EtA:APTES=1:0.9:0.1					
PAAOHns 25/55/90°C	MBA:EtA=1:1	No solvent			Fast mixed with each other	

PAAOH = Polyamidoamine with hydroxyl functionality; **SiPAA** = Polyamidoamine with siloxane functionality; **a** =water, **b** = ethanol; **d** = methanol; **e** = Augeo SL 191; **ns** = no solvent; **1** = MBA not completely dissolved into solvent before amine dropwise addition; **2** = MBA completely dissolved; **3** = MBA completely dissolved into the solvent and added dropwise to EtA.

B. 2.2 - Synthesis of protective formulations

B. 2.2.1 - Synthesis of polyamidoamine with hydroxyl functionality (PAAOH).

The reaction scheme is show in Fig. B.10.

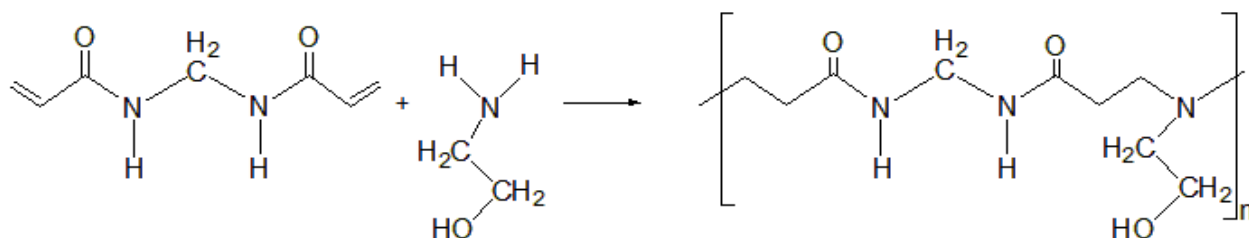


Fig. B.10 - Reaction scheme of polyaddition of *N,N'*-methylenebisacrylamide (MBA) and ethanolamine (EtA).

B.2.2.1.1 - PAAOH 1:1 (1M, 0.5M, 0.15M)

PAAOH was prepared by MBA and EtA in molar ratio 1:1 in a round bottom flask, equipped with a stirrer, a thermometer and a dropping funnels. 1g (6.5×10^{-3} mol) of MBA was dissolved (eventually using the sonicator) in the amount of solvent (water, methanol, ethanol, Augeo SL191) required to achieve the desired molarity. The temperature was 40 ± 1 °C for 30 min. Then, the solution of MBA was cooled at 25 ± 1 °C. 0.19 ml of EtA (6.4×10^{-3} mol) were mixed in a different beaker with 1.5 ml of solvent and stirred for a few minutes. Then the solution was introduce into dropping funnel and added to MBA.

Three types of mixing mode of the reagents were attempted:

PAAOH 1: MBA not completely dissolved; EtA solution slowly added to MBA solution;

PAAOH 2: MBA completely dissolved; EtA solution slowly added to MBA solution;

PAAOH 3: MBA completely dissolved added slowly into EtA solution.

The reaction was left at 30 ± 1 °C under vigorous stirring for 4 h or more until the solution became clear. The solution was pale yellow and transparent. The solvent was evaporated *in vacuo* to give the crude product.

The white powder obtained by drying the sol was characterized by ESI-MS, NMR, FTIR and Raman spectroscopy.

B. 2.2.1.2 - PAAOH - No solvent

To evaluate the influence of the temperature on the polymerization, a test was made by mixing MBA and EtA without solvent in equimolar ratio. The reaction was followed with μ -Raman spectroscopy. The two reactants were vigorously mixed together to obtain an emulsion that was put into an aluminum container of 1 cm diameter and 2 mm in height. The emulsion was gently pressed and inserted in a hot stage, with continuous flow of nitrogen. Raman spectra were acquired at 25 °C, 55 °C, 90 °C, by maintaining each temperature for 40 min. The heating rate was 10 °C/min up to 10 °C before the temperature selected and then 1 °C/min.

B. 2.2.2 - Synthesis of Polyamidoamines with siloxane functionality: SiPAA and SiPAAOH.

In Fig. B.11 is reported the reaction scheme:

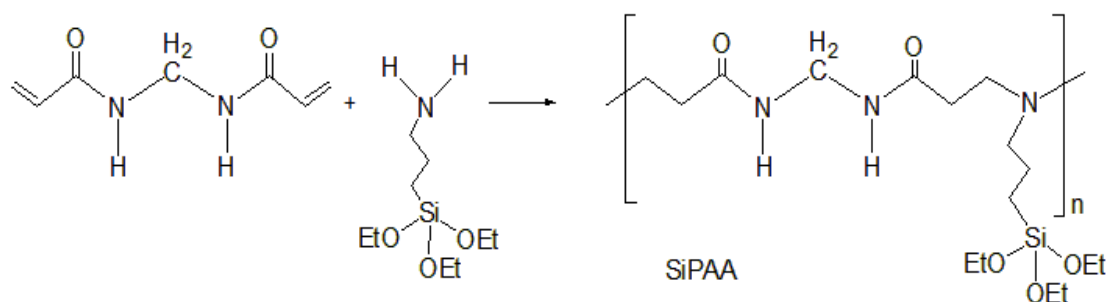


Fig. B.11 - Reaction scheme of polyaddition of *N,N'*-methylenebisacrylamide and 3-aminopropyltriethoxysilane.

SiPAA was synthesized by taking monomer of MBA and APTES in molar ratio 1:1 and SiPAAOH by adding to the MBA a solution of EtA and APTES in different ratios molar ratios (see Table B.3). The reactions were made as described in 2.2.1.1 section

The reaction was left at 23 ± 1 °C under vigorous stirring for 4 hours or more, until the solution became clear and then was kept in a Petri dish and left on air until gelation and drying. The xerogel obtained was transparent, homogeneous and slightly yellow coloured.

Table B.3 - Polyamidoamines functionalized with EtA and APTES.

Molar ratio MBA:EA:APTES	MBA in g ($\text{mol} \times 10^{-3}$)	EtA in ml ($\text{mol} \times 10^{-3}$)	APTES in ml ($\text{mol} \times 10^{-3}$)
1:0.3:0.7	1 (6.24)	0.11 (1.87)	1.06 (4.54)
1:0.5:0.5		0.19 (3.24)	0.75 (3.24)
1:0.6:0.4		0.23 (3.88)	0.60 (2.59)
1:0.7:0.3		0.27 (4.54)	0.45 (1.87)
1:0.8:0.2		0.31 (5.18)	0.30 (1.29)
1:0.9:0.1		0.35 (5.84)	0.15 (0.64)

B. 2.3 - PAA characterization

Polyamidoamines synthesized as described in the previous paragraph, were characterized by ESI-MS, NMR, FTIR and Raman spectroscopies, DSC. As regards the FTIR and Raman spectroscopies and ESI-MS, see Chapter A (par. A. 2.3.1 - A. 2.3.4, Solid state NMR and DSC will be described below.

B. 2.3.1 - Solid State NMR Spectroscopy (SS-NMR): ^{13}C -NMR, ^{29}Si -NMR

The solid state NMR analyses were done at the Department of Materials Engineering and Industrial Technologies, Laboratory of Nuclear magnetic resonance “Klaus Mueller”- University of Trento Italy.

^{29}Si and ^{13}C spectra were recorded with a Bruker 300 spectrometer equipped with a double band probe. The NMR spectra were analyzed using Bruker and MestRe-C software. Samples were packed in 4 mm zirconia rotors and spun at 9 kHz.

^{13}C SS-NMR spectra were obtained at a frequency of 75.47 Mhz. ^{13}C proton decoupling spectra were acquired with 90° pulse, length 2.2 μs , decoupling pulse length 6 μs , delay 10 s. Adamantane was used as external secondary reference (38.56 and 29.6 ppm).

^{29}Si spectra were recorded with pulse length 4.3 μs , delay 5 s; CPMAS ct 5 ms, ct pulse 3 μs . Q8M8 was used as external secondary reference (12.6 and -108 ppm). Si units are labeled according to the usual NMR notation.

B. 2.3.2 - Differential scanning calorimetry (DSC)

The thermal analysis of polymers were carried out at the Department of Materials Engineering of the University of Trento.

The analysis of differential scanning calorimetry were done with a DSC TA Instrument 2920 (modulated DSC): heating/cooling rate 0.2-20 $^\circ\text{C}/\text{min}$ - Sample weight 1-20 mg - Temperature Sensitivity 0.1 $^\circ\text{C}$.

B 2.4 - Wood samples

To evaluate the preservative effectiveness of PAAOH and SiPAA treatments, Scots pine (*Pinus sylvestris* L.) sapwood was used. *Pinus sylvestris* L. sapwood is characterized by high impregnability and low durability especially to biological attacks of fungi and termites. Samples of beech wood (*Fagus sylvatica*) were also used for tests on basidiomycetes: this wood is characterized by high impregnability and low durability.

Dimensions and number of samples were selected according to the European Standards recommendations EN 113:1996/A1:2004 [B71]: each sample was cut from untreated boards, without defects, with their longitudinal faces parallel to the grain. The dimensions were measured along the three principal axes of wood with respect to grain direction and growth rings: radial (rad), tangential (tang) and longitudinal (long) (Fig. B.12). The maximum tolerance accepted for each sample dimension was of ± 0.5 mm.

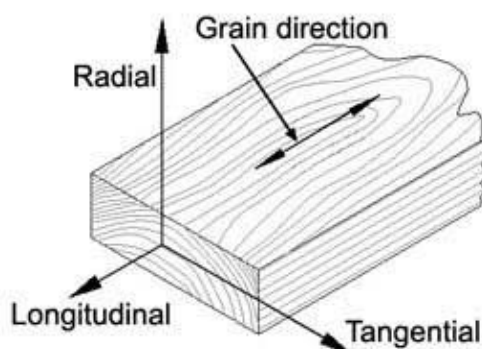


Fig. B.12 - The three principal axes of wood with respect to grain direction and growth rings.

- *Pinus sylvestris* L. sapwood mini-block samples were used for the accelerated efficacy tests against fungi basidiomycetes (*Coniophora puteana* L, *Trametes versicolor* and *Poria placenta*) and for the characterization of the wood treatments and sapwood standard-block samples for the standard efficacy tests against fungi basidiomycetes;
- *Fagus sylvatica* L. sapwood standard-block samples were used for the standard efficacy tests against fungi basidiomycetes [B71];
- *Pinus sylvestris* L. sapwood standard-block samples were employed for the evaluation of impregnation and preservative effectiveness of the treatments against termites *Kaloterms flavicollis* (Fabricius) and *Reticulitermes Lucifugus* (Rossi) [B72]

In Table B.4 are summarized the samples used in the different tests.

Table B.4 - Wood samples used in efficacy tests against fungi and termites.

Wood species	Name	Sizes cm	Test
<i>Pinus sylvestris</i> L. sapwood	Mini block	0,5 _{rad} x 1.0 _{tang} x 3.0 _{long}	<i>Coniophora puteana</i> ; <i>Poria placenta</i> ; <i>Trametes versicolor</i>
<i>Pinus sylvestris</i> L. sapwood	Standard samples	1,5 _{rad} x 2,5 _{tang} x 5.0 _{long}	<i>Coniophora puteana</i> ; <i>Poria placenta</i> ; <i>Trametes versicolor</i>
<i>Fagus sylvatica</i> L. sapwood	Standard samples	1,5 _{rad} x 2,5 _{tang} x 5.0 _{long}	<i>Coniophora puteana</i> ; <i>Poria placenta</i> ; <i>Trametes versicolor</i>
<i>Pinus sylvestris</i> L. sapwood	Standard samples	1.0 _{rad} x 5.0 _{tang} x 5.0 _{long}	<i>Reticulitermes lucifugus</i>
<i>Pinus sylvestris</i> L. sapwood	Standard samples	1.0 _{rad} x 6.0 _{tang} x 6.0 _{long}	<i>Kaloterms flavicollis</i>

B. 2.5 - Wood treatments

Wood specimens were conditioned at 20 °C and 65% relative humidity (RH) weighed until constant mass. Therefore they were oven-dried at 103 ± 2 °C for 18 hours. After cooling in desiccator, the anhydrous mass (m_0) was taken. Finally, samples were conditioned at 20 °C and 65% relative humidity (RH%) and stoked in a sealed container until utilization. Before the preservative treatment samples were weighed (m_h) and the wood initial humidity ($H_{max}\%$) was calculated by the following equation:

$$H_{max}\% = [(m_h - m_0) / m_0] \times 100 \quad (B1)$$

The tests were made on the applications of the polymers on wood by dipping and vacuum impregnation. The following synthesized formulations, previously described, were employed for the treatment of wood samples:

- 1) PAAOH a2/b2/d2e2: polyamidoamine with “OH” functionality; (MBA:EA=1:1);
- 2) SiPAA b2/d2e2: polyamidoamine with “Si-O-Si” functionality; (MBA:APTES=1:1);
- 3) SiPAAOH a2/d2/e2: polyamidoamine with either “Si-O-Si” and “OH” functionality; (MBA:EA:APTES=1:0.5:0.5);

The solvent used are water (a), ethanol (b), methanol (d) and Augeo SL 191 (e); mixing mode 2: MBA completely dissolved, EtA slowly dropping (see table B.2 in section B. 2.2).

B. 2.5.1 - Polymer application by dip coating (type 1)

Conditioned wood samples were dipped for 30 sec into a volume of preservative solution corresponding to 10/1 of sample volume. This was followed by 24 hours of air-drying at room temperature. This procedure (as suggested by Renner Italia spa) was adopted to simulate the spray coating made in industrial plants. This application produces shallow penetration of the protective.

B. 2.5.2 - Polymer application by impregnation (type 2a and 2b)

Coating by impregnation consists of wood treatment under vacuum followed by exposition to preservative solution, at a certain pressure.

Vacuum impregnation/nitrogen (type 2a)

The PAA solution was prepared as described in the synthesis section. Two 250-ml Schlenk flasks connected together by a Schlenk-frit were used. In a flask the polymer solution was introduced and in the other from 5 (blocks) to 10 (mini-blocks) wood samples. The “Schlenk-Schlenk” system was connected to Schlenk lines and put under vacuum. The Schlenk flask containing the solution was cooled by a cooling bath to avoid solvent evaporation during vacuum-nitrogen cycles described below. Wood samples were exposed to vacuum conditions (55 mbar) at room temperature for 1 hour. The vacuum cycles were set to 15 s every 3 min. Subsequently, the whole was turned 180° and the solution was poured into the flask with wood samples, maintained under vacuum for 4 min and gently stirred under nitrogen at 1 atm for 1 hour. Then, the samples were recovered, weighed and dried at room temperature and atmospheric pressure for 24 hrs. Finally, they are dried in oven-dry at 103 ±2° C for 18 hrs. The equipment used for the impregnation procedure is shown in Fig. B.13a.

Impregnation by laboratory system (type 2b) - CNR-IVALSA laboratory

Treatment of samples by impregnation was performed according to EN 113:1996/A1:2004 [B71]. An impregnation chamber (vacuum/atmospheric pressure) with 6 L total capacity was used (Fig. B.13b). Wood specimens were placed into the chamber, covered with a net and ballasted to prevent floating. Air was pumped at 0.7 kPa for 15 minutes and the fluid treatment was made to flow into the chamber. After adding the solution, the chamber was slowly brought to atmospheric pressure. Specimens were soaked in the PAA for two hours, then were extracted, gently wiped, weighed and placed in the conditioning room. The samples conditioned were oven dried (103±1 °C for 18 h) to determine dried mass. The heat treatment accelerates the adhesion of the protective to the cellular structure of wood through the crosslinking of the polymer [B39, B70].

The impregnation process was characterized by determining the Weight Percent Gain (WPG₁), referred to the anhydrous mass of untreated wood by the Donath et al. [B33] equation:

$$\text{WPG}_1\% = [(M_t - M_0)/M_0] \times 100 \quad (\text{B2})$$

where M_t and M_0 are anhydrous mass of treated and untreated wood, respectively. Impregnation treatment was used for all kinds of formulations synthesized.

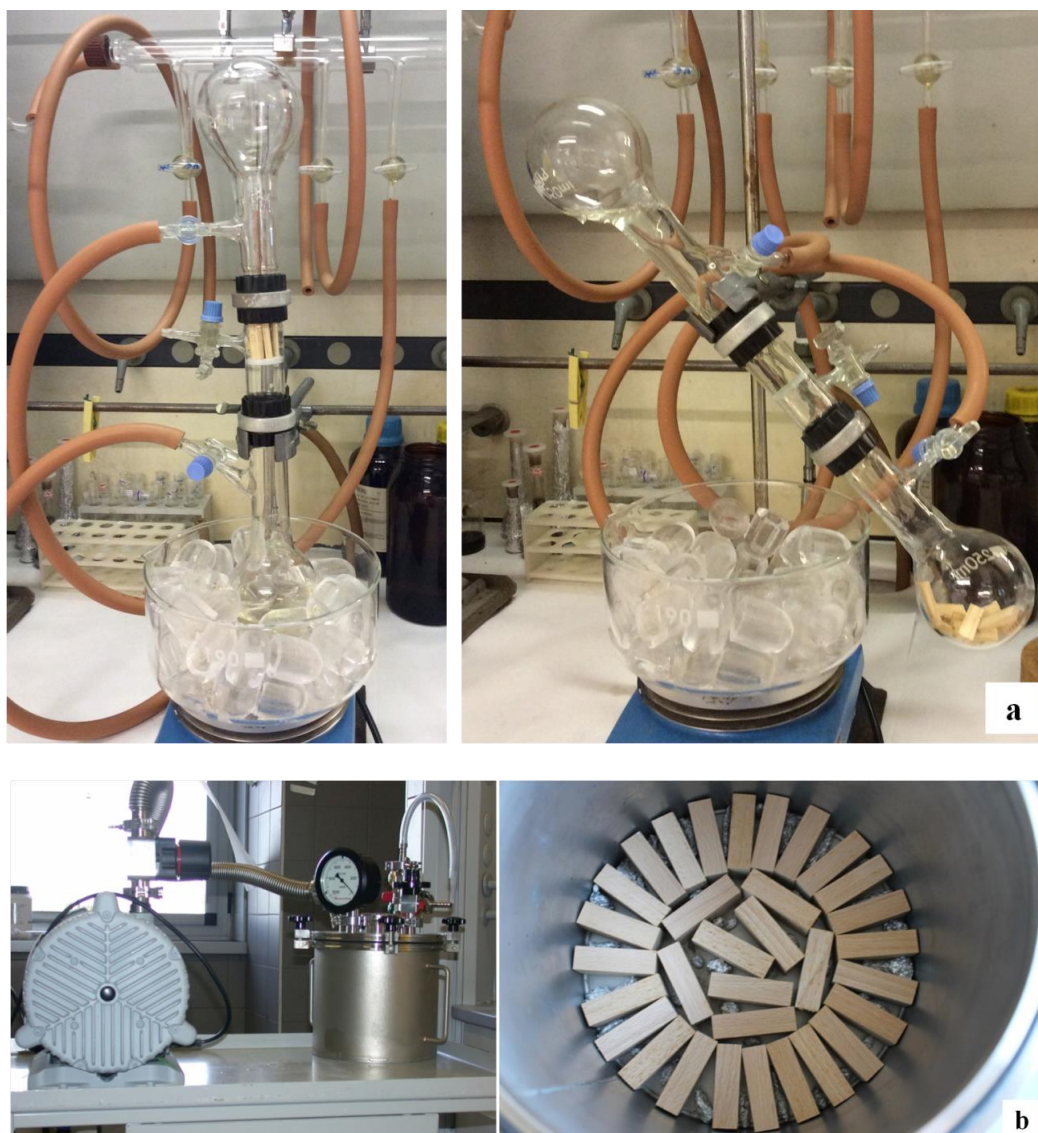


Fig. B.13 - (a) Impregnation system (vacuum/nitrogen), type 2a; (b) Impregnation chamber (vacuum/atmospheric pressure), type 2b [CNR-IVALSA].

B. 2.6 - Characterization of treated wood

SEM/EDS, ^{13}C -NMR and ^{29}Si -NMR solid state, FTIR and FT-Raman spectroscopy were used to characterize the treated wood samples. The colour changes have been measured according to the normal UNI-EN 15886:2010 [B73].

B. 2.6.1 - Scanning Electron Microscopy - SEM/EDS micro-analysis

Morphology and compositional data were obtained using a Jeol 6400 Scanning Electron Microscope (SEM) equipped with an Oxford INCA Energy Dispersive System (EDS) microanalysis (15-20 kV, 1.2 nA, electron beam about 1 mm in diameter, 60 s counting time; pure elements, simple oxides or simple silicate compositions as standard).

B. 2.6.2 - Environmental Scanning Electron Microscopy (ESEM)

An Environmental Scanning Electron Microscope FEI QUANTA FEG250 ESEM equipped with a EDAX TEAM EDS microanalysis with detector Apollo XL was employed. The measurements were made on areas of 500 and 200 μm^2 , through the section.

B. 2.6.3 - Colorimetric measurements

To evaluate the changes of the wood surface appearance due to the TiO_2 coatings, colorimetric analysis was performed by a Techkon Spectrodens colorimeter. At least three regions of a few mm^2 area were examined and averaged on each wood sample, using three samples for each case.

According to UNI EN 15886 (2010) [B73], the colour difference (ΔE) due to PAA applications with respect to the untreated samples was measured in the CIELab space:

$$\Delta E = \sqrt{\Delta L^{*2} + \Delta a^{*2} + \Delta b^{*2}}, \quad (\text{B3})$$

where ΔL^* is the change in lightness, Δa^* and Δb^* the change in hue (a^* is the red (>0)/green (<0) coordinate and b^* the yellow (>0)/blue (<0) coordinate, in the CIELab notation).

B. 2.7 - Accelerated aging test UNI EN 84 (1997)

Prior to fungi testing, a number of wood specimens were subjected to an accelerated aging test (leaching procedure) according to the standard EN 84:1997 [B74]. The wood samples were placed into a container, submerged in distilled water in a volume ratio water to wood 5:1 and maintained in deionised water for 14 days. To prevent the floating, the wood samples were anchored with loads. The beaker was placed in a desiccator and vacuum was applied down to a residual pressure of 4 kPa, maintained for 20 minutes, then released to return to normal pressure. Over a period of 14 days the water was changed nine times. Then samples were conditioned at 20 C and 65 % RH until constant mass. Anhydrous mass was measured after 18 h drying in oven at 103 ± 2 °C. The Weight Percent Gain of the leached mass (WPG_2) and the leached mass (LM) are calculated as follow:

$$\text{WPG}_2\% = [(M_L - M_0)/M_0] \times 100. \quad (\text{B4})$$

where M_0 and M_L are anhydrous mass of untreated and leached samples, respectively.

$$\text{LM}\% = [(M_t - M_L)/(M_t - M_0)] \times 100 = [(\text{WPG}_2 - \text{WPG}_1)/\text{WPG}_1] \times 100 \quad (\text{B5})$$

where M_t , M_0 and M_L are anhydrous mass of treated, untreated and leached samples respectively.

B. 2.8 - Efficacy tests against biological attack

B. 2.8.1 - Brown rot and white rot fungi - *C. puteana*, *T. versicolor*, *P. placenta*

The preservative properties of the different PAA formulations against basidiomycetes fungi in wood were evaluated according to European Standard EN 113 [B71]. The test requires the inclusion of three certified fungi, one mandatory and two additional - one for particular hazard and one supplementary fungus - chosen from a list of fungi used for testing a wood treatment. Brown rot fungus *Coniophora puteana* (Schumacher ex Fries) Karsten strain BAM Ebw. 15, as mandatory

fungus for wood; white rot fungus *Trametes versicolor* (L.) Lloyd, strain CTB 863 A, as fungus for particular hazard and brown rot fungus *Poria placenta* (Fries) Cooke sensu J. Eriksson strain FPRL280 as supplementary fungus, were selected.

Both treated and untreated control specimens were conditioned (20 °C e 65 % RH) and γ -sterilized before fungal exposure. The virulence of fungal strain, both in the accelerated and standard test, was assessed by placing a treated sample with an untreated reference in a Kolle flask inoculated with one of the fungus above described, grown on 20 ml of 4% malt and 2.5% agar medium. Another set of six untreated wood specimens for each tested fungus was used to check for fungus virulence. The test was considered valid if virulence control samples (untreated samples exposed to the fungal strain) showed a weight loss not lower than 20% and if samples final humidity was in the range 25% - 80%.

The antifungal resistance was evaluated through the measurement of the percentage mass loss (ML) of wood, defined as the difference between dry mass before and after the fungal exposure (M_F) corrected by a correction coefficient (C) or, in leached samples, by WPG₂.

$$ML = \frac{M_0 \times M_F}{M_0} \times 100 + C \quad (B6)$$

$$ML = \frac{M_0 \times M_F}{M_0} \times 100 + WPG_2 \quad (B7)$$

where M_0 and M_F are the dry mass before and after the fungal exposure; C=correction coefficient; WPG₂=gain mass due to treatment after the leaching procedure.

At the end of the test, the final moisture percentage (H_F) was calculated also in the exposed samples by eq.8:

$$H_F = \frac{M_{HF} \times M_F}{M_F} \times 100 \quad (B8)$$

where M_{HF} and M_F are the final mass and dry mass after the fungal exposure.

B. 2.8.1.1 - Accelerated test against *C. puteana* in mini-block samples

The accelerated methodology proposed by Bravery [B75] was employed with some modifications, due to the use of Kolle flasks in place on Petri dishes and arrangement of the samples [B30].

Scots pine (*Pinus sylvestris* L.) mini-block samples (4 replicates for each formulation), after conditioning (20 °C e 65 % RH) and sterilization (flame sterilization), were exposed to selected fungi. Each treated sample was placed side by side with one untreated reference sample (control) in a Kolle flask, containing the brown rot fungus previously grown on 20 ml of 4% malt, 2.5 % agar medium (Fig. B.14). The wood blocks were incubated with the fungus for four/eight/twelve weeks at 22 °C and 75% RH. At the end of the test, the samples were dried in an oven at 103±2 °C for 18h to determine the anhydrous mass. The accelerated test was made on all formulations of protective coatings as an explorative screening prior to standard test. Description of screening test, formulations and the fungi species used are reported in table B.5.

Table B.5 - Screening tests made on *Pinus sylvestris* L. mini-block samples treated with different PAAs.

PAA	Test time (weeks)	Application Method	Species of fungi	Leaching (YES/NO)	Efficacy YES/NO)
Step 1: Comparison between PAAOH and SiPAA					
PAAOH b	8	<i>Vacuum/nitrogen impregnation (type</i>	<i>C. puteana</i>	YES	NO
SiPAA b	8	<i>Vacuum/nitrogen impregnation (type</i>	<i>C. puteana</i>	YES	YES
Step 2: Comparison between SiPAAOH in different solvent					
SiPAAOH a	12	<i>Vacuum/nitrogen impregnation (type</i>	<i>C. puteana</i>	NO	YES
SiPAAOH e	12	<i>Vacuum/nitrogen impregnation (type</i>	<i>C. puteana</i>	NO	NO
Step 3: Comparison between PAAOH and SiPAA					
PAAOH e	8	<i>Fast dipping (type1)</i>	<i>C. puteana</i>	NO	YES
SiPAA e	8	<i>Fast dipping (type1)</i>	<i>C. puteana</i>	NO	YES
Step 4: PAAOH b					
PAAOH b	8	<i>Vacuum/nitrogen impregnation (type</i>	<i>C. puteana</i>	NO	YES
PAAOH b	8	<i>Vacuum/nitrogen impregnation (type</i>	<i>P. placenta</i>	NO	YES
PAAOH b	8	<i>Vacuum/nitrogen impregnation (type</i>	<i>T. versicolor</i>	NO	YES
Step 5: Comparison between SiPAA and SiPAAOH in different solvent					
SiPAA d	8	<i>Vacuum/nitrogen impregnation (type</i>	<i>C. puteana</i>	NO	YES
SiPAA d	8	<i>Vacuum/nitrogen impregnation (type</i>	<i>P. placenta</i>	NO	YES
SiPAAOH b	8	<i>Vacuum/nitrogen impregnation (type</i>	<i>C. puteana</i>	NO	YES
SiPAAOH b	8	<i>Vacuum/nitrogen impregnation (type</i>	<i>P. placenta</i>	NO	YES
SiPAA e	8	<i>Vacuum/nitrogen impregnation (type</i>	<i>C. puteana</i>	NO	NO
SiPAA e	8	<i>Vacuum/nitrogen impregnation (type</i>	<i>P. placenta</i>	NO	NO
SiPAAOH e	8	<i>Vacuum/nitrogen impregnation (type</i>	<i>C. puteana</i>	NO	NO
SiPAAOH e	4	<i>Vacuum/nitrogen impregnation (type</i>	<i>P. placenta</i>	NO	NO

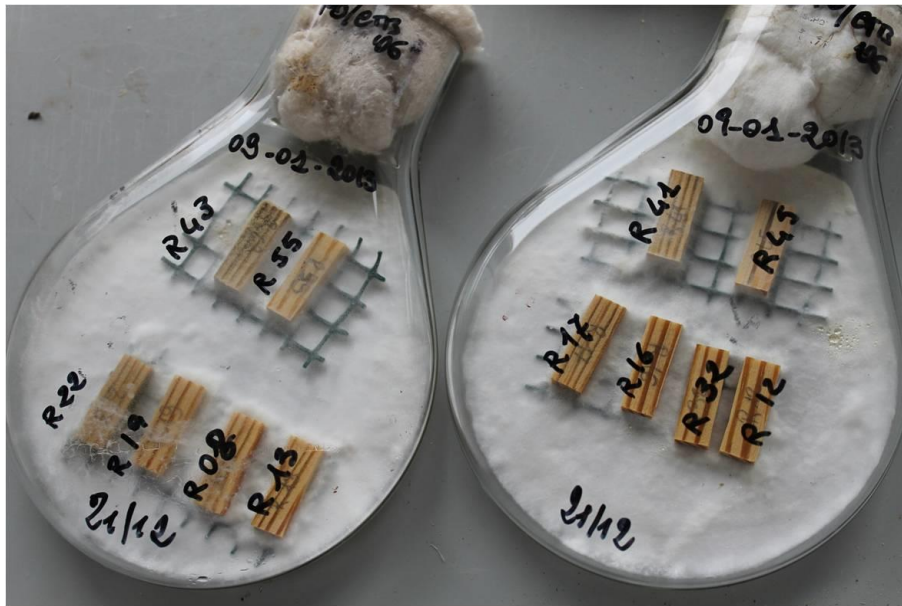


Fig. B.14 - Screening tests: preparation of mini-specimens at the end of the test.

B. 2.8.1.2 - Standard test according to UNI EN 113:1996/A1:2004

One treated sample and one reference untreated sample (control) sized $1.5 \times 2.5 \times 5 \text{ cm}^3$ were kept in a Kolle flask where the fungus was previously grown on the same 4% malt, 2.5 % agar medium. Eight repetitions for each fungus were used. The Kolle flasks were placed in a climatic chamber at $22 \text{ }^\circ\text{C}$ and 75% RH for sixteen week. In addition, treated samples (called check blocks), in number of three for each fungus tested, were put in contact with the culture medium, under the same environmental conditions of the previous specimens, but without fungal strains. These specimens were utilized for the determination of the correction coefficient used to calculate the possible mass loss due to factors different from fungal decay. At the end of the test, samples were dried in an oven at $103 \pm 2 \text{ }^\circ\text{C}$ for 18h to determine the anhydrous mass. The resistance against *C. puteana* was evaluated by the wood loss mass calculated as difference between the dry mass before the impregnation process and after the fungal exposure, corrected by the WPG_2 due to the impregnated treatment and by the correction coefficient (equation 6 and 7). The treatment that results in a mass loss of less than 3% is considered effective. The test was considered valid if final humidity of the control samples was in the range 20% - 80% and if their virulence showed a weight loss not lower than that indicated in Table B.6.

Table B.6 - Minimum mass loss for each species of fungus, as required by EN 113.

Fungus species	Minimum mass loss
<i>C. puteana</i> (Schumacher ex Fries) Karsten (BAM Ebw 15)	20% <i>Pinus sylvestris</i>
<i>P. placenta</i> (Fries) Cookie sensu J. Eriksson (FPRL 280)	20% <i>Pinus sylvestris</i>
<i>T. versicolor</i> (L.) Lloyd, strain CTB 863 A	15% <i>Pinus sylvestris</i> 20% <i>Fagus sylvatica</i>

B. 2.8.2 - Efficacy test of treatments against termites: laboratory no-choice test

The no-choice test was carried out to evaluate the termiticidal activity of wood treated with polyamidoamines with hydroxyl and siloxane functionalities in a force-feed environment.

The main termites of the dry wood belong to the Kalotermitidae family as *Kalotermes flavicollis* or *Cryptotermes brevis* and are highly dangerous pests of different types of wooden artefacts and structural elements for houses/buildings. Given the lack of international standards to verify the effectiveness of treatments against termites species of the dry wood, a specific protocol has been developed by Maistrello L.³ taking advantage of the internationally bibliography on tests with this kind of termites. The protocol was then submitted to the European working group CEN TC 38 WG 24 (Durability of wood and wood-based products) to evaluate the addition in the test of the standard EN350. To assess the resistance of the treatment on wood against subterranean termites also the European Standard UNI EN 118:2013 [B72] was followed.

To examine the effects of new synthesized treatments on termites resistance, the subterranean termite *Reticulitermes Lucifugus* (Rossi 1792) (Fig. B.7, section B. 1.2.2) and dry-wood termites *Kalotermes flavicollis* (Fabricius 1793) (Fig. B.8, section B. 1.2.2), the two most common species found in Italy, were chosen. All tests were carried out using termite colonies from within naturally infested wood, collected a few days before the tests at the natural reserve "Parco di San Rossore" near Pisa and maintained in the laboratory under suitable temperature and humidity conditions. In all cases it is a "no-choice" test, ie the only source of food for the termites is represented by wood specimen used for the test.

The tests were arranged as described by UNI EN 118:2013 [B72].

The specimens for the test were $1.0_{\text{rad}} \times 5.0_{\text{tang}} \times 5.0_{\text{long}} \text{ cm}^3$ and $1.0_{\text{rad}} \times 6.0_{\text{tang}} \times 6.0_{\text{long}} \text{ cm}^3$ of sapwood from Scots pine (*Pinus sylvestris* L.) employed with *Reticulitermes Lucifugus* and *Kalotermes flavicollis*, respectively. Six specimens were treated for each preservative solution as described in paragraph B. 2.5.2. At the end of the tests, the samples were dried to determine the final anhydrous mass post-test and therefore the consumption percentage of wood by termites.

From the collected termites two large colonies (named A and B) were obtained and 6 replicates per treatment have been set up, using both colonies, 3 for each colony. The UNI EN 118 norm [B72], adopted for experiments with *Reticulitermes lucifugus* requires 250 workers for each replicate, which must be added of a number of soldiers proportional to the original colony: with the colony A, for all replicas, 15 soldiers and 12 nymphs were added, while for the colony B 7 soldiers and 12 nymphs were added. Colonies were accomodated in 200 ml glass jars ($\varnothing 25$ mm, length 110 mm) with moisturised sand (Fontainebleau, sand silica 99.5% and water 4:1 v/v) as substrate. According to specific protocol for trials with dry-wood termites (*Kalotermes flavicollis*) 50 workers/ninphae and 1 soldier for each replica were employed. Each colony was put into a glass jars with perforated bottom, fixed to the sample. The duration of the test was twelve weeks.

In both tests, the lateral area of specimen was sealed with paraffin or inert adhesive. The treated wood, three replicates per treatment, were exposed to the colonies inside the containers and these were placed in a climatic room at 26 ± 2 °C and $70 \pm 5\%$ RH for eight weeks. Untreated specimens were also included as reference (check). During the exposure time, weekly observations were carried out to assure appropriate substrate moisture and to monitor the presence of termites and their activity.

After the exposure, the evaluation was done using a visual rating system according to EN 117:2012 [B76] and subsequently classified according to EN 350-2:1994 [B77] with values from 0 (no attack) to 4 (strong attack). Additionally, mass losses and the number of survived individuals were also measured. Results are expressed as survival percentage of workers, soldiers and nymphs and as

³ Prof. Maistrello Lara, Università degli Studi di Modena e Reggio Emilia – Centro Interdipartimentale BIOGEST-SITEIA, Dipartimento di Scienze della vita.

attack average degree, obtained in each replica. When in the virulence control test the worker survivors percentage is greater than 50% and the visual level is 4, the test is considered valid. Description of samples and termites species used are reported in Table B.7 and the testing procedure in Fig. B.15 and B.16. Samples were signed by capital letter for the specimens sized $1\text{ cm}_{\text{rad}} \times 5\text{ cm}_{\text{tang}} \times 5\text{ cm}_{\text{long}}$ and a capital letter with G subscript for specimens $1\text{ cm}_{\text{rad}} \times 6\text{ cm}_{\text{tang}} \times 6\text{ cm}_{\text{long}}$: A = treated with SiPAA; E = only solvent (methanol) is the reference sample (control); P = PAAOH; S = SiPAAOH.

Table B.7 - Description of samples and termites species used in efficacy test UNI EN 118.

Weeks	Samples	Application Method	Species of insects	Sizes
SiPAA_d2 formulation				
8	A	Vacuum/nitrogen impregnation (type 2a)	<i>Reticulitermes Lucifugus</i>	$1\text{ cm}_{\text{rad}} \times 5\text{ cm}_{\text{tang}} \times 5\text{ cm}_{\text{long}}$
12	A _G	Vacuum/nitrogen impregnation (type 2a)	<i>Kaloterme flavicollis</i>	$1\text{ cm}_{\text{rad}} \times 6\text{ cm}_{\text{tang}} \times 6\text{ cm}_{\text{long}}$
Methanol				
8	E - control	Vacuum/nitrogen impregnation (type 2a)	<i>Reticulitermes Lucifugus</i>	$1\text{ cm}_{\text{rad}} \times 5\text{ cm}_{\text{tang}} \times 5\text{ cm}_{\text{long}}$
12	E _G - control	Vacuum/nitrogen impregnation (type 2a)	<i>Kaloterme flavicollis</i>	$1\text{ cm}_{\text{rad}} \times 6\text{ cm}_{\text{tang}} \times 6\text{ cm}_{\text{long}}$
PAAOH_d2 formulation				
8	P	Vacuum/nitrogen impregnation (type 2a)	<i>Reticulitermes Lucifugus</i>	$1\text{ cm}_{\text{rad}} \times 5\text{ cm}_{\text{tang}} \times 5\text{ cm}_{\text{long}}$
12	P _G	Vacuum/nitrogen impregnation (type 2a)	<i>Kaloterme flavicollis</i>	$1\text{ cm}_{\text{rad}} \times 6\text{ cm}_{\text{tang}} \times 6\text{ cm}_{\text{long}}$
SiPAAOH_d2 formulation				
8	S	Vacuum/nitrogen impregnation (type 2a)	<i>Reticulitermes Lucifugus</i>	$1\text{ cm}_{\text{rad}} \times 5\text{ cm}_{\text{tang}} \times 5\text{ cm}_{\text{long}}$
12	S _G	Vacuum/nitrogen impregnation (type 2a)	<i>Kaloterme flavicollis</i>	$1\text{ cm}_{\text{rad}} \times 6\text{ cm}_{\text{tang}} \times 6\text{ cm}_{\text{long}}$

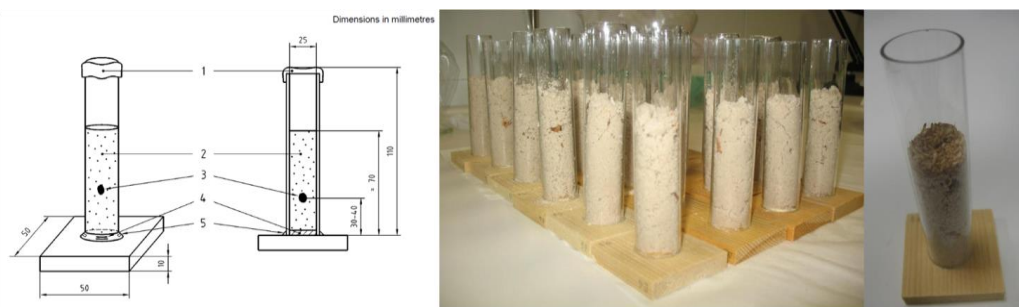


Fig. B.15 - Testing procedure for *Reticulitermes lucifugus*.



Fig. B.16 - Testing procedure for *Kaloterme flavicollis*.

B. 3 - RESULTS AND DISCUSSION

To get the most convenient method for synthesizing the polyamidoamines, to be tested as protective for wood, we checked different reaction conditions. The reactions were made as described in the experimental section B. 2.2.

The polymerization reaction is an "aza-Michael" addition, i.e. 1,4-addition of a nitrogen nucleophile to the vinyl β -carbon attached to an electron-withdrawing group, as explained in par. A.1.1.1.

The PAAs polymerization reaction is affected by different parameters such as mixing method, solvent, time and temperature [B55]. When the reagents were slowly added in the reactor, the reaction was almost complete. Among the different solvents, water appears to be the best one [B60]. In this study different solvents were compared: ethanol, methanol, 2,2-dimethyl-4-hydroxymethyl-1,3-dioxolane (called Augeo SL191) and water. Three different ways to mix the reagents were also used. The high temperature, as expected, favors the reaction even at short time but the polymers obtained do not have high molecular weight [B43]. We have verified the reaction rate for short times (about 4-5h) at room temperature, at 55 °C and 90°C.

B. 3.1 - Characterizations of protective treatments

In the following paragraphs are reported the results obtained on the synthesized polymers with different techniques: ESI-MS, NMR, IR and Raman spectroscopy.

B. 3.1.1 - Polyamidoamine with hydroxyl functionality: PAAOH

The pH of the PAAOH solutions, synthesized in different solvents mixing modes, was measured with an immersion tip pH-meter and the glass transition temperature was determined using a Gallenkamp capillary melting point apparatus (model MPD 350 BM 2.5; SANYO Gallenkamp. PLC, Loughborough, UK).

The pH values were in the range 9.7 ÷ 10.5 (9.7-9.9 in water; 10.2-10.5 in alcohols) and glass transition temperatures at 108 ÷ 120 °C for PAAOH synthesized in water and in methanol, slightly lower when synthesized in ethanol, 103 ÷ 115 °C.

B. 3.1.1.1 - ESI - MS

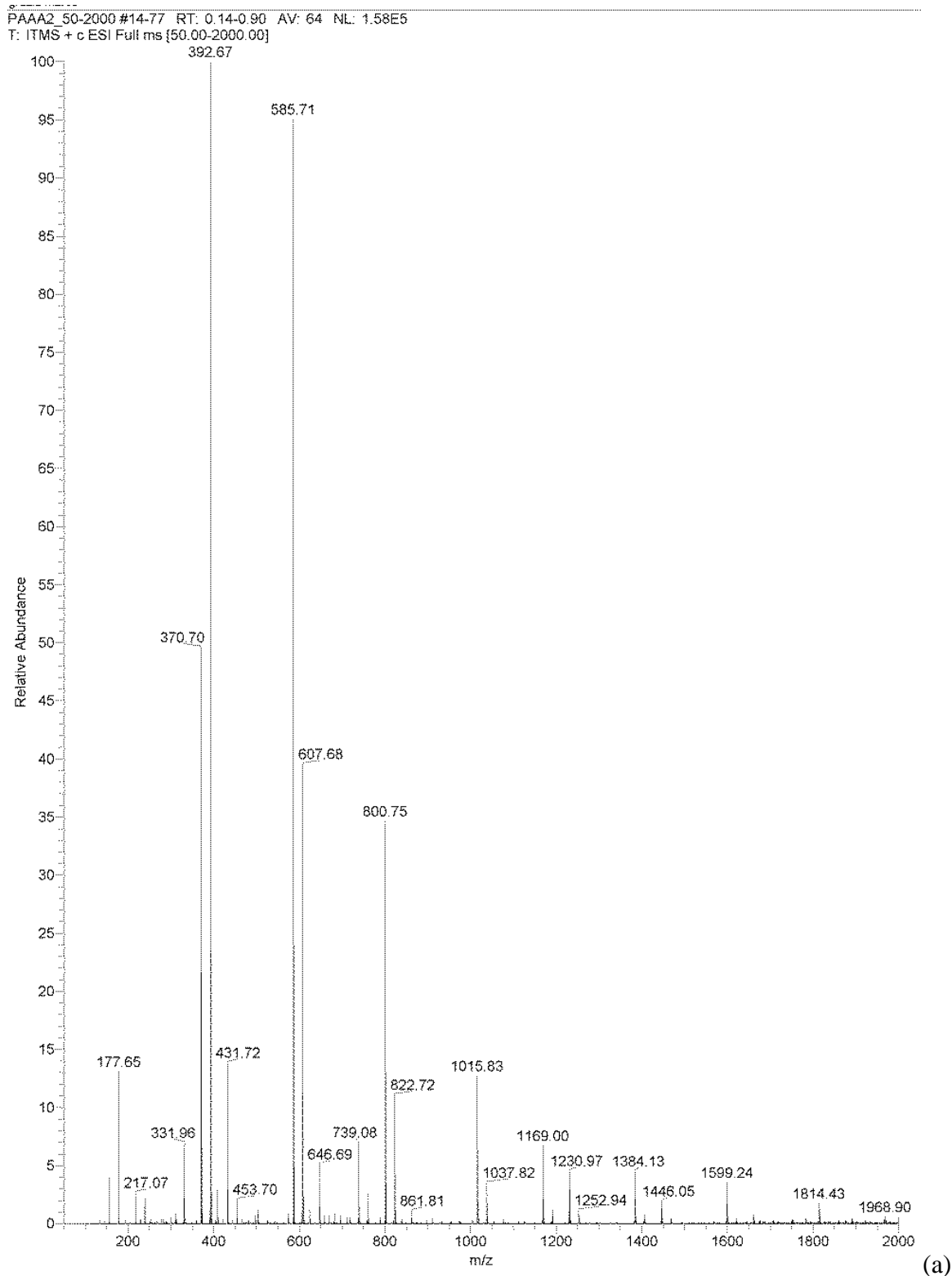
The ESI-MS analyses were made on all the formulations synthesized. As an example, the ESI-mass spectra of PAAOH synthesized by reacting N,N'-methylenebisacrylamide (henceforth called "A") and ethanolamine (henceforth called "B") obtained in water with two different mixing modes, 2 and 3 (see Experimental Section 2.2) are reported in Fig. B.17 a and b.

In Fig. B.17a is shown the ESI-MS spectrum of PAAOH, obtained by slowly dropping EtA into MBA solution (mixing mode 2). The signals observed can be divided in two main series: the first series starts at m/z 370.70 and corresponds to ABA sequence whereas the second series starts at m/z 392.67 which is the sodium adduct, (ABA + Na). Within each series, the peaks are separated by the mass value 216.6, i.e. a monomer AB.

These groups of signals correspond to molecules that have both ends terminating with MBA. The single charge sodium adduct $[M+Na]^+$ at m/z 392.67 is the strongest signal. The signal due to ABABA sequence at m/z 585.71 is the second most intense signal. In addition, signals at m/z 217.07, 431.72, 646.7 are also observed. They, too, are separated by the mass value 216.6 which corresponds to the molecule of mono-adduct AB. This group corresponds to molecules terminating with EtA and MBA.

In Fig. B.17b is shown the ESI-MS spectrum of PAAOH, obtained by slowly dropping MBA into EtA solution (mixing mode 3). As in the previous spectrum, there are two main sets of signals: in

each set the signals are separated by the AB mass value 216.6. The signals starting at m/z 217.21 $[M+H]^+$ correspond to AB sequence and those starting at m/z 276.39 correspond to BAB. The last group is due to the molecules in which the end group is a *sec*-amino group. The strongest signal at m/z 707.95 is due to sequence BABABAB. The signal due to ABABAB is also intense at 646.97. This group corresponds to products terminated with either *sec*-amine and acrylamide groups.



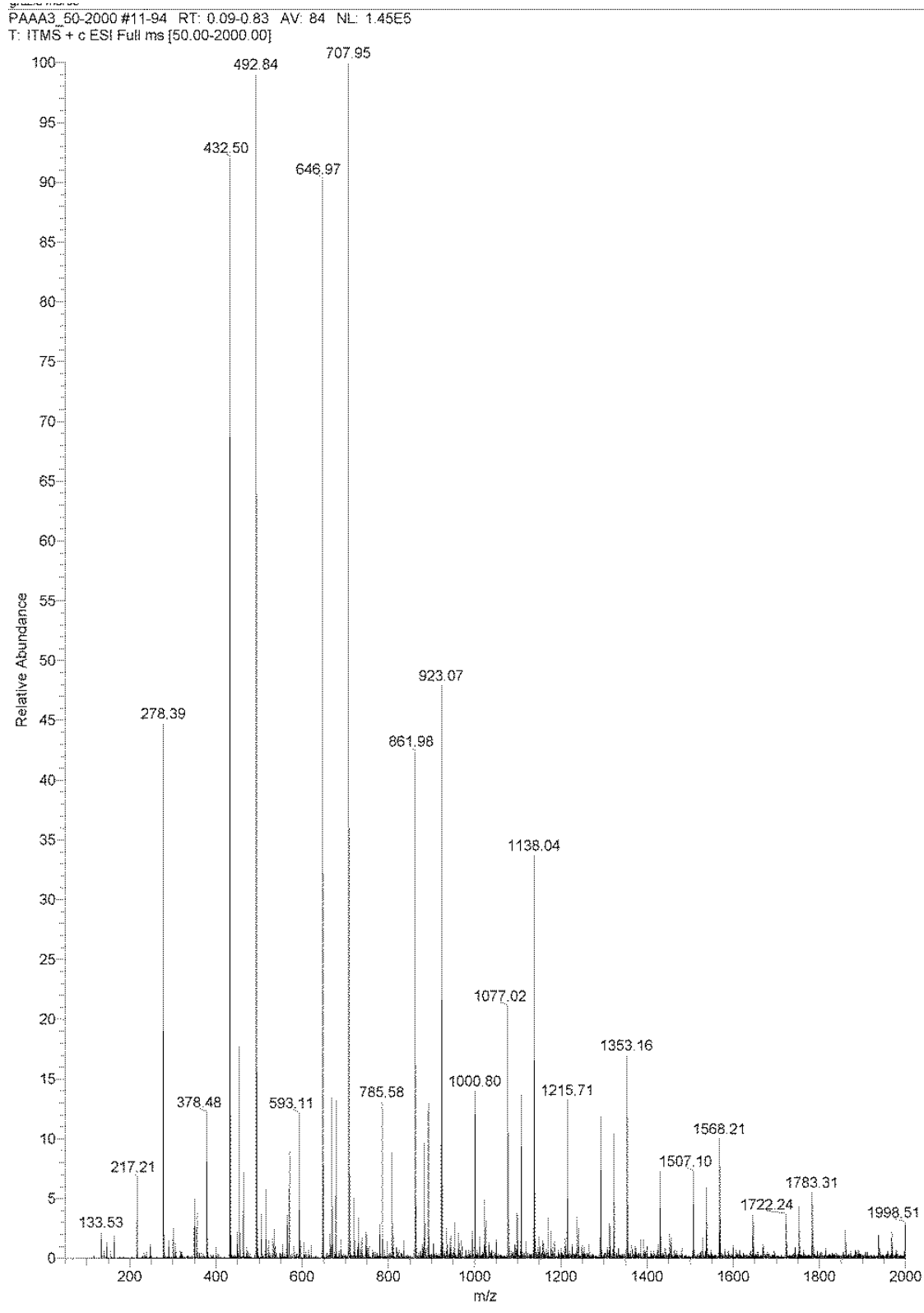


Fig. B.17 - ESI-MS spectrum of PAAOH obtained with water as solvent. Comparison between two mixing modes: EtA slowly added into MBA solution (a) or MBA slowly added into EtA (b).

Polyamidoamines obtained in other solvents show a distribution of average molecular weights centered on sequences of two/three monomers up to 9 repeating units. The type 2 mixing mode seems to promote the formation of oligomers with higher molecular weight. The oligomers are mainly composed of ABA sequences that have double bonds as terminal groups at both ends. In

water and ethanol, the adduct with sodium of each oligomer is present. The type 3 mixing mode favors the formation of oligomers of type BAB with amine terminal groups and ABAB with both groups.

The results suggest that performing the polymerization reaction with different mixing modes, PAAs prevailingly or totally terminated with either of the two groups (A-PAAs and B-PAAs) can be obtained. End-functionalized PAAs may be employed for preparing block and graft copolymers, as well as crosslinked resins [B5].

B. 3.1.1.2 - NMR

The addition of amine nitrogen to the double bond of amide was followed by NMR spectroscopy. Fig. B.18 shows the reaction scheme of PAAOH: the functional groups under investigation are highlighted.

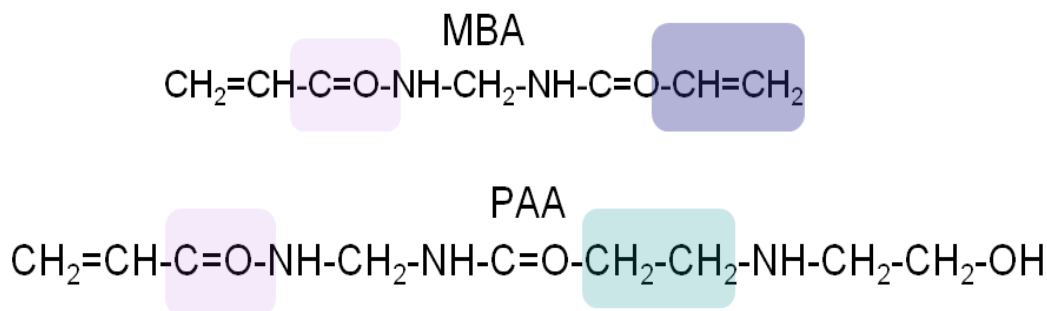


Fig. B.18 - Reaction scheme of PAAOH.

In Fig. B.19-21 are reported the ^1H -NMR and ^{13}C -NMR spectra of polyamidoamine with hydroxyl functionality.

Fig. B.19 displays the ^1H -NMR of PAAOH synthesized by slowly adding the MBA dissolved in water at 40 ± 1 °C in ethanolamine solution (mode mixing 3). The sol is dried in vacuum and completely re-dissolved in D_2O . The spectrum consists of two triplets due to new aliphatic protons at δ 2.43 (J 6.8; $-\text{NCH}_2\text{CH}_2\text{C}=\text{O}$) and δ 2.83 (J 6.9; $-\text{NCH}_2\text{CH}_2\text{C}=\text{O}$), and two triplets of the methylene protons from the ethanolamine at δ 2.62 (J 6.0; $-\text{NCH}_2\text{CH}_2\text{OH}$) and δ 3.64 (J 6.1; $-\text{NCH}_2\text{CH}_2\text{OH}$). These signals confirm that the amine nitrogen addition to the double bond took place. The signals by protons of the double bonds from the unreacted MBA are also present at 5.78 and 6.23 ppm. The protons of the methylene bridge, between the two NH of amide [$-\text{NHCH}_2\text{NH}-$], resonate at 4.55 ppm. The signals due to NH protons of amide and of unreacted amine molecule are not visible in D_2O .

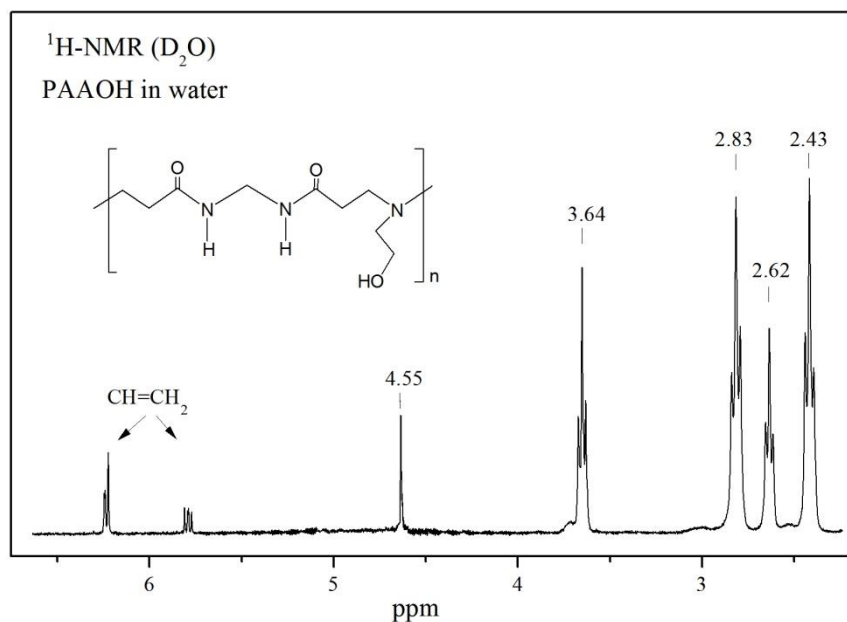


Fig. B.19 - ¹H-NMR (D₂O) of PAAOH.

The ¹³C-NMR spectra were acquired on PAAOH polymers synthesized without solvent at 25 °C and 55 °C and in ethanol and methanol under different reaction procedures (Fig. B.20 and B.21, respectively).

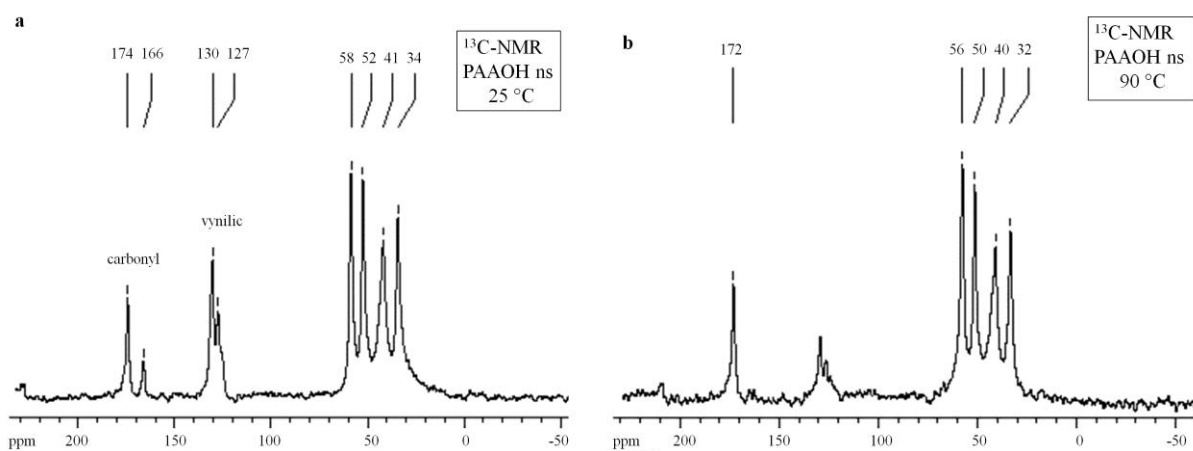


Fig. B.20 - ¹³C-NMR spectrum of PAAOHns at 25 °C (a) and after heating at 55 °C (b).

In Fig. 20 are reported the ¹³C-NMR spectra of PAAOHns (no solvent) obtained at 25 °C (a) and at 55 °C (b).

The observed resonances at 25 °C are a doublet at 174 and 166 ppm attributed to quaternary carbon, a doublet at 130 and 127 ppm due to unreacted vinyl carbon and signals from the aliphatic carbon due to alcohol chain of EtA and new methylene groups from the partially reacted bisacrylamide. In the spectrum in Fig. B.20b is noticeable only one signal of the amide carbonyl, slightly shifted (172 ppm) and the decrease of the signals due to vinyl carbon at about 130 ppm. Ando et al [B78] in a ¹³C-NMR study of solid polypeptides demonstrated that ¹³C-NMR chemical shift of the C_α, C_β and carbonyl carbons are considerably displaced depending on the conformations adopted. It is

reasonable to ascribe conformation-dependent ^{13}C chemical shifts to changes of electronic structure accompanying changes of dihedral angles of the skeletal peptide bonds.

^{13}C chemical shifts of carbonyl (amide) carbons are displaced downfield at DPn around 11-16 by 5.2 and 4.6 ppm. Such behavior is ascribed to the conformational change from the β sheet form to the α helix form the oligomers with DPn between 4 and 10 take the β sheet form, the oligomers with DPn >16 adopt the α helix conformation [B79].

Fig. B.21 shows the ^{13}C -NMR spectra recorded on PAAOH polymers obtained in ethanol and methanol with the three modes of mixing (see par. B. 2.2). The solvent has a significant influence on the addition reaction: polar solvents accelerate the reaction. The reaction in methanol is almost complete, while in ethanol signals of the unreacted double bonds are still observed. As regards the mode of mixing, only in methanol there are large differences. Mixing mode 3, in which a solution of MBA is slowly added to ethanolamine (EtA) gave the best results. Unlike to what was observed in the case of polymers synthesized in methanol, in ethanol the three procedures show similar results.

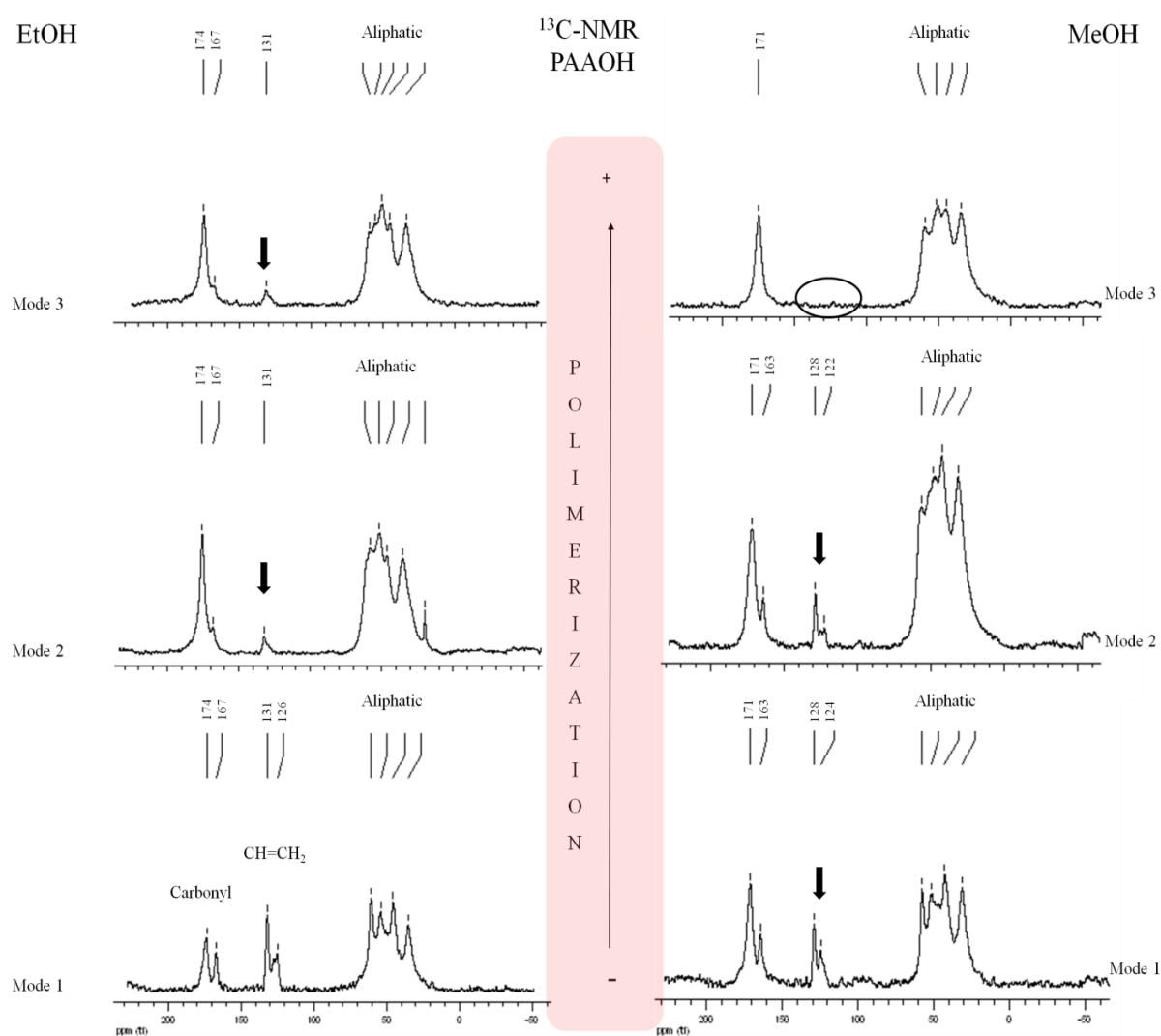


Fig. B.21 - ^{13}C -NMR of the polymers PAAOH b (ethanol) and PAAOH d (methanol). The direction of the polymerization is indicated according to the conditions of synthesis.

B. 3.1.1.3 - Vibrational spectroscopies: FTIR and μ -Raman

In order to get a more complete characterization of the synthesized polyamidoamines, the analysis was also carried out by FTIR and μ -Raman spectroscopies. The spectra of the reagents and of PAAOH synthesized in different solvents were acquired.

In the analysis of the spectra the attention is focused on the vibrational modes involving the double bond C=C: the corresponding bands should decrease and eventually disappear in the final product [B80-82].

In Fig. B.22 are compared the FTIR spectra of the PAAOH powders, obtained by drying *in vacuo* the synthesized sols, using as solvent water (a), ethanol (b) and methanol (d), with that of MBA. As can be seen, in the spectrum of the polymer, the band intensity at $\approx 1630\text{ cm}^{-1}$, very strong in pure MBA, and attributed to the stretching mode $\nu(\text{C}=\text{C})$, is decreased indicating advancing polymerization. Furthermore, in the region typical of the stretching vibrations of the CH bonds there are noticeable differences between the pure reagent and the polymers. The reduction of the peak relative to the vinyl CH stretching at $\approx 3050\text{ cm}^{-1}$ and the appearance of a new broad peak at about 2800 cm^{-1} , attributable to stretching vibrations of CH_2 formed following the addition reaction, are observed.

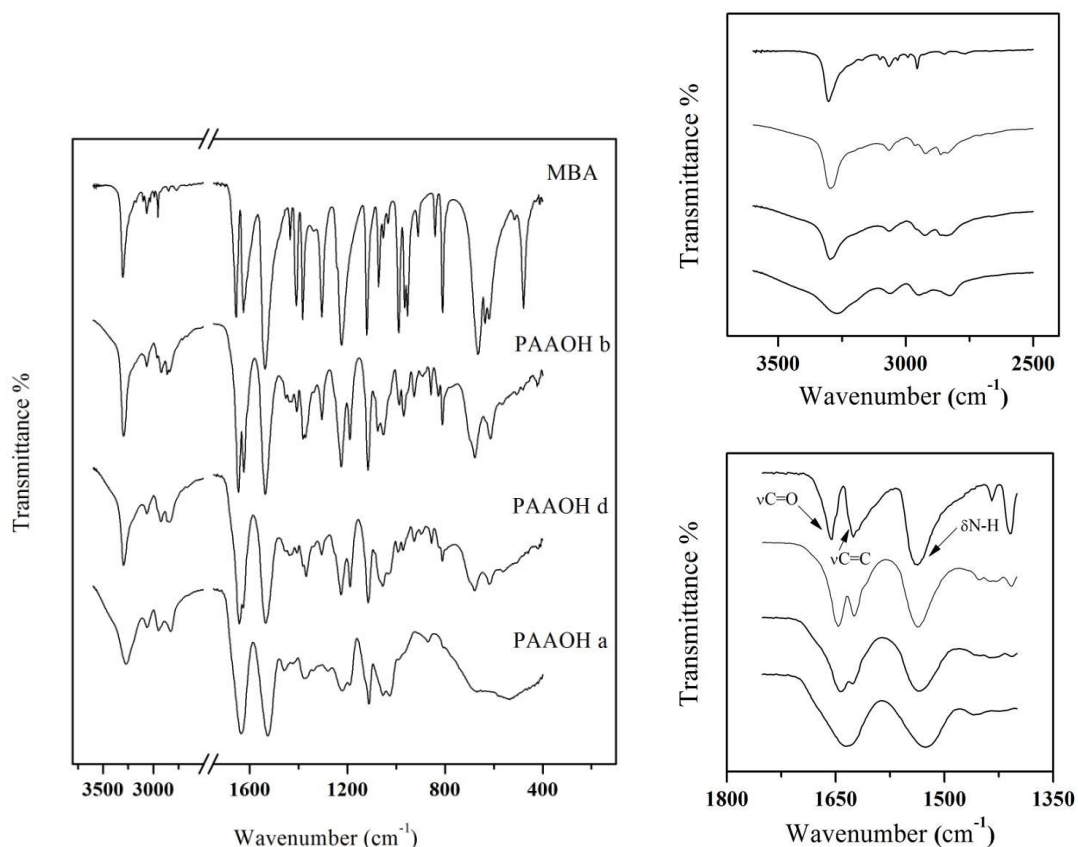


Fig. B.22 - FTIR spectra of PAAOH in water (a), ethanol (b) and methanol (d) compared with that of MBA. On the right are shown details of the spectral regions $3500\div 2500\text{ cm}^{-1}$ (top) and $1700\div 1400\text{ cm}^{-1}$ (bottom).

In the following Fig. B.23 and B.24 are shown the Raman spectra acquired on PAAOHns and PAAOH in water, ethanol and methanol to investigate the solvent effect on the reaction.

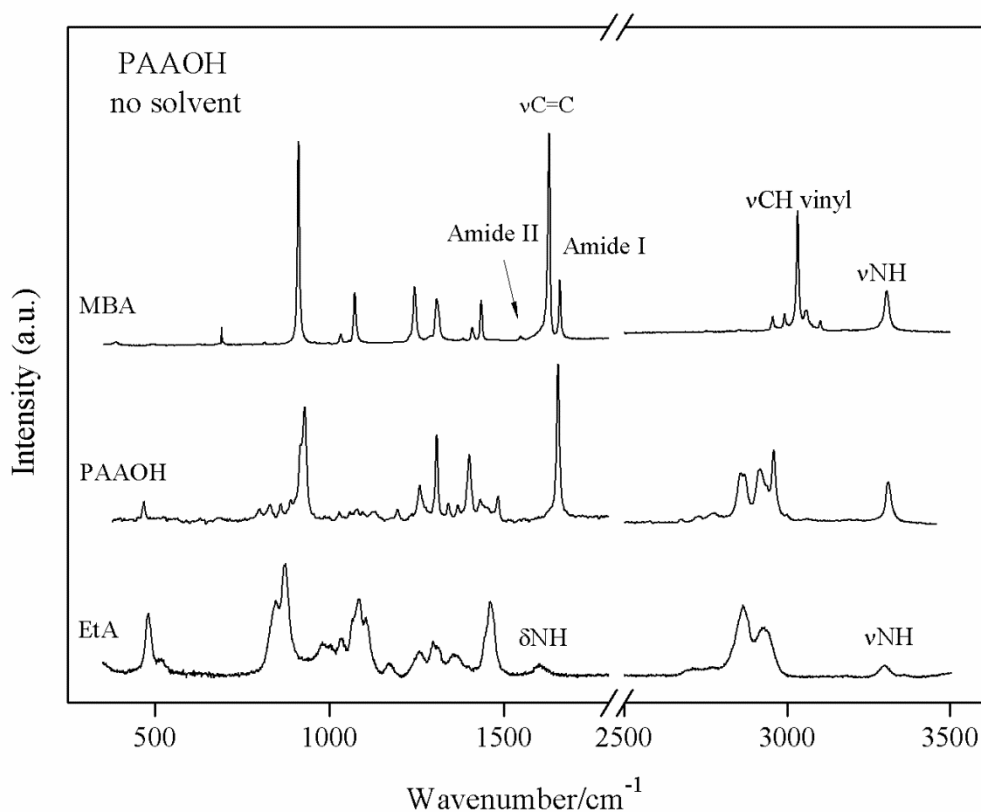


Fig. B.23 - Raman spectrum of PAAOH synthesized without solvent and of the pure reagents.

As previously explained, the degree of polymerization between acrylamide and amine is monitored by following the variations in the characteristic peak at $\sim 1630\text{ cm}^{-1}$: with the progress of the reaction, the monomers are consumed to give the polymer, the addition of amine nitrogen to the double bond leads to its conversion in simple C-C bond. In the Raman spectrum this is evidenced by the disappearance of the associated peak (1633 cm^{-1}).

As can be seen from Fig. B.24 a - b, PAAOH synthesized without solvent shows only the signal due to the stretching vibration of the carbonyl (at 1655 cm^{-1}). The band is relatively sharp and is located in an intermediate position with respect to the doublet evident in pure MBA. The shift is due to the disappearance, following the addition reaction, of the conjugated double bond. As regards the polymers in ethanol and methanol under different mixing conditions, the Raman spectra confirm the results obtained from ^{13}C -NMR analysis: PAAOHs synthesized in methanol have a degree of polymerization higher than those synthesized in ethanol. In addition, MBA completely dissolved in the solvent, slowly added to the EtA, seems to favor the progress of the reaction.

The evolution of the reaction between MBA and EtA at $55\text{ }^{\circ}\text{C}$ in water was also followed by μ -Raman spectroscopy. The spectra were acquired at time intervals of 30 minutes up to 3 hours (Fig. B.25). Arrows indicate the bands associated to the C=C and C=O stretching modes, at 1633 and 1653 cm^{-1} , respectively. At 1410 and 1457 cm^{-1} are found the scissoring modes of vinyl CH and CH_2 , respectively. During the polymerization reaction, the Raman intensity of the peaks associated with the double bond stretching in MBA decreases considerably.

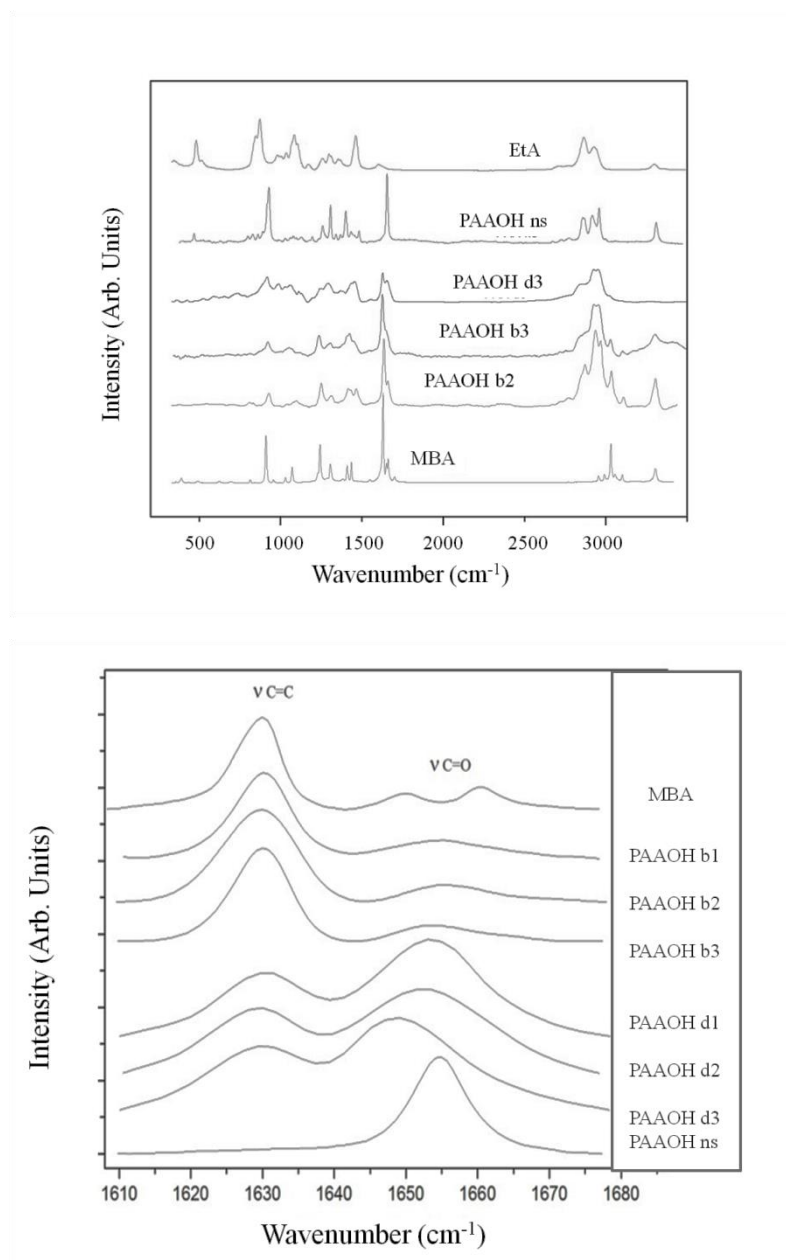


Fig. B.24 - Raman spectra: comparison between PAAOH in different solvents and 1-2-3 mixing modes (a); Raman spectra of PAAOH in C=O and C=C region (b).

To evaluate the influence of the temperature on the polymerization, Raman spectra (Fig. B.26) were acquired at 25 °C, 55 °C, 93 °C (the experimental conditions was described in B.2.2...). Each temperature is maintained for 40 min.

At 55 °C the peaks related to the double bond begin to decrease, with respect to the 25 °C case. At 925 cm⁻¹ a new peak appears, attributed to the C-N stretching of the *tert*-amino nitrogen formed by the reaction [B83]. At 93 °C the band associated with C=C has almost disappeared and the narrow band at 925 cm⁻¹ is increased, evidence that the monomers are consumed and the addition product is nearly formed.

These results are in agreement with those obtained on the amidoamine model, AADEtA, AAEtA, MBADEtA, obtained by aza-Michael addition, which were discussed in Part A (see par. A.3.1.2): the reactions are favored when water is used as a solvent and at temperatures > 55 °C.

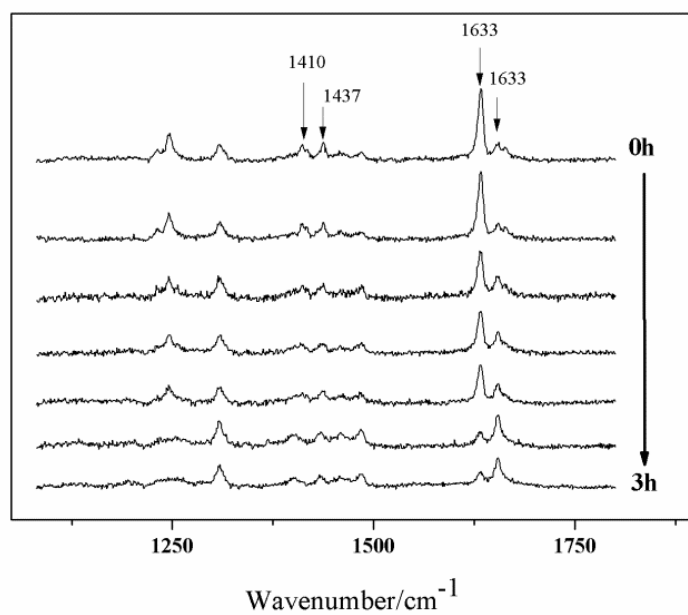


Fig. B.25 - Time evolution of the Raman spectra on PAAOH at 55 °C.

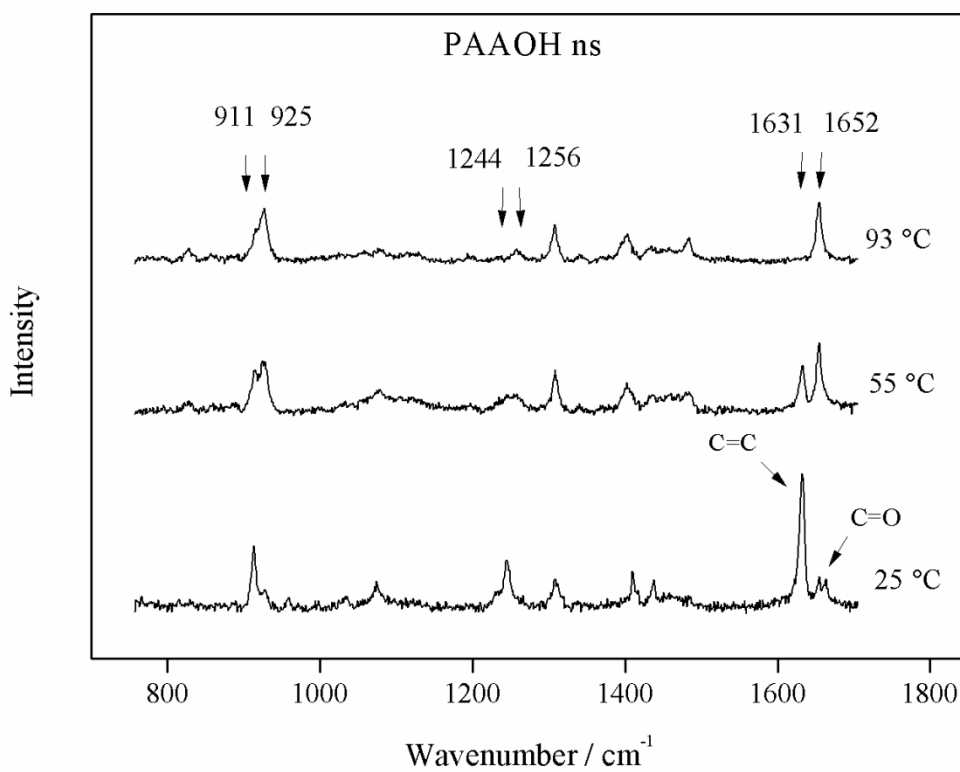


Fig. B.26 - Raman spectra of PAAOHns taken at different temperatures..

B. 3.1.1.4 - Differential scanning calorimetry (DSC)

Fig. B.27 shows the DSC behavior of the monomer MBA. In all experiments, the rate of heating / cooling was 10 °C/min.

In the first experiment (figure on the left) the sample was brought up to decomposition and then cooled. As can be seen from the heating run, at 185 °C and 199 °C there are two well defined endothermic peaks, due to the change of phase (fusion). It should be emphasized that N, N'-methylenebisacrylamide has crystalline structure and has a defined melting temperature while amorphous substances have a range of temperatures (glass transition temperature t_g). The decomposition of the sample occurs at 262 °C. The cooling run is indeed flat.

In the second experiment (center figure), the sample was heated until melting and then cooled: the re-crystallization is evidenced by the exothermic peak at 170.2 °C.

In the last experiment (right figure) two scans were performed continuously: both the endothermic peaks due to the melting and the exothermic peak due to re-crystallization (during cooling) are evident. In the second scan either melting and re-crystallization temperatures are lower.

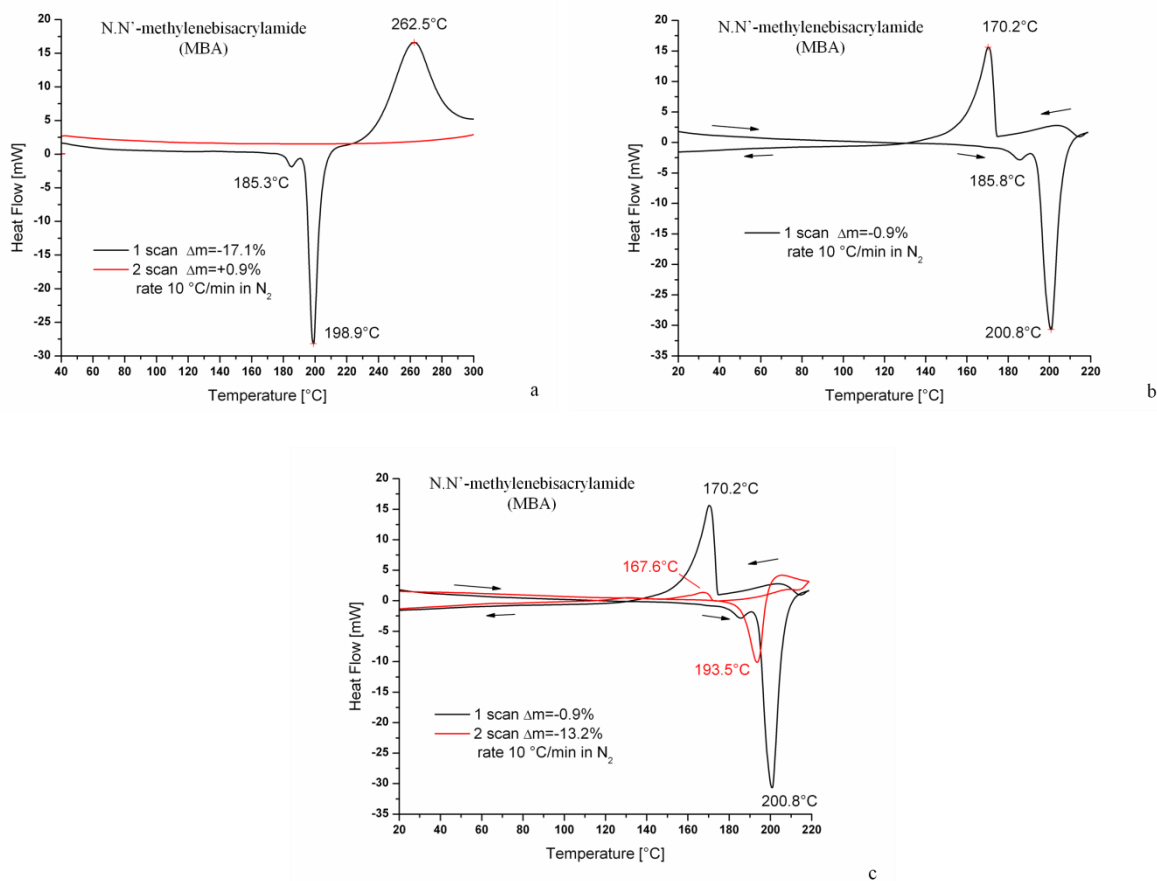


Fig. B.27 - DSC of N,N'-methylenebisacrylamide (MBA): heating up to 300 °C (a); one scan up to fusion (b); two repeated scans until fusion (c).

In Fig. B.28 are compared the DSC curves for PAAOH polymers synthesized in ethanol and obtained in different mixing modes (b1 and b2, see table B.2 par. B. 2.2). In contrast to what observed for MBA, there is no defined endothermic peak but a wide and asymmetric curve: the polymer has a predominantly amorphous structure. The glass transition temperature is higher ($t_g =$

111.7 °C) when the polymer is synthesized by dissolving completely MBA and slowly dropping EtA into the reaction mixture with respect to the polymer obtained without dissolving MBA ($t_g = 100.9$ °C). Around 200 °C the curve shows an endothermic "shoulder", probably due to residual unreacted monomer. The meltig point is higher than that of the starting monomer.

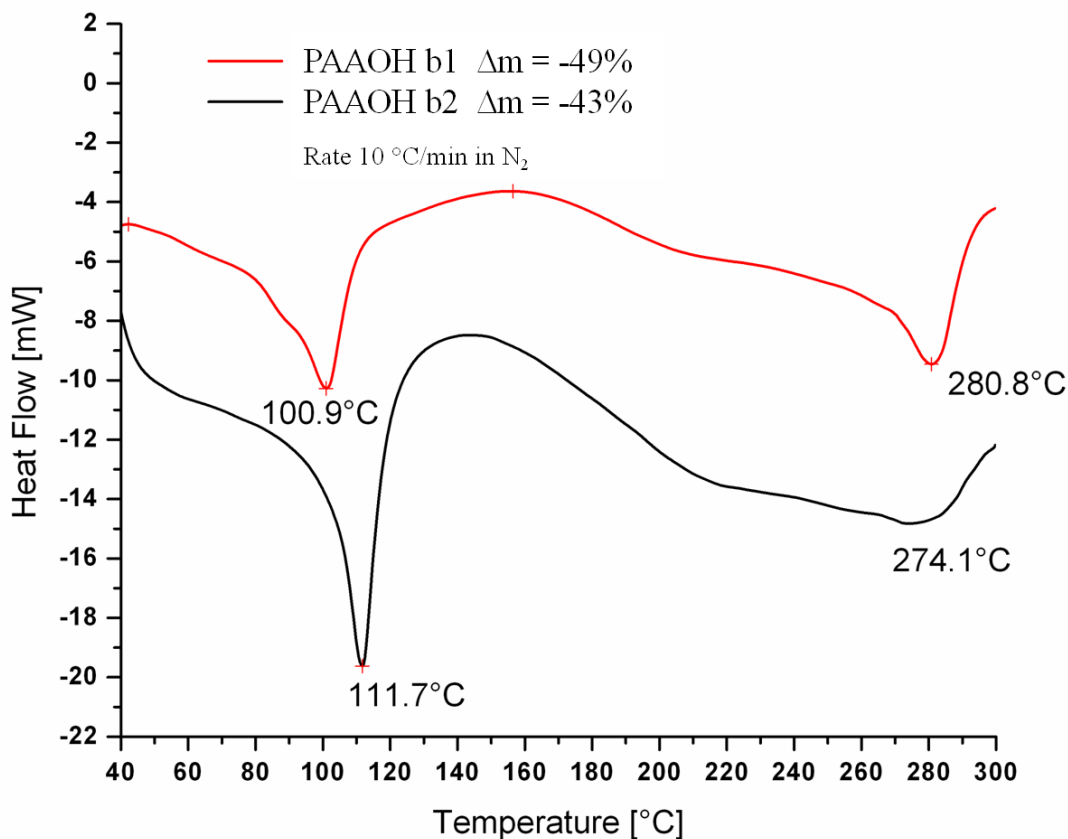


Fig. B.28 - DSC of PAAOH b1 and PAAOH b2: one scan up to 300 °C.

Given the above results, the PAAOHb2 polymer was treated at 90 °C in a muffle furnace for 3 hrs, and then subjected to DSC analysis. The DSC run in Fig. B.29 shows significant differences with respect to that reported in Fig. B.28: the endothermic peak has almost disappeared and the onset of fusion is shifted to higher temperature. It might be expected that the heat treatment causes the complete amorphization of the polymer making it more resistant to heat. The polymer decomposes without melting.

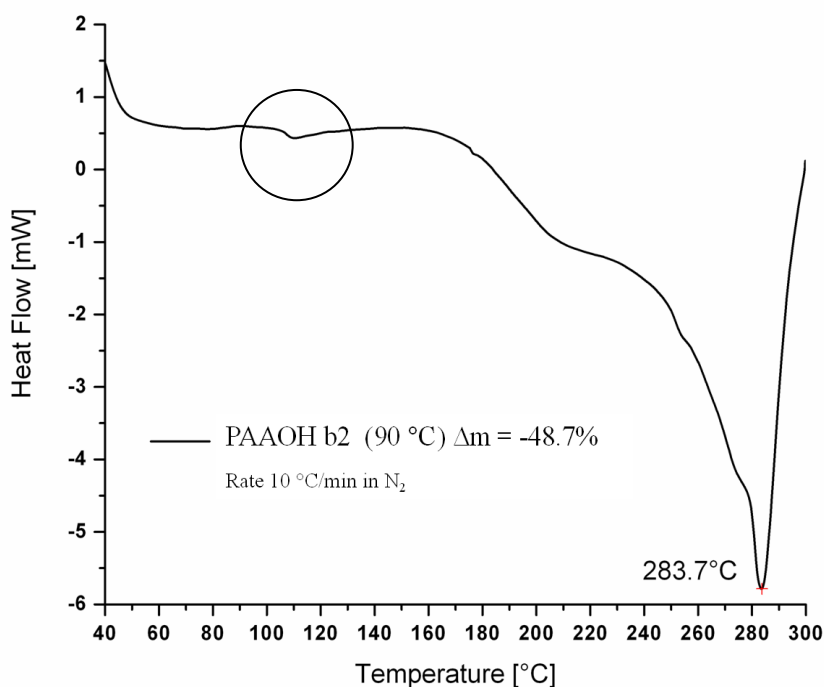


Fig. B.29 - DSC of PAAOH b2 after heat treatment.

B. 3.1.2 - Polyamidoamines with siloxane functionality: SiPAA and SiPAAOH

A method which allows improving wood durability is based on wood modification by in situ polymerization of alkoxy silanes. The wood preservative organo-alkoxy silane based, causes a delay of fungal attack on wood [B30, B34-35, B70, B84]. Polyamidoamines with siloxane functionality, SiPAA and SiPAAOH, were obtained using water and ethanol as solvent, respectively. The gelation time [B42] increases with the ratio EtA/APTES. Also the molar concentration of the solution has a significant importance on the condensation reaction of the sol-gel process. The concentration of the polymers synthesized and tested for evidence of biocidal activity was 0.15 M. The gelation time for the different polymers ranges from 8h to 24h.

B. 3.1.2.1 – NMR

^{13}C -NMR and ^{29}Si CP/MAS NMR spectra were acquired on SiPAAOH and SiPAA xerogels synthesized in ethanol and dried by evaporation at room temperature.

The ^{13}C -NMR spectrum presented in Fig. B.30 of the SiPAA polymer functionalized with silicon (MBA:APTES=1:1), shows only one signal of the carbonyl carbon (170 ppm) whereas the signal of the vinyl carbons has completely disappeared. As discussed above (B.3.1.1.2) in the ^{13}C -NMR analysis of PAAOH, there is a correlation between the disappearance of the peak of the carbonyl and the disappearance of the peak of the vinyl and both are related to the degree of polymerization [B78].

In Fig. B.31 are shown the ^{13}C -NMR spectra of SiPAAOH at different EtA/APTES ratios.

Compared to SiPAA, that shows a high degree of polymerization, in SiPAAOH, functionalized with hydroxyl and siloxane groups, the signals of the vinyl group decrease with increasing EtA/APTES

ratio. The steric hindrance introduced by the highly cross-linked siloxane groups hampers the ethanolamine attack to the double bond. In addition, with advancing APTES condensation, the structure becomes more rigid, further limiting the nucleophilic attack of the aminic nitrogen.

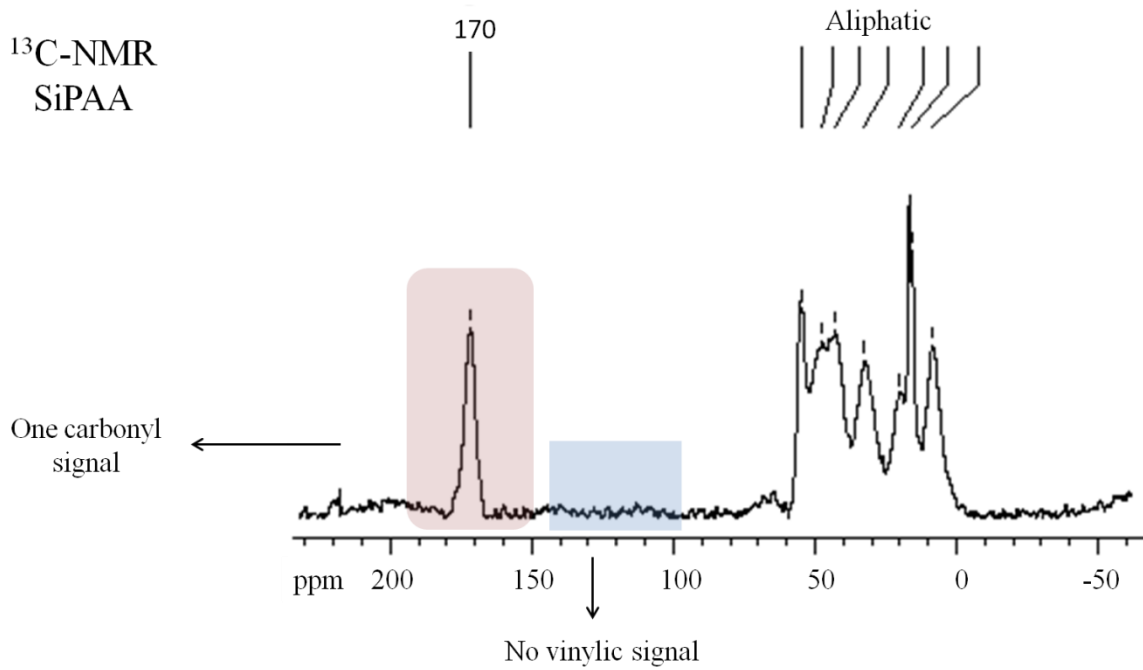


Fig. B.30 - ¹³C-NMR of SiPAA (MBA:APTES=1:1) polymer.

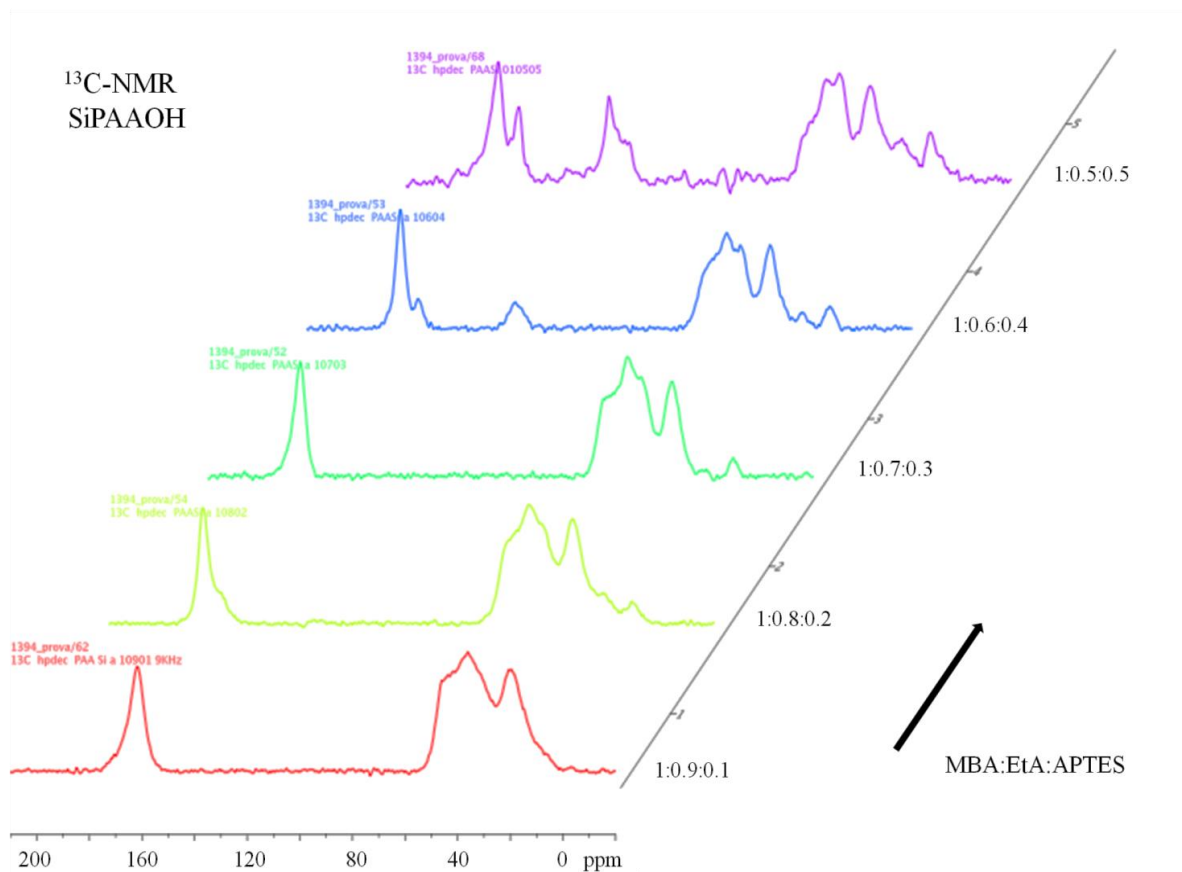


Fig. B.31 - ^{13}C -NMR spectra of SiPAAOH with different EtA/APTES ratios.

The aliphatic carbon from APTES propylene chain and the residual ethoxy groups due to a non-complete APTES hydrolysis are not distinguishable, being superimposed signals of methylene groups of PAAOH and ethanol side chain of the EtA. In Table B.8 are summarized the chemical shifts and related assignments.

Table B.8 - ^{13}C -NMR chemical shifts and related assignments.

ppm	Assignment	
174-170	$>\text{C}=\text{O}$	PAAAs, MBA
168-164		
132	$-\text{CH}=\text{CH}_2$	MBA
128		
60	$-\text{CH}_2-\text{CH}_2-$	PAAAs, APTES, EtA
55		
45	$-\text{CH}_2-\text{NH}$	MBA, PAAAs, EtA, APTES
35		
18	$-\text{CH}_3$	APTES

^{29}Si CP/MAS NMR spectra were performed to evaluate the degree of condensation (DOC) of the siloxane xerogel, obtained by SiPAA and SiPAAOH. The progressive replacement of the Si-OH groups (produced by the hydrolysis of Si-OR groups, with R = ethyl) with Si-O-Si, involves appreciable variations of the chemical shift of silicon.

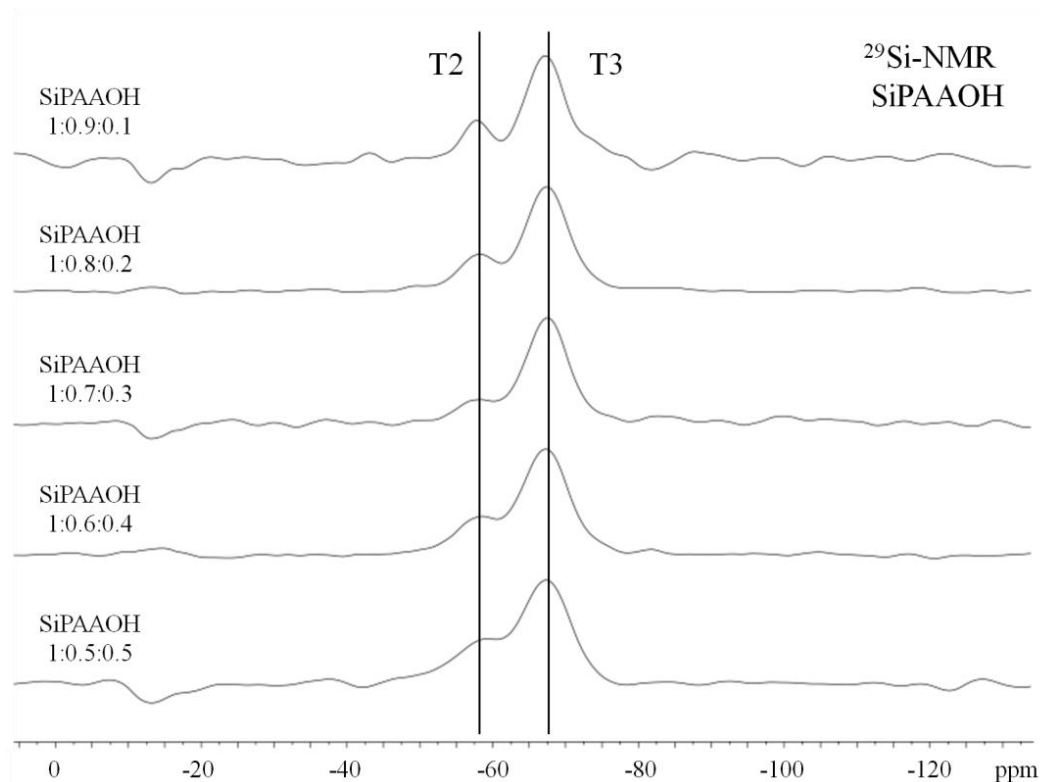


Fig. B.32 - ^{29}Si -NMR spectra: comparison between SiPAAOH polymers synthesized at different EA/APTES ratios.

Table B.9 - ^{29}Si NMR chemical shifts and related assignments (spectra in Fig. B.32).

Sample	ppm	Label	Area	DOC
SiPAA 1:0.5:0.5	-59	T2	103338	78
	-67	T3	202858	
SiPAA 1:0.6:0.4	-59	T2	84176	91
	-67	T3	234029	
SiPAA 1.0.7:0.3	-58	T2	38425	94
	-68	T3	176985	
SiPAA 1:0.8:0.3	-58	T2	166537	92
	-67	T3	496451	
SiPAA 1:0.9:0.1	-58	T2	38064	92
	-67	T3	128212	

In Fig. B.32 are reported ^{29}Si spectra acquired on different SiPAAOH, indicating the position of bi- and tricondensate species with T2 and T3, respectively. It should be noted that using APTES, a trifunctional silane, the T3 species represents the maximum degree of condensation. Two intense signals are visible, associated to T3 [$\text{RNSi}(\text{OSi})_3$] at 67 ppm and T2 [$\text{RNSi}(\text{OSi})_2\text{OR}$] at 58-59 ppm units [B70, B85].

The deconvolution of the T2 and T3 peaks allows calculating the degree of condensation DOC of the siloxane matrix. All samples show a high degree of condensation (Table B. 9).

B. 3.1.2.2 - Vibrational spectroscopies

The polymers functionalized with crosslinking siloxane, as was done for polymers with hydroxyl side chains, were investigated by FTIR and Raman spectroscopies. The bands related to the main functional groups observed in Fig. B.33 showing SiPAA and SiPAAOH (obtain in ethanol) are described below. Spectra were acquired on xerogel dried by evaporation at room temperature.

In the spectra show in Fig. B.34 at $\approx 3500\text{ cm}^{-1}$ is clearly a shoulder attributable to the OH stretching vibration, introduced by Ethanolamine (only in SiPAAOH) and/or APTES silanol groups not yet condensed. To the stretching vibration of the NH group (at 3298 cm^{-1}) contribute both MBA that the two amines (EtA and APTES) who have not completely reacted. The peak at 3060 cm^{-1} , due to the CH stretching vibration of the vinyl group from MBA, confirms that the reaction is not complete. This peak is clearly visible in the spectrum of SiPAAOH while in the spectrum of SiPAA is visible as a shoulder on the side of the strong peak due to the NH. In the $2950 \div 2800\text{ cm}^{-1}$ range are the stretching vibrations of the aliphatic chains from APTES and EtA, following the addition reaction. In the SiPAAOH spectrum at 1655 cm^{-1} (C = O) and 1625 cm^{-1} (C = C) there are the two characteristic peaks of MBA, while in the spectrum of PAASib2, there is a single peak at 1637 cm^{-1} , suggesting the reduction of the C = C double bond due to advanced polymerization. The features bands of silicates are recognizable in both spectra and are between $860\text{-}1175\text{ cm}^{-1}$ (with usually a strong peak centered at about 1080 cm^{-1}) around $750\text{-}800\text{ cm}^{-1}$ and between $470\text{-}570\text{ cm}^{-1}$. In the spectra is indistinguishable a strong peak at 1070 cm^{-1} which is attributed to Si-O-Si lattice inorganic formed following the condensation reaction of APTES. The peak at 987 cm^{-1} is likely due to the Si-OH stretching vibration APTES not yet totally synthetic and the broad peak at 685 cm^{-1} is associated with the Si-O stretching and bending of OCC APTES aliphatic chain.

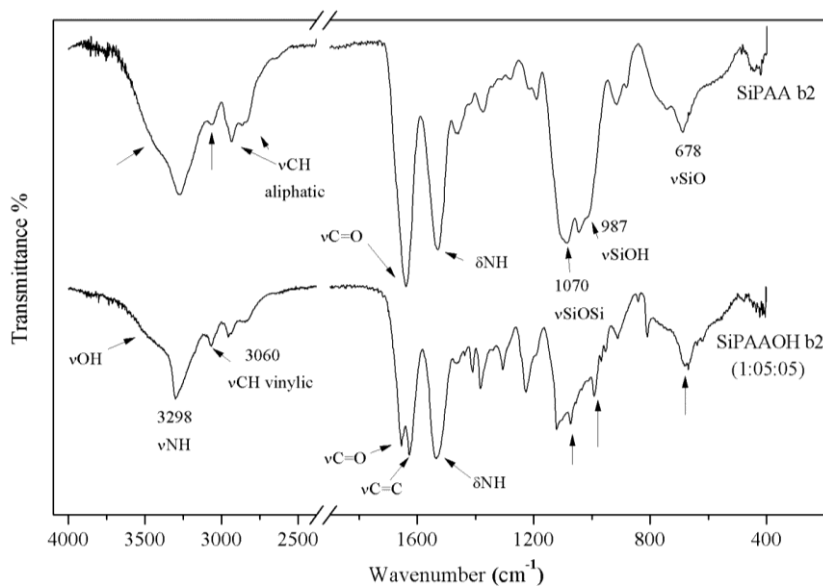


Fig. B.33 - FTIR spectra of SiPAA b2 and SiPAAOH b2, 1:0.5:0.5.

Fig. B.34 and B.35 show the Raman spectra of SiPAA b2 and SiPAAOH b2 (different Si/EtA molar ratios) respectively. In the spectrum of the SiPAA it can be seen that the peak relative to the C = C stretching vibration and also the vinyl CH stretching peak are very small, although not completely disappeared. This suggests that the product obtained is probably constituted by many oligomers ended with MBA (the results of ESI-MS had highlighted this behavior in polymers with hydroxyl functionality). The peaks that originated from the inorganic chain of the APTES are visible at 991 cm^{-1} and 1066 cm^{-1} . The CH propyl chain causes the very strong peak in the region of the CH stretching aliphatic. In the spectra of the SiPAAOH at different EtA/APTES ratio (Fig. B. 35), decreasing the concentration of APTES, we observe the gradual disappearance of the strong band at 1631 cm^{-1} and the bands due to the stretching vibrations of the vinyl CH of the MBA. The band at 1662 cm^{-1} , attributed to the stretching vibration of the carbonyl of the amide, is shifted to lower wavenumbers due to the reduction/disappearance of the vinyl group during the addition reaction.

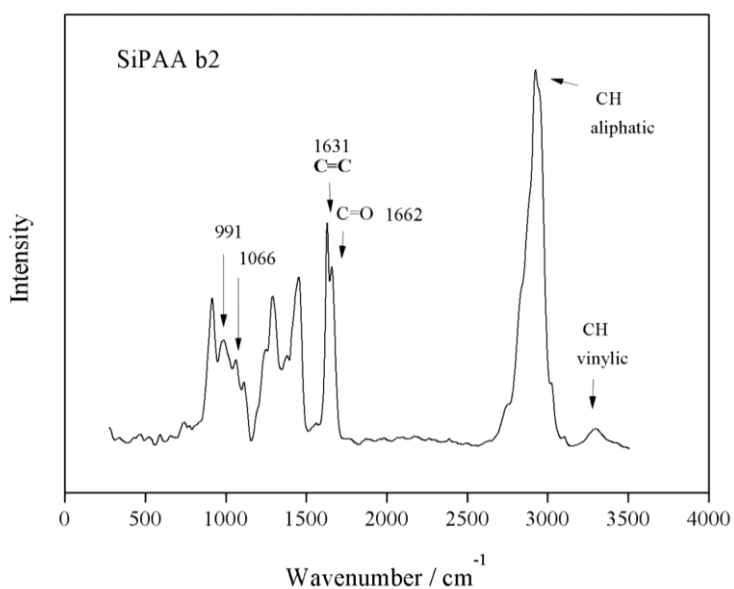


Fig. B.34 - Raman spectrum of SiPAA in ethanol (MBA:APTES = 1:1).

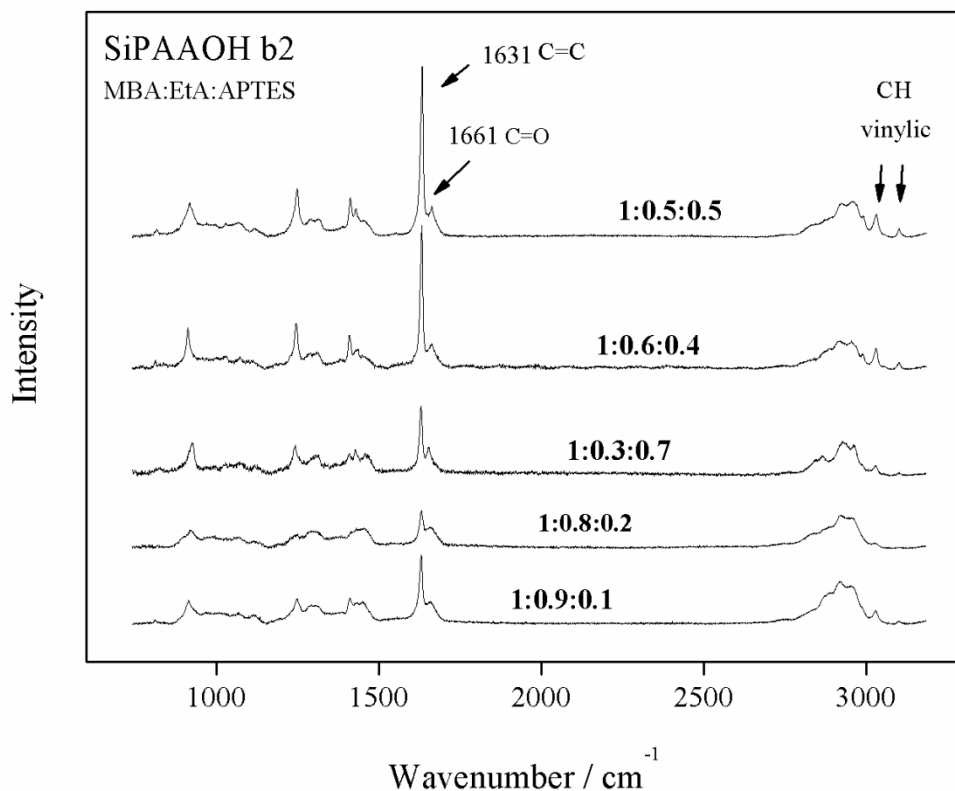


Fig. B.35 - Raman spectra of pure reagents and polymers SiPAAOH.

By observing the spectra presented in Figs B.33 to B.35 it can be hypothesized that in the functionalized polymers with silicon there is a lower degree of polymerization than those synthesized with ethanolamine alone. However, by IR and Raman investigations is not possible to establish whether there is a clear trend related to the silicon content. We can only assume that with the progress of the condensation of the silanol groups, the inorganic lattice makes the structure more rigid, slowing the kinetics of polymerization. This hypothesis is confirmed from the results obtain from the NMR study.

B. 3.2 - Characterization of treated wood

Treatments with polyamidoamines functionalized with OH and Si groups have been performed on *Pinus sylvestris* L. wooden samples, as described in the experimental part.

The hydroxyl group, introduced on the skeleton of the PAA as a side chain by ethanolamine, makes these polymers soluble in water and easily conveyable within the wood where it can form hydrogen bonds with the OH group of the cellulose. The siloxane chain introduced by APTES may polymerize inside the material and by hydrolysis and condensation makes it possible to create an inorganic-organic hybrid network that can improve the natural resistance of the wood.

The improvement of the resistance to biodeterioration given by the silica xerogel is well reported in literature and seems to be due both to changes of the wooden substrate that becomes no more suitable for biological development, to the reduction of the moisture absorption, which limit the biological attacks and also the survival of biodeteriogen [B1, B35, B40, B86]. The improvement of

durability should be due to the presence of secondary and tertiary amine groups that have biocidal properties [B6-7, B35, B40, B86].

B. 3.2.1 – ESEM

The efficacy of the treatment methods, by dip coating (type 1) and impregnation under vacuum (type 2a), has been assessed also by a measure of the penetration depth of the sols.

The penetration depth of SiPAAH and SiPAA, obtained in methanol and 2,2-dimethyl-4-hydroxymethyl-1,3-dioxolane (Augeo SL191), was verified by environmental scanning electron microscope (ESEM) with X-ray energy dispersive system (EDS).

Treated and untreated sapwood samples of *Pinus sylvestris*, 3 x 1 x 0.5 cm³, cut in cross section, were observed to see the distribution of silicon along the profile section and deduce the depth reached by the treatment.

In Fig. B.36 are reported the micrograph, the relative microanalysis along the cross section of a sample treated by dip coating with SiPAAOH in Augeo SL 191. Si is detected up to 1000 μm of depth.

Fig. B. 37 and B. 38 show the values of Si% with respect to O₂, starting from the surface at a step of 200 μm up to the opposite surface, of the SiPAA and SiPAAOH polymers in methanol and in Augeo SL 191 by vacuum impregnation, respectively. The results for the untreated samples are shown for comparison.

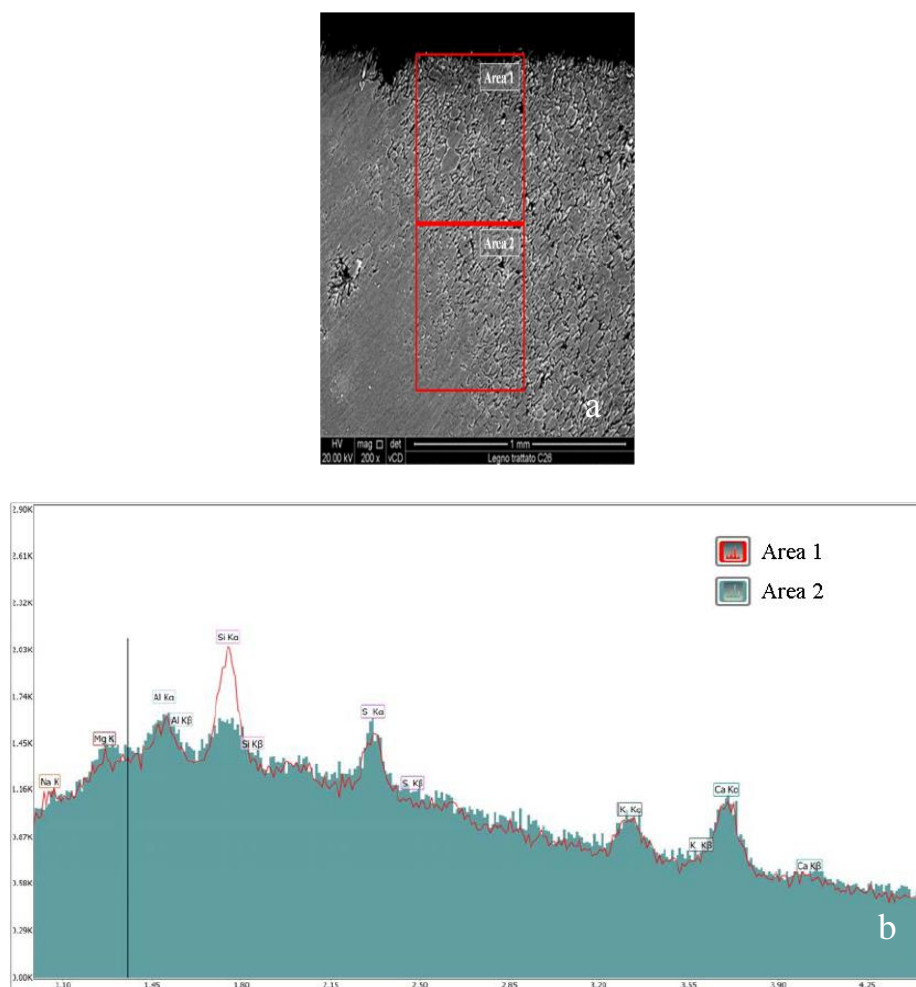


Fig. B.36 - (a) ESEM image along the cross section of a wood sample treated with SiPAAOH in Augeo by dip coating; (b) EDS microanalysis in the two areas indicated.

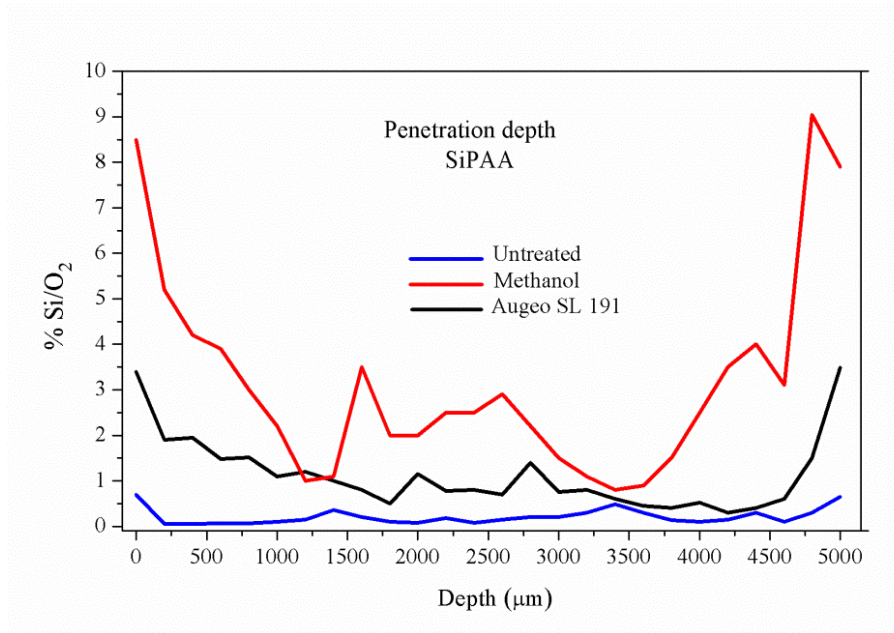


Fig. B.37 - EDS microanalysis results for %Si, with respect to O₂, along the whole thickness of the SiPAA treated sample compared to the untreated sample.

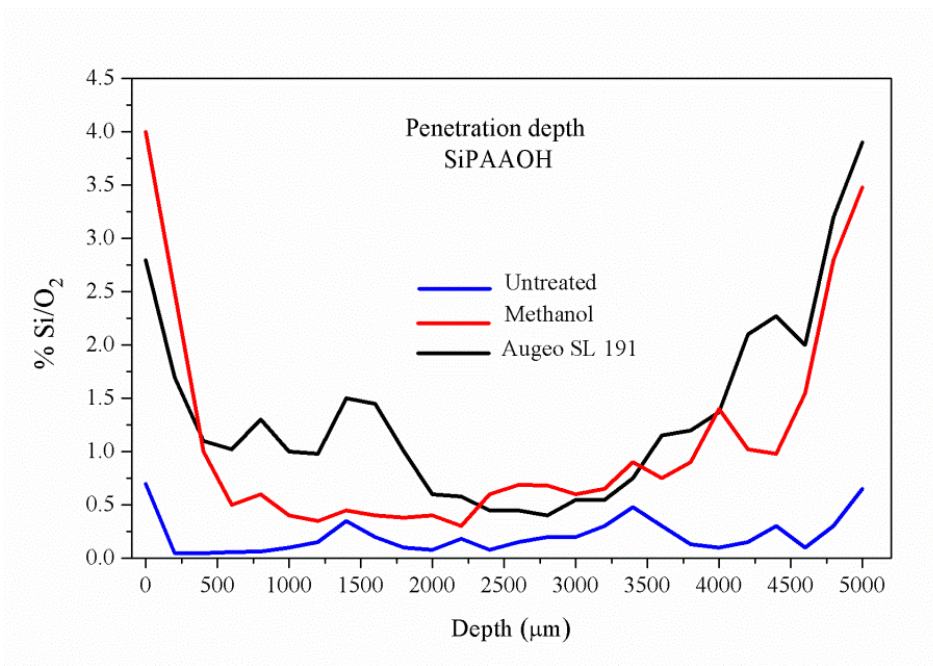


Fig. B.38 - EDS microanalysis results for %Si, with respect to O₂, along the whole thickness of the SiPAAOH treated sample compared to the untreated sample.

The tests show that all solvents are good carriers of the PAA polymers in the wood. The impregnation by total immersion under vacuum (type 2a) is very efficient and the polymer has penetrated throughout the section. The treatment by dip coating (type 1) proved to be an effective method to treat the samples: the polymer has penetrated to a depth of $\approx 2.5 \mu\text{m}$.

B. 3.2.2 - ^{13}C and ^{29}Si CP/MAS solid state NMR

^{13}C and ^{29}Si CP/MAS solid state NMR investigations were performed on SiPAA treated wood.

^{13}C CP/MAS NMR spectrum is shown in Fig. B.39. The identification of peaks due to the coating is difficult because the main wood components, i.e. cellulose, hemicelluloses and lignin partially overlap with the organic part of APTES [B70, B84-B86]. Main peaks are identified and listed in Table B.10

Table B.10 - ^{13}C NMR chemical shifts and related assignments.

δ (ppm)	Molecule
15.1	Hemicellulose/APTES
27.8	APTES
32.3	Cellulose (C_6) crystalline domains
38.4	Cellulose (C_6) crystalline domains
42.3	APTES
47.2	Lignin (OCH_3)
54.9	Cellulose (C_4) crystalline domains
60.8	Cellulose (C_4) crystalline domains
76.5	Lignin
103.4	Lignin
131.3	Lignin
146.9	Lignin (aromatic)

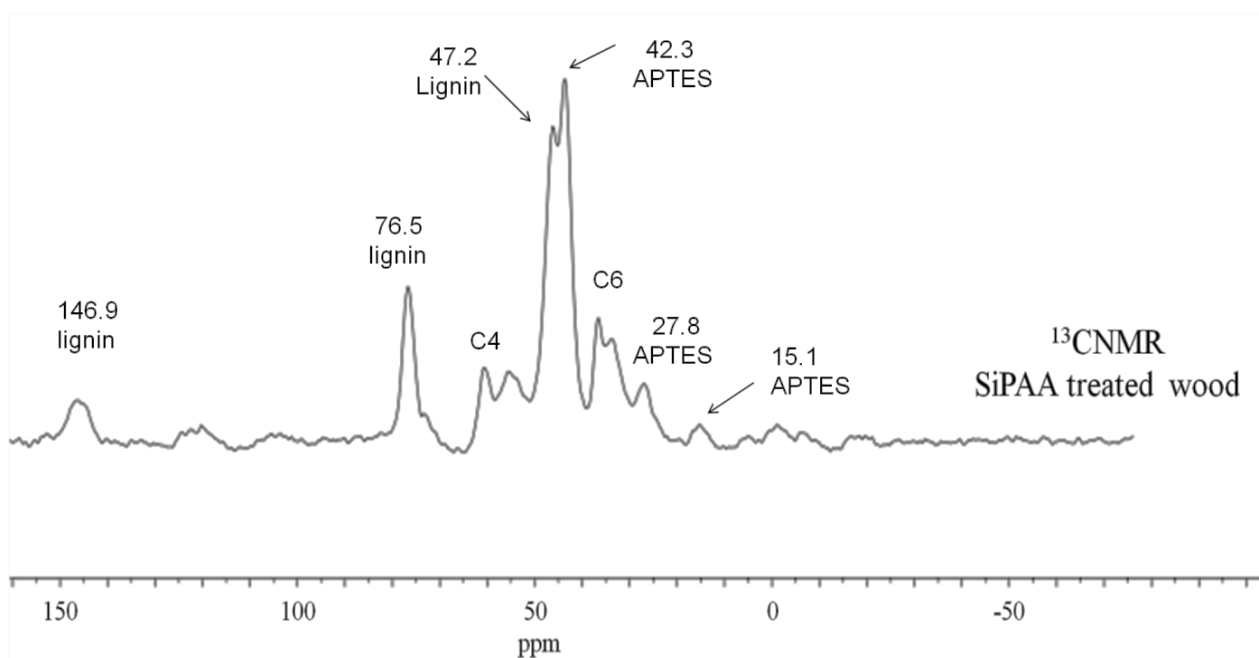


Fig. B.39 - ^{13}C CP/MAS NMR spectrum of SiPAA-impregnated wood.

The ^{29}Si CP/MAS NMR spectrum of SiPAA treated wood is reported in Fig. B.40.

In the spectrum of coated wood are present the same signal of the bulk material (see Fig. B. 32, par. B. 3.1.2.1). The similarity among the spectra obtained in the SiPAA suggests that siloxane reticulation of the two materials is analogous. The intense signals are associated to condensed APTES T units: T3 [$\text{RNSi}(\text{OSi})_3$] at 67 ppm and T2 [$\text{RNSi}(\text{OSi})_2\text{OR}$] at 58-59 ppm. The main species are T3, which indicated a high condensation degree of the siloxane. The presence of T2 units is probably due to the linking with the substrate. In fact the hydroxyl groups of the wood could react with the silanols of the coating: the hydrolysis/condensation process occurs in situ, by using the water adsorbed onto cell walls of wood. The hydroxyl groups of cellulose, hemicellulose and lignin can act as binding site and facilitate the adhesion of gel [B70].

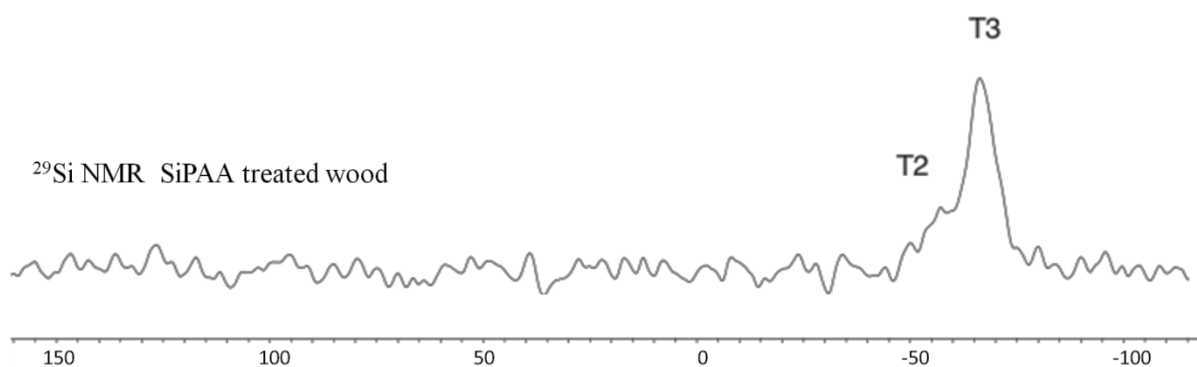


Fig. B.40 - ^{29}Si CP/MAS solid NMR spectrum of SiPAA treated wood.

B. 3.2.3 - FT- Raman

Fig. B.41 shows the FT-Raman spectrum of untreated *Pinus sylvestris* wood (a) and a detail in the region $1800\text{-}700\text{ cm}^{-1}$ (b). The main components of wood are cellulose, the most abundant component, followed by lignin and hemicellulose. In softwood hemicellulose consist principally of glucomannan and xylan and lignin consists of various hydroxyl- and methoxyl-substituted phenyl propane units.

The main bands in spectrum of scots wood are identified according to literature [B70, B87-B88]. The broad band at about 3330 cm^{-1} is assigned to $\nu(\text{OH})$ from the cellulose and hemicellulose and the weak peak at 3073 cm^{-1} is due to the $\nu(\text{CH}_2)$ aromatic (phenyl units) of the lignin. In the region $2930\text{-}2894\text{ cm}^{-1}$ are the stretching vibrations of the aliphatic CH: the shoulder at 2938 cm^{-1} is attributed to $\nu(\text{CH}_2)$ of the lignin and also of the glucomannan while the very strong peak at 2962 cm^{-1} and the weak peak at 2739 cm^{-1} are assigned to $\nu(\text{CH}_2)$ and $\nu(\text{CH})$ of the cellulose[B87]. The main bands of the lignin are due to aromatic ring stretch vibration at 1600 cm^{-1} and 1464 cm^{-1} , and to the $\nu(\text{C}=\text{O})$ at 1658 cm^{-1} [B88]. At $1378, 1337, 1272\text{ cm}^{-1}$ there are the $\delta(\text{OH})$ rings vibration and $\delta(\text{CH})$ of cellulose and hemicellulose [B70, B88]. The strong peaks at 1126 and 1096 cm^{-1} are associated to $\nu(\text{C}-\text{O}-\text{C})$ of cellulose and xylan and glucomannan (hemicellulose) and at 903 cm^{-1} there is the β -glycosidic linkage, besides $\delta(\text{CH})$ of cellulose [70].

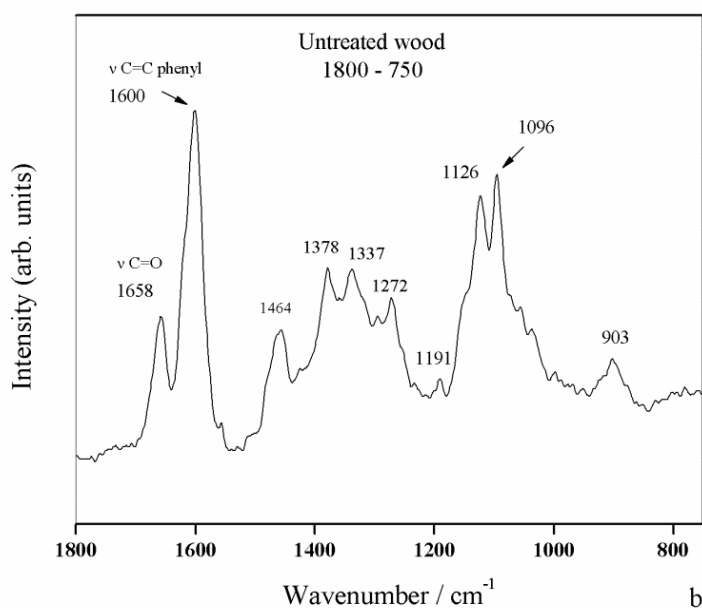
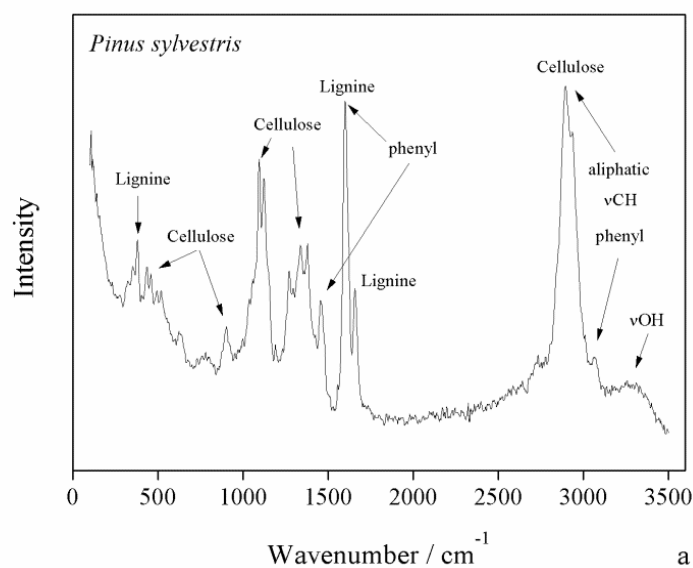


Fig. B.41 - a) FT-Raman of *Pinus Sylvestris* wood, untreated. b) Detail of the spectrum in the 1800-700 cm^{-1} range.

Fig. B.42 shows the FT-Raman spectrum of SiPAA treated wood, compared with untreated one. The interpretation is rather difficult, because the many bands of the wood (cellulose, hemicellulose and lignin) are superimposed to those of the coating. In the treated wood, in the spectral region of the amide bond, emerges a new peak at 1635 cm^{-1} , associated to the C=C stretching mode of SiPAA (see spectrum in fig. B. 34, par, B. 3.1.2.2). The presence of the silica gel in the impregnated wood samples is shown also in the region of CH stretching and bending modes (2950-2800 cm^{-1} and 1480-1300 cm^{-1}), where new peaks appear due the contribution of the methylene groups from the propyl chain of the APTES [B89-90]. Moreover for impregnated wood, shoulders appeared at about

1090 due to the Si-O-Si cm^{-1} stretching vibration and about 940 cm^{-1} , which can be assigned to external Si-OH groups [B91]. No significant differences were observed in the OH and NH region ($3500\text{-}3400 \text{ cm}^{-1}$).

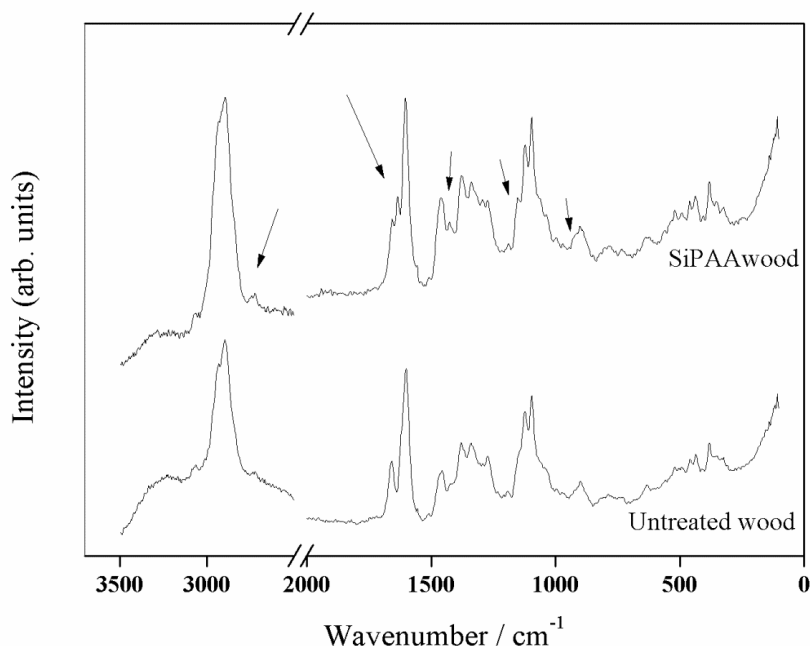


Fig. B.42 - FT- Raman of untreated and SiPAA treated wood.

B. 3.2.4 - Colour changes

Table B.11 shows the colour difference of the wood samples before and after PAAOH, SiPAAOH and SiPAA treatments, expressed as ΔE^* . All treatments cause a yellowing of the surface sample, as can be inferred from the increase in a^* values. SiPAA coating, with only siloxane functionality, gives relatively low ΔE^* value: at a visual examination, the colour difference is barely perceptible. The treatments containing hydroxyl functionality show higher ΔE^* values and actually the wood looks more yellowish

Table B.11 - Colorimetric changes for the different treatments of the *Pinus Sylvestris* wood.

Formulation		Untreated wood	Treated wood	ΔE^*
PAAOH	L*	87.3	83.8	8.7
	a*	2.8	6.5	
	b*	21.9	28.9	
SiPAA	L*	86.4	86.8	5.3
	a*	3.2	5.9	
	b*	21.5	26.0	
SiPAAOH	L*	86.4	89.2	6.1
	a*	3.2	4.5	
	b*	21.5	26.7	

B. 3.3 - Efficacy tests against biological attack

The efficacy of the synthesized preservative for the treatment of wood samples was evaluated against fungi and termites.

B. 3.3.1 - Brown rot and white rot fungi: *C. puteana*, *T.versicolor*, *P. placenta*

B. 3.3.1.1 - Accelerated test against *C. puteana* in mini-block samples

Sapwood samples of *Pinus sylvestris* L. and *Fagus Sylvatica* were employed to test the preservative treatments efficacy to biological attacks. These wood species are characterized by high impregnability and low durability. WPG values of the wood samples after treatment was dependent on the treatment procedure and type of solvent used to convey the protective solution. To make sure that the weight change is induced solely by the protective, the WPG is calculated as the difference between the initial and final dry masses. The efficacy of wood impregnation in mini-block samples for all treatments was evidenced by weight percent gain WPG_1 (%). The WPG_1 obtained in sample tablets used in xilophagous tests, treated by vacuum/nitrogen impregnation using methanol as solvent, is reported in table B.12. As regards the SiPAA impregnations, the values depend on the total content of silicon in the sol-gel solutions. WPG_1 indicates the increase of mass due to the presence of the xerogel into the wood after thermal drying. In the case of PAAOH and SiPAAOH treatments, one observes a lower value of WPG. This could be due to the lower concentration of silicon in the starting solution. [B84, B92].

Table B.12 - Max humidity before impregnation and weight percent gain (WPG_1) values after impregnation of pinewood samples treated with different sol-gel solutions, used in accelerated efficacy tests against *C. puteana*.

Formulation	$H_{max}(\%) \pm sd$	$WPG_1 (\%) \pm sd$
SiPAA b2	8.5±0.2	13.2±5.9
PAAOH b2	9.1±1.2	8.1±2.8
SiPAAOH a2	9.3±1.1	6.9±1.2
SiPAA e2	8.6±0.2	7.4±1.1
SiPAAOH e2	14.0±0.8	4.4±1.1
PAAOH e2	13.1±0.1	3.4±0.8
PAAOH a2	9.5±0.1	9.8±1.0

$H_{max}\%$: $[(m_H - m_t)/m_t] \times 100$; $WPG_1\%$: $[(M_T - M_0)/M_0] \times 100$; SD: standard deviation.

The preservative properties of the different PAAs against the brown rot fungus *Coniophora puteana* was previously evaluated by accelerated test (Accelerated Bravery efficacy test) on all kind of protective coatings formulation. Efficacy was evaluated by comparison of the percentage mass loss of the reference untreated samples (control) with that of the treated ones after exposure to the fungus for four/eight/twelve weeks.

The screening tests were carried out in parallel to the development of the PAA formulations and have been made with the aim to choose the most effective formulations.

Step 1: comparison between PAAs with hydroxyl and siloxanic functionality in ethanol (PAAOH b and SiPAAb)

In this first step, the influence of hydroxyl and siloxanic functionality was evaluated on biocide activity against *Coniophora puteana*. Was also checked the adhesion of the PAAs to the wood by leaching tests. The PAAs were applied to mini-block wood samples by vacuum/nitrogen impregnation (type 2) as described in the experimental section (B. 2.5.2). Evaluation of the efficacy of wood preservative was carried out with accelerated procedure [B75], 8 weeks of contact to the fungus. According to UNI EN 84 [B74], samples of treated wood, before the efficacy test against *C. puteana*, were subjected to leaching process. In parallel, virulence tests of the *C. puteana* on untreated specimens have been carried out: the average value of mass loss was 33.3% with a final moisture average 70.9%. In agreement with the Normal, mass loss and moisture values of control samples allow to consider valid the test. The results are shown in table B. 13.

The vitality of the fungal strain is confirmed by the average mass loss of 33.3% on six replicates used to control the fungal virulence. Samples treated by PAAOH gave a mass loss 10% while the control mass loss was 37.8%. SiPAA treated samples mass loss was -3.6 % despite the 45.4% of the controls (Table B.13). A negative value of mass loss after fungal exposure obtained in SiPAA treatment could be due to water incorporated in the siloxane matrix, accumulated by the fungus on the surface of the wood sample and introduced inside: the Si-O-Si bonds react with H₂O, giving rise to two Si-OH groups in the network causing a mass increase in the samples. Actually, after drying the samples at increasing temperatures (103,130, 140 °C) for 18 hours a decrease of the final mass is observed. PAAOH exhibits a quite high mass loss. It has to be stressed that the formulation with OH functionality shows a leaching percentage between 64% and 97%, having a poor ability to fasten to the wood.

Table B.13 - Weight Percent Gain, leached formulation, mass loss due to exposure to C. puteana and moisture content of the treated sample.

PAA	WPG ₂ (%)	LF (%)	ML (%)	MC (%)
SiPAAb	8.3 (1.2)	19.4(11.2)	-3.6 (0.4)	71.6 (7.5)
Control			45.4 (1.4)	108.6* (22.2)
PAAb	0.4 (0.2)	93.6 (64.7)	10.3 (15.7)	74.5 (7.5)
Controll			37.8 (5.5)	85.9 (25.9)
Virulence			33.3 (1.9)	70.9 (3)

WPG₁=Weight Percent Gain; WPG₂= Weight Percent Gain after leaching; LF%: leached formulation percentage; ML%: mass loss percentage; MC%: moisture content percentage; in parentheses are the standard deviations.

Step 2: comparison between PAAs with alcoholic and siloxane functionality in water and Augeo 191 SL

The evaluation of the efficacy of wood preservatives was performed on four treated samples and four untreated samples for each treatment, with accelerated procedure [B30, B34-B35], but with a longer contact time with the fungus, that is, 12 weeks. The fungal virulence was verified as reported in the experimental section. In this case no leaching test was performed. The mini-block samples

were coated by impregnation type 2. The SiPAAOH treatment in water gives a mean WPG₂ of 7.0%. The preservative formulation was effective against *C. puteana*. The formulation carried out in solvent Augeo SL 191, was however not effective. The loss mass was ≈ 8% and moisture content ≈ 87%. The results obtained from the two formulations are shown in Table B.14.

Table B.14 - Weight Percent Gain, mass loss due to exposure to C. puteana and moisture content of the treated sample.

PAA	WPG ₁	ML (%)	MC (%)
SiPAA a	7.0 (1.5)	0.3 (0.6)	73.8 (24.0)
SiPAA e	7.1(0.9)	7.9 (2.3)	86.5 (7.0)

Step 3: Comparison between PAAs with hydroxyl and siloxane functionality, solvent Augeo 191 SL, impregnation by fast dipping.

The efficacy test was made on four (eight for Augeo solvent) treated samples and on four control samples, leaving them for eight weeks in contact with the fungus, inoculated on the culture medium (see details in par. B. 2.5). The specimens were treated by fast dipping, type 1 (par. B2.5.1). Due to the high humidity measured at the end of test, this screening check cannot be considered valid. Indeed, one cannot exclude that the effectiveness of treatments is mainly due to the inactivity of the fungus, because the too high humidity, not suitable for its growth. Augeo 191SL probably is incorporated in the woody structure even after the heat treatment at 103 °C, displaying a high hydrophilicity. The results are reported in Table B.15.

Table B.15 - Weight Percent Gain, mass loss due to exposure to C. puteana and moisture content of samples treated with PAAOH and SiPAA by fast dipping, in Augeo191 SL.

PAA	WPG ₁	ML (%)	MC (%)
SiPAA e	4.6 (1.1)	0.5 (0.2)	100.1* (14.8)
PAAOH e	3.7 (0,3)	-1.8 (0.5)	112.1* (27.0)

Step 4: PAAOH with hydroxyl functionality in water, impregnated by type 3 method. Efficacy test against C. puteana, P. placenta, T. versicolor.

According to European Standard EN 113 (1996)/A1:2004 [B71], *Coniophora puteana* and *Poria placenta*, as brown rot fungi, and *Trametes versicolor*, as white rot fungus, were selected. 41 specimens were treated with PAAOH in water by vacuum/nitrogen impregnation (type 3). As correction factor, the loss mass obtained on six samples (check) treated by the same formulation and kept in the same culture medium, but not inoculated by fungi, was used. In this test no accelerated aging was carried out. Eight treated and four untreated samples for each fungus were used. The virulence of fungi was determined on six untreated samples for each species. Table B.16 reports the results of the loss mass of all samples and the mass corrected with respect to check samples.

Table B.16 - Mass loss *ML*, mass loss corrected due to exposure to *C. puteana* *ML** and moisture content *MC* of treated samples

<i>PAAOH in water</i>	<i>Vacuum/nitrogen (type 3)</i>	<i>WPG_I(%) = 1.18 ± 0.04</i>	
<i>Fungus</i>	<i>ML (%)</i>	<i>ML* (%)</i>	<i>MC (%)</i>
<i>C. puteana</i>	-3.6	-0.2	
Control	20.1		
<i>P. placenta</i>	-3.5	-0.3	
Control	-1.7		
<i>T. versicolor</i>	-4.1	-0.7	
Control	8.2		
Check	-3.4		
<i>Virulence</i>	<i>ML (%)</i>	<i>ML (%)*</i>	<i>MC (%)</i>
<i>C. puteana</i> (N=6)	31.4		87.7
<i>P. placenta</i> (N=6)	-1.4		84.7
<i>T. versicolor</i> (N=6)	5.8		85.1

ML*%: mass loss percentage corrected with respect to check samples.

As regards the fungi *P. placenta* and *T. versicolor*, due to the low virulence (-1.4 and 5.8 respectively), the results of the screening test cannot be considered valid. Only *C. puteana* showed a virulence above the limit (31%). The PAAOH formulation was effective versus *C. puteana*, with mass loss -3.6% and lost correct mass of -0.2%.

Step 5: SiPAA and SiPAAOH in methanol and Augeo 191SL, impregnated by type 3 method. Efficacy test against C. puteana and P. placenta.

The accelerated efficacy tests against brown rot fungus were carried out on sapwood mini-block *Pinus sylvestris* samples. *Coniophora puteana* and *Poria placenta* were selected as brown rot fungi. The formulations tested were the SiPAA and SiPAAOH, synthesized in methanol or in Augeo 191SL. Nine specimens for each formulation were treated: five of them were kept in contact with *C. puteana* and four with *P. placenta*. Polymer in water by vacuum/nitrogen impregnation (type 3) and no treatment of leaching. The virulence of fungi was determined on five untreated sample for each species. In table B.17 and B.18 are reported the results of the Weight Percent Gain (*WPG_I*) and loss mass of all samples, respectively.

Table B.17 - WPG₁ and standard deviation of PAAs obtained from nine samples.

PAA	WPG ₁
SiPAA d2	10.7
SiPAAOH d2	6.7
SiPAA e2	30.8
SiPAAOH e2	33.4

As regards the fungi *P. placenta*, due to the low virulence shown in virulence tests (8.6), the results cannot be considered valid. Only *C. puteana* gave a virulence higher the limit (31%). Both formulations synthesized in methanol, SiPAA and SiPAAOH, were effective versus *C. puteana* having a mass loss 1.4 and 0.8, respectively.

Like in previous screening tests, all formulations synthesized in Augeo 191SL have proved ineffective against tested fungi.

Table B.18 - Efficacy test on *pinus sylvestris* sample treated with SiPAA and SiPAAOH in methanol and Augeo against *C. puteana* and *P. placenta*.

PAA	Species	ML (%)
SiPAA d2	<i>C. puteana</i>	1.4
Control		43.4
SiPAA d2	<i>P.placenta</i>	-0.9
Control		9.6
SiPAA e2	<i>C. puteana</i>	10.7
Control		34.7
SiPAA e2	<i>P.placenta</i>	7.2
Control		30.3
SiPAAOH d2	<i>C. puteana</i>	0.8
Control		40.1
SiPAAOH d2	<i>P.placenta</i>	-0.2
Control		-0.8
SiPAAOH e2	<i>C. puteana</i>	17.1
Control		16.3
SiPAAOH e2	<i>P.placenta</i>	28.8
Control		28.1
Virulence	<i>C. puteana</i>	39.3
Virulence	<i>P. placenta</i>	8.6

B. 3.3.1.2 - Standard test according to UNI EN 113:1996/a1:2004

Samples of *Pinus sylvestris* sapwood, with SiPAA and SiPAAOH in water and samples of *Fagus sylvatica*, with PAAOH in water, both by vacuum/nitrogen impregnation (type 3), were considered for the standard efficacy tests. The size of wood-blocks was 1.5x2.5x5 cm³. Five repetitions for each fungus species were used. The test was made as described in the experimental part (B. 2.8.1.2). The wood species are both considered not durable species and therefore do not affect the effectiveness of the treatment applied to the wood.



Fig. B.43 – SiPAA - Left, fungus *C. puteana*, sample 911 (treated) and 40 (control). Center: *T. versicolor*, samples 867 (treated) and 54 (control). Right: *P. placenta*, samples 940 (treated) and 53 (control).

According to UNI EN 84 [B74], samples of treated wood were subjected to leaching process before the effectiveness test against *C. puteana*. WPG₁, WPG₂ and leached formulation percentage were calculated. The resistance against *C. puteana* and *T. versicolor* was evaluated by the wood mass, calculated as difference between the dry mass before the impregnation process and after the fungal exposure, corrected by the WPG₁ due to the treatment and by the correction coefficient (Table B.19).

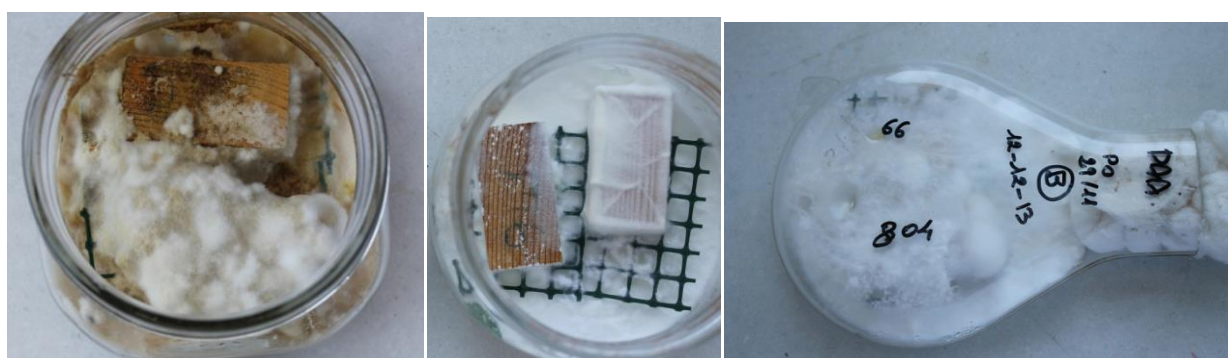


Fig. B.44 – SiPAAOH - Left: *C. puteana*, samples 954 (treated) and 63 (control). Center: *T. versicolor*, samples 941 (treated) and 70 (control). Right: *P. placenta*, samples 804 (treated) and 66 (control).

The process of leaching causes a mass loss of 37% for the SiPAA formulation, 59% for SiPAAOH and 84% for PAAOH. This emphasizes the importance of siloxane for anchoring to the wood. Formulation SiPAA was effective against *C. puteana* but not against *T. versicolor* (Fig. B.43). SiPAAOH is found to be ineffective for both fungal species (Fig. B.44). Also PAAOH is ineffective for both fungi (Fig. B.45).

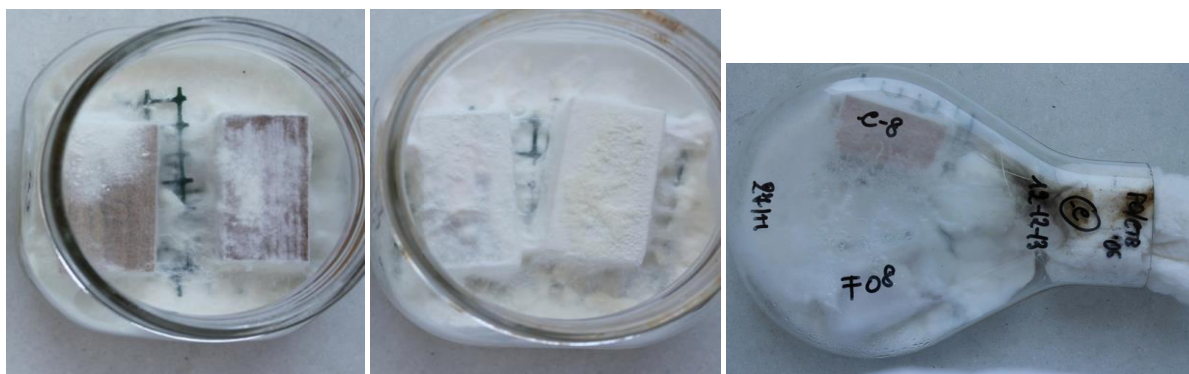


Fig. B.45 - PAAOH - Left: *C. puteana*, samples F17 (treated) and C15 (control). Center: *T. versicolor*, samples F11 (treated) and C11 (control). Right: *P. placenta*, samples F08 (treated) and C8 (control).

The results obtained in the efficacy tests against *C. puteana* and *T. versicolor* for each set of formulations are summarized in Table B.19.

Table B.19 - Weight Percent Gain of the treated sample (WPG_1) and of leached mass (WPG_2) with respect to untreated mass and the leached formulation (LF).

PAA	Wood	WPG_1 (%)	WPG_2 (%)	LF (%)	ML* (%)	MC (%)
<i>Coniphora puteana</i>						
SiPAAa/b	<i>Pinus sylvestris</i>	7.1 (0.4)	4.5 (0.2)	37.0 (2.2)	4.1 (8.02)	49.0 (5.1)
Control					36.2 (8.8)	69.3 (14.3)
SiPAAOH a/b	<i>Pinus sylvestris</i>	6.4 (0.2)	2.7 (0.3)	58.9 (4.1)	16.21 (14.8)	56.2 (2.8)
Control					40.8 (7.5)	85.9 (25.9)
PAAOH a	<i>Fagus sylvatica</i>	2.7 (0.1)	0.4 (0.2)	84.4 (-)	13.7 (18.0)	49.3 (1.2)
Control					22.9 (5.1)	47.1 (5.6)
<i>Trametes versicolor</i>						
SiPAAa/b	<i>Pinus sylvestris</i>	7.2 (0.1)	4.5 (0.2)	37.0 (2.2)	13.0 (2.3)	73.3 (2.1)
Control					21.6 (3.5)	76.8 (9.1)
SiPAAOH a/b	<i>Pinus sylvestris</i>	6.1 (0.5)	2.4 (0.2)	58.9 (4.1)	15.6 (1.1)	92.9 (24.7)
Control					18.0 (3.8)	64.0 (11.9)
PAAOH a	<i>Fagus sylvatica</i>	2.7 (0.1)	0.4 (0.2)	84.4 (-)	4.4 (-)	57.0 (-)
Control					24.3 (-)	60.5 (-)

WPG_1 =Weight Percent Gain; WPG_2 = Weight Percent Gain after leaching; LF%: leached formulation percentage; ML*%: corrected mass loss percentage; MC%: moisture content percentage; in parentheses are the standard deviations

All used fungi have high virulence (Table B.20, Fig. B.46). The efficacy test against fungi can be considered valid.

Table B.20 - Samples used to evaluate the fungi virulence.

Species	N° samples	LM%	MC%
<i>Coniophora puteana</i>	8	37.6	81.1
<i>Poria placenta</i>	6	40.5	87.4
<i>Trametes versicolor</i>	6	21.6	67.5



Fig. B.46 - Reference samples for the virulence of *C. puteana*.

B. 3.3.2 - Efficacy test of treatments against termites: laboratory no-choice test

B 3.3.2.1 - Subterranean termites - *Reticulitermes lucifugus*

Pinus sylvestris L. sapwood was treated with synthesized preservative treatments and termites resistance was assessed following the procedure described in experimental part (par.B.2.5). Both treated and untreated specimens were exposed to *Reticulitermes lucifugus* feeding according to UNI EN 113 [B71]. The tests lasted eight weeks. For each colony, three replicates were used. During the test, once a week, the state of the equipment and the humidity of the sand, were checked. After the first week, in one of the replicas of the control group an "overrunning" outside of the experimental apparatus was observed. In the following checks was found an intense activity of termites of the "control" and of some other samples. In some cases it was observed that the activity was so high as to be visible on the bottom of the experimental apparatus. At the end of the eight-week test, the containers were emptied, survived individuals were counted and the wood samples were gently cleaned with a brush (Fig. B.47). The results are reported in Table B.21. The control group "E" (methanol) was the only one in which there were survived termites: 57% on average live individuals

for replica. Visual examination of the attack degree is based on the observation of the surface and depth of the tunnels made by termites: it varies from 0 to 4, where 4 is the highest degree of intensity of attack. The obtained results indicate highly significant differences between the "control" and the other treatments (ANOVA, $F = 27.27$, $p < 0.00001$), as evident in Fig. B.48. The Fisher's Least Significant Difference (LSD) test, for the separation of the averages, has shown significant differences only between the group E ("control") and other treatments, while the separation between different treatments are not statistically significant. The results for the actual eating of wood by termites are reported in Fig. B.48. The data (percentage wood consumption) were subjected to the Kruskal Wallis non-parametric (ANOVA) statistical analysis and the results show highly significant divergences ($H = 15.9$, $P = 0.001$) between treatments and "control", indicating a wood percentage consumption in the control clearly higher than the other groups, while between treatments A, S and P there are not significant differences. It was also considered the "survival" of the colony, i.e. the number of days required for the death of all individuals of the colony. Statistical analysis of the data have emphasized significant differences between treatments (ANOVA, $F = 23.03$, $p < 0.00001$) and the results are shown in Fig. B.48. The LSD test for the separation of the averages shows significant differentiation only between the group E (witness) and other treatments, while variations of the treatments A, S and P between them are not statistically significant.

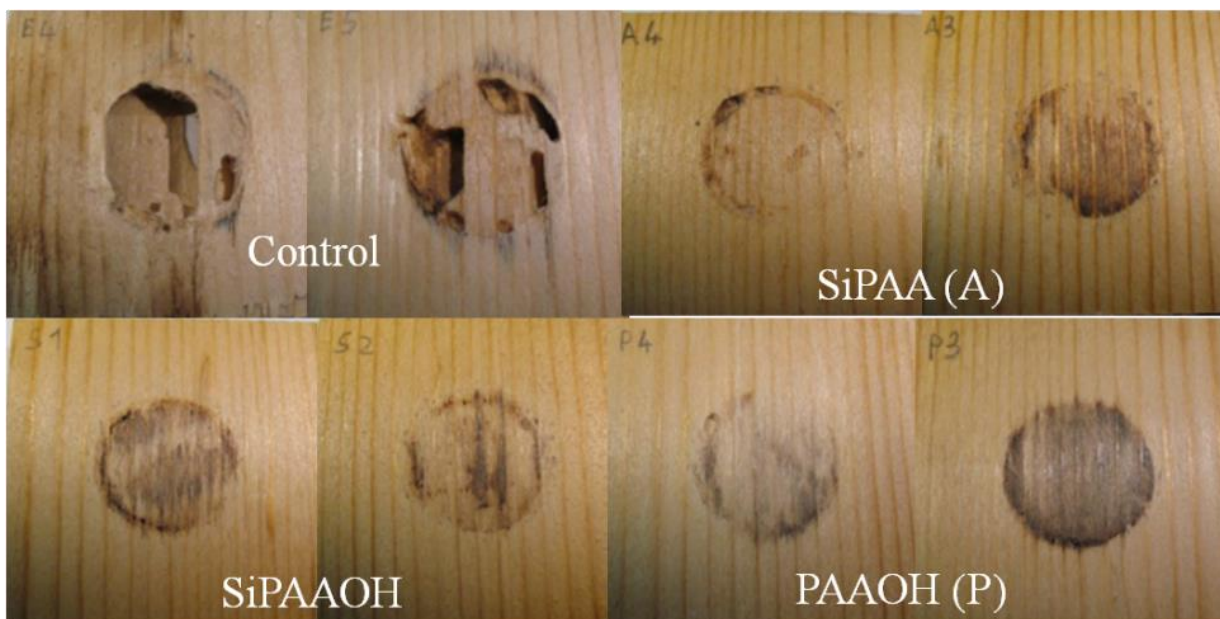


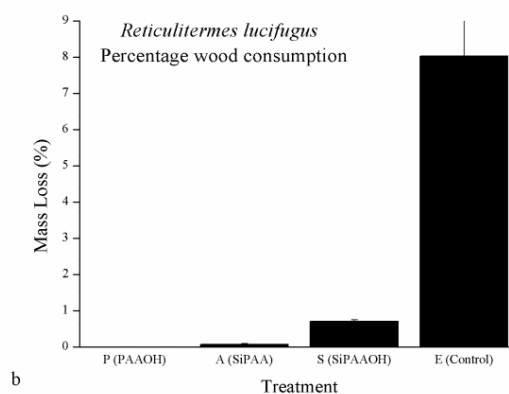
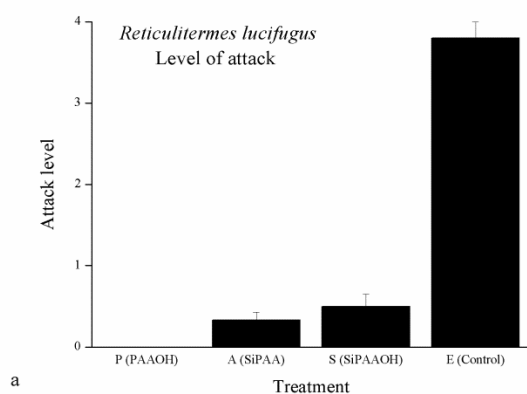
Fig. B.47 - *Reticulitermes lucifugus*. Visual examination of the attack degree.

In conclusion, efficacy tests against *Reticulitermes lucifugus* made according to UNI EN 113 [B71] show that the treated wood is more resistant than untreated sample (control). The treatments not differ significantly between them. The attack degree in all formulations is about 1 and in "control" 4; the colony survival is, on average, 26 days, while in the colony control the individuals survived until the end of test.

Table B.21- Results of the no-choice test for *Reticulitermes lucifugus*.

Av = average; sd = standard deviation.

Treatment	Sample code	Starting	Mortality (%)	Attack level (0-4)	Mass Loss (%)	Survival days
PAAOHd2	P1	250	100	0	0.00	24
	P2	250	100	0	0.00	24
	P3	250	100	0	0.00	24
	P4	250	100	0	0.00	31
	P5	250	100	0	0.00	31
	P6	250	100	0	0.00	24
	Av (sd)			100	0	0.00
SiPAA d2	A1	250	100	0	0.00	24
	A2	250	100	0	0.00	24
	A3	250	100	0	0.00	24
	A4	250	100	1	0.20	24
	A5	250	100	0	0.00	24
	A6	250	100	1	0.23	38
	Av (sd)			100	0.3	0.06
SiPAAOHd2	S1	250	100	0	0.00	24
	S2	250	100	0	0.00	24
	S3	250	100	0	0.01	24
	S4	250	100	1	0.10	31
	S5	250	100	1	0.19	31
	S6	250	100	1	0.22	31
	Av (sd)			100	0.5	0.07
MeOH (control)	E1	250	34	4	8.12	56
	E2	250	36	4	7.63	56
	E3	250	41	4	6.53	56
	E4	250	49	4	10.23	56
	E5	250	52	4	7.64	56
	E6	250	-	-	-	-
	Av			42.6	4	8.03



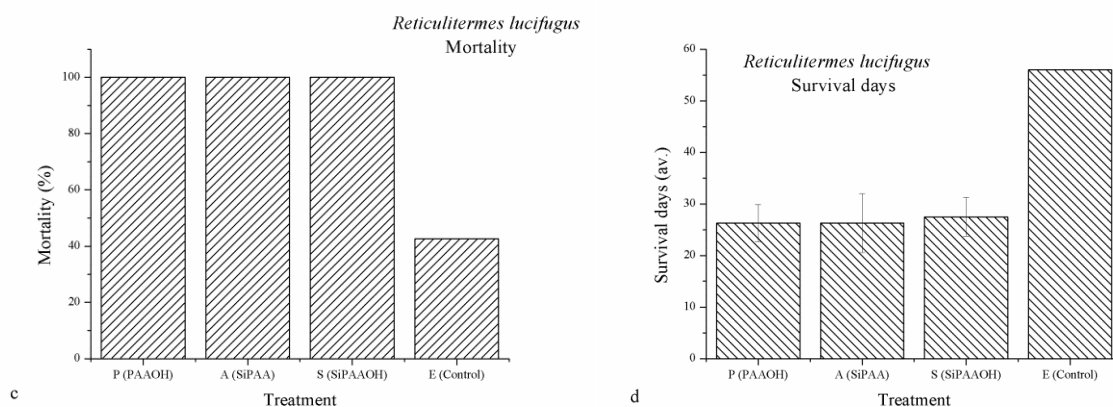


Fig. B.48 - (a) Level of attack; mass loss of the samples after the attack (b) and survival of the colonies (c, d).

B. 3.3.2.2 - Dry-wood termites - *Kaloterme flavicollis*

As described in experimental part (par. B. 2.8.2), for each colony three replicates were used and the tests lasted twelve weeks. To detect the state of the equipment, checks were performed once a week. In the apparatus relative to the "control" group, since first days, there was a vigorous activity of the termites, with obvious erosion on the specimens and an "ordered" distribution of termite droppings, visible as small pieces light brown coloured. In addition, starting at 63th day, winged individuals (alates) are observed, derived from the metamorphosis of the nymphs. In the equipment relative to A, P and S treatments, dead individuals in increasing number are noticed and a disordered arrangement of the fecal pellets inside the container is observed. In particular, in the treatment "A", dead individuals starting as early as the fifth day are present. At the end of the twelve-week test, the containers were emptied, survived individuals were counted and the wood samples are gently cleaned with a brush (Fig. B.49). The results are reported in Table B.22. The "untreated virulence control specimens" (E series) exhibit, on average, 68% survival rate, about 30 live individuals for replica, and 4 as visual rating. The comparison of the level of attack among the treatments indicates highly significant differences between the "control" and other treatments (ANOVA, $F = 40.44$, $p < 0.00001$) as seen in Fig. B.50a. The Fisher's Least Significant Difference (LSD) test, for the separation of averages, showed significant differences between the group E (control) in which the attack degree (degree 4) was significantly higher of those the other treatments (average degree of "S" group = 2 and "A,P" groups = 1). The results for the actual eating of wood by termites are reported in Fig. B.50b. The data (percentage wood consumption) show highly significant differences (ANOVA, $F = 34.47$, $P = 0.00001$) between treatments and "control", indicating a wood percentage consumption in the control clearly higher than the other groups, while between treatments A, S and P there are not significant differences. According to data reported in normal SNI 01.7207.2006 summarized in table B.23, the treatments A,P,S can be classified very resistant (resistance degree 1). The "survival" of the colony, i.e. the number of days required for the death of all individuals of the colony has also been considered. Statistical analysis of the data highlighted significant differences between treatments (ANOVA, $F = 4.37$, $p < 0.016$): the results are shown in Fig. B.50c. The LSD test shows significant differentiation only between the group A (SiPAA) and other treatments, while variations between the treatments E, S and P are not statistically significant with respect to this test.

Table B.22 - Results of the no-choice test for *Kalotermes flavicollis*.
Av = average; *sd* = standard deviation.

Treatment	Sample code	Starting	Mortality (%)	Attack level	Mass Loss (%)	Survival days
PAAOHd2	P _G 1	50	100	0	0.00	56
	P _G 2	50	100	0	0.00	79
	P _G 3	50	91	1	0.55	84
	P _G 4	50	100	0	0.00	56
	P _G 5	50	98	1	0.13	84
	P _G 6	50	92	1	0.19	84
	Av			98	0.5	0.15
SiPAAAd2	A _G 1	50	98	1	0.26	84
	A _G 2	50	100	0	0.00	56
	A _G 3	50	100	1	0.20	72
	A _G 4	50	100	1	0.27	79
	A _G 5	50	96	1	0.32	84
	A _G 6	50	100	1	0.25	63
	Av			99	0.83	0.22
SiPAAOHd2	S _G 1	50	88	2	0.70	84
	S _G 2	50	100	1	0.15	72
	S _G 3	50	100	2	0.60	84
	S _G 4	50	100	2	0.40	84
	S _G 5	50	100	1	0.24	72
	S _G 6	50	100	1	0.24	84
	Av			98	1.5	0.39
MeOH (control)	E _G 1	50	31	4	2.81	84
	E _G 2	50	29	4	2.25	84
	E _G 3	50	47	4	1.40	84
	E _G 4	50	20	4	2.95	84
	E _G 5	50	24	4	2.25	84
	E _G 6	50	43	4	1.17	84
	Av			32.4	4	2.14



Fig. B.49 - *Kalotermes flavicollis*. Visual examination of the attack degree.

Table B.23 – Level of attack and mass loss

Sample condition	Mass loss (%)
I: Very resistant	<2.0
II: Resistant	2.0-4.4
III: Moderate	4.4-8.2
IV: Poor	8.2-28.1
V: Very Poor	>28.1

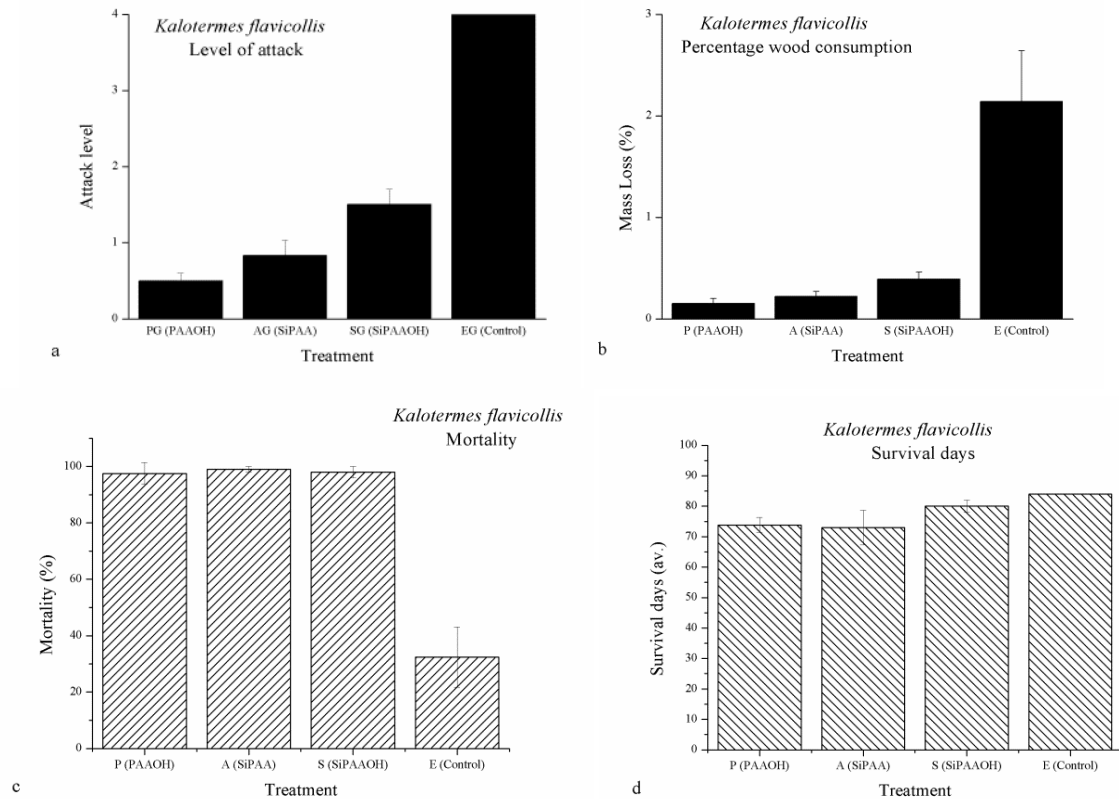


Fig. B.50 - (a) Level of attack; mass loss of the samples after the attack (b) and survival of the colonies (c, d).

In conclusion, treated wood samples (A, P and S) show an attack degree and percentage consumption significantly lower than those for the control group. With respect to the wood consumption, the treatments do not differ statistically while, in relation to the degree of attack, they are significantly different. As for the percentage wood consumption, the control group consumed about three times higher than that consumed in each of the three different treatments. Furthermore, in presence of treatments, the termites survive much less (never more than 2% on average) compared to the control group (mean value 56% and 68%).

A comparison between treated samples and the "control" group gives very encouraging results. All treatments are effective against the attacks by both species of termites (*Reticulitermes lucifugus* and *Kaloterme flavicollis*). The attack degree and the percentage of eating are about 1 for the subterranean termite and about 2 for the dry-wood termite. The treatments induce a high mortality

in either kinds of termites. In *Reticulitermes lucifugus* there are not significant differences between formulations, in *Kaloterme flavicollis* in formulation with only siloxane functionality (“A”) the consumption of woods and survival are always lower than “P” and “S” formulations.

B. 4 - CONCLUSIONS

Polyamidoamines, functionalized with OH groups (PAAOH) and siloxane groups (SiPAA, SiPAAOH) were synthesized in different reaction conditions. The alkoxy silane function may undergo hydrolysis and condensation to form an inorganic network inside the wood.

The characterization, made by spectroscopic techniques (ESI-MS, NMR, FTIR, Raman) and with thermal analysis, showed that the polymerization reaction for the polymers with hydroxyl side chain is favored when the amide is completely dissolved in the solvent and added slowly into the solution containing the ethanolamine, in particular when using water or methanol as the solvent.

The tests carried out on the polymers obtained without solvent at 90 °C show that the reaction proceeds up to completeness in less than 3 hours. As regards the polymers functionalized with silicon, it is noticed that with increasing EtA/APTES ratio the degree of polymerization increases. The DSC has allowed evaluating the glass transition temperature of the polymers in the range 109 ÷ 120 °C.

The hybrid polymers have been incorporated in the lignocellulosic structure of the wood and subjected to heat treatment (103 ± 1 °C for 18h) in order to increase the crosslinking. The high degree of crosslinking (DOC Degree of Condensation) within the wood has been demonstrated by ²⁹Si-NMR spectra. Thanks to electron microscopy SEM it has been possible to verify the successful impregnation of wood specimens with different treatments. The synthesis of these new polymeric wood preservatives has the advantage that no molecular fragment is released as a by-product of the reaction; the reactions are conducted in water, alcohols or in low molecular weight solvent (Augeo SL191). Three different preparations were applied as a protective coating on wood samples (sapwood of *Pinus sylvestris*) and tested for efficacy against biotic attack, both xilophagous insects and fungi. A comparison between treated samples and the “control” group gives very encouraging results. All formulations synthesized in methanol, PAAOH, SiPAA and SiPAAOH, were effective versus fungi species, in particular against *C. Puteana*. After aging tests the polymers with siloxane functionality (SiPAA, SiPAAOH) are effective on wood-decay fungi.

All treatments are effective against the attacks by both species of termites (*Reticulitermes lucifugus* and *Kaloterme flavicollis*). The attack degree and the percentage of eating are about 1 for the subterranean termite and about 2 for the dry-wood termite. The treatments induce a high mortality in either kinds of termites. In *Reticulitermes lucifugus* there are not significant differences between formulations, in *Kaloterme flavicollis* in formulation with only siloxane functionality (“A”) the consumption of woods and survival are always lower than “P” and “S” formulations.

The results obtained by biocidal effectiveness tests are very promising and have been protected by an international patent application [B93].

B. 5 - REFERENCES

- [B1] Hill C.A.S., Farahani M.R.M., Hale M.D.C., *The use of organo alkoxysilane coupling agents for wood preservation*. Holzforschung, 58 (2004) 316-325.
- [B2] Homan W.J., Jorissen A.J.M., *Wood modification developments*. Heron, 49 (2004) 361-385.
- [B3] Manfredi A., Ranucci E., Morandi S., Mussini P. R. Ferruti, P., *Fast and quantitative manganese sorption by polyamidoamine resins*. J. Polym. Sci. A Polym. Chem. 51 (2013) 769-773.
- [B4] Emilritri E., Ranucci E., Ferruti P., *New Poly(amidoamine)s Containing Disulfide Linkages in Their Main Chain*. J. Polym. Sci. A Polym. Chem., 43 (2005) 1404-1416.
- [B5] Ferruti P., Marchisio M.A., Duncan, R., *Poly(amido-amine)s: Biomedical Applications*. Macromol. Rapid Commun. 23 (2002) 332-355.
- [B6] Tsunoda K., Nishimoto K., *Effectiveness of alkylammonium compounds as above-ground wood preservatives*. Journal of the Japan Wood Research Society 33 (1987) 589-595.
- [B7] Hwang W.J., Kartal S.N., Yoshimura T., *Synergistic effect of heartwood extractives and quaternary ammonium compounds on termite resistance of treated wood*. Pest Management Science 63 (2007) 90-95.
- [B8] Nardi R., Berti S., Fioravanti M., Macchioni N. (2006) *La struttura anatomica del legno ed il riconoscimento dei legnami italiani di più corrente impiego* (II ed.). CNR-IVALSA, Firenze.
- [B9] Wiedenhoef A., *Structure and function of wood*. Wood handbook: wood as an engineering material: chapter 3. Centennial ed. General technical report FPL; GTR-190. Madison, WI: U.S. Dept. of Agriculture, Forest Service, Forest Products Laboratory, 2010: p. 3.1-3.18.
- [B10] Campanella L., Casoli A., Colombini M.P., Marini Bettolo R., Matteini M., Migneco M., Montenero A., Nodari L., Piccioli C. Plossi Zappalà M., Portalone G., Russo U., Sammartino M.(2007). *Chimica per l'arte*. Zanichelli.
- [B11] Cave I. D., *Modelling moisture-related mechanical properties of wood Part II: Computation of properties of a model of wood and comparison with experimental data*. Wood Science and Technology 12 (1978) 127-139.
- [B12] Eckelman, C. (1998). *The shrinking and swelling of wood and its effect on furniture*. Pub. FNR 163. Purdue Univ. Cooperative Extension Serv. West Lafayette, Indiana.
- [B13] Forsthuber B., Schaller C., Grüll G., *Evaluation of the photo stabilising efficiency of clear coatings comprising organic UV absorbers and mineral UV screeners on wood surfaces*. Wood Science and Technology, 47 (2012) 281-297.
- [B14] Evans P.D., Michell A.J., Schmalzl K.J., *Studies of the degradation and protection of wood surfaces*. Wood science and technology, 26 (1992) 151-163.

- [B15] Schmidt O., Czeschlik D., (2006). *Wood and tree fungi: biology, damage, protection, and use*. Springer-Verlag Berlin Heidelberg.
- [B16] Eaton R.A., Hale M.D.C. (1993) *Wood: Decay, Pests, and Protection*. Chapman and Hall, London.
- [B17] Maistrello L., Sbrenna G., *Frequency of some behavioural patterns in colonies of Kaloterme flavicollis (Isoptera Kalotermitidae): the importance of social interactions and vibratory movements as mechanisms for social integration*. *Ethology Ecology & Evolution* 8 (1996) 365-375.
- [B18] Fauchadour D., Jeanson T., Bousseau J.-N., Echalié B., *Nanoparticles of Ceranium Oxide -- Applications to Coatings Technologies*. *Nano and Hybrid Coatings* 19 (2005) 24-25.
- [B19] Lesar B, Humar M., *Use of wax emulsions for improvement of wood durability and sorption properties*. *European Journal of Wood and Wood Products*, 69 (2010) 231-238.
- [B20] Bongiovanni R., Montefusco F., Priola A., Macchioni N., Lazzeri S., Sozzi L, Ameduri B., *High performance UV-cured coatings for wood protection*. *Progress in Organic Coatings* 45 (2002) 359-363.
- [B21] Mahltig B., Gutmann E., Meyer D.C., Reibold M., Bund A., Böttcher H., *Thermal preparation and stabilization of crystalline silver particles in SiO₂-based coating solutions*. *Journal of Sol-Gel Science and Technology* 49 (2009) 202-208.
- [B22] Schultz T.P, Nicholas D.D., *Development of environmentally-benign wood preservatives based on the combination of organic biocides with antioxidants and metal chelators*, *Phytochemistry* 61 (2002) 555-560.
- [B23] Temiz A., Alfredsen G., Yildiz U.C., Gezer E.D., Kose G., Akbas S. Yildiz S., *Leaching and decay resistance of alder and pinewood treated with copper based wood preservatives*. *Maderas. Ciencia y tecnología* 16 (2014) 63-76.
- [B24] Thaler N, Humar M., *Copper Leaching from Copper-ethanolamine Treated Wood: Comparison of Field Test Studies and Laboratory Standard Procedures*. *BioResources* 9 (2014) 3038-3051
- [B25] Hingston J.A., Collins C.D., Murphy R.J., Lester J.N., *Leaching of chromated copper arsenate wood preservatives: a review*, *Environmental Pollution* 11 (2001) 53-66.
- [B26] Mantanis G., Terzi E., Kartal S.M., Papadopoulos A.N., *Evaluation of mold, decay and termite resistance of pine wood treated with zinc- and copper-based nanocompounds*. *International Biodeterioration & Biodegradation* 90 (2014) 140-144.
- [B27] Hattori T., Hisamori H., Suzuki S., Umezawa T., Yoshimura T., Sakai H., *Rapid copper transfer and precipitation by wood-rotting fungi can effect copper removal from copper sulfate-treated wood blocks during solid-state fungal treatment*. *International Biodeterioration & Biodegradation* 97 (2015) 195-201.
- [B28] Habibzade S., Omidvar A., Reza M., Farahani M., Mashkour M., *Effect of Nano-ZnO on Decay Resistance and Artificial Weathering of Wood Polymer composite*. *J Nanomater Mol Nanotechnol* 3:3 (2014) DOI: 10.4172/2324-8777.1000146.

- [B29] Treu A., Larnøy E., Militz H., *Process related copper leaching during a combined wood preservation process*. Eur. J. Wood Prod. 69 (2011) 263-269.
- [B30] Palanti S., Feci E., Predieri G., Vignali F., *A wood treatment based on siloxanes and boric acid against fungal decay and coleopter *Hylotrupes bajulus**. International Biodeterioration & Biodegradation 75 (2012) 49-54.
- [B31] Schultz T.P., Nicholas D.N. Preston A.P., *A brief review of the past, present and future of wood preservation*. Pest Management Science 63 (2007) 784-788.
- [B32] de Meijer M., Thurich K., Militz H., *Comparative study on penetration characteristics of modern wood coatings*. Wood Science and Technology 32 (1998) 347-365.
- [B33] Donath S, Militz H, Mai C., *Wood modification with alkoxy silanes*. Wood Sci Technol 38 (2004) 555-566.
- [B34] Palanti S., Feci E., Predieri G., Vignali F., *Copper anchored to amino-group functionalized silica gel as wood preservative against brown-rot decay*. Maderas. Ciencia y tecnología 12(2010) 259-266.
- [B35] Palanti S., Predieri G., Vignali F., Feci E., Casoli A, Conti E., *Copper complexes grafted to functionalized silica gel as wood preservatives against the brown rot fungus *Coniophora puteana**. Wood Science and Technology. 45 (2011) 707-718.
- [B36] Kartal S.N, Hwang W.J, Yamamoto A, Tanaka M., Matsumara K., Imamura Y., *Modification of wood with a commercial silicon emulsion: Effects on boron release and decay and termite resistance*. International Biodeterioration and Biodegradation 60 (2007) 189-196.
- [B37] Roberts] G.A.F., Wood F.A., *A study of the influence of structure on the effectiveness of chitosan as an anti-felting treatment for wool*. Journal of Biotechnology 89 (2001) 297-304.
- [B38] Devi R.R., Maji T.K., *In situ Polymerized Wood Polymer Composite: Effect of Additives and Nanoclay on the Thermal and Mechanical Properties*. Materials Research 16 (2013) 954-963.
- [B39] Nikkola J., Mahlberg R., Mannila J., Jämsä S., *Effect of curing process on simulated anti-soiling properties of sol-gel coating on pine sapwood*. J. Coat. Technol. Res., 7 (2010) 441-448, 2010.
- [B40] Terziev N., Panov D., Temiz A., Palanti S., Feci E., Daniel G. *Laboratory and above ground exposure efficacy of silicon-boron treatments*. (2009) IRG/WP 09 30510. International Research Group on Wood Protection, Stockholm, Sweden.
- [B41] De Vetter L., Depraetere G., Stevens M., Janssen C., Van Acker J., *Potential contribution of organosilicon compounds to reduced leaching of biocides*. Wood protection Annual Forest Science 66 (2009) 209.
- [B42] Brinker J., Scherer W. *Sol-gel science: the physics and chemistry of sol-gel processing*. (1990). Elsevier, San Diego.
- [B43] Danusso F., Ferruti P., *Synthesis of tertiary amine polymers*. Polymer 11 (1970) 88-113.

- [B44] Vaughn W.E., Rust F.F., *The photo-addition of hydrogen sulfide to olefinic bonds*. J. Org. Chem., 07 (1942) 472-476.
- [B45] Bayer O., *"Das Di-Isocyanat-Polyadditionsverfahren (Polyurethane)"*. Angewandte Chemie 59 (1947) 257-272.
- [B46] Marvel C. S., Caesar P. D. *Polyarylene-alkylene Sulfides*¹. J. Am. Chem. Soc., 73 (1951) 1097-1099.
- [B47] Breslow D. S., Hulse G. E., Matlack A. S., *Synthesis of Poly- β -alanine from Acrylamide. A Novel Synthesis of β -Alanine*. J. Am. Chem. Soc., 79 (1957) 3760.
- [B48] Danusso, P. Ferruti, G. Ferroni, Chim. Ind. (Milano) 49 (1967) 271-278 (a). Danusso F., P. Ferruti, G. Ferroni, Chim. Ind. (Milano) 49 (1967) 453-457 (b). F. Danusso, P. Ferruti, G. Ferroni, Chim. Ind. (Milano) 49 (1967) 587-590 (c). F. Danusso, P. Ferruti, G. Ferroni, Chim. Ind. (Milano) 49 (1967) 826-830 (d). P. Ferruti, R. Alimardanov, Chim. Ind. (Milano) 49 (1967) 831-834 (e).
- [B49] Danusso F., Ferruti P., Chim. Ind. (Milano), 50(1968) 71-80 (a). P. Ferruti, Z. Brzozowski, Chim. Ind. (Milano) 50 (1968) 441-445 (b).
- [B50] Murfin D. L., Hayashi K., Miller L. E., *N,N'-(disubstituted methylene)bisacrylamides: Preparation and polymerization*. J. Polym. Sci. Part A-1: Polym. Chem. 8 (1970) 1967-1980.
- [B51] Caldwell G., Neuse E., Stephanou A., *Synthesis of water-soluble polyamidoamines for biomedical applications. II. Polymers possessing intrachain-type secondary amino groups suitable for side-chain attachment*. J. Appl. Polym. Sci. 50 (1993) 393-401.
- [B52] Ranucci E., Spagnoli G., Ferruti P., Sgouras D., Duncan R., *Poly(amidoamine)s with potential as drug carriers: degradation and cellular toxicity*. Journal of Biomaterials Science, Polymer Edition, 2 (1991) 303-315.
- [B53] Cauzzi D., Stercoli A., Predieri G., *Hybrid Siloxane-Polyaminoamides for the Absorption of Heparin from Blood*. Sol-Gel Methods for Materials Processing. Springer Netherlands (2008) 277-282.
- [B54] Ferruti P., Marchisio M. A., Barbucci, R., *Synthesis, physico-chemical properties and biomedical applications of poly(amidoamine)s*. Polymer 26 (1985) 1336-1348.
- [B55] Ferruti P., *Poly(amidoamine)s: Past, Present, and Perspectives*. Journal of Polymer Science, Part A: Polymer Chemistry, 51 (2013) 2319-2353.
- [B56] Tomalia D. A., *Interview: An architectural journey: from trees, dendrons/dendrimers to nanomedicine*. Nanomedicine 2012, 7, 953-956.
- [B57] Tomalia D. A., Fréchet J.M. J. *Discovery of Dendrimers and Dendritic Polymers: A Brief Historical Perspective*. J. Polym. Sci. Part A: Polym. Chem.: 40 (2002) 2179-2728.
- [B58] Tarazona-Vasquez F., Balbuena P.B., *Ab Initio Study of the Lowest Energy Conformers and IR Spectra of Poly(amidoamine)-G0 Dendrimers*. J. Phys. Chem. B, 108 (2008) 15982-15991.

- [B59] Esfand R., Tomalia D.A., *Poly(amidoamine) (PAMAM) dendrimers: from biomimicry to drug delivery and biomedical applications*. DDT 6 (2001) 427-436.
- [B60] Manfredi A., Ranucci E., Suardi M., Ferruti P., *Polymerization kinetics of poly (amidoamine) s in different solvents*. Journal of Bioactive and Compatible Polymers. 22 (2007) 219-231.
- [B61] Mauro N., Manfredi A., Ranucci E., Procacci P., Laus M., Antonioli D., Mantovani C., Magnaghi V., Ferruti P., *Degradable Poly(amidoamine) Hydrogels as Scaffolds for In Vitro Culturing of Peripheral Nervous System Cells*. Macromolecular Bioscience, 13 (2013) 332-347.
- [B62] Barbucci R., Casolaro M., Ferruti P., Barone V., Lelj F., Oliva L., *Macroinorganics. 7.7 Property-Structure Relationships for Polymeric Bases whose Monomeric Units Behave Independently toward Protonation*. Macromolecules 14 (1981) 1203-1209.
- [B63] Martell A. E., Motekaitis R. J., *Determination and Use of Stability Constants*, (1992) 2nd ed.; Wiley-VCH: New York.
- [B64] Amiji M. M., *Polymeric Gene Delivery: Principles and Applications*. (2004) CRC Press Taylor and Francis Group, pag 267.
- [B65] Casolaro M., Bignotti F., Sartore L., Penco M., *The thermodynamics of basic and amphoteric poly(amido-amine)s containing peptide nitrogens as potential binding sites for metal ions. Part 1*. Polymer 42 (2001) 903-912.
- [B66] Abboto A, Beverina L, Chirico G, Facchetti A, Ferruti PG, Gilberti M, et al. *Crosslinked poly(amido-amine)s as superior matrices for chemical incorporation of highly efficient organic nonlinear optical dyes*. Macromol Rapid Commun 24 (2003) 397-402.
- [B67] Punyacharoenon P., Srikulkit K., Preparation of hyperbranched polyamidoamine polymer-ultrafine silica hybrid composite. Journal of Applied Polymer Science. 109 (2008) 3230-3237.
- [B68] Franchini J., Ferruti P., *Perspectives on: Recent Advances in Poly(amidoamine)s Chemistry*. Journal of Bioactive and Compatible Polymers, 19 (2004) 221-236.
- [B69] Gao C., Yan D., *Hyperbranched polymers: from synthesis to applications*. Prog. Polym. Sci. 29 (2004) 183-275.
- [B70] Girardi F., Cappelletto E., Sandak J., Bochicchio G., Tessadri B., Palanti S., Feci E., Di Maggio E., *Hybrid organic-inorganic materials as coatings for protecting wood*. Progress in Organic Coatings 77 (2014) 449- 457.
- [B71] EN 113:1996/A1:2004: Wood preservatives — Test method for determining the protective effectiveness against wood destroying basidiomycetes — Determination of the toxic values.
- [B72] EN 118:2013: Wood preservatives - Determination of preventive action against Reticulitermes species (European termites) (Laboratory method).
- [B73] UNI EN 15866:2010 - Conservation of cultural property - test methods - colour measurement of surfaces, UNI Ente Nazionale Italiano di Unificazione, 2010.

[B74] EN 84:1997 - Wood preservatives - Accelerated ageing of treated wood prior to biological testing - Leaching procedure.

[B75] Bravery A. F., *A miniaturised wood-block test for the rapid evaluation of wood preservative fungicides.* (1979). IRG/WP 2113. International Research Group on Wood Protection. Stockholm, Sweden.

[B76] EN 117:2012 - Wood preservatives - Determination of toxic values against Reticulitermes species (European termites) (Laboratory method).

[B77] EN 350-2:1994 - Durability of wood and wood-based products - Natural durability of solid wood - Part 2: Guide to natural durability and treatability of selected wood species of importance in Europe.

[B78] Isao A., Saito H., Tabeta R., Shoji A., Ozaki T., *Conformation-Dependent ^{13}C NMR Chemical Shifts of Poly(L-alanine) in the Solid State.* Macromolecules, 17 (1984) 457-461.

[B79] Shoji A., Ozaki T., Saito H., Tabeta R., Ando I., *Conformational Characterization of Solid Polypeptides by ^{13}C NMR recorded by the Cross Polarization-Magic Angle Spinning Method: conformation-dependent carbon-13 chemical shifts of oligo- and poly(γ -benzyl L-glutamates) and sequential copolymers of γ -benzyl and γ -methyl L-glutamates and qualitative evaluation of side-chain orientation.* Macromolecules 17 (1984) 1472-1479.

[B80] Deutsch D. S., Siani A., Fanson P.T., Hirata H., Matsumoto S., Williams C.T., Amiridis M.D., *FT-IR Investigation of the Thermal Decomposition of Poly(amidoamine) Dendrimers and Dendrimer-Metal Nanocomposites Supported on Al_2O_3 and ZrO_2 .* J. Phys. Chem. C, 111 (2007) 4246-4255.

[B81] Murugan R., Mohan S., Bigotto A., *FTIR and Polarised Raman Spectra of Acrylamide and Polyacrylamide.* Journal of the Korean Physical Society, 32 (1998) 505-512.

[B82] Raghavendra, R., Byrne, H., Martin, S., Howard, R., Toal, V.: *Raman spectroscopy for the characterization of the polymerization rate in an acrylamide-based photopolymer.* Applied Optics, 47 (2008) 206-212.

[B83] Socrates G. *Infrared and Raman Characteristic Group Frequencies. Tables and Charts.* Third Edition (2001) John Wiley & Sons, Ltd.

[B84] Vignali F, Predieri G, Baratto MC, Basosi R, Müller K, Callone E, Palanti S, Feci E, *Interpenetration of wood with NH_2R -functionalized silica xerogels anchoring copper(II) for preservation purposes,* Journal of Sol-Gel Science and Technology, 60 (2011) 445-456.

[B85] Rahman I.A., Jafarzadeh M., Sipaut C.S., *Synthesis of organo-functionalized nanosilica via cocondensation modification using aminopropyltriethoxysilane (APTES).* Ceramics International. 35 (2009) 1883-1888.

[B86] Cappelletto E., Maggini S., Girardi F., Bochicchio G., Tessadri B., Maggio R., *Wood surface protection with different alkoxysilanes: a hydrophobic barrier* Cellulose, 20 (2013) 3131-3141.

[B87] Agarwal U. P., Ralph S. A., *FT-Raman Spectroscopy of Wood: Identifying Contributions of Lignin and Carbohydrate Polymers in the Spectrum of*

Black Spruce (Picea mariana). Applied Spectroscopy 51 (1997) 1468-1655.

[B88] Agarwal U. P., Reiner R. S., Pandey A. K., Ralph S. A., Hirth K. C., Atalla R. H., *Raman spectra of lignin model compounds*. In: Proceedings of the 59th APPITA Annual Conference and Exhibition incorporating the 13th ISWFPC (International Symposium on Wood, Fibre, and Pulping Chemistry) (2005).

[B89] Girardi F., Maggini S., Della Volpe C., Cappelletto E., Mueller K., Siboni S., Di Maggio R., *Hybrid organic-inorganic materials on paper: surface and thermo-mechanical properties*. Journal of Sol-Gel Science and Technology, 60 (2011) 315-323.

[B90] Müller G, Schöpfer C, Vos H, Kharazipour A, Polle A: *FTIR-ATR spectroscopic analysis of changes in wood properties during particle- and fibreboard production of hard- and softwood trees*. Bioresources, 4 (2009) 49-71.

[B91] Klonkowsky, A.M., Grobelna, B., Widernik, T., Jankowska-Frydel, A., Mozgawa, W., *The coordination state anchored and grafted onto the surface of organically modified silicates*. Langmuir 15 (1999) 5814-5819.

[B92] Unger B., Bücken M., Reinsch S., Hübert T., *Chemical aspects of wood modification by sol-gel-derived silica*. Wood Sci Technol 47 (2013) 83-104.

[B93] L. Bergamonti, E. Chiappini, G. Predieri, S. Palanti, L. Maistrello, “*Wood preservative composition*” Int. Patent application WO 2015/004590 A1.

PART C

TiO₂ by sol-gel in acid and basic environments: characterization and photocatalytic activity for calcarenites stone protection

In this chapter, we focus on the assessment of the rate of the photocatalytic activity and the harmlessness of TiO₂ based coatings on different calcarenite stones.

We describe the sol-gel synthesis and characterization of some TiO₂ sols in a large pH range (from 1.3 to 10.6) including the study of their photocatalytic activity for the degradation of cationic and anionic dyes used as staining agents. The differences in the particle size and photocatalytic performance of TiO₂ sols have been evidenced as depending on the type of complexing ligands (acetic and malonic acid), peptizers and pH environment. To evaluate the photocatalytic performance of the prepared TiO₂ sols, we have monitored the time degradation of Methyl Orange (MeO, anionic dye) and Methylene Blue (MB, cationic dye) under UV irradiation.

The TiO₂ based nano-sols were also tested on *calcarenite* stone samples to evaluate the harmlessness of the coatings at different pH, the de-soiling properties and the rate of the photocatalytic activity. Besides to the tests on the photoactivity of the coatings, we have also analyzed their colouring effects and changes in water absorption properties of the investigated stone.

The efficacy of titanium dioxide coating was tested on porous calcarenites, widely used in Southern Italy in historical buildings and for sculptures for a long time, especially during the Baroque period.

C. 1 - INTRODUCTION

Since ancient times, natural stone (granites, marbles, sandstone and limestone) has been widely used as a material for artistic artefacts, from the construction of ancient monuments and historic buildings to the realization of small-scale sculptures. The decay of stone artifacts represents an irretrievable loss of our heritage and history.

The stone artefacts are subject to degradation processes, both natural and anthropogenic, whose speed and type strongly depend on the nature of the constituent materials and on the characteristics of the surrounding environment (pollutants, moisture, salts, temperature excursions, mechanical stress, etc.) [C1]. Physical, chemical, and biological agents act in association in deteriorating stone [C2-3].

The main forms of decay for building surfaces and monuments are related to environmental pollution causing high levels of sulphate and nitrate deposition [C4], with the development of black crusts, and to climate conditions, that accelerate the degradation processes [C5-7] and produce an aesthetically unacceptable staining of the stone surfaces [C2].

Compared to other types of stones, limestone has low mechanical strength due to high content of carbonates (mainly calcite) therefore it is very sensitive to the action of chemical agents and, in particular, to atmospheric pollutants. The decay processes caused by physical and chemical agents are further amplified by the high open porosity of the stone, especially in the case of calcarenites [C8-9].

Great interest is currently devoted to the study of efficient processes and eco-friendly technologies, in particular towards the application of photocatalysis to transform pollutants into harmless elements [C10]. The development of self-cleaning surface treatments may be also promising to preserve the original appearance of the monument and to slow down the degradation processes of stone surfaces [C11-13].

An efficient protective/self-cleaning coating must preserve the initial stone colour and must be harmless towards the stone substrate [C14].

Titanium dioxide (TiO₂, also known as titania) is well known for its photocatalytic activity and is currently widely investigated for numerous applications, such as environmental purification, decomposition of organic contaminants and self-cleaning coatings in Cultural Heritage conservation science.

C. 1.1 - TiO₂ and its photocatalytic activity

Titanium dioxide (TiO₂) is considered the most promising material for the photocatalytic degradation of environmental pollutants, being highly efficient, non-toxic and stable under irradiation. TiO₂ has been intensively investigated during the last decades due to its outstanding physicochemical properties for environmental applications. Main current interest is focused on the use of nanocrystalline TiO₂ for the development of dye-sensitized solar cells (DSSCs) [C15-18] and of heterogeneous photocatalysts for the degradation of pollutants by advanced oxidation processes (AOPs) [C19-20].

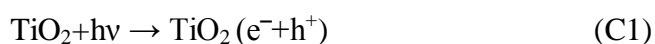
The most important applications of the photocatalytic activity of titania are in wastewater and air treatments [C21-25], but in recent years it has also been investigated for possible use in cultural heritage conservation science, for its self-cleaning and antipollution properties [C13,C26-28]. Other applications in cultural heritage science include the prevention of biodeterioration [C29-30] and the protection of historical buildings and stone monuments [C11-12, C31].

Various material parameters such as the powder morphology [C32], specific surface-area [C33- 34], average pore size, pore volume and its distribution [C35-36], average nanocrystallite size [C37-39], amount of rutile or brookite phase [C40-42], and amount and nature of dopants [C43-52] significantly affect the photocatalytic activity of nanocrystalline TiO₂.

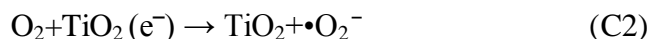
TiO₂ is found in nature in three different polymorphs, rutile, anatase (both crystallizing in the tetragonal system) and brookite (orthorhombic). Rutile is thermodynamically the most stable phase, anatase and brookite phases being readily transformed to rutile when heated at high temperature (brookite to anatase and anatase to rutile transformations at 1053 K and 1123 K, respectively) [C53-54]. All phases are photoactive: anatase phase is thought to be the most active [C55-56], even if important results were also obtained with TiO₂ in brookite and rutile pure or mixed forms [C57-63]. Among the several factors influencing the TiO₂ photoactivity, the particle size seems to play a major role, enhancing the available surface for the photocatalysis effect. Although, in literature, you can find opposite data [C64], in general the smaller the size of crystalline domains of TiO₂, the higher the reported photo-catalytic activity. Accordingly, nanocrystalline titania, having possibly anatase structure, is imperative for this application.

The simplest test for the photocatalytic activity of nanocrystalline titania is the degradation of organic synthetic-dyes diluted in aqueous sols. Depending on dye, several mechanisms have been proposed for dye decomposition involving both oxidative (electron transfer from the dye) and reductive (electron transfer to the dye) processes. The light absorption can occur in the dye or in the semiconductor or both.

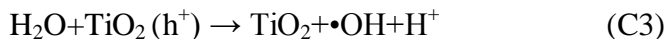
Photocatalytic reactions are initiated when UV light is absorbed by TiO₂ catalyst (TiO₂ in the anatase form has a band gap of ~3.2 eV, corresponding to λ~388 nm) [C25, C65-66]: the photon absorption results in the production of electron-hole pairs, promoting an electron (e⁻) from the valence band to the conduction band, with simultaneous generation of a positive hole (h⁺) in the valence band:



The electrons can recombine with the holes or the electron-hole pairs can participate in red-ox reactions, leading to the formation of reactive oxygen species. Electrons may reduce the dye or react with electron acceptors such as O₂ adsorbed on the Ti-surface or dissolved in water reducing it to superoxide radical anion •O₂⁻:



The photo-generated holes can oxidize the dye organic molecule to form R⁺, or react with surface hydroxyls or H₂O, oxidizing them into •OH radicals:



The •OH radicals are formed also by direct oxidation of the pollutant molecules under UV radiation [C67].

The surface-adsorbed water and hydroxyl groups play therefore a very important role in the photocatalytic reaction [C68].

In dye reduction processes, as for example for methylene blue, the photogenerated electrons may react with an electron acceptor located on the catalyst surface, i.e. the dyes themselves, giving the corresponding “leucobase” [C69].

Decomposition of most organic compounds occurs as the result of subsequent stepwise hydroxylation of the primary reduction products [C70]. Also the reactions of organic compounds with the radical anion •O₂⁻ and with radicals formed upon the photo-protonation of •O₂⁻, may lead to the decomposition of organic compounds [C71]. Both •OH and •O₂⁻ radicals are then effective to drive the dye degradation. The electron transfer between dye and nanosized semiconductor particles can degrade the dye to smaller organic substances and ultimately mineralize completely to water, carbon dioxide, and other inorganic ions.

A possible use of nanocrystalline TiO₂ based products with a self-cleaning activity on architectural elements requires that the coatings do not alter the original aspect of stone substrates and do not produce physical and chemical changes causing harmful effects [C12].

In most cases, the titania nanosols are synthesized in acid conditions and their efficiency for photocatalytic degradation of pollutants is well known [C72-73]. The use of acid coatings on carbonatic stones used as building stone in Cultural Heritage may be dangerous [C28].

In this context, we have recently described the use of TiO₂ sols, peptized in acidic environment, as protective coatings on southern Italy *biocalcarenites* [C28, C31]. Although they were found to be active for pollutants photodegradation on the stones, however their acidic character gave rise to some micro-solubilization of calcareous material resulting in undesirable micro-degradation of the stone. For this reason, we attempted the sol-gel synthesis of TiO₂ nanosols in a basic medium by using triethylamine as peptizing agent. For this synthesis, we had to use malonic acid as ligand in the place of acetic acid in order to ensure greater stability to the sol.

C. 1.2 - Stone materials

The limestones selected to evaluate the de-soiling properties and the harmlessness of the titania coatings were: *Comiso*, *Modica* and *Noto* stones from Sicily, Italy and *Lecce* stone from Apulia, Italy.

These calcarenites, mainly made of calcite, are collected in Eastern Sicily and were largely used in the monuments of the Baroque cities of the “Val di Noto” (i.e. Catania, Siracusa, Noto, Ragusa and Modica) included in the UNESCO’s World Heritage List, completely destroyed following the earthquake of 1693 [C74].

Modica and *Comiso* stones belong to the Ragusa Formation of Burdigalian age, which is largely investigated from the petrographic and geological point of view [C75-77]]. The Ragusa Formation (Upper Oligocene-Miocene) consists of two members: a) the lower Leonardo Member (Upper Oligocene), formed of alternating calcareous and marly layers; b) the upper Irminio Member (Lower Miocene), consisting of three different levels: i) a calcarenitic basal level; ii) an

intermediate marly-calcarenitic alternance; iii) an upper marly-calcarenitic alternance. *Comiso* and *Modica* stones are quarried from Leonardo member.

The *Noto limestone*, known as "*Pietra di Noto*" - *yellowish lithofacies* is a soft, fine grained and yellowish in color calcarenite widely used in the Baroque monuments of the Noto Valley (Sicily).

From a geological point of view, it belongs to Palazzolo Formation (Lower Oligocene - Pliocene): it outcrops in the Hyblean Plateau and consists of two different lithofacies [C78]: an alternation of fine-grained grey limestones and soft marly limestones (Noto white-cream limestone) and a yellowish limestones outcropping in large bank levels (Noto yellowish limestone). Petrographically, Noto yellowish limestone is a biomicrite or wakestone, with high percentage of insoluble residue clay fraction [C74].

The "*pietra di Lecce*" is typical of the Salento region, southeastern extremity of the Apulia Region of Italy. It is characterised by white-yellow creamish colour and shows high porosity and ease of machinability. It is a homogeneous planktonic foraminiferal biomicrite largely investigated from the petrographic and geological point of view [C79-81]. The "*pietra di Lecce*" consists predominantly of calcium carbonate (93-97%) and lower amounts of granules of quartz, glauconite, feldspars, and clay minerals (i.e. kaolinite, illite, smectite) [C82, C9].

C. 2 - EXPERIMENTAL

C. 2.1 - Materials and syntheses of TiO₂

Titanium (IV) isopropoxide (97%) and Malonic Acid (99%) were purchased from Sigma-Aldrich. Acetic acid (99-100%) was purchased from Riedel-de Haen, Nitric acid from Carlo Erba (65%) and Triethylamine (>98%) from Fluka. All reagents were used without further purification.

Starting TiO₂ (0.1 M) sols were obtained by mixing, under dry conditions, titanium isopropoxide Ti{OCH(CH₃)₂}₄ with glacial acetic acid or malonic acid in 1/1 molar ratio; after 30 min of stirring distilled water was added. At this stage two synthetic routes were followed which differ for the choice of the peptizing medium, acid in the first case (i), basic in the second one (ii).

(i) The sols henceforth called TiAcAc, TiAcN, TiAcNNa and TiAcAu were then prepared in the following ways:

- *TiAcAc* sol was obtained after refluxing TiO₂ sol at 100 °C for 3 hours in the original acetic medium. The refluxing was necessary to promote the transformation from amorphous to nanocrystalline titania. The final milky *TiAcAc* sol contained a small amount of precipitate. The pH was 3.05
- *TiAcN* sol was achieved by adding HNO₃ as peptizer to the TiO₂ starting sol till to pH≈1 and refluxed as before. The resulting sol was completely transparent.
- *TiAcNNa* sol was prepared by adding a solution of sodium hydroxide (0.1 M) to the *TiAcN* sol up to pH 4.1; a milky sol was obtained with a small amount of precipitate.
- *TiAcAu* sol was obtained modifying a *TiAcAc* sol by adding dropwise a solution of HAuCl₄•3H₂O (2mM) during the refluxing process. The Au concentration in the sol was 0.03M. The pH was 2. The sol appeared of a purple transparent color.

(ii) The sols named TiMaA and TiMaAN were both synthesized from the starting sols containing malonic acid as complexing agent.

- *TiMaA* sol was obtained by refluxing the starting sol in a basic environment after addition of triethylamine until to the complete peptization. *TiMaA* sol results transparent and *stable* and the pH was 10.62.
- *TiMaAN* sol was prepared by acidification of *TiMaA* with nitric acid down to pH 1.4.; the sol gave a white precipitate.

Table C.1 reports the list of the sols along with the synthetic conditions.

Table C.1- The synthesized sols.

Sample	Complexing	Peptizer	Environment	pH	Photocatalysis
TiAcAc	Acetic acid	Acetic Acid	-	3.1	T
TiAcAu	Acetic acid	Acetic Acid	HAuCl ₄ •3H ₂ O	2.0	T
TiAcN	Acetic acid	Nitric Acid	-	1.3	T
TiAcNNa	Acetic acid	Nitric Acid	NaOH	4.1	NT*
TiMaA	Malonic acid	Triethylamine	-	10.6	T
TiMaAN	Malonic acid	Triethylamine	HNO ₃ **	1.4	NT*

T: tested; NT: not tested

* Scarcely *stable*: formation of precipitates

** Nitric acid was added in order to test the stability of the sol by lowering pH

The titania powders for XRD and micro-Raman measurements were obtained by drying the different sols in an oven at 50 °C.

C. 2.2 - Stone samples

As anticipated, the stones selected to test the TiO₂ coatings synthesized as described in the previous section were the calcarenites outcropping in the southern of Italy and widely used in the Baroque period: *Comiso*, *Modica* and *Noto* stone (from Sicily) and *Lecce* stone (from Apulia).

Comiso and *Modica* stones were coated with TiAcN sol. The surface of stones were also pretreated with a SiO₂ sol (0.4M) prepared by mixing TEOS (tetraethyl-orthosilicate, Aldrich 98%), distilled water and hydrochloric acid, in the molar ratio 1:8:0.025 using 2-propanol as solvent. *Lecce* stone was coated with TiO₂-based sols TiAcAc, TiAcN, TiAcNa and TiAcAu. *Noto* stone was treated with TiAcN and TiMaA sols.

The stone samples were obtained from fresh quarry by a clean diamond saw without any lubricating agent. The sizes of the samples were different depending on the kind of measurement (see Table C.2). Before the application of the coatings, the stone specimens were washed with deionized water in order to remove dust deposits, dried 24 hours at 60 °C and then kept three hours in a dry atmosphere and weighted. The procedure was repeated until constant weight ($\pm 0.1\%$) was attained [C83]. The titania coatings were applied directly on the stone samples by brushing.

After each treatment the samples were kept again at 60 °C for 24 hours and then dried in a desiccator and weighted, repeating the cycle up to weight stabilization. It was assumed that the dry weight is reached when the difference between two consecutive weight measurements is less than 0.1% of the initial weight of the sample. The amount of sol applied was therefore determined by the difference of the dry weight after and before the treatment. The stone samples were then stored in a desiccator at a temperature of 23 ± 1 °C.

Table C.2 - The stone samples investigated.

Stone samples	Sizes	Test	Normal
<i>Comiso stone</i>	5 x 5 x 2 cm ³	Water absorption; salt crystallization, colour changes; self-cleaning	<i>UNI EN 15801:2010</i>
<i>Modica stone</i>	5 x 5 x 2 cm ³	Water absorption; salt crystallization, colour changes; self-cleaning	<i>UNI EN 12370:2001</i>
<i>Lecce stone</i>	5 x 5 x 1 cm ³	Water absorption; colour changes; self-cleaning	<i>UNI EN 15866:2010</i>
<i>Noto stone</i>	5 x 5 x 1 cm ³ 4 x 4 x 4 cm ³	Water absorption; salt crystallization, colour changes; self-cleaning	<i>UNI EN 11259:2008</i>

C. 2.3 - Characterization of TiO₂ sols

C. 2.3.1 - XRD measurements

To determine the structure and the crystallites size of TiO₂ particles, all powdered samples were examined by X-ray diffraction (XRD). XRD patterns of the dried sols were obtained by Thermo ARL X'TRA X-ray diffractometer with Si-Li detector, using Cu-K_α radiation at 40 kV and 40 mA, at 0.2° scan rate (in 2θ) in the range 10-60°. The measurements were performed at room temperature by dispersing the powders on a glass sample holder. The XRD pattern of powdered crystalline silicon was used for 2θ calibration.

C.2.3.2 Micro-Raman spectroscopy

Non-polarized Raman spectra on the powdered TiO₂ samples were recorded at 632.8 nm in a nearly backscattered geometry with a Horiba - Jobin Yvon LabRam micro-spectrometer (300 mm focal length spectrograph) equipped with an integrated Olympus BX40 microscope provided with x10-x50-x100 objectives. The spectral resolution was about 1.5 cm⁻¹.

The Rayleigh radiation was blocked by an edge filter and the backscattered Raman light was dispersed by a 1800 grooves/mm holographic grating on a Peltier cooled CCD, consisting of an array of 1024/256 pixels. The entrance slit width was fixed at 100 μm. The laser power was adjusted by means of density filters to avoid uncontrolled thermal effects. The power on the sample was always less than 1 mW.

Spectra were collected using both x100 and long working distance x50 microscope objectives. Typical exposures were 10-60 s, with 5-9 repetitions. The system was regularly calibrated using the 520.6 cm⁻¹ Raman band of silicon or by means of reference emission lines of Ne or Cd light sources. The data analysis was performed by LabSpec built-in software.

C. 2.3.3 - TEM

TEM samples were prepared by dropping a sonicated suspension of TiO₂ onto a 300-mesh carbon-coated copper grid.

TEM investigations have been carried out with a JEOL 2200FS field emission microscope operated at 200 kV, with 0.185 nm point-to-point resolution, equipped with in-column Ω filter, X-ray microanalysis, and two High Angle Annular Dark Field (HAADF) detectors for chemical imaging.

C. 2.3.4 - DLS and ELS

The hydrodynamic size and surface charge (zeta potential) of the titania particles in the sols were measured using a Delsa Nano C (Beckman Coulter) instrument for Dynamic Light Scattering (DLS) and Electrophoretic Light Scattering (ELS), respectively. DLS measures the intensity of the laser light that is scattered from suspended particles. The average hydrodynamic diameter of the particles is derived from the temporal evolution of the scattered light intensity using the Stokes-Einstein equation [C84]. ELS measures the frequency or phase shift of an incident laser beam caused by electric field driven particle migration, reported as the electrophoretic mobility. Particle zeta potential is calculated from the measured electrophoretic mobility using the Smoluchowski equation [C85]. In order to examine the effect of pH on the zeta potential and to measure the Iso-Electric Point (IEP), ten measurements of the surface charge were performed varying the pH of TiAcN sol, from 1 to 7 with a NaOH 0.1M solution, and that of TiMaA, from 11 to 6 with a HCl 0.1M solution. Titania sols were sonicated for 15 min using a bath sonicator (40 W, 35 kHz, Elma 460/H) before the size and zeta potential measurements. All data were taken at 25 °C, kept constant by the Delsa Nano C instrument. Reliability of hydrodynamic size and zeta potential values was ensured, according to the standard procedure, by almost 10 scans for each analysis.

C. 2.3.5 - Photocatalytic activity of the nanosols

Methylene blue (MB) and methyl orange (MeO) dyes (staining agents) were chosen as model compounds for the photocatalytic degradation induced by titania nanoparticles (Fig. C.1)

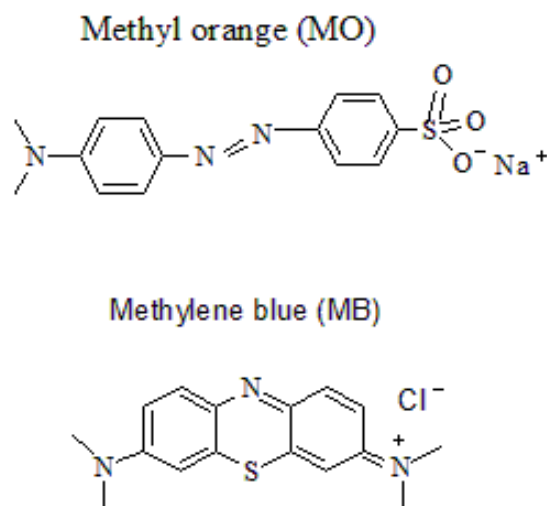


Fig. C.1 - The chemical structure of methyl orange (MeO) and Methylene blue (MB).

MB is a brightly coloured blue cationic thiazine dye (a heterocyclic aromatic compound) with absorption λ_{\max} values at 664 nm, 614 nm and 292 nm. Solutions of MB are blue when in an oxidizing environment, but turn colorless if exposed to a reducing agent. In the absence of a catalyst, it is relatively stable to photodegradation for UV irradiation [C69].

Methyl orange is an anionic azo-dye, orange in basic medium and red in acidic medium. MeO is rather stable in visible and near UV light [C86-87]. When dissolved in water, the UV-VIS spectrum

of Methyl Orange exhibits a broad peak at about 465 nm, typical of a substituted azobenzene. The wavelength of the absorption maximum does not depend on pH in the range $5 < \text{pH} < 11$; below pH 5, the dye protonates and the spectrum shifts to longer wavelength (510 nm), via an isosbestic point at 469 nm [C88-89].

MB and MeO dyes were selected as performance indicators of the photocatalytic activity of the TiO_2 nanosols. Their degradation was monitored through the change in optical absorption of dye solutions under fluorescent lamp irradiation. Experimental conditions: 125 W Helios-Italquartz medium pressure, mercury-vapour, water-jacketed lamp, with maximum emission line at 365.4 nm. Aqueous solutions of the dye were added to the TiO_2 sols: the resulting solutions (MB or MeO 0.03 mM and TiO_2 9.22 mM) were placed in a 100 ml quartz round-bottomed flask. Calibration plots (absorbance vs. concentration) based on Beer-Lambert's law at the maximum of absorbance of each dye were obtained.

The mixtures were magnetically stirred in the dark for 40 min to ensure that a suitable adsorption/desorption equilibrium of the dye on the surface of TiO_2 had been established [C67] as deduced from the achievement of a final constant concentration. The UV-visible absorbance at equilibrium A_0 was taken as a reference for the initial dye concentration C_0 .

The solution was transferred to a quartz reactor and then was put at a distance of 10 cm from the UV light source, under continuous magnetic stirring. During irradiation, the sol was sampled at regular time intervals and the sample was centrifuged to ensure separation of the dye solution from the catalyst. The color of the dispersion disappeared gradually indicating that the chromophore structure of the dye was being destroyed. The absorbance decrease was measured by a Perkin Elmer Lambda-Bio 20 UV/Vis Spectrometer using the corresponding TiO_2 sol as a blank. Control experiments were carried out by irradiating the dyes (MeO and MB) with UV light without catalyst. The normalized intensity (A_t/A_0) of the main absorbance peak of dye solution was taken as the measure of residual dye concentration C_t/C_0 at time t .

C. 2.4 - Characterization of TiO_2 -based coatings on calcarenite stones

C. 2.4.1 - The stone samples: petrographic analysis

The petrographic analysis of cross sections of the samples was carried out using a *Nikon Eclipse E 400 POL* polarizing optical microscope, in order to assess if the compositional and textural (grain size, matrix, cement, porosity) features may influence the photocatalytic activity of protective coatings.

C. 2.4.2 - ESEM and SEM-EDS

Morphological observations by Environmental Scanning Electron Microscopy (ESEM, Mod. XL30, FEI Company) were performed on Lecce stone in order to study the distribution of the treatments and the induced changes on the stone surface. Elemental analysis by Energy-Dispersive X-ray spectroscopy (EDS) was also performed for the evaluation of Ti presence on the stone surface. Both BSE and GSE detectors were used in low vacuum modality (pressure: 0.6 torr, acceleration voltage: 25 kV). The EDS spectra were acquired on surface areas $10 \times 10 \mu\text{m}^2$ and with respect to calcium as reference.

Changes in the morphology of the stones due to treatments and the penetration depth of TiO_2 were evaluated through SEM and EDS analyses at the surface and on stratigraphic sections by a Scanning Electron Microscope + Jeol 6400 equipped with an Oxford Instruments Link Analytical Si(Li) Energy Dispersive System detector. The data analysis was performed with INCA software.

C. 2.4.3 - Chromatic changes

To evaluate the changes of the stone surface appearance due to the TiO₂ based coatings the colorimetric analysis was performed on spectral images of stone samples acquired by a Techkon Spectrodens colorimeter for the Noto stone and by a spectrophotometric scanner [90] using a D65 illuminant, with 500 lines/scan at 3 mm/sec for Comiso, Modica and Lecce stones. At least nine regions of a few mm² area were examined and averaged on each stone sample, using three samples for each case.

According to UNI EN Normal [C91] the color difference (ΔE^*) due to TiO₂ applications with respect to the uncoated stone was measured in the CIELab space:

$$\Delta E^* = \sqrt{\Delta L^{*2} + \Delta a^{*2} + \Delta b^{*2}}, \quad (C4)$$

where ΔL^* is the change in lightness, Δa^* and Δb^* the change in hue (a^* is the red (>0)/green (<0) coordinate and b^* the yellow (>0)/blue (<0) coordinate, in the CIELab notation).

C. 2.4.4 - Self-cleaning tests on the stone

The self-cleaning properties of the TiO₂ coatings were checked by the colorimetric method as a function of time. Untreated and treated stone samples were stained with methylene blue (MB) and/or methyl orange (MeO) dyes and placed at 10 cm from the UV source (125 W Helios-Italquartz medium pressure, mercury-vapour, water-jacketed lamp, with maximum emission line at 365.4 nm).

To evaluate the time dependence of the photocatalytic discoloration of the stains, colorimetric measurements were performed by the Techkon Spectrodens colorimeter. The normalized chroma change ΔC was obtained by the chromatic coordinates $a^*(t)$ and $b^*(t)$ at different exposure time t :

$$\Delta C = \sqrt{\frac{(a^*(t) - a^*(0))^2 + (b^*(t) - b^*(0))^2}{(a_c^* - a^*(0))^2 + (b_c^* - b^*(0))^2}} \quad (C5)$$

where $a^*(t)$ and $b^*(t)$ are the colorimetric coordinates at time t , whereas a_c^* and b_c^* are measured on clean stones before the staining with methyl-orange dye [C27-28, C92].

At least three regions of a few mm² area were examined and averaged on each stone sample, using three samples for each case.

C. 2.4.5 - Water absorption by capillarity

The determination of the water absorption by capillarity was carried out on 5x5x2 cm³ samples, following the recommendations UNI EN 15801:2010 [C94]. Three samples for each coating were placed in a vessel on a blotting paper stratum saturated with demineralized water: the treated samples were lying on the coated side. The water level was maintained constant throughout the test. The amount of absorbed water Q_i at time t_i was calculated by

$$Q_i = \frac{M_i - M_0}{A} \quad (C6)$$

where M_0 is the mass of the dry specimen, M_i the mass at time t_i and A is the area in contact with the wet paper. Measurements were made at regular steps (1-5, 10, 20, 30, 45, 60 min, 4h, 6h, 24h) and then at subsequent 24h intervals until $t=t_f$, when the difference between two consecutive weighing was less than 1% of the initial mass of the specimen. The calculated values of Q_i are reported (in kg/m²) as a function of the square root of time ($t_i^{1/2}$).

The absorption coefficient AC (in $\text{kg}/(\text{m}^2\text{s}^{1/2})$) is evaluated as the slope of the curve Q_i at low times ($< 1\text{h}$), where the amount of the absorbed water vs. $t^{1/2}$ should be approximately linear according to the model for the capillarity absorption [95]. The slope was calculated by a linear fitting of the data requiring that $Q_i=0$ for $t_i=0$.

An additional parameter frequently reported [C28,C31,C96] is the relative capillarity index RCI, defined as the ratio between the amount of water absorbed by the treated sample for the whole duration of the test and the amount absorbed by the untreated one. It is calculated from the ratio of the area below the Q_i curve up to t_f of the treated stone to the corresponding one for the untreated sample:

$$\text{RCI} = \frac{\int_0^{t_f} f(Q_i)_{\text{tr}} dt}{\int_0^{t_f} f(Q_i)_{\text{unt}} dt} \quad (\text{C7})$$

C. 2.4.6 - Salt Crystallization

The salt crystallization test was performed according to UNI EN 12370-2001 [C97] by immersion of cubic $4 \times 4 \times 4 \text{ cm}^3$ samples in a solution of $\text{Na}_2\text{SO}_4 \cdot 10\text{H}_2\text{O}$ (14% volume), which is one of the most dangerous salts detected in historical buildings [C12], especially in marine environment. The saturated solution was decanted for 24 h in order to eliminate non dissolved sulphate crystals. The samples of *pietra di Noto*, eight untreated and eight for each coating, were initially placed in an oven at $105 \pm 5 \text{ }^\circ\text{C}$ up to weight stabilization and subsequently stored in a desiccator. The samples were immersed in the solution in a closed container for two hours at $20 \pm 0.5 \text{ }^\circ\text{C}$, and then they were placed in an oven at $105 \pm 5 \text{ }^\circ\text{C}$ for 16 hours, allowed to cool and then weighted: this cycle was repeated 15 times. The mass difference before and after each cycle is reported as mass percentage variation with respect to the initial dry mass. At the end of the 15 cycles, the samples were washed from salts to evaluate further mass changes.

C. 3 - RESULTS and DISCUSSION

C. 3.1 - The TiO_2 sols and powders

C. 3.1.1 - Syntheses

As described in section 2.1, the sol-gel syntheses of water-based nanocrystalline TiO_2 sols were carried out by preliminary acid hydrolysis of titanium (IV) isopropoxide with acetic acid or malonic acid both acting also as complexing agents. This preliminary synthetic stage was followed by peptization with acid or basic species in order to obtain TiO_2 nanosols in a large pH range (1.3 - 10.6). The aim was to vary the pH in order to investigate its influence on the formation of aggregates and on the stability.

The sols called TiAcAc, TiAcN and TiAcNNa were prepared from the starting sols containing acetic acid, whereas TiMaA and TiMaAN were both synthesized from the starting sols containing malonic acid as complexing agent. TiAcAc and TiAcN are *stable* acid sols, whereas TiMaA is a *stable* basic sol. TiAcNNa, which derives from TiAcN by treatment with NaOH, and TiMaAN, obtained from TiMaA by treatment with HNO_3 , resulted *unstable* and gave significant amount of precipitates. The sol-gel synthesis in a basic medium, achieved using triethylamine as peptizing agent, was carried out in order to get products suitable to be placed on materials subjected to acid deterioration, like carbonatic stones.

In the sol called TiAcAu, synthesized starting from TiAcAc sol, Au particles (formed *in situ*) were added to evaluate possible increase of the photocatalytic activity by noble metals doping, through an increase of the electron-hole recombination time [C51]. The Au concentration in the sol was 0.03M. The sol appears of a purple transparent color.

It is known that transition metal isopropoxides in their parent alcohol mainly form dimeric or trimeric species and the modification with complexing agents is necessary in order to prevent fast hydrolysis and condensation. It has been found that the average size of the oligomers decreases when the complexation molar ratio x ($x = \text{mol ligand/mol Ti}$) increases, since complexing ligands limit condensation.

C. 3.1.2 - XRD

The crystalline phase purity and the size of the particles of TiO₂ powders, obtained by drying at 50 °C the sols, synthesized with different reagents under different pH conditions, were determined by X-Ray diffraction (XRD).

The XRD results of the TiO₂ powders obtained from all sols are shown in Fig. C.2 with the exception of TiAcNNa that is reported in Fig. C.3. The XRD patterns are compared with the XRD reference of anatase (JCPDS card no. 21-1272) and brookite (JCPDS card no. 29-1360). The anatase phase is predominant, with a small percentage of brookite, which is evident in TiAcAc, TiAcN and TiAcAu, all deriving from sols with acetic acid as the complexing agent. The anatase diffraction peaks at $2\theta = 25.28^\circ$, 37.98° , 47.66° and $54.6^\circ + 55.8^\circ$ are due to the reflections planes (101) (004) (200) and (105) + (211), respectively [C99], and the brookite phase is clearly identified by its peak at 30.81° due to the (121) reflection. The main (101) diffraction peak of anatase at 25.28° overlaps with the (120) and (111) reflections of brookite at 25.34° and 25.69° , respectively [C62].

The diffractogram of TiAcNa in Fig. C.3 clearly evidences the peaks of NaNO₃ crystals in addition to the broad bands of the nanocrystalline titania. Only a small feature (*) at about 22.38° could not be indexed.

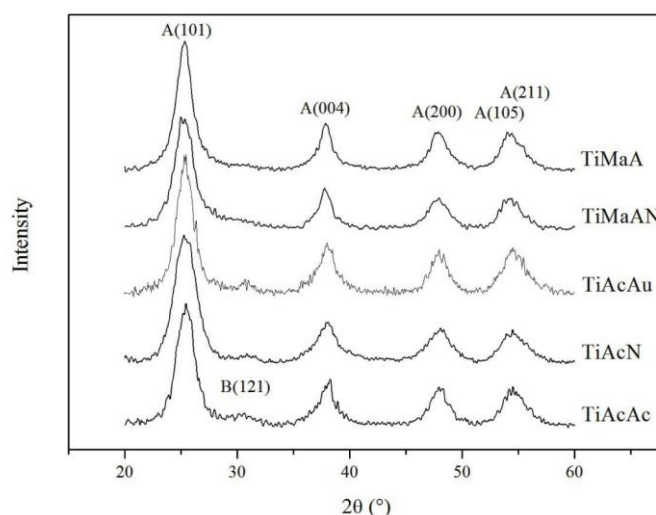


Fig. C.2 - XRD patterns of the nanocrystalline titania powders obtained from the nanosols: A and B indicate anatase and brookite reflections, respectively.

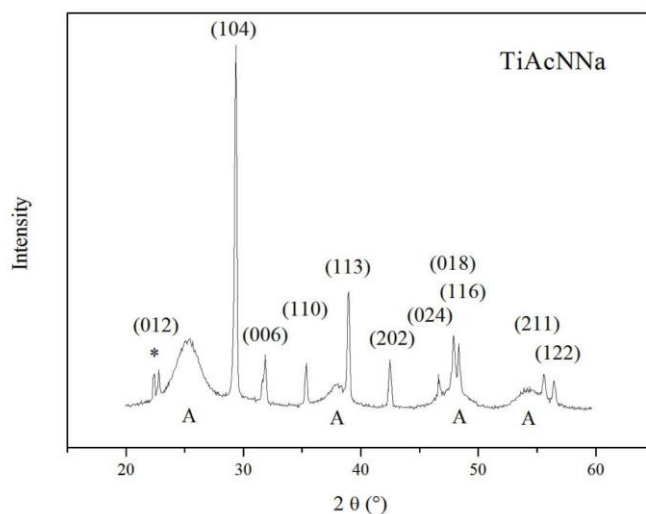
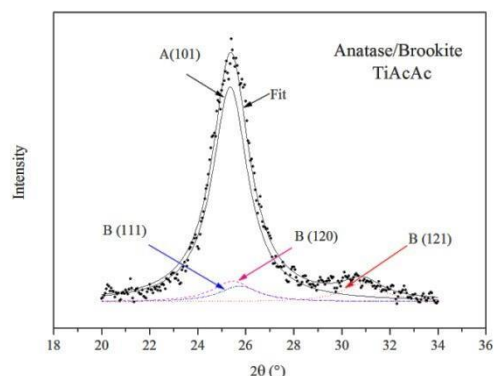
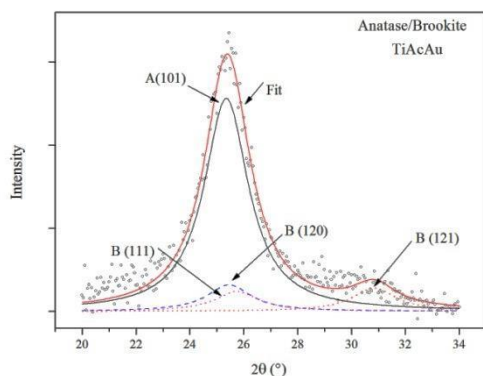


Fig. C.3 - XRD pattern of the TiAcNNa powder showing the NaNO_3 reflections. The small feature (*) at about 22.38° could not be indexed.

The weight ratio between anatase and brookite phases was calculated by the method proposed by Zhang and Banfield [C100]. The weight fraction of brookite (W_B) can be estimated from:

$$W_B = \frac{k_B A_B}{(k_A A_A + k_B A_B)} \quad (\text{C8})$$

where A_B and A_A are the integrated intensities of the brookite (121) peak and of the anatase (101) peak, respectively, and $k_A = 0.884$ and $k_B = 2.721$ are coefficients determined by calibration [C100]. The integrated intensity of the anatase (101) peak was evaluated by Lorentzian de-convolution to take into account the contribution of brookite. In the fitting procedure, (see Fig. C.4a-d) it is assumed that the brookite (120), (111), and (121) peaks have the same FWHM, while their intensities were fixed by the ratios 100/80/90, respectively (JCPDS card no. 29-1360). The weight percentage of brookite phase results ~ 15 -18 % for TiAcAc, ~ 7 -10 % for TiAcN, ~ 5 -7 % for TiAcAu, whereas for TiMaA and TiMaAN may be estimated to be less than 4 %. The brookite content in TiAcNNa cannot be determined with enough accuracy.



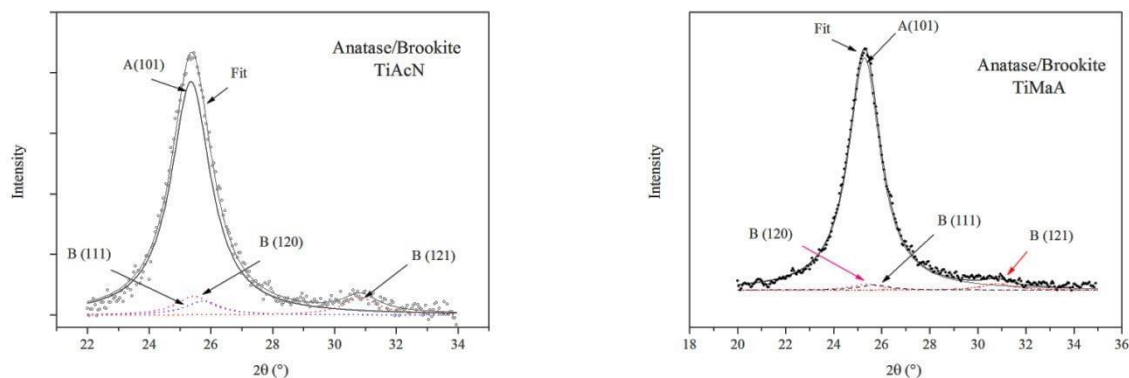


Fig. C.4 - Fit of the main anatase and brookite diffraction peaks to determine the brookite content.

The crystallite size of TiO_2 particles was determined from the line broadening of the main diffraction peak ((101) at $2\theta = 25.28^\circ$ for anatase and (121) at 30.81° for brookite) using Scherrer equation $D = k\lambda/\beta\cos\theta$ where D is the average crystal diameter (nm), k is the shape factor (usually taken = 0.89 for spherical particles), λ the X-ray wavelength (Cu-K α $\lambda=0.15406$ nm), β is the full width at half-maximum (FWHM) intensity (in radians) of the main diffraction peak and θ is the Bragg diffraction angle (radians). The parameter β is defined as $\beta = (B^2 - b^2)^{1/2}$, where B and b are the linewidths of the main TiO_2 reflections ((101) for anatase, (121) for brookite) and the (111) line of the silicon standard, respectively.

The crystallites size of anatase particles may be estimated for all compositions as essentially constant in the 4-6 nm range, slightly larger (> 6 nm) for TiMaA. The XRD data were also analysed using the Material Analysis Using Diffraction (MAUD) software package [C101] to work out quantitative crystallographic and microstructural information through a Rietveld code, exploiting the entire diffraction pattern for quantitative phase analysis and line profile analysis.

The percentages of phases and the TiO_2 crystallite size for anatase and brookite are summarised in Table C.3.

Table C.3 - Proportion ($\pm 5\%$) of anatase and brookite and crystallite sizes (± 0.5 nm) in TiO_2 powders from the sols.

Sample	Anatase	Brookite
TiAcAc	85% (6 nm)	15% (6 nm)
TiAcAu	90% (4 nm)	10% (10 nm)
TiAcN	90% (5 nm)	10% (10 nm)
TiMaA	95% (7 nm)	5% (6 nm)
TiAcNNa	nd	nd
TiMaAN	95% (6 nm)	5% (6 nm)

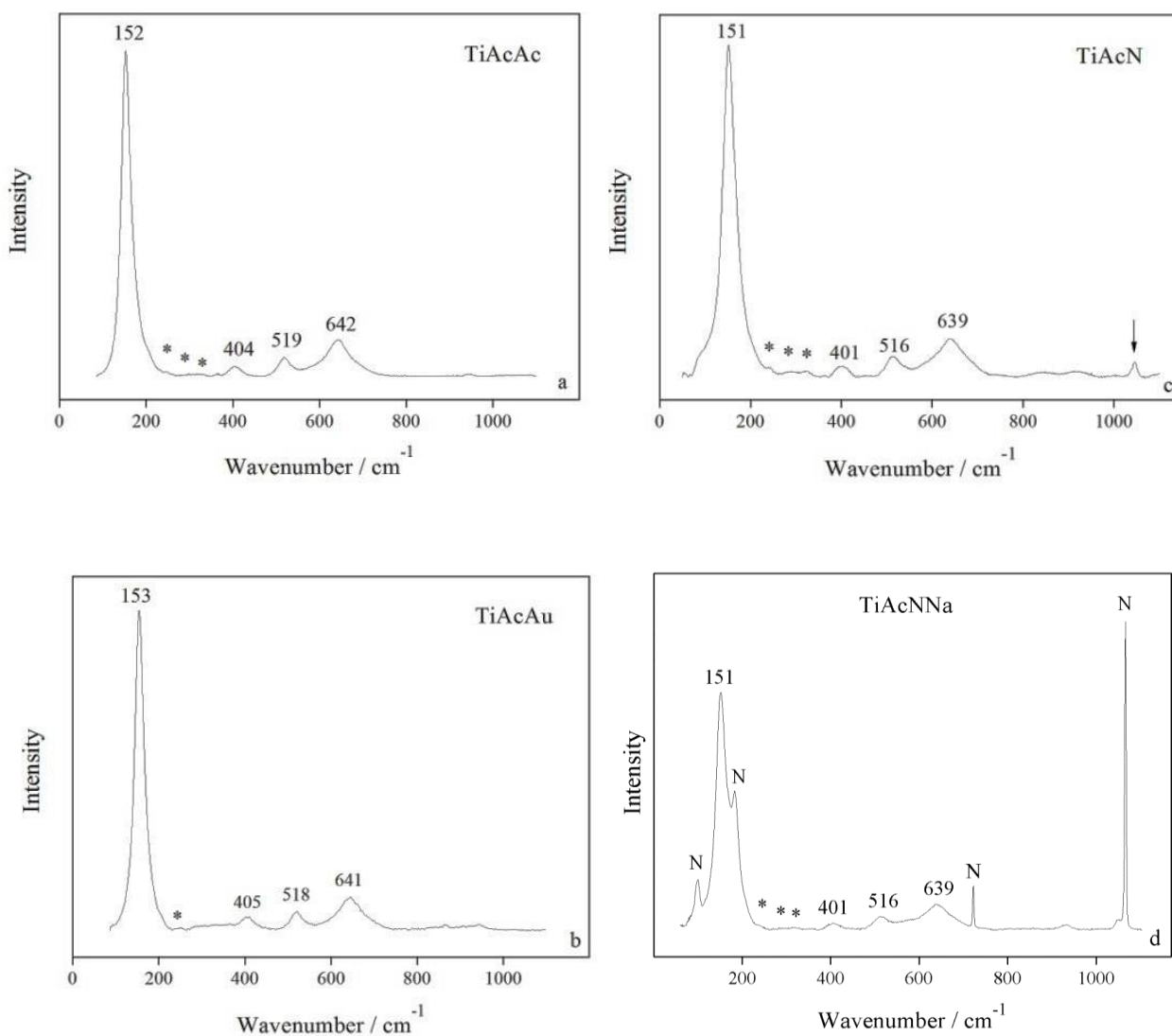
C. 3.1.3 - μ -Raman

The Raman spectra of the same TiO_2 nanopowders studied by XRD (see above) are shown in Fig. C.5 a-f. The features at about 150 cm^{-1} ($E_{g(1)}$ symmetry), 196 cm^{-1} ($E_{g(2)}$), 403 cm^{-1} ($B_{1g(1)}$), 516 cm^{-1} ($A_{1g} + B_{1g(2)}$) and 643 cm^{-1} ($E_{g(3)}$) can be assigned to the Raman active modes of the anatase crystal

[C102]. Although anatase nanoparticles are the predominant species, brookite phase is observed, as already seen in the XRD pattern. Asterisks in Fig. C.5 indicate the Raman features due to brookite: the strongest peak of brookite at about 153 cm^{-1} superimposes to the anatase main peak, contributing to its broadening (FWHM). The most intense anatase mode, as the particle size decreases, shows increasing broadening and frequency blue-shift with respect to bulk crystalline anatase [C103]. An increased broadening with decreasing crystallite size is clearly seen for all vibrational modes [C104-107].

The position of $E_{g(1)}$ Raman peak, with respect to crystalline anatase, is shifted from 144 cm^{-1} to about $151\text{-}154\text{ cm}^{-1}$ and its width (FWHM) is more than doubled (from 12 cm^{-1} to $\approx 24\text{ - }27\text{ cm}^{-1}$), for all the nanopowders investigated.

The broadening and the shift of the main peak are also partly due to the brookite content ($\sim 4\text{ - }20\%$ as suggested by XRD analysis). In any case, the frequency shift observed and the FWHM of the most intense peak is compatible [C102] with anatase nanocrystals of $\sim 5\text{-}8\text{ nm}$ size, as determined by XRD. It is not possible to extract precise information on the size of the brookite nano-crystals from the collected Raman data.



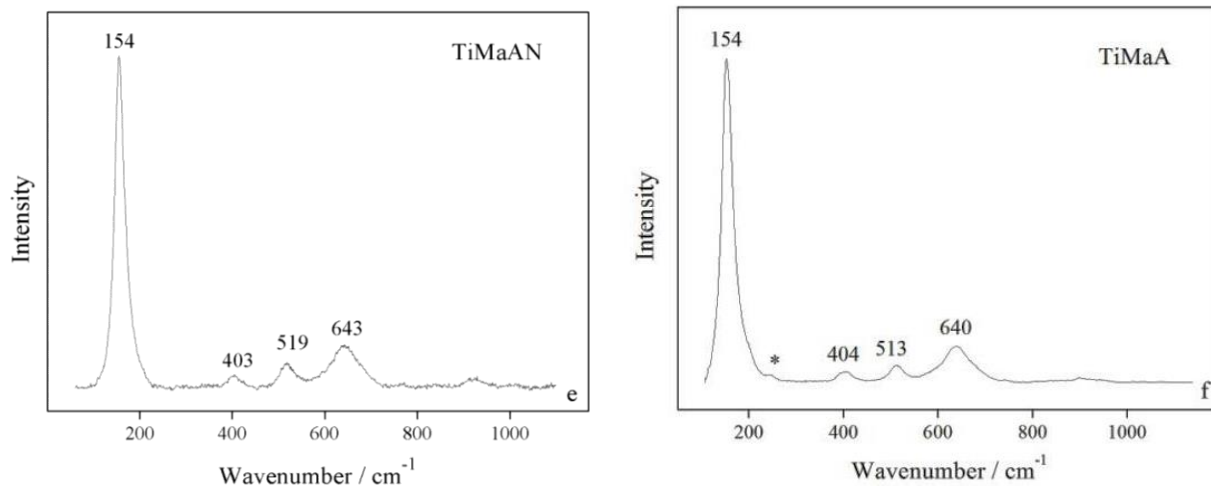


Fig. C.5 - Raman spectra of TiO_2 powders: the wavenumbers of the anatase peaks are indicated. Asterisks indicate some brookite features. In spectrum of TiAcNNa , the peaks of “nitratine” are indicated by N.

C. 3.1.4 - TEM

The structural properties of TiAcAu , TiAcN and TiMaA particles have also been investigated by TEM techniques. The intensity profiles of the electron diffraction pattern agree with those determined by XRD. The TiO_2 nanocrystals present mainly anatase phase, with a small amount of brookite. Their size is of the order of ≈ 5 nm. The TiO_2 particles tend to cluster in agglomerates.

In Fig. C.6a, a typical High Resolution TEM image of the TiAcN nanoparticles is reported. In Fig. C.6b, the Fourier Transform (FT) of a), reproduces all the spatial frequencies, corresponding to the direct lattice periodicities present in a). While the reflection A stays on the ring corresponding to the lattice periodicity 0.35 nm that is common to both phases (101 reflection of anatase or 120 reflection of brookite), the one marked as (B) is peculiar to brookite and corresponds to the 121 lattice spacing, equal to 0.29 nm.

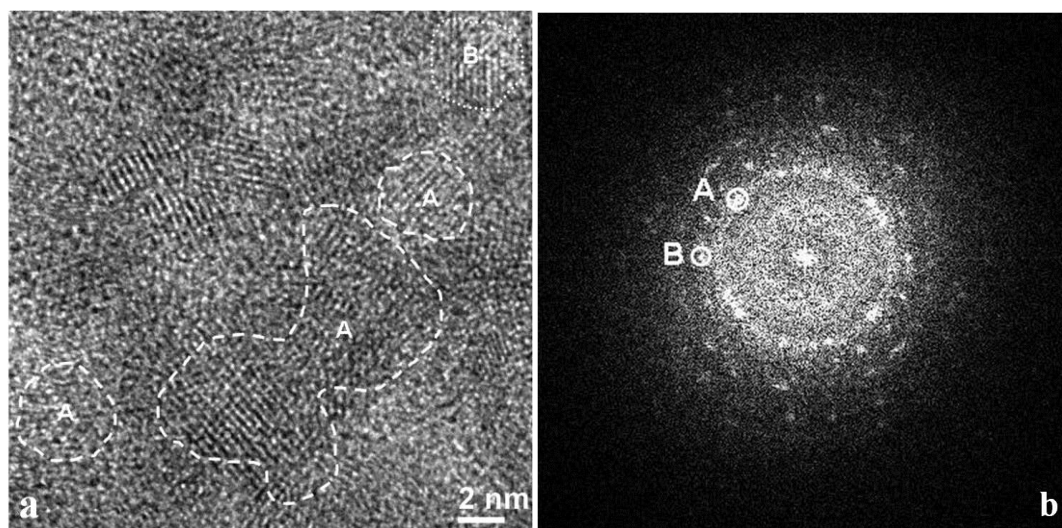


Fig. C.6 - a) HRTEM image of TiAcN ; b) Fourier Transform of a): the reflections named A and B are originated from the regions in a) marked with the same letter.

By selecting one reflection at a time in the FT, and making the inverse FT procedure, it is possible to localize which area in the real space (on a picture) originated which reflection in the reciprocal space (on the FT). An example of such inverse transformation is shown superimposed on Fig. C.6a, where the regions responsible of the reflection (A) are marked as dashed contour areas, whereas a single brookite particle is identified in the region B with dotted contour.

A typical TEM image for TiMaA is shown in Fig. C.7a with the diffraction pattern taken from the same zone reported as inset. The rings correspond to the d-spacing of the anatase crystal structure only, so that the presence of the brookite phase can be ruled out, in the limits of the resolution of the technique. Although the particles have been dispersed on the grids with the same procedure for all the samples, here the agglomerate is less dense and there are regions where single crystalline defect free particles can easily be distinguished, as in Fig C.7b. The average particle size measured by electron diffraction is ~ 6 nm, slightly larger than in the case of TiAcN, in agreement with the XRD findings.

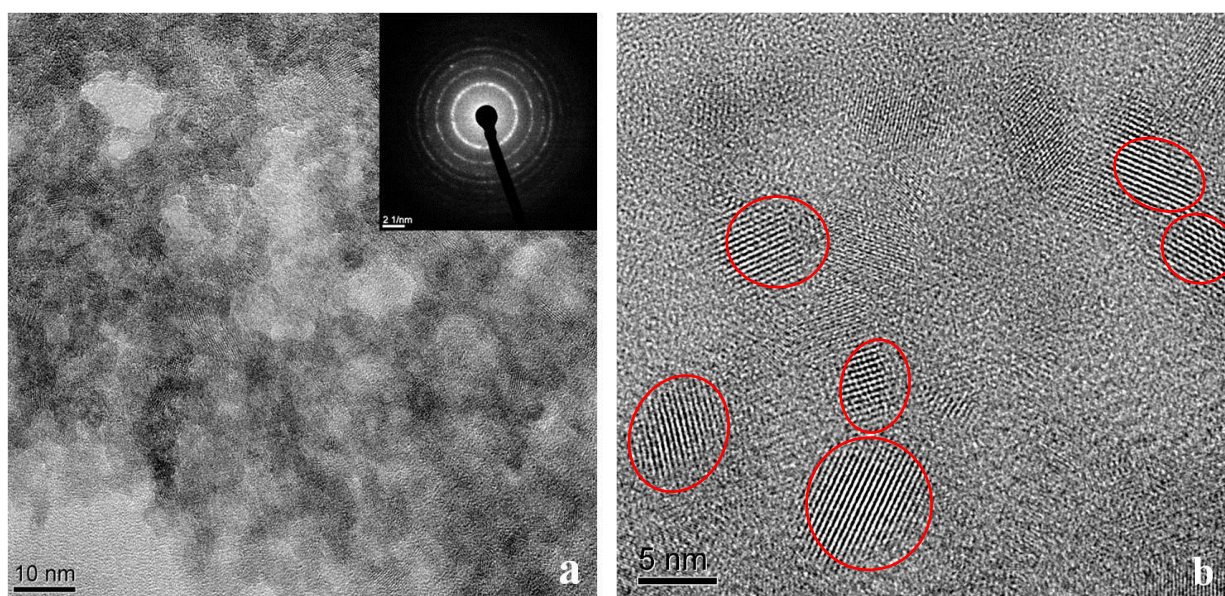


Fig. C.7 - a) Bright field zero-loss TEM typical image of the TiMaA sample with the diffraction pattern taken from the same region as inset; b) HRTEM image where isolated anatase titania particles are clearly identified.

TEM images (HAADF - STEM mode) of the TiAcAu powder (Fig. C.8a) reveal the presence of gold nanoparticles, with sizes of the order of tenths of nanometers. The Au particles appear very bright on a background formed by irregular agglomeration of TiO_2 particles. The TEM image of an Au particle, taken in conventional bright field mode, is reported in Fig. C.8b.

Electron diffraction allows to determine the crystal structure of the TiO_2 particles in TiAcAu. A typical ring diffraction pattern from TiO_2 originated by a $100 \times 100 \text{ nm}^2$ region is shown in Fig. C.9a. The intensity profile of the pattern, averaged over 360° angle, is reported in Fig. C.9b. All the peaks correspond to the TiO_2 anatase phase, except a small contribution positioned at about 3.5 nm^{-1} that can be attributed to the brookite phase. An average crystallite size for the predominant anatase phase of about 4.5 nm can be estimated by the ring thickness analysis. These data are in agreement with those found by XRD and Raman measurements.

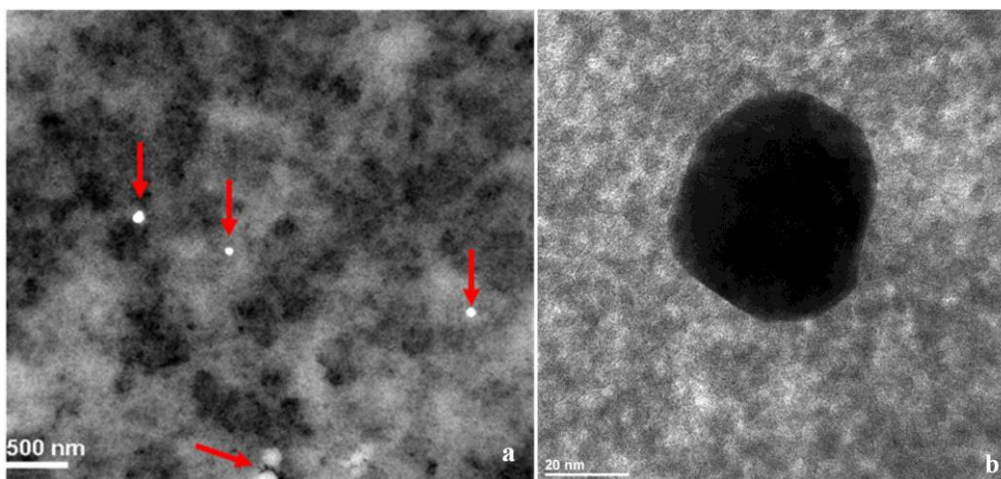


Fig. C.8 - (a) Large area HAADF - STEM image (essentially Z-contrast) of TiAcAu powder. Gold particles are visible over agglomeration of TiO₂ nanoparticles. (b) TEM image in bright field mode of an Au particle in TiAcAu, revealing the very fine grain of TiO₂ particles on the background.

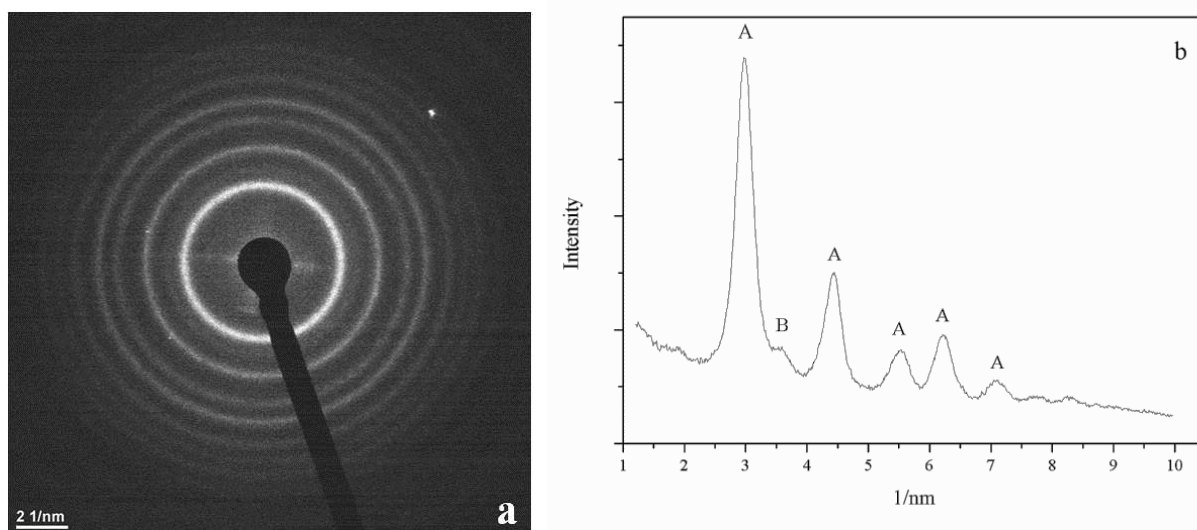


Fig. C.9 - (a) Ring diffraction pattern from TiO₂ nanoparticles in a 100x100 nm² region in TiAcAu. (b) Intensity profile of the diffraction pattern. The crystalline phase is anatase (A). The feature (B) at about 3.5 nm⁻¹ is due to brookite.

C. 3.1.5 - DLS - ELS

The results of the Electrophoretic Light Scattering (ELS) measurements, in terms of zeta potential, carried out on the sols, are summarized in Table C.4. The zeta potential of TiAcAc sol (pH = 3.1) is 51 mV, indicating a good stability of the sol. The size analysis of the particles (consisting of nanocrystalline domains of a few nanometres as revealed by XRD and Raman analyses) showed a bimodal distribution: though the average hydrodynamic diameter is 1521 nm, both small (peaked at 200 nm) and large (peaked at 3400 nm) particles are present. The status of TiAcAc sol changes dramatically, when modifying its pH by adding acid or base: agglomeration of the particles is

affected by surface charge. In TiAcN sol, obtained from TiAcAc with nitric acid, the pH and zeta potential decreased to 1.3 and 31 mV, respectively, approaching the stability limit. In this sol, the average hydrodynamic diameter of the particles was peaked at 52 nm (Fig. C.10), suggesting a negligible agglomeration of the particles. The surface charge of the particles of TiAcN sol was measured varying the pH from 1.3 to 6 (Fig. C.10). The IEP was found at pH ~ 6, in agreement with the values reported in literature [C108-109]. Given that the particle surface charge at IEP is nearly zero, the attractive van der Waals forces dominate and significant agglomeration takes place and large flocs are observed.

TiAcNNa sol, formed by adding a base, shows a bit increase of pH from 3.1 to 4.1, and 22 mV of zeta potential. Actually, this modification is not sufficient to turn away the sol from the instability limit and an average hydrodynamic diameter of 8834 nm is determined by the size analysis. This accounts for the formation of a white precipitate observed after the addition of the base. Thus, acetic acid demonstrated to be not a suitable complexing agent under the conditions of sol preparation. For this reason malonic acid was chosen as ligand, in 1/1 molar ratio respect to the titanium isopropoxide, instead of acetic acid and a sol (TiMaA) was formulated. In order to study the effects on particles aggregation of TiMaA sol, its pH was varied adding nitric acid. The resulting sol, TiMaAN, was *unstable*. Hence, the zeta potential was difficult to determine, because particles agglomeration occurred during the measurement, the equilibrium was hardly attained and a bit of white precipitate formed. Nevertheless a value of 16 mV, consistent with the observed instability and the diameter of particles peaked between 2000 and 3000 nm, was finally measured. However, TiMaA appears the most interesting sol because, with a zeta potential of -26 mV and pH of 10.6, it is *stable*. Moreover, the particles size distribution in Fig. C.10 indicates a nearly monodisperse sol with a hydrodynamic average diameter of 24 nm. This interesting result can be explained with the high pH and the adsorption of hydroxyls groups on the titania particles. The negatively charged particles repel each other and their initial size stabilizes. The measurement of IEP of TiMaA sol, varying the pH from 10.6 to 6, was also carried out (Fig. C.11). It is worth noting that, decreasing pH, the zeta potential becomes even more negative until pH=6, when IEP is attained. The unevenness of the curve in Fig. C.11 was due to the change of surface charges after the acid addition.

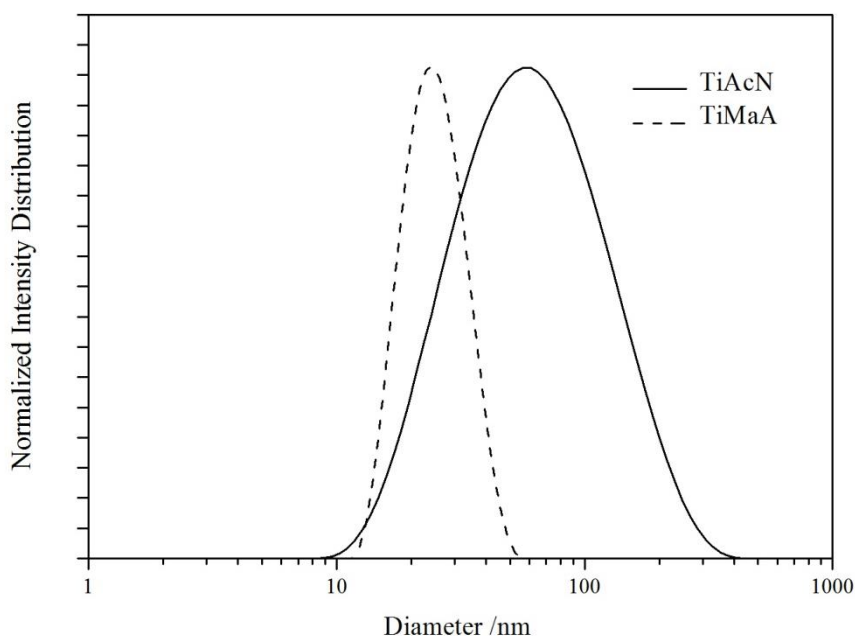


Fig. C.10 - Particle size distribution for TiAcN (full line) and TiMaA (dashed line) sols.

Table C.4 - pH and Zeta potential of the nano-sols.

Sol	pH	Zeta potential [mV]
TiAcAc	3.1	51
TiAcN	1.3	31
TiAcNNa	4.1	22
TiMaN	1.4	16
TiMaA	10.6	-26

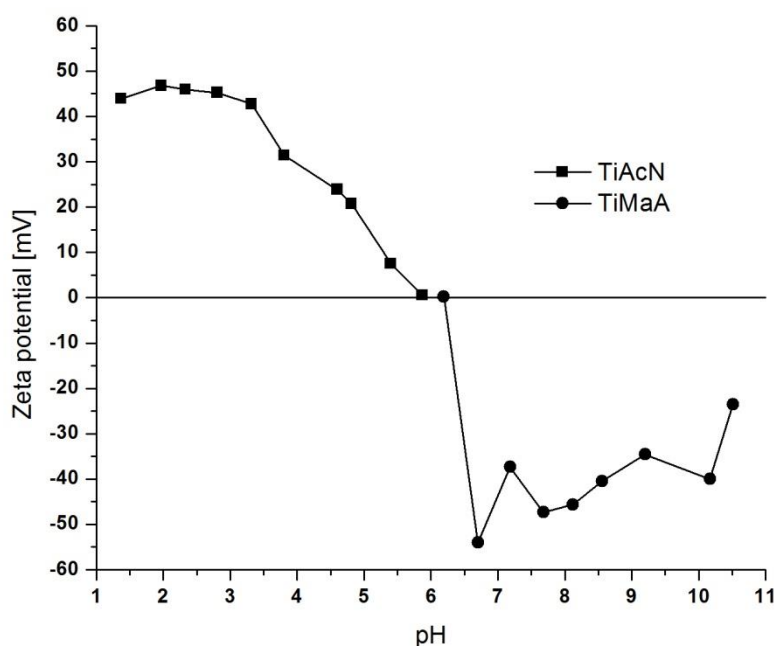


Fig. C.11 - Influence of pH on the zeta potential for the TiAcN and TiMaA sols.

C. 3.1.6 - Photocatalytic activity of the sols

The stability of the MeO and MB dyes in aqueous solutions, under UV irradiation, was tested in absence of the titania sols. The absorbance (A_t) of the main absorption peak of dye solution was taken as a measure of residual dye concentration (C_t) at a given time t after UV irradiation. The decrease of the peak intensity of the MeO and MB dyes under UV light due to the photocatalytic activity of the TiAcAc, TiAcN and TiMaA sols is illustrated in Fig. C.12 and C.13, respectively. UV absorbance measurements for the *unstable* sols TiMaAN and TiAcNNa gave unreliable results owing to their intrinsic instability and the corresponding curves are not reported.

Fig. C.12a-c clearly evidence that TiAcAc, TiAcN and TiMaA titania sols possess good photo-activity against MeO under UV irradiation, the time degradation of the dye ranging from 40 min (TiAcN) to 3 h (TiMaA).

As anticipated in the Experimental section, for MeO a large shift in the absorption maximum from 462 nm to 508 nm is observed, corresponding to different pH values (10.6 for TiMaA and 1.3 for TiAcN) [C87-89].

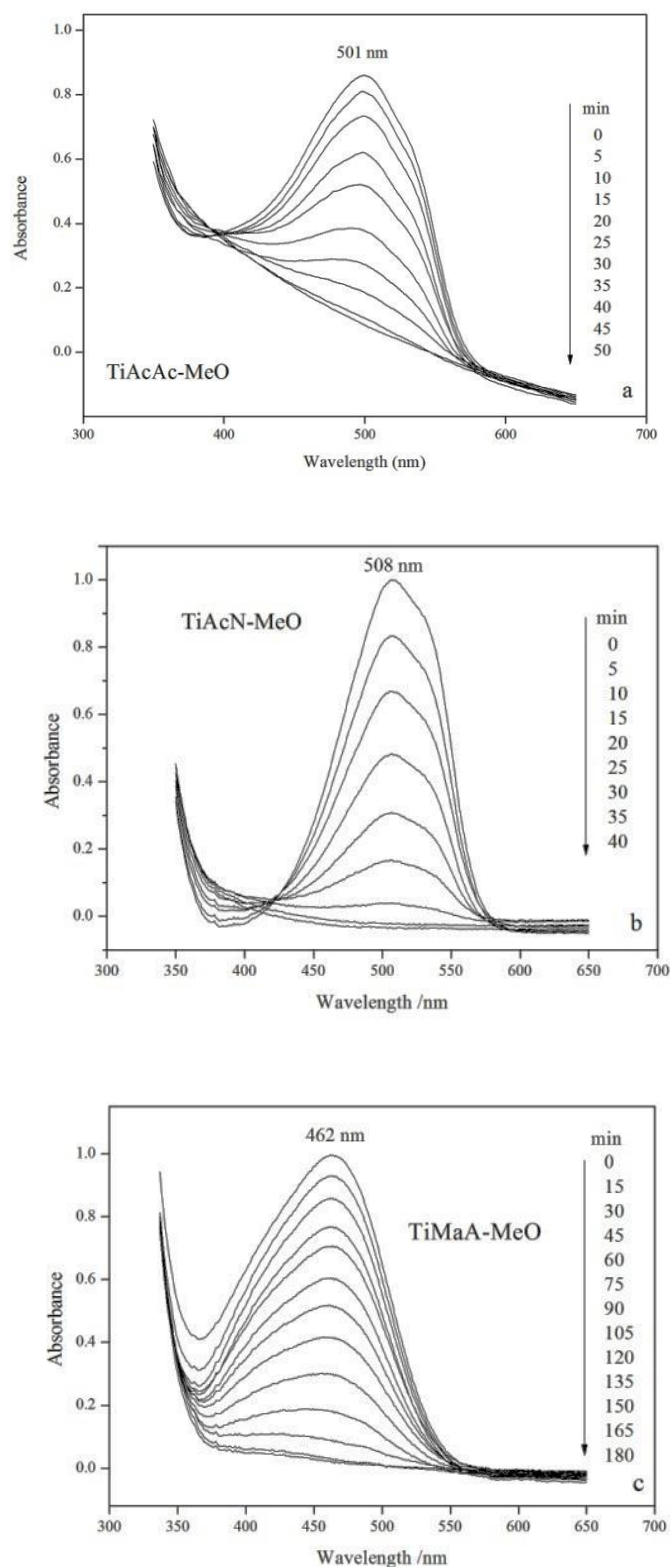


Fig. C.12 - Methyl orange photo-catalytic degradation measured by the decrease of the dye absorbance at different UV irradiation time.

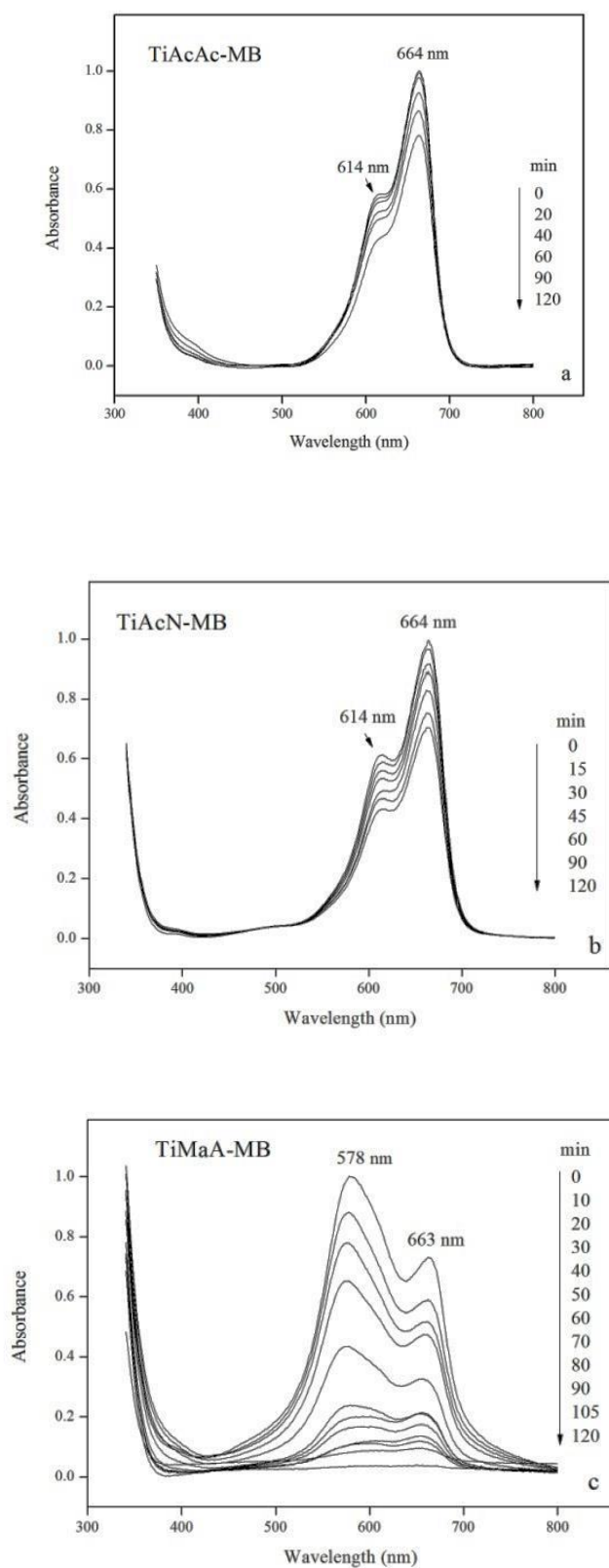


Fig. C.13 - Methylene blue photo-catalytic degradation measured by the decrease of the dye absorbance at different UV irradiation time.

As concerns MB dye (Fig. C.13a-c), the TiAcAc and TiAcN sols, after 2 hours of UV irradiation, give degradation values of only 20% and 30%, respectively. On the other hand, TiMaA sol for the same irradiation time gives complete degradation of the dye.

One expects [C110] that the predominant species at the titania surface are Ti-OH_2^+ and Ti-O^- at low pH (TiAcAc and TiAcN) and at high pH (TiMaA), respectively. Therefore, cationic dyes like MB are readily adsorbed on TiO_2 in alkaline sols and these accounts for the strong photoactivity of the basic sol TiMaA. This fact explains the poor photocatalytic performance for MB of TiAcAc, TiAcN acid sols. On the other hand, anionic dyes, like MeO, are expected to be effectively adsorbed on TiO_2 in strongly acid sols and actually TiAcAc, TiAcN show very good photocatalytic performances towards MeO. Nevertheless, the TiMaA basic sol appears rather effective also for the degradation of the anionic dye MeO, although the process is significantly slower. This suggests that the degradation of MeO could occurs in solution, where, as reported by Kodom et al. [C87], the photooxidation of OH^- , present at high concentration, produces hydroxyls radicals by holes formed on the TiO_2 nanoparticles.

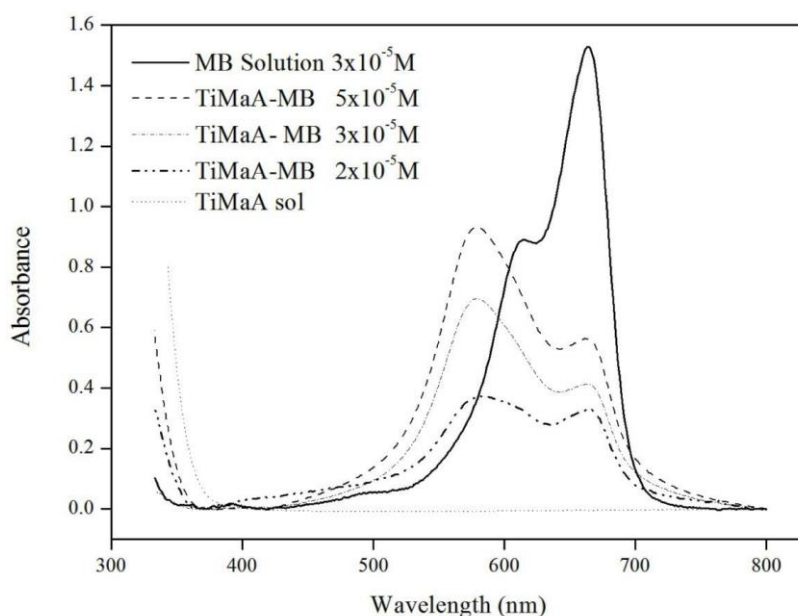


Fig. C.14 - UV/Vis absorption spectra of: MB water solution ($3 \times 10^{-5} \text{ M}$), TiMaA sols with different concentrations of MB (MB/TiMaA) and pure TiMaA sol ($9.22 \times 10^{-3} \text{ M}$).

From Fig. C.13c it is apparent that, when MB is dissolved in the basic TiMaA sol, the intensities of the visible-light absorption peaks before irradiation, are different from those observed in water (Fig. C.14) or in the acid sols TiAcAc and TiAcN (Fig. C.13a,b). In fact, Fig. C.14 shows that the absorption spectrum of MB in water solution exhibits a maximum at 663 nm (due the MB monomer in water) and a shoulder at 610 nm due to the so called H-dimer of MB, which results from the aggregation of the dye molecules in a parallel way (plane-to-plane stacking) forming a sandwich-type arrangement [C111]. Fig. C.14 also shows that, in the MB/TiMaA sols, the absorption band at 663 nm decreases and that a strong band at about 570 nm increases by increasing MB concentration. This band has been associated with the formation of trimeric aggregates [C110, C112-114].

It is known that ionic dyes like MB tend to aggregate in water, leading to dimer and higher order “polymers”, which are mainly observed in concentrated solutions and show different absorption characteristics [C115-118]. In the concentration ranges commonly used for MB (10^{-3} to 10^{-6} M), mainly monomer-dimer equilibrium exists (10^{-5} M in Fig. C.14) and there is no evidence for trimerization. In agreement with the results of Liu et al. [C112], we assume therefore that TiO_2 nanoparticles of the TiMaA sol can provide a suitable surface for the formation of MB dimers and trimers, the oligomerization process occurring very rapidly when TiMaA sols is added to the MB solutions.

Fig. C.15 reports the photo-degradation rate of the MeO and MB dyes, obtained by the spectral data of Fig. C.12 and C.13 and displayed by the ratio $A_t/A_0 = C_t/C_0$, A_0 and C_0 being respectively the initial absorbance value at the absorption maximum and the initial dye concentrations (mg/l).

The degradation kinetics may be fitted with specific models. The most referred model for surface catalyzed reactions is the Langmuir-Hinshelwood mechanism [C119] in which the degradation rate R (mg/l min) of the dye, neglecting the concentration of the $\bullet\text{OH}$ radicals involved in the photocatalytic oxidation, is given by:

$$R = -dC/dt = k_I KC / (1 + KC) \quad (\text{C9})$$

where C is its concentration at time t , t the irradiation time, k_I is the reaction rate constant (mg/l min) and K is the adsorption equilibrium constant (l/mg).

When the product $KC \ll 1$, the rate equation may be approximated by a *pseudo* (or apparent) first-order equation, with rate constant $k = k_I K$ (min^{-1}), leading to the exponential solution $C = C_0 \exp(-kt)$, where C_0 is the initial concentration of the dye. In the opposite limit $KC \gg 1$ the reaction kinetics is of zero-order with reaction rate constant k_1 , leading to $C_t = C_0 - k_1 t$ or, equivalently to

$$C_t = C_0(1 - k_0 t) \quad (\text{C10})$$

where $C_0 k_0 = k_1$ and k_0 , a zeroth order rate constant, is expressed in min^{-1} . This behavior is reported, even if much less frequently than a pseudo-first order behavior, in a number of instances in the organic dye photocatalysis literature [C120-121].

The curves reported in Fig. C.15 suggest a zero-order kinetics behavior for the degradation. The straight-line interpolation to the data gives the set of k_0 values in min^{-1} reported in Table C.5. It is interesting to note that, in the case of MB/TiMaA, there is a significant decreasing of the kinetic constant after 40 min, when the MB concentration is reduced to about 20 %. This could be simply due to the reduction of active sites of the TiO_2 surface. However, the simultaneous modification of the absorption spectrum of MB, with an apparent lowering of the trimer/monomer peaks ratio, could suggest a dependence of the reaction rate on the degree of oligomerization on the TiO_2 surface.

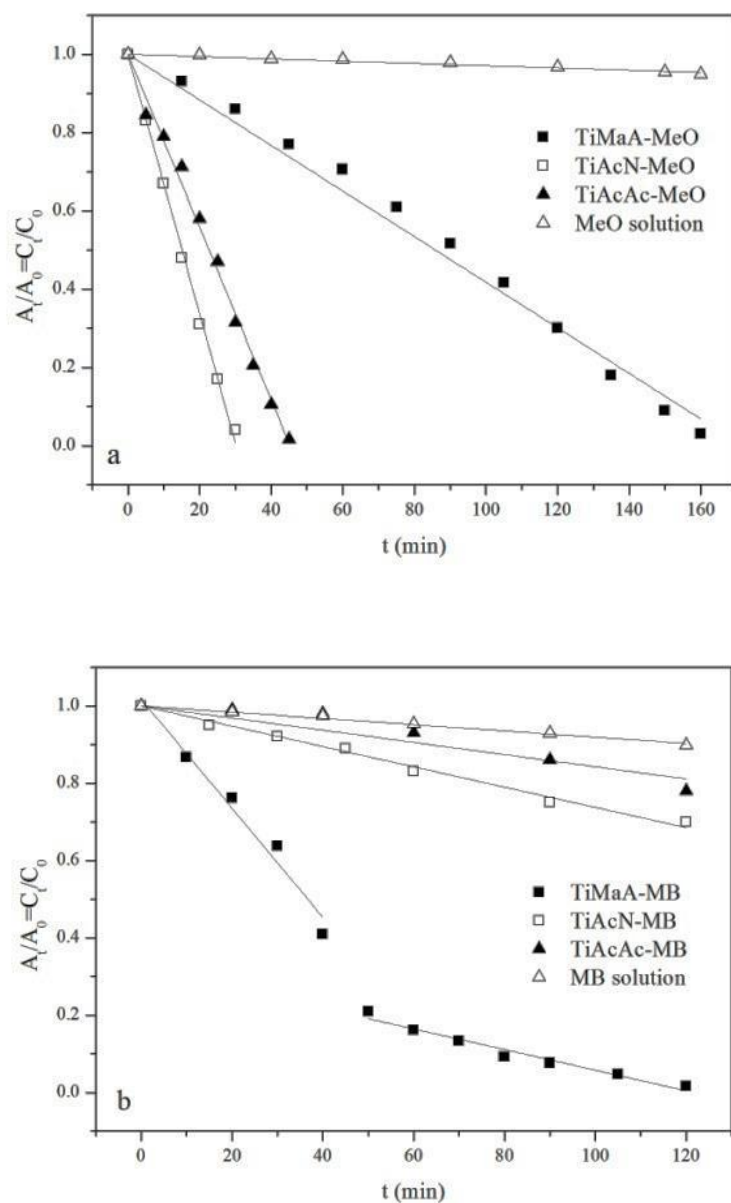


Fig. C.15 - Photodegradation rate under UV irradiation:
a) MeO and b) MB without and with TiAcAc, TiAcN and TiMaA catalysts.

Table C.5 - Zeroth-order rate constant k_0 (min^{-1}) for the photodegradation of the sols, from the linear fits to the curves in Fig. C.15.

	TiAcAc	TiAcN	TiMaA	Water
MeO	2.2×10^{-2}	3.3×10^{-2}	5.8×10^{-3}	2.9×10^{-4}
MB	1.6×10^{-3}	2.6×10^{-3}	$1.4 \times 10^{-2} / 2.7 \times 10^{-3}$	8.1×10^{-4}

C. 3.2 - Coatings applied to the calcarenite stones

C. 3.2.1 Modica and Comiso stones (Pietra di Modico e Pietra di Comiso)

A self-cleaning photocatalytic coating for limestone materials, based on TiO₂ nanoparticles obtained by the sol-gel process has been studied. TiO₂ sol was applied directly to the surface or after a SiO₂ intermediate layer. The selected test materials are the Modica and the Comiso calcarenites, limestones of Ragusa Formation outcropping in the South Eastern Sicily (Italy). SEM-EDS, XRD and Raman investigations were carried out to characterize the TiO₂ coating. To evaluate the harmlessness of the treatment, colorimetric tests, water absorption by capillarity and crystallization of salts measurements were performed. Photocatalytic activity of the TiO₂ of the coatings (TiO₂ and SiO₂/TiO₂) was assessed under UV irradiation through methyl orange dye degradation tests.

C. 3.2.1.1 - Stone treatments

The TiO₂ sol (0.1 M), called TiAcN, was prepared *via sol-gel*, by hydrolysis of titanium isopropoxide in acidic ambient, using nitric acid as peptizer. The synthesis was described in experimental section 2.1.1.

The TiAcN sol was applied by brushing directly on the *Comiso* and *Modica* stones (henceforth TiO₂ coating) and on stones treated with a preliminary sol-gel SiO₂ based coating (henceforth SiO₂/TiO₂ coating).

Three samples for each stone and for each treatment were prepared for the subsequent analyses. The tests were performed also after a pre-treatment with SiO₂ of the stone surface.

The amount of titania applied was 0.32±0.05 mg/cm² for *Modica* stone and 0.25±0.05 mg/cm² for *Comiso* stone.

C. 3.2.1.2 - Petrographic analysis

The *Modica* and *Comiso* stone samples are characterised by white-cream and white-greyish colour, respectively, show low porosity, good compactness and hardness. They have a carbonatic composition and are mainly made of calcite.

Petrographic analysis showed the peculiar structure and texture of *Modica* and *Comiso* calcarenites. The *Comiso* stone presents abundant foraminifera and calcareous algae as the prevalent allochems (35 %) embedded in sparitic matrix (45 %) (Fig. C.16a). The porosity is intergranular. The *Modica* Stone is formed by fine grained allochems (40 %) mainly made by fragments of echinoderms, peloids, foraminifera, scaphopoda worms and shellfish. Orthochems (25 %) are micrite and microsparite (Fig. C.16b). The porosity is mainly intergranular or, subordinately, due to fossil moulds. The silicoclastic fraction is composed by rare quartz grains.

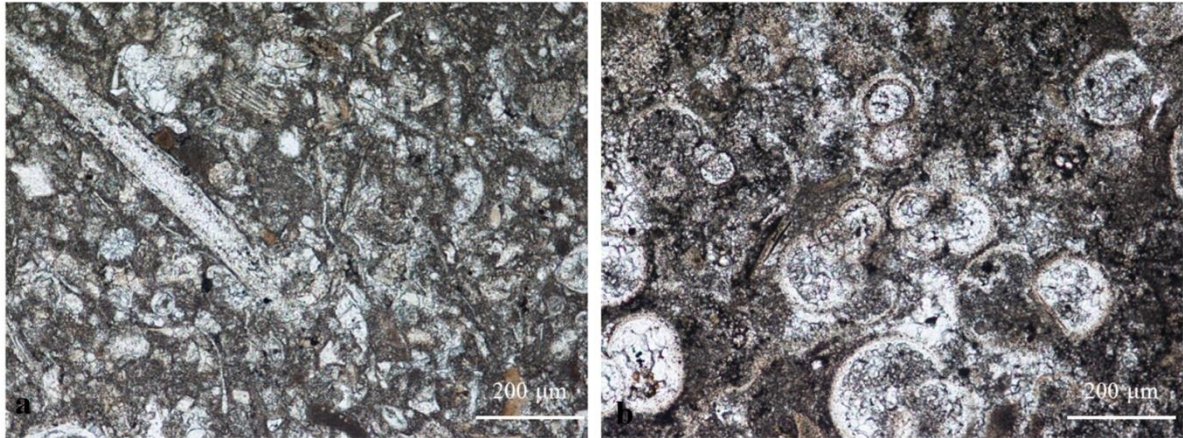
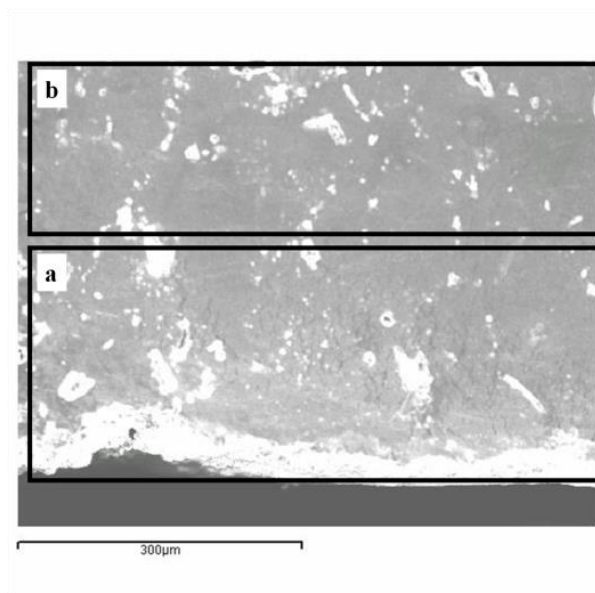


Fig. C.16 - Polarizing optical microscope images of thin sections of *Comiso* (a) and *Modica* (b) stones.

Considering the textural features, the *Comiso* and the *Modica* stones can be classified grainstone and packstone, respectively [C122]. Both rocks may be classified as calcisiltites (limestone consisting predominantly of detrital silt-size, 0.062 to 0.002 mm, grains [C123]). The porous structure was determined by means of mercury intrusion porosimetry. The *Modica* and *Comiso* limestones are characterised by low porosity (24.2% and 22.9% respectively) with comparable average pore radius (0.226 μm and 0.210 μm , respectively).

C. 3.2.1.3 - SEM-EDS

The SEM-EDS results enabled to determine the penetration depth of the TiO_2 and SiO_2 coatings. Some SEM images and EDS spectra on coated samples are reported in Figs. C.17, C.18 and C.19. In the untreated *Comiso* and *Modica* stone, the average atomic content of silicon $\text{Si}/(\text{Ca}+\text{Si})$ is about 3%. The SiO_2 pre-treatment increases the Si content within the *Comiso* stone: the ratio $\text{Si}/(\text{Ca}+\text{Si})$ changes from about 10% within 250 μm from the surface to 6% at 250-450 μm depth (Fig.C.17). For the *Modica* stone the ratio $\text{Si}/(\text{Ca}+\text{Si})$ is $\approx 6\%$ at the surface ($<200 \mu\text{m}$) and $\approx 3\%$ at 400-600 μm depth.



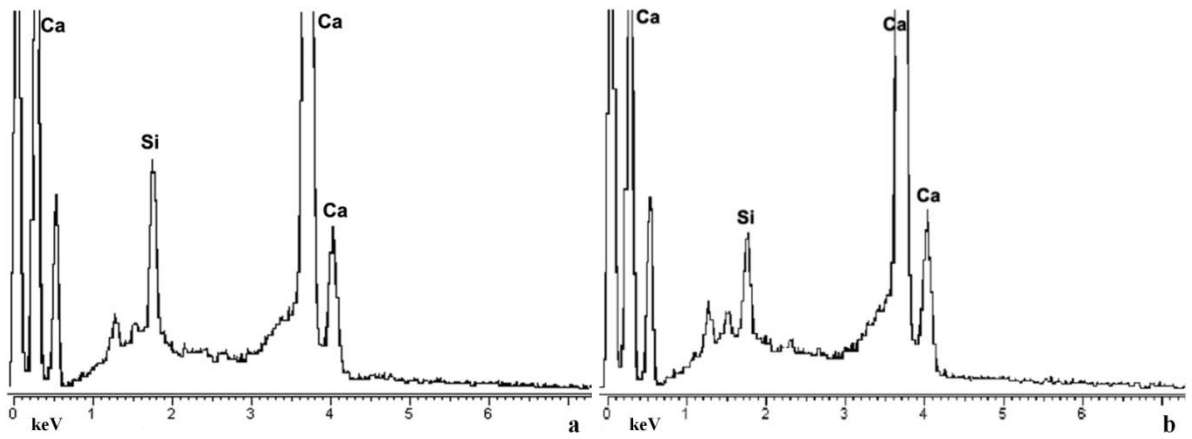
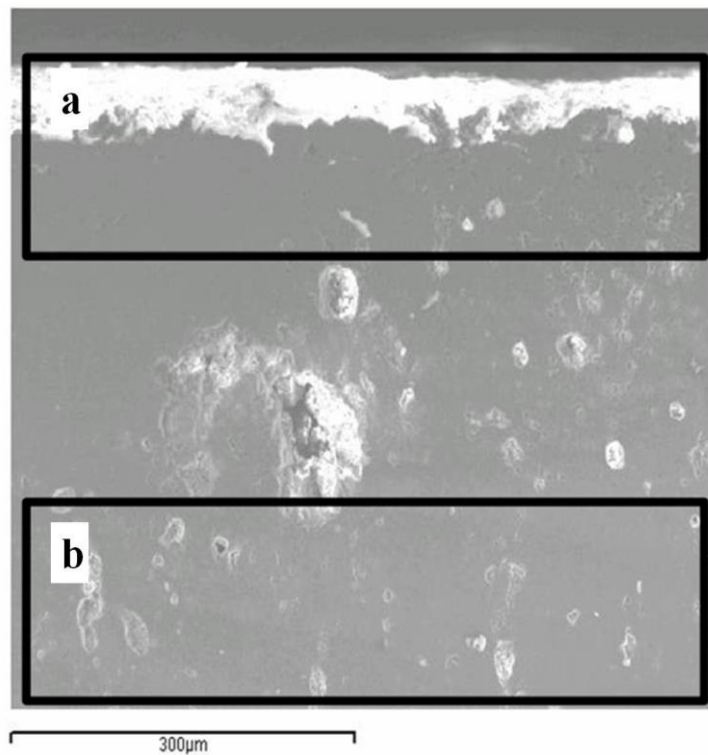


Fig. C.17 - SiO_2 pretreated Comiso stone: the EDS spectra refers to the a and b areas indicated on the SEM image.

The TiO_2 coating TiAcN on the *Comiso* stone without any SiO_2 pre-treatment gives an average relative percentage $\text{Ti}/(\text{Ca}+\text{Ti}) \approx 0.4\%$ on the sample surface (within $150 \mu\text{m}$ depth) and $\approx 0.1\%$ at $350\text{-}500 \mu\text{m}$ depth. For the *Modica* stone the TiO_2 coating gives $\text{Ti}/(\text{Ca}+\text{Ti}) \approx 0.5\%$ on the surface (within $150 \mu\text{m}$ depth) and $\approx 0.3\%$ at $350\text{-}500 \mu\text{m}$ depth (Fig. C.18).



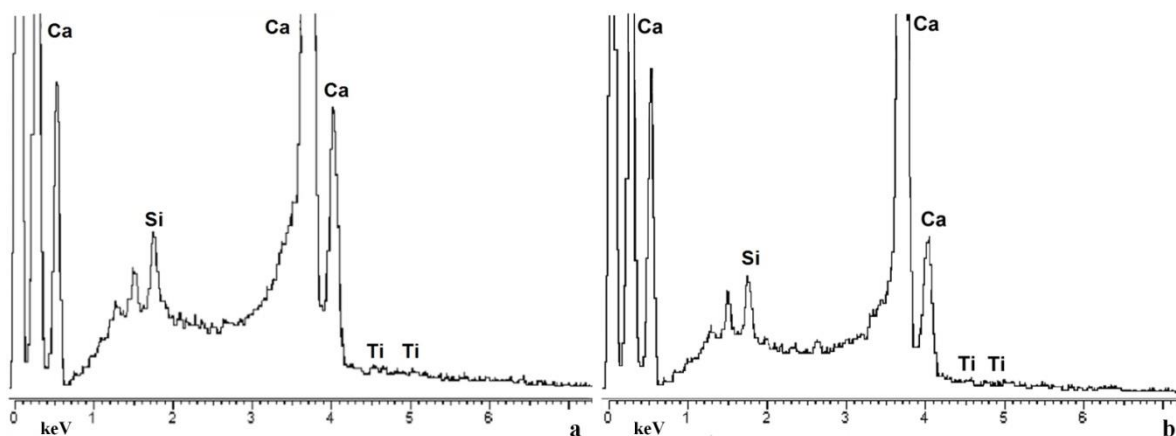


Fig. C.18 - TiO_2 (TiAcN) coated Modica stone: a low amount of Ti is visible down to 500 μm . The EDS spectra refers to the areas a (left) and b (right) indicated on the SEM image.

On the other hand, both for *Comiso* and *Modica* stone, the $\text{SiO}_2/\text{TiO}_2$ treatment gives Ti only on the surface of the samples, with relative percentage $\text{Ti}/(\text{Ti}+\text{Ca}) \approx 0.4\%$. No titanium is found at depth $> 0.150 \mu\text{m}$. In Fig. C.19 is reported the EDS spectrum for the *Comiso* stone. The pre-treatment with SiO_2 coating seems therefore to be effective in keeping the TiO_2 on the surface.

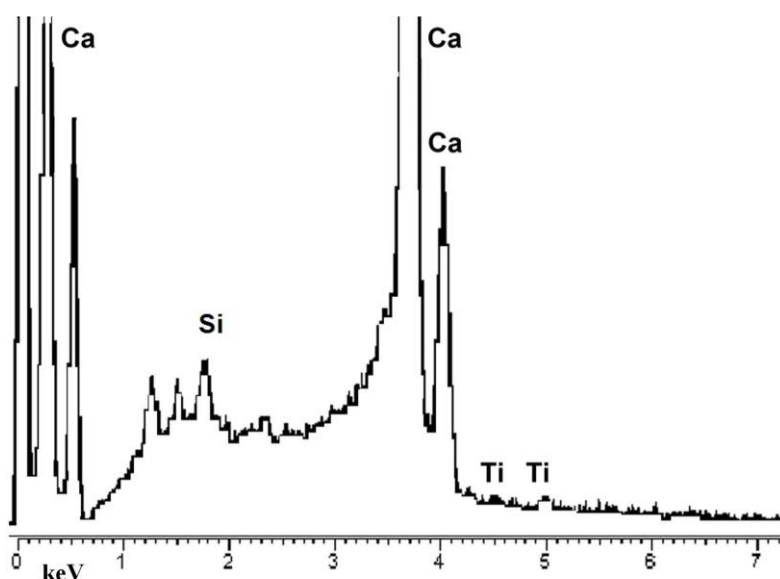


Fig. C.19 - $\text{SiO}_2/\text{TiO}_2$ pretreated *Comiso* stone. The EDS spectrum was taken from the surface of the sample. The Ti features are indicated.

C. 3.2.1.4 - μ -Raman

Micro-Raman spectra taken on the stones after the TiO_2 (TiAcN) coating (Fig. C.20) give, in addition to the calcite peaks at 1086, 712 and at 282 cm^{-1} from the bulk limestone, the anatase features observed in the powder and some residual brookite contribution. Some differences in the

position of the minor bands are known to depend also on the local temperature induced by the laser beam [C124]. The Raman signal of titania coating is more easily observed for samples with SiO_2 pre-coating. Raman maps (spatial distribution of anatase determined by the intensity of the main Raman peak) show generally an inhomogeneous distribution of nano- TiO_2 , as expected from a coating made by free nano-crystallites that can aggregate after solvent evaporation. An example of a Raman map is reported in Fig. C.21 for a *Modica* sample.

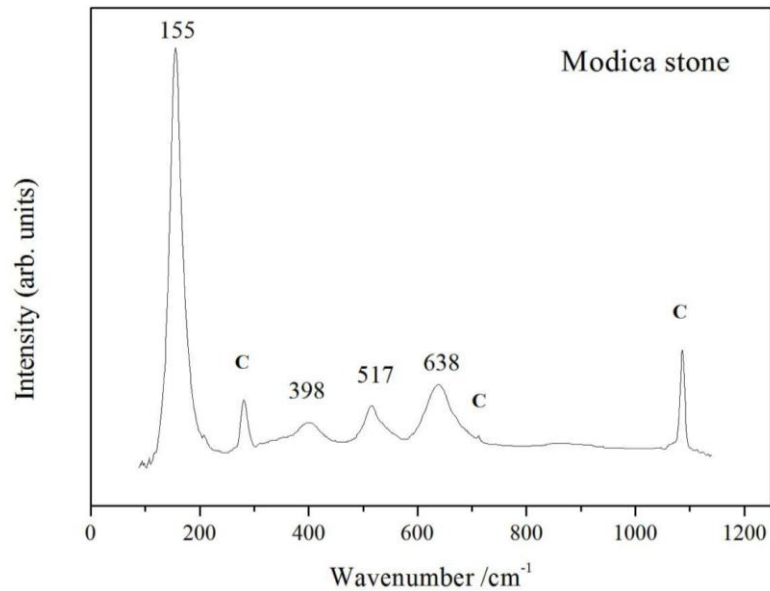


Fig. C.20 - Raman spectrum on *Modica* stone treated with $\text{SiO}_2/\text{TiO}_2$. C=calcite from the bulk limestone. SiO_2 does not give an observable spectrum.

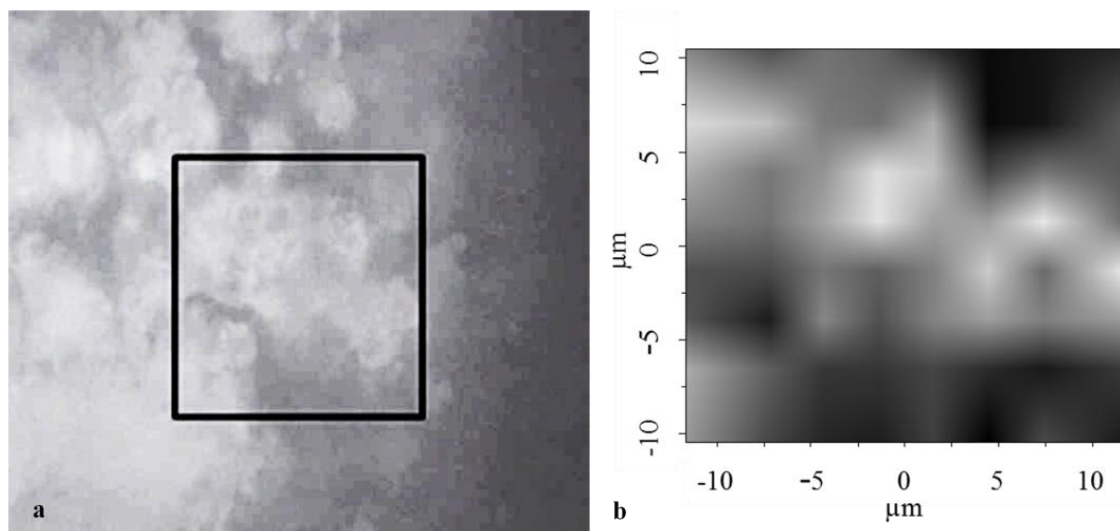


Fig. C.21 - Microscopic image (a) and Raman map (b), on the area indicated, of the distribution of anatase/brookite nanocrystals obtained through the (smoothed) intensity map of the blue-shifted main anatase/brookite Raman peak at $\sim 15 \text{ cm}^{-1}$. The map has been acquired with 100x magnification on an 8×8 array.

C. 3.2.1.5 - Colour changes

After the application of the coatings, the treated stone surfaces appeared slightly darker for all samples. The L*, a*, b* color coordinates measured in the TiO₂ and SiO₂/TiO₂ coated *Comiso* and *Modica* stones samples with respect to the uncoated ones are shown in Table C.6. A small decrease in the values L* and an increase in b* occurs but the values of overall color difference ΔE are acceptable (2.9 < ΔE < 4.8) after the application of both TiO₂ and SiO₂/TiO₂.

Table C.6 - Colorimetric data (mean values) of the *Modica* and *Comiso* stone samples before and after the application of the TiO₂ TiAcN coatings.

<i>Modica</i>				<i>Comiso</i>			
Uncoated				Uncoated			
L*	a*	b*		L*	a*	b*	
84.86	0.76	6.41		83.54	0.72	5.84	
TiO ₂ coated				TiO ₂ coated			
L*	a*	b*	ΔE	L*	a*	b*	ΔE
80.17	1.35	7.13	4.78	80.15	1.29	6.8	3.57
SiO ₂ /TiO ₂ coated				SiO ₂ /TiO ₂ coated			
L*	a*	b*	ΔE	L*	a*	b*	ΔE
81.07	0.8	7.40	3.92	81.96	1.22	8.26	2.93

C. 3.2.1.6 - Photocatalytic activity

To test the photocatalytic activity of the TiO₂ coating on *Comiso* and *Modica* stones, coated and untreated samples were stained with MeO and placed under UV lamp at 15 cm. Three different concentrations of the MeO dye (0.1, 0.01, 0.001 M) were employed. The normalized colorimetric changes measured by changes in the chroma, as defined in Eq. 5, are reported for 0.001 M and 0.1 M as a function of the irradiation time in Fig. C.22a, b and for 0.1 M in Figs. C.23a,b, respectively. The coated samples show in general a good degradation of the dye under UV irradiation, faster than for uncoated ones, both for *Comiso* and *Modica* stones. The photocatalytic activity of the titania particles produces most of the total degradation effect on the stain in the first few hours of exposure. As a major result, the presence of the silica interlayer seems to have little or no influence on the results.

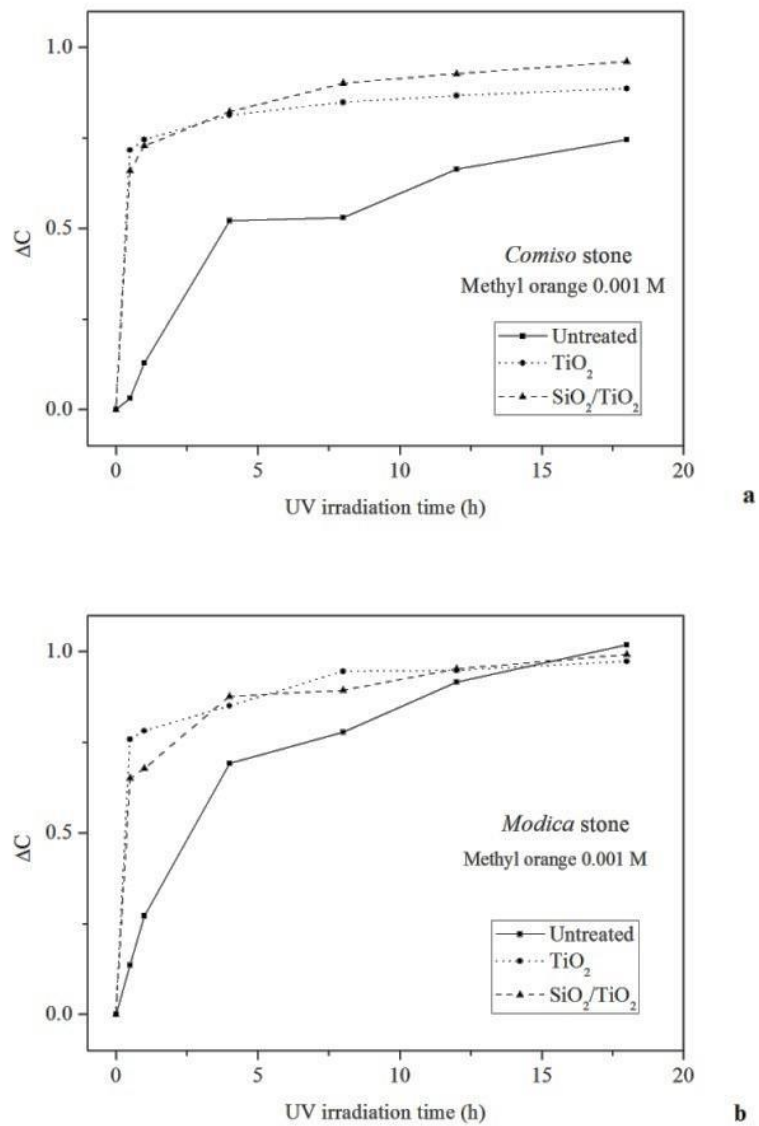


Fig. C.22 - Normalized chromatic changes ΔC (chroma) of the MeO stained (0.001 M) Comiso (a) and Modica (b) stone samples, as a function of the irradiation time with the UV source. The comparison between untreated and SiO₂/TiO₂ or TiO₂ coated surfaces is reported.

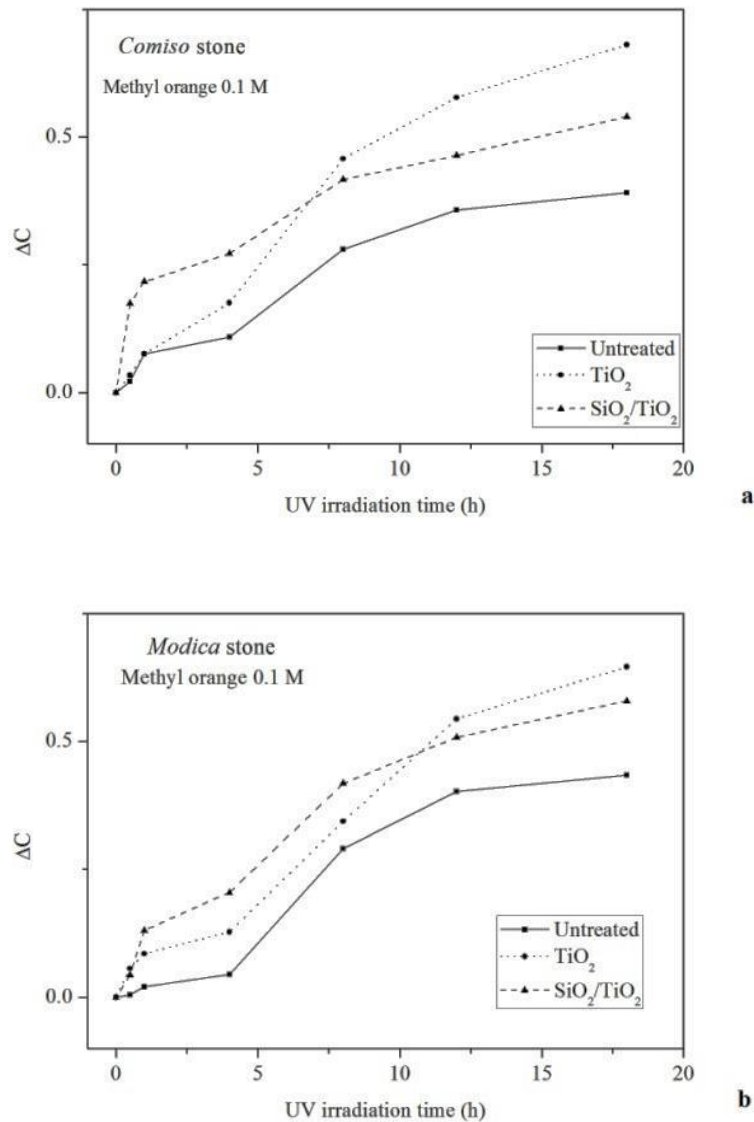


Fig. C.23 - Normalized chromatic changes ΔC (chroma) of the MeO stained (0.1 M) Comiso (a) and Modica (b) stone samples, as a function of the irradiation time with the UV source. The comparison between untreated and $\text{SiO}_2/\text{TiO}_2$ or TiO_2 coated surfaces is reported.

C. 3.2.1.7 -Water absorption by capillarity

To evaluate the effects of the coating on the behaviour of the stones against water, comparative measurements of water absorption by capillarity were carried out on untreated samples and on TiO_2 and $\text{SiO}_2/\text{TiO}_2$ coated samples. In Fig. C.24 the curves of the capillarity absorption (Q_i) are plotted as a function of the square root of time (in seconds). The average of measurements on three samples for each case is reported. The absorption coefficient AC, evaluated as the slope of the fitted line (correlation not lower than 0.95) to the Q_i curve vs. $t^{1/2}$ in the 0-1 h interval, is reported in Table C.7. In the case of *Modica* stone, the treated samples show capillarity absorption curves nearly indistinguishable with respect to the untreated stones. For *Comiso* samples, the $\text{SiO}_2/\text{TiO}_2$ coating

gives for all times higher absorption values, whereas for the TiO₂ coating the capillarity absorption is slightly lower only at low times (t < 1 day). In any case, the difference is barely larger than the expected error. The non-homogeneity of the samples and the different porosity of the two stone species could cause these differences.

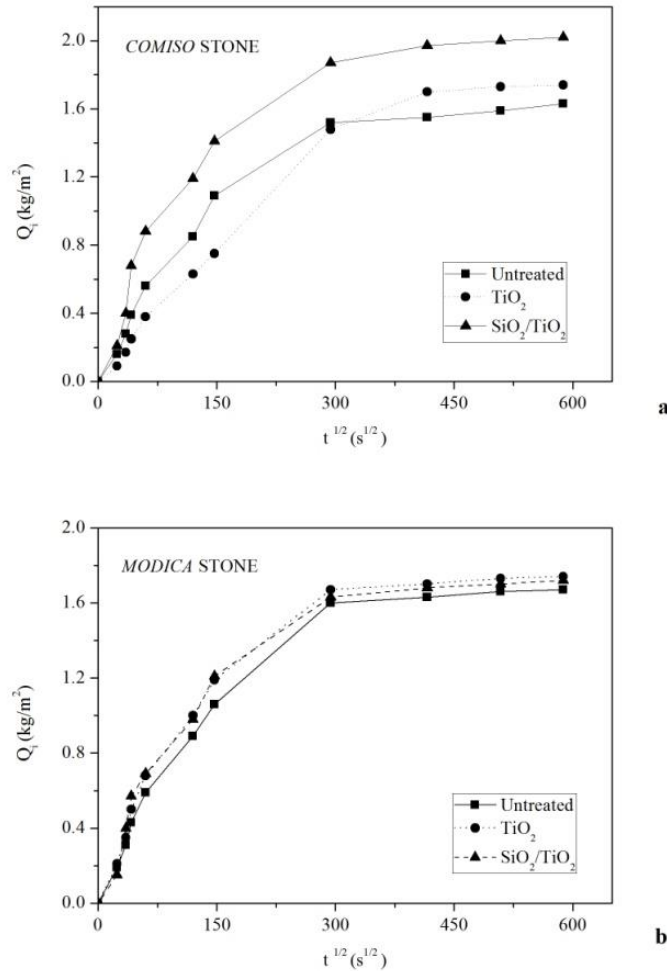


Fig. C.24 - Capillarity water absorption curves (in kg/m²) of Comiso and Modica stone samples before and after the application of TiO₂ and SiO₂/TiO₂ coatings.

Table C.7 reports also the values (± 6 %) of the relative capillarity index (RCI). The RCI values, i.e. the amounts of water absorbed during 96 h by the samples relative to the untreated ones, confirm that for Comiso stones the SiO₂/TiO₂ coating gives slightly higher absorption.

Table C.7 - Water absorption coefficient (AC) in kg/(m²s^{1/2}) by capillarity, estimated in the first hour and relative capillarity index (RCI) on the whole duration of the test.

	MODICA STONE			COMISO STONE		
	Untreated	TiO ₂ (TiAcN)	SiO ₂ /TiO ₂	Untreated	TiO ₂ (TiAcN)	SiO ₂ /TiO ₂
AC 0-1 h	0.01	0.01	0.01	0.009	0.006	0.014
RCI 0-96 h	1	1.06	1.05	1	0.97	1.28

C. 3.2.1.8 - Salt crystallization test

Salt crystallization accelerated laboratory tests were performed to evaluate the effects of the TiO₂ coatings on one of the most important degradation processes. The percentage of mass variation after each crystallization cycle is shown in Fig. C.25: the average values calculated on six untreated and on four TiO₂ and four SiO₂/TiO₂ treated samples are reported.

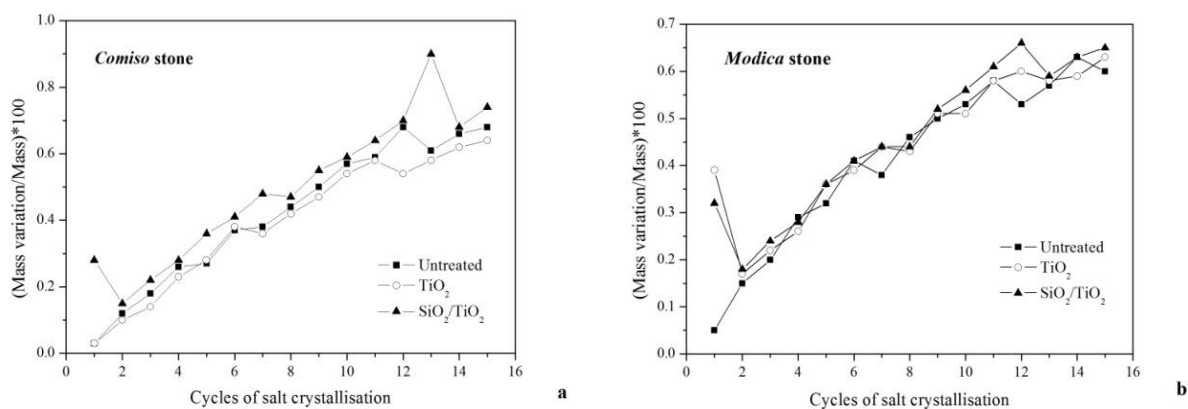


Fig. C.25 - Percentage mass difference during the 15 crystallization cycles of Comiso (a) and Modica (b) stones.

The tests carried out on untreated samples evidenced a constant mass increase: the porous structure of the rocks stores the salts also after washing in deionized water. For both the stone species, the mass variation curves of the coated samples are very close to that of the untreated samples. We notice that the mass increases in the first cycle in the treated *Modica* samples and in the SiO₂/TiO₂ treated *Comiso* samples. This result mimics what found for capillarity absorption, where both coatings show a similar behavior in the *Modica* stone, whereas the TiO₂ coating in the *Comiso* stone induces a lower absorption

C. 3.2.2 - Lecce stone (Pietra di Lecce)

Self-cleaning photocatalytic coatings for biocalcarene stones, based on TiO₂ nanoparticles obtained by sol-gel processes at different pH and adding gold particles, have been investigated. The selected test material is a biocalcarene named "*pietra di Lecce*" (*Lecce stone*), outcropping in South of Italy. SEM-EDS, TEM, XRD and Raman investigations were carried out to characterize the TiO₂ coatings. Photocatalytic activity of the coatings on "*pietra di Lecce*" was assessed under UV irradiation, monitoring the methyl orange dye degradation as a function of time. To evaluate the harmlessness of the treatment, colorimetric tests and water absorption by capillarity were performed.

C. 3.2.2.1 - Stone treatment

The TiO₂ based coatings, prepared at different pH, were tested on limestone "*Pietra di Lecce*".

The sols henceforth called TiAcAc, TiAcN, TiAcNa were all obtained starting from the same TiO₂ sol (0.1M) by a solution of titanium isopropoxide Ti{OCH(CH₃)₂}₄ and acetic acid mixed with distilled water, as described in the experimental section 2.1.

In addition, a test has been made on the sol called TiAcAu, in which Au particles (formed *in situ*) were added to evaluate possible increase of the photocatalytic activity by noble metals doping, through an increase of the electron-hole recombination time.

The sols were applied on stone samples with bristle brush. The amount of sol applied was therefore determined by the difference of the dry weight after and before the treatment. Typical amounts of titania for three applications were 0.8 ±0.1 mg/cm² (TiAcAc, TiAcN), 1.0 ±0.1 mg/cm² (TiAcNa), 1.2 ±0.1 mg/cm² (TiAcAu).

C. 3.2.2.2 - Petrographic analysis

Petrographic analysis shows that "*pietra di Lecce*" has a carbonatic composition, mainly composed of micritic fraction, mixed with fine clay minerals and poor cryptocrystalline calcitic cement. It contains fine microfossil fragments, grains of glauconite, sporadic quartz grains and phosphatic nodules (Fig. C.26). *Pietra di Lecce* has about 80% calcium carbonate and the insoluble residue is essentially made of clay minerals and glauconite: it may be classified as biomicrite (Folk 1962). The total open porosity is generally around 40%, with pore radius mainly between 4 and 0.5 microns [C82].

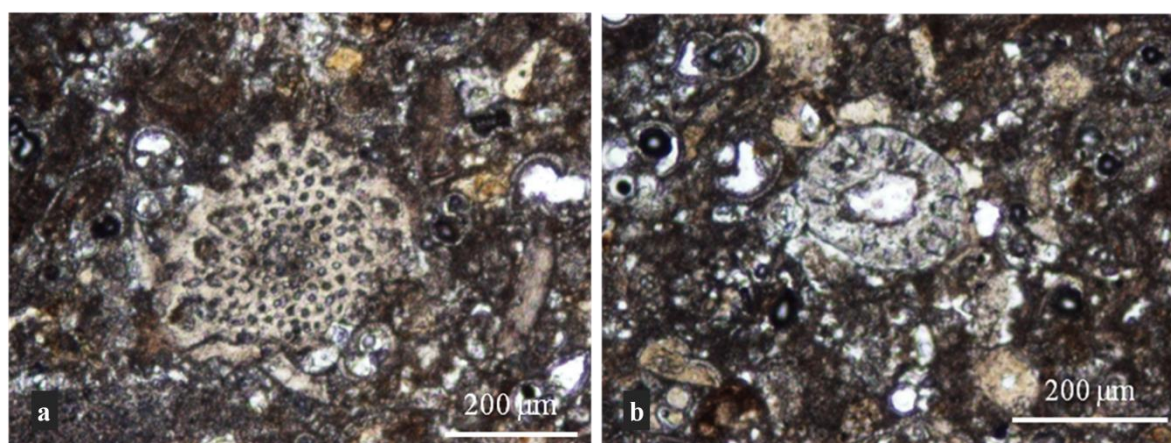


Fig. C.26 - Polarizing optical microscope images of thin sections of "*pietra di Lecce*". The characteristic fossils of Lecce stone, planctonic foraminifera (*Globigerinoides sp* and *Globorotalia sp*) and calcareous nanofossils, are detectable.

C. 3.2.2.3 - Electron microscopy and EDS

The morphology of the coatings has been investigated by ESEM images. TiAcAc, TiAcN and TiAcNa coatings give similar results: we report in Fig. C.27 the case of TiAcN for five applications. The coating on the surface of the stone is inhomogeneous and largely cracked (Fig. C.27a). Rounded cavities are observed: radial micro-cracks starting from these cavities are often observed leading to a peculiar "flower" morphology (Fig. C.27b).

The coating obtained by the TiAcAu nanosol is thick and discontinuous, with an extended network of large microcracks (Fig. C.28a), but no cavities were observed.

EDS microanalysis shows in all cases lower Ti/Ca ratio within the crack space with respect to the amount detected on the continuous surface area of the coating (Figs. C.27 c,d and Figs. C.28 b,c).

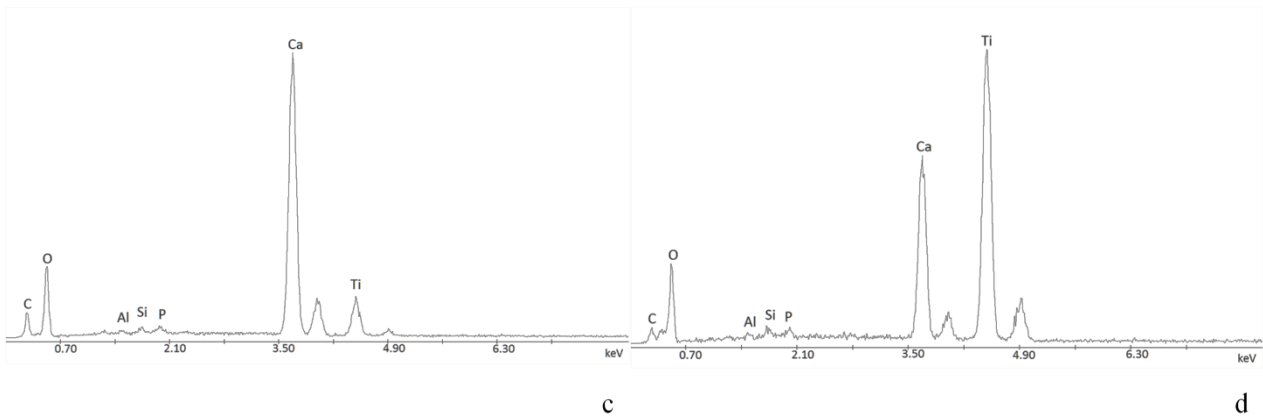
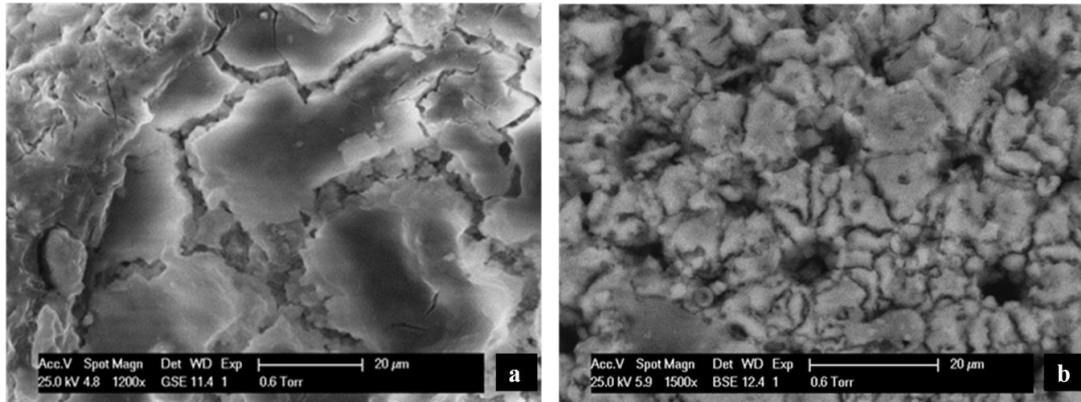
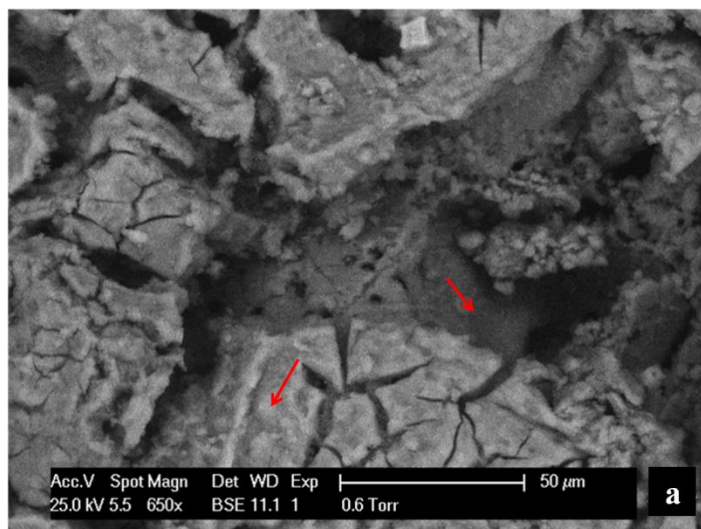


Fig. C.27 - (a-b) ESEM images of TiAcN film after five applications: extended microcracks and cavities and radial microcracks in the form of “flowers” are evident. (c) and (d) EDS spectra taken within a microcrack and on the continuous film between the microcracks, respectively.



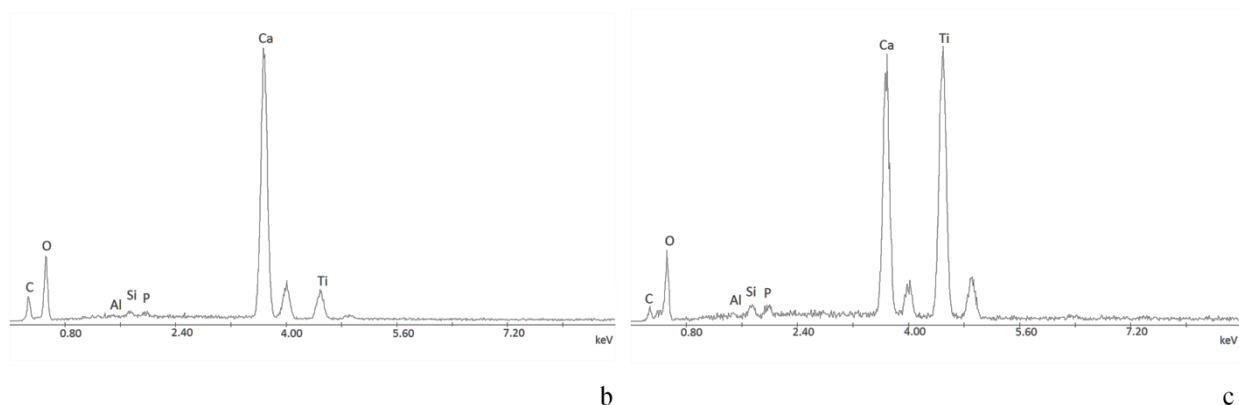


Fig. C.28 - (a) ESEM image of the TiAcAu film (three applications) with large microcracks. (b) EDS spectrum within a microcrack of the TiAcAu film; (c) EDS spectrum between the microcracks.

We report also in Fig .C.29 an example (TiAcAc) after 3 applications of the coating) of an EDS map of the distribution of Ti on the stone surface (a) and along a cross section (b), respectively. The penetration depth of the TiO₂ coating is about 1.5 mm.

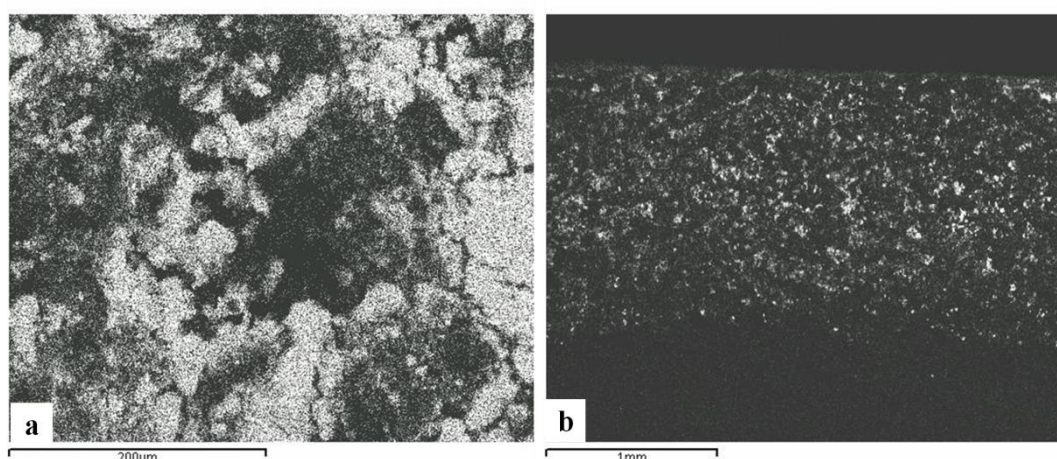


Fig. C.29 - (a) EDS map of Ti distribution on the "pietra di Lecce" surface coated with three applications of TiAcAc nanosol; (d) EDS map of the Ti depth distribution for the TiAcAc coating.

C. 3.2.2.4 - Chromatic changes

As concerns the chromatic changes due to the application of the coating to the calcarenite "pietra di Lecce", Table C.8 reports the L*, a*, b* color coordinates measured for the TiO₂ coated stone samples and the corresponding ones for the uncoated stone. A small decrease in the values L* and an increase in a* occurs for all coatings, except for TiAcN, where a slight increase of colorimetric coordinates produces a slight lightening in colour appearance. The total color difference after the application of TiAcAc, TiAcN and TiAcNa coatings is relatively low ($\Delta E^* \approx 2.8$) whereas $\Delta E^*=4.9$ for TiAcAu. Even if for the restoration of stone buildings $\Delta E^* < 5$ may be tolerated [C125], nevertheless, due to the pale purple/violet coloring of the stone surface, TiAcAu coating is not acceptable.

Table C.8 - Colorimetric data of the "pietra di Lecce" samples before and after the application of the coatings.

<i>"pietra di Lecce"</i>			
L* (± 0.1)	a* (± 0.1)	b* (± 0.1)	ΔE* (±0.2)
Uncoated			
81.6	1.1	13.4	
TiAcAc coated			
82.8	0.8	11.0	2.7
TiAcN coated			
79.4	1.2	11.6	2.8
TiAcNa coated			
79.5	1.2	11.5	2.8
TiAcAu coated			
81.8	1.8	8.6	4.9

C. 3.2.2.5 - Photocatalytic activity of the coatings

To test the photocatalytic activity of the TiO₂ coatings on *Lecce stone*, coated and untreated samples were stained with MeO and placed under UV irradiation at 10 cm from the lamp. The normalized colorimetric changes in the chroma, as defined in Eq. 5, are reported as a function of the irradiation time in Fig. C.30.

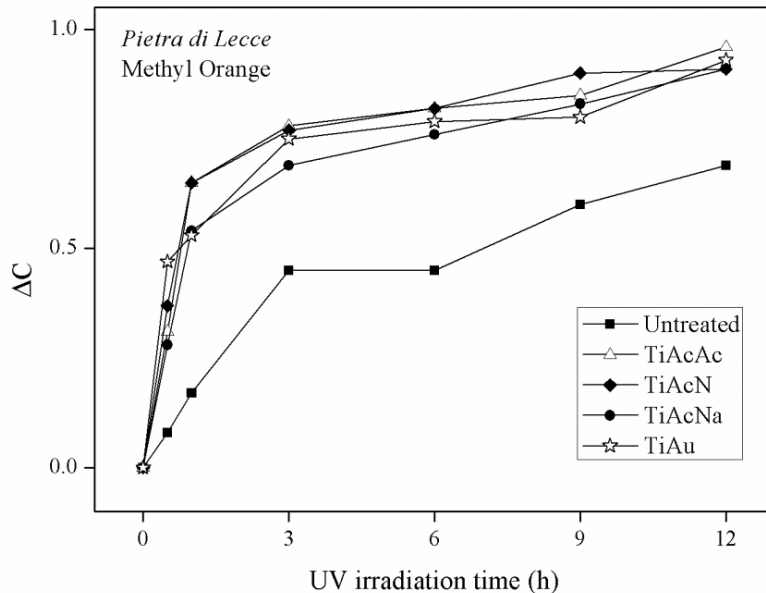


Fig. C.30 - Normalized chroma changes ΔC of the MeO stained Lecce stone samples, as a function of the irradiation time with the UV source. The comparison between untreated and different TiO₂ coated surfaces is reported.

The coated "*pietra di Lecce*" samples show in general a good degradation of MeO under UV irradiation: the photocatalytic activity of the titania particles produces most of the total degradation effect on the stain in the first few hours of exposure (the first part of the curves). The presence of Au nanoparticles, giving poor results as to the chromatic changes, nevertheless seems to enhance slightly the photocatalytic activity in the first few minutes.

C. 3.2.2.6 - Capillarity absorption

To evaluate the effects of the coating on the behaviour of the stones against water, comparative measurements of water absorption by capillarity were carried out on untreated samples and TiO₂ coated samples. In Fig. C.31 the curves of the capillarity absorption (Q_i) are plotted as a function of the square root of time (in seconds). The average of measurements on three samples for each case is reported.

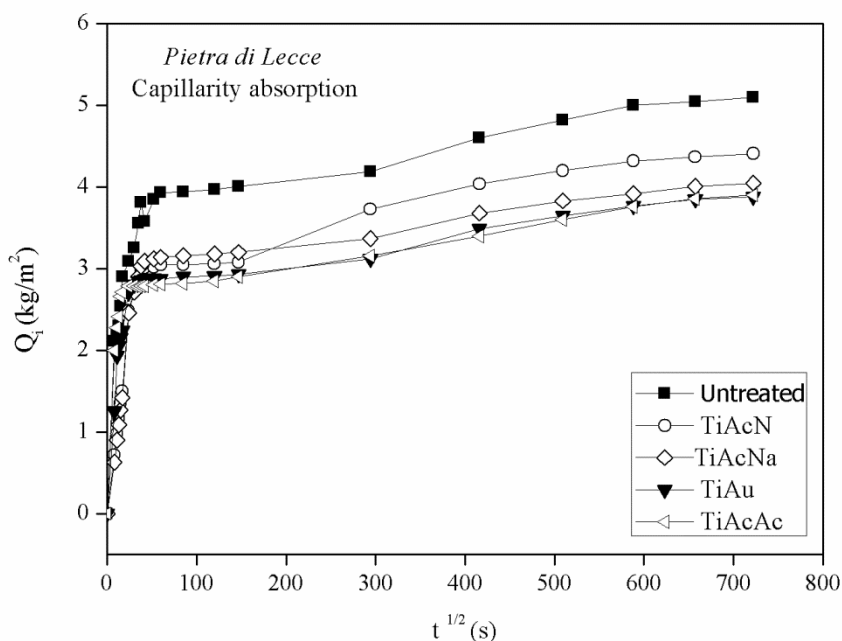


Fig. C.31 - Capillarity absorption Q_i (in kg/m^2 units) plotted as a function of the square root of time (in seconds) of Lecce stone samples before and after the application of TiAcAc, TiAcAu, TiAcN and TiAcNa coatings.

Table C.9 - Water absorption coefficient (AC) in $\text{kg}/(\text{m}^2 \text{s}^{1/2})$ calculated in the first five minutes and relative capillarity index (RCI) on the whole duration of the test.

		<i>"pietra di Lecce"</i>				
		Untreated	TiAcAc	TiAcN	TiAcNa	TiAcAu
AC	0-5 min (± 0.01)	0.18	0.15	0.09	0.08	0.18
RCI	0-144 h (± 0.04)		0.75	0.85	0.79	0.75

The absorption coefficient AC, evaluated as the slope of the fitted line to the Q_i curve vs. $t^{1/2}$ in the first 5 minutes, is reported in Table C.9. The treated samples generally show a small decrease of the capillarity absorption with respect to the untreated stones. Table C.9 reports also the values ($\pm 6\%$) of the relative capillarity index (RCI). The RCI values, i.e. the amounts of water absorbed during 144 h by the samples relative to the untreated ones, confirm that all coatings give lower absorption for the calcarenite stone investigated [C96]. The differences in the capillary absorption between the different treatments are small: this is in agreement with the similar morphology and comparable penetration depth of the various coatings found by SEM-EDS analyses.

C. 3.2.3 - Noto stone (*Pietra di Noto*)

Self-cleaning photocatalytic coatings based on TiO_2 nanoparticles obtained by sol-gel techniques at two different pH (1.3-10.6), have been investigated on carbonatic stone. The selected material is the yellowish lithofacies of *Palazzolo* Formation calcarenite, commonly named *Pietra di Noto*, widely used in the Baroque monuments of the Noto Valley (Italy, Sicily). SEM-EDS, and Raman investigations were carried out to characterize the TiO_2 coatings on *pietra di Noto*. To evaluate the effects of the treatments at two different pH values, changes of the stone color appearance, water absorption by capillarity and the behavior for salt crystallization were measured. The photocatalytic activity of the coatings was evaluated under UV irradiation, by monitoring methyl orange and methylene blue dye degradation as a function of time.

C. 3.2.3.1 - Petrographic analysis

Thin section analysis allows to highlight structure and texture features of the *pietra di Noto*. Petrographically, it can be classified as biomicrite [C122]. The allochemical components (25-30%) mainly consist of bioclasts (foraminifera, worms, echinoida and mollusca) and peloids (Fig. C.32). Micritic and microsparitic matrix is predominant (60-65%) while sparry cement occurs only within foraminifera (10%). Sporadic grains of quartz are also present. Considering the textural features, it can be classified as wackestone. Porosity (about 35%) is mainly intergranular and subordinately moldic [C122, C126].

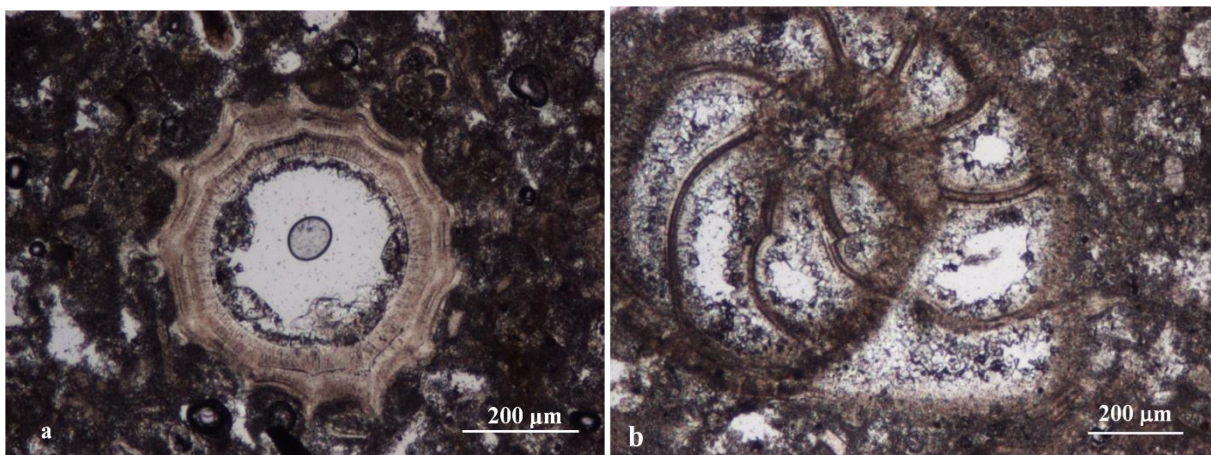


Fig. C.32 - Polarizing optical microscope images of thin sections of *Pietra di Noto*, where micro- and macrofossils are easily identified: a) Foraminifera; b) Echinoidea

C. 3.2.3.2 - Synthesis and application of the coatings

As described in section 2.2, two sols (called TiAcN and TiMA) at different pH have been synthesized using different complexing and peptizing agents. The sol TiAcN obtained with nitric acid gave pH=1.3 whereas TiMaA sol, obtained with triethylamine, gave pH=10.6 (Table C.10).

Table C.10 - The synthesized sols.

Sample	Complexing agent	Peptizer	pH
TiAcN	Acetic acid	Nitric Acid	1.3
TiMaA	Malonic acid	Triethylamine	10.6

The amount of sol applied by brushing was calculated from the weight difference after and before the application of the coating: 0.7 mg cm^{-2} and 0.9 mg cm^{-2} (± 0.1) for TiMaA and TiAcN, respectively.

C. 3.2.3.3 - SEM and EDS spectra

In Fig. C.33 the surface microstructure of the *Pietra di Noto* before (Fig. C.33a) and after the application of TiAcN (Fig. C.33b) and TiMaA (Fig. C.33d) coatings is shown. Moreover, distribution of Ti after TiAcN and TiMaA treatments collected through EDS are reported in Figs. C.5c and C.5e, respectively.

Fig. C.33a shows representative SEM photomicrographs of the surface of untreated Noto limestone. The calcarenite is made up of calcite microfossils, and it displays large intra- and inter-particle pores. Two types of calcite crystals were observed: micrite, characterized by subangular grains with size $<2\mu\text{m}$ and micro sparite crystals with size $>10\mu\text{m}$.

The stone surface treated with the nanosol coating TiAcN (Fig. C.33b) has a more grainy look with holes between the TiO_2 plates. Both coatings are largely cracked, but in the samples treated with TiMaA (Fig. C.33d), the TiO_2 plates are larger and the surface coverage is more homogeneous than samples treated with the acid nanosol.

By using EDS maps of Ti distribution along a cross section, the penetration depth of the TiO_2 coatings can be obtained; the results indicate that titanium is not present, for both treatments, at depths $> 150\text{-}200 \mu\text{m}$.

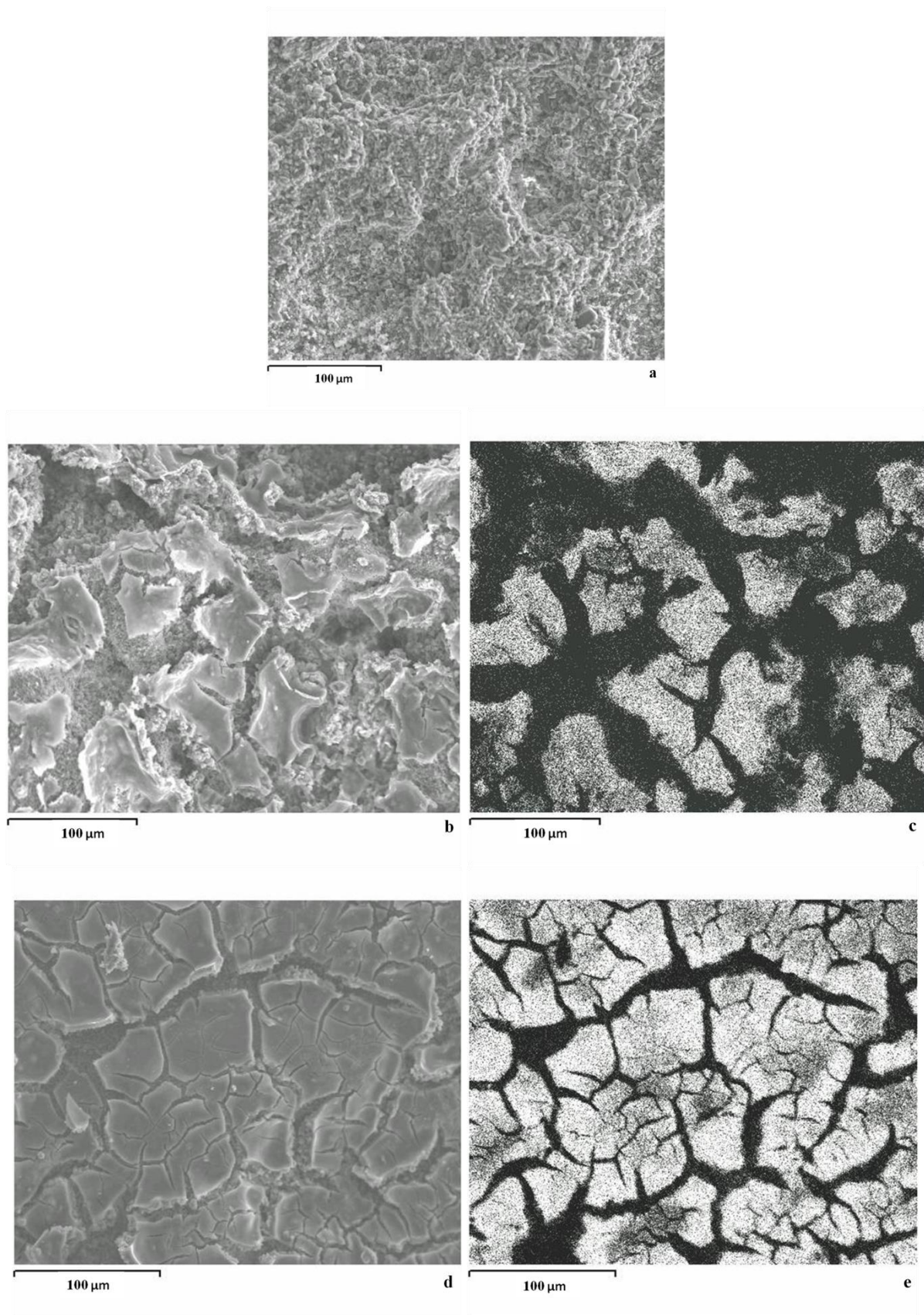


Fig. C.33 - SEM images (350x) and EDS maps of Ti on the pietra di Noto surface coated with three applications of TiAcN and TiMaA nanosols. a) Uncoated pietra di Noto surface; b) TiAcN coating; c) Ti distribution for TiAcN coating; d) TiMaA coating; e) Ti distribution for TiMaA coating.

C. 3.2.3.4 - Chromatic changes

The chromatic changes due to the application of the coatings to the Noto limestone are summarized in Table C.11, where the average L^* , a^* , b^* color coordinates for the TiO_2 uncoated and coated samples are reported. As human eye is able to detect colour changes such as $\Delta E^* \geq 1$, the values of overall color difference ΔE^* are more than acceptable after the application of the TiO_2 treatments.

Table C.11 - Colorimetric parameters of the uncoated and coated stone.

<i>Noto limestone</i>			
$L^* (\pm 0.1)$	$a^* (\pm 0.1)$	$b^* (\pm 0.1)$	$\Delta E^* (\pm 0.2)$
Uncoated			
85.6	2.4	15.5	
TiAcN coated			
85.6	2.6	16.2	0.7
TiMaA coated			
85.2	2.2	14.9	0.8

C. 3.2.3.5 - Capillarity absorption

The effects of the coating on the behaviour of the stones against water was evaluated by comparative measurements of water absorption by capillarity on untreated samples and titania coated samples. In Fig. C.34 the curves of the capillarity absorption (Q_i) are plotted as a function of the square root of time (in seconds). The average of measurements on three samples for each case is reported. The absorption coefficient AC is evaluated as the slope of the linear fit to the Q_i curve vs. $t^{1/2}$ in the first 30 minutes and is reported in Table C.12. An inspection of the curves and the obtained AC data suggest that the samples coated with TiAcN and TiMaA show a small decrease of the capillarity absorption with respect to the untreated ones.

In Table C.12, the values of the relative capillarity index (RCI), i.e. the amounts of water absorbed during 96 h by the coated samples relative to the untreated ones are also reported. Even if both coatings do not change significantly the water absorption behavior of the investigated calcarenite, the TiMaA treatment gives back a lower capillary absorption.

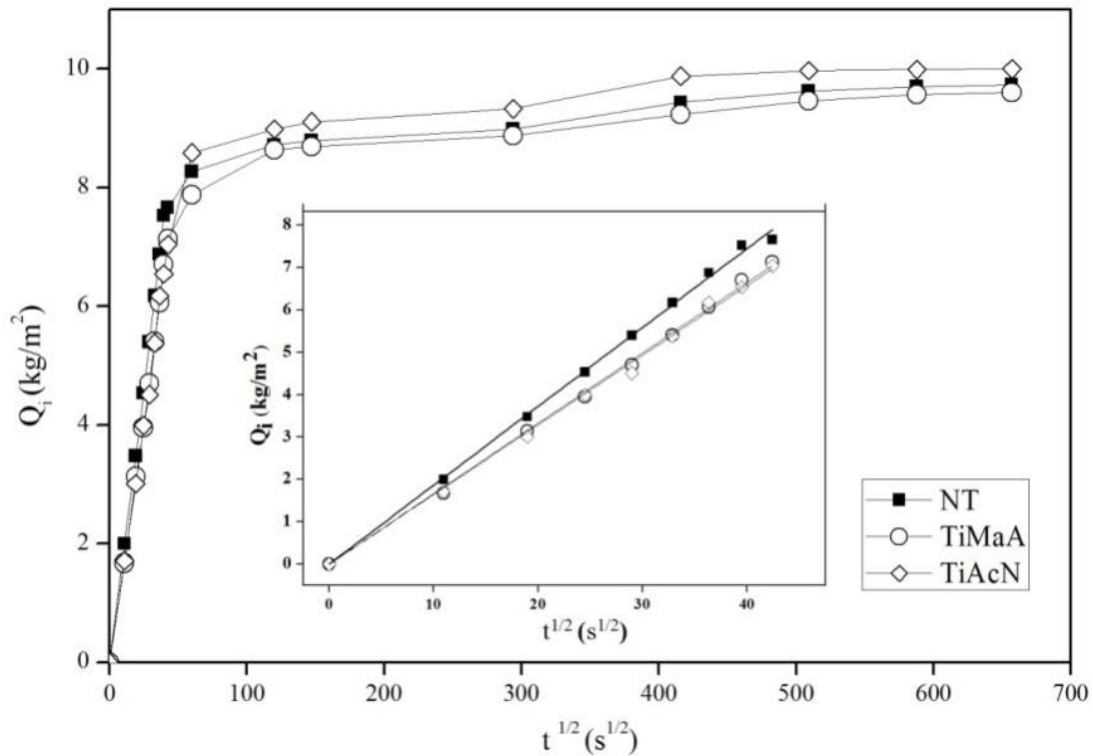


Fig. C.34 - Capillarity absorption curves Q_i vs $t^{1/2}$ for non-treated (NT), TiAcN and TiMaA coated samples.

Table C.12 - Water absorption coefficient (AC) in $\text{kg}/(\text{m}^2 \text{s}^{1/2})$ calculated in the first 30 minutes and relative capillarity index (RCI) on the whole duration of the test.

<i>Pietra di Noto</i>			
	Untreated	TiAcN	TiMaA
AC 0-0.5 h	0.186	0.164	0.166 (±0.05)
RCI 0-96 h		1.03	0.98 (±0.04)

C. 3.2.3.6 - Salt crystallization

Comparative accelerated aging tests were performed in order to evaluate the effects of the TiO_2 coatings against salts crystallization. According to UNI EN 12370 standard [C97], data are reported as total mass loss percentage versus the number of crystallization cycles.

Fig. C.35 displays the average mass loss for each salt crystallization cycle for untreated and treated stone samples (eight samples for each set). The results show a similar trend for coated and uncoated stones. The mass loss curves are, in both cases, roughly “salt-controlled” up to the second cycle (*i.e.*, a slight increase of the total mass) and “weathering-controlled” from the third cycle, as suggested by a decrease of total mass.

The presence of the coatings causes a decrease of the total loss mass and a consequent improvement of stone durability against salts, especially for the basic one (TiMaA).

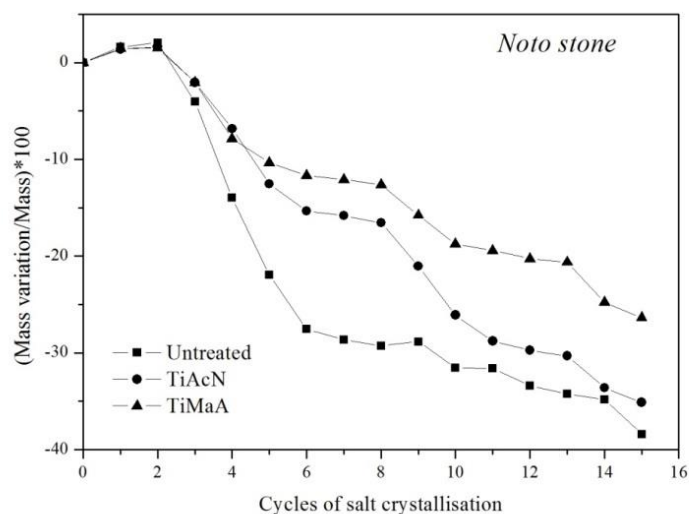


Fig. C.35 -Mass-loss percentage vs. salt crystallization cycles for untreated and treated pietra di Noto.

Moreover, with the aim at verifying the persistence of the coating after weathering processes due to salts, Raman spectra were taken on samples at the end of the test. The obtained results highlight that after 15 salts crystallization the titanium dioxide coating, clearly visible on the stone before the aging test, seem to disappear: only sodium sulphate (thenardite) and calcite are observed (Fig. 36).

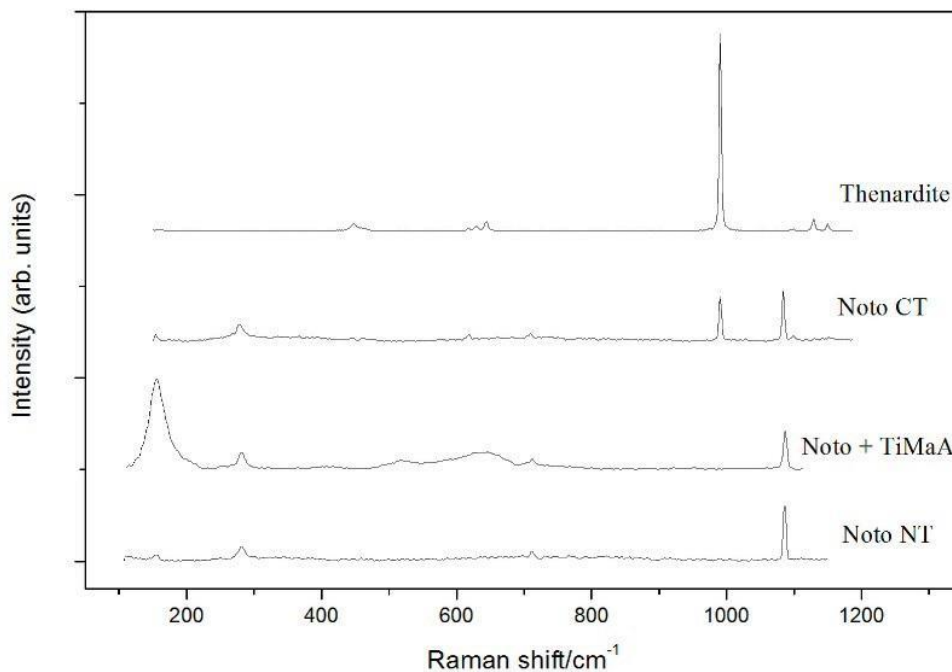


Fig. C.36 - Raman spectra of pietra di Noto, untreated (NT), coated with TiMaA, and after the crystallization test (CT). Thenardite spectrum is reported for comparison.

C. 3.2.3.7 - Photocatalytic activity of the coatings

The photocatalytic activity of the TiAcN and TiMaA nanosols was discussed in C.3.1.6 on Methylene blue (MB) and methyl orange (MeO) dyes, selected as performance indicators. Their degradation was monitored through the change in optical absorption under UV lamp irradiation of aqueous solutions of the dye added to the TiO₂ nanosols. Both TiAcN and TiMaA titania sols show good photo-activity on the dyes under UV irradiation. The complete degradation time of MeO ranges from 40 min (TiAcN) to 3 h (TiMaA) whereas for MB dye, after 2 hours of UV irradiation, the TiAcN sol gives a degradation of only 30% whereas the TiMaA sol yields complete degradation.

To test the photocatalytic activity of the TiO₂ coatings on *Noto limestone*, untreated and coated samples were stained with MeO and MB and placed under UV irradiation at 10 cm from the lamp. The normalized colorimetric changes measured by changes in the chroma ΔC , as defined in Eq. 5, are reported for MeO and MB as a function of the irradiation time in Fig. C.37.

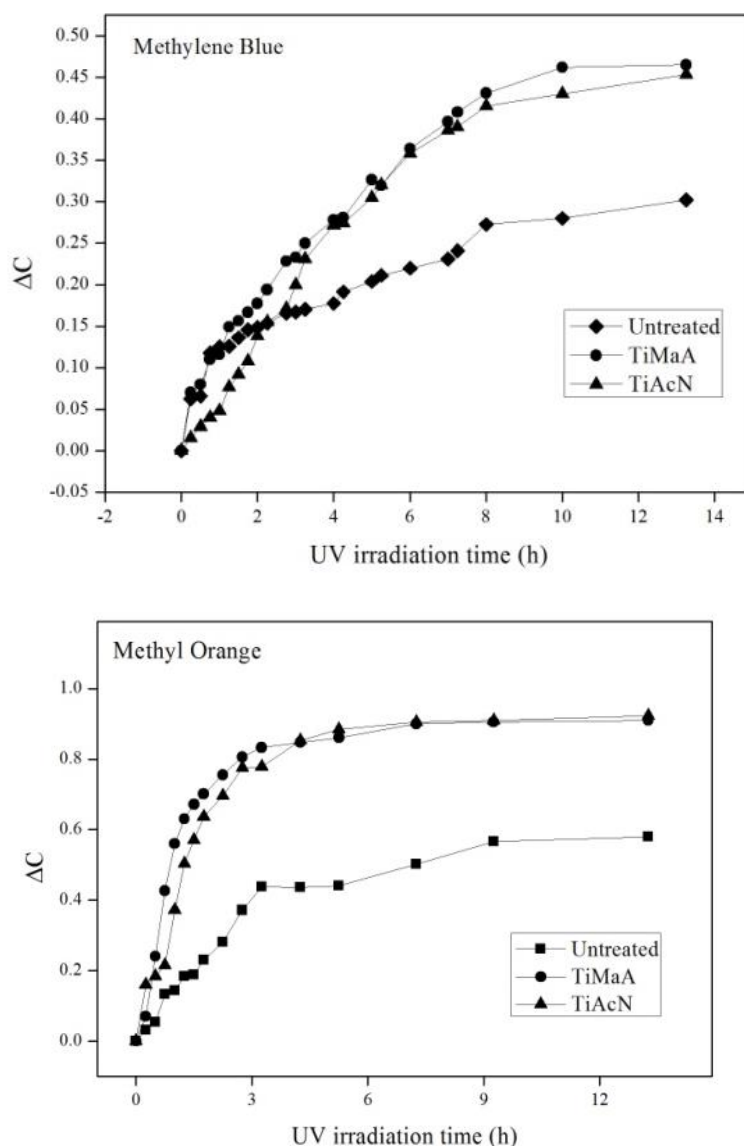


Fig. C.37 - Photocatalytic activity vs. time of the TiMaA and TiAcN coatings on Methylene Blue and Methyl Orange dyes, measured by chromatic changes ΔC of the stained stone.

In general, the coated samples show faster degradation of the dyes under UV irradiation than the uncoated ones, for both coatings. In detail, in samples stained with MeO, the photocatalytic activity of the TiO₂ coatings occurs mainly in the first few hours of exposure, while in samples stained with MB more time is required for the complete photodegradation of the dye. Overall, the basic nanosol TiMaA exhibits a slightly higher efficiency than the acid one for both methylene blue and methyl orange.

C. 4 – CONCLUSIONS

The sol-gel synthesis of water-based sols of nanocrystalline titania sols in acid and basic aqueous environments (TiAcAc, TiAcAu, TiAcN, TiAcNNA, TiMaA, TiMaAN) was carried out by acid hydrolysis of titanium(IV) isopropoxide with acetic acid or malonic acid acting also as complexing agents. Subsequent peptization was achieved in acid medium, in the case of acetic acid, and in basic medium (through triethylamine), in the case of malonic acid

XRD, Raman and TEM measurements on the corresponding titania powders have revealed nanocrystalline particles of anatase (5-6 nm) and of brookite in lesser amount.

DLS and ELS-IEP analyses have indicated that preparations with acetic acid, acetic/nitric acids or malonic/triethylamine (basic) gives *stable* sols, namely TiAcAc, TiAcN and TiMaA.

Methyl orange (MeO) and methylene blue (MB) were used as model contaminants to investigate the degradation activity of the different sols under UV irradiation. The catalytic photoactivity of the sols under UV irradiation for the degradation of the anionic azo-dye MeO is much faster with acid sols than with the basic one. The cationic MB dye is completely photodegraded only by the basic TiO₂ sol TiMaA, on which the dye is adsorbed with the formation of trimeric species.

TiO₂ based-coatings at different pH were applied to biocalcarenes typical of southern Italy (Comiso, Modica, Noto and Lecce stones) used in the Baroque period of interest for cultural heritage.

Satisfactory results are obtained for the TiO₂ based-coating tested. The coatings slightly reduce the capillarity water absorption and referring to durability of the stone, the resistance to salt crystallization is generally improved. Colorimetric analyses show that the coatings, with the exception of TiAcAu do not significantly alter the original colour of the stones. As concerns the self-cleaning properties, all TiO₂ coatings exhibit a good photodegradation activity of both dyes: the addition of gold nanoparticle improves the cleaning in the first minutes, but the purple coloring prevents its use.

This study has revealed that the TiMaA sol, thanks to its basic nature, is particularly suited for the self-cleaning of carbonatic stones, widely employed in ancient and modern architecture, opening further perspectives for the conservation in the field of Cultural Heritage.

C. 5 - REFERENCES

- [C1] Warscheid T., Braams J., *Biodeterioration of stone: a review*, Int Biodeter Biodegr, 46 (2000) 343-368.
- [C2] Dornieden T., Gorbushina A.A., Krumbein W.E., *Biodecay of cultural heritage as a space/time-related ecological situation an evaluation of a series of studies*, Int Biodeter Biodegr, 46 (2000) 261-270.
- [C3] Webster A., May E., *Bioremediation of weathered-building stone surfaces*, Trends Biotechnol, 24 (2006) 255-260.
- [C4] Camaiti M., Bugani S., Bernardi E., Morselli L., Matteini M., *Effects of atmospheric NO_x on biocalcarenite coated with different conservation products*. Appl Geochem 22 (2007) 1248-1254.
- [C5] Perez-Monserrat E.M., Varas M.J., Fort R., de Buergo M.A., *Assessment of Different Methods for Cleaning the Limestone Facades of the Former Workers Hospital of Madrid, Spain*. Stud Conserv, 56 (2011) 298-313.
- [C6] Fronteau G., Schneider-Thomachot C., Chopin E., Barbin V., Mouze D., Pascal A., *Black-crust growth and interaction with underlying limestone microfacies*, Geol. Soc. Spec. Publ. 333 (2010) 25-34.
- [C7] Grossi C.M., Brimblecombe P., *Effect of long-term changes in air pollution and climate on the decay and blackening of European stone buildings*. Geol Soc Spec Publ 271 (2007) 117-130.
- [C8] Andriani G.F., Walsh N., *Fabric, porosity and water permeability of calcarenites from Apulia (SE Italy) used as building and ornamental stone*. Bull. Eng. Geol. Environ. 62 (2003) 77-84.
- [C9] Bugani S., Camaiti M., Morselli L., Van de Castele E., Janssens K., *Investigating morphological changes in treated vs. untreated stone building materials by x-ray micro-CT*. Anal. Bioanal. Chem. 391 (2008) 1343-1350.
- [C10] Panniello A., Curri M.L., Diso D., Licciulli A., Locaputo V., Agostiano A., Comparelli R., Mascolo G., *Nanocrystalline TiO₂ based films onto fibers for photocatalytic degradation of organic dye in aqueous solution*. Appl. Catal. B Environ. 121-122 (2012) 190-197.
- [C11] Pinho L., Elhaddad F., Facio D.S., Mosquera M.J., *A novel TiO₂-SiO₂ nanocomposite converts a very friable stone into a self-cleaning building material*. Appl. Surf. Sci. 275 (2013) 389-396.
- [C12] Quagliarini E., Bondioli F., Goffredo G., Licciulli A., Munafò P., *Self-cleaning materials on Architectural Heritage: Compatibility of photo-induced hydrophilicity of TiO₂ coatings on stone surfaces*. J. Cultural Heritage 13 (2012) 204-209.
- [C13] Licciulli A., Calia A., Lettieri M., Diso D., Masieri M., Franza S., Amadelli R., Casarano G., *Photocatalytic coating on limestone*. J Sol-Gel Sci Technol 60 (2011) 437-444.

- [C14] Tsakalof A., Manoudis P., Karapanagiotis I., Chryssoulakis I., Panayiotou C., *Assessment of synthetic polymeric coatings for the protection and preservation of stone monuments*. J. Cult. Herit. 8 (2007) 69-72.
- [C15] Hore S., Palomares E., Smit H., Bakker N.J., Comte P., Liska P., Thampi K.R., Kroon J.M., Hinsch A., Durrant J.R., *Acid versus base peptization of mesoporous nanocrystalline TiO₂ films: functional studies in dye sensitized solar cells*. J Mater Chem 15 (2005) 412-418.
- [C16] Mor G.K., Shankar K., Paulose M., Varghese O.K., Grimes C.A., *Use of Highly-Ordered TiO₂ Nanotube Arrays in Dye-Sensitized Solar Cells*. Nano Lett 6 (2006) 215-218.
- [C17] Zhu K., Neale N.R., Miedaner A., Frank A.J., *Enhanced charge-collection efficiencies and light scattering in dye-sensitized solar cells using oriented TiO₂ nanotubes arrays*. Nano Lett 7 (2007) 69-74.
- [C18] Jennings J.R., Ghicov A., Peter L.M., Schmuki P., Walker A.B., *Dye-Sensitized Solar Cells Based on Oriented TiO₂ Nanotube Arrays: Transport, Trapping and Transfer of Electrons*. J Am Chem Soc 130 (2008) 13364-13372
- [C19] Arabatzis I.M., Stergiopoulos T., Andreeva D., Kitova S., Neophytides S.G., Falaras P., *Characterization and photocatalytic activity of Au/TiO₂ thin films for azo-dye degradation*. J Catal 220 (2003) 127-135.
- [C20] Mehrjouei M., Müller S., Möller D., *Treatment of pyrolysis wastewater using heterogeneous advanced oxidation processes* Environ Prog Sustainable Energy 33 (2014) 178-183.
- [C21] Kamegawa T, Suzuki N, Yamashita H *Synthesis of Structured Macroporous TiO₂ Thin Films and Investigation on Their Photocatalytic Activities*. IOP Conf Series: Mat Sci Eng 18 (2011) 172002.
- [C22] Kuwahara Y., Kamegawa T., Mori K., Yamashita H., *Design of New Functional Titanium Oxide-based Photocatalysts for Degradation of Organics Diluted in Water and Air*. Curr Org Chem 14 (2010) 616-629.
- [C23] Rajeshwar K., Osugi M.E., Chanmanee W., Chenthamarakshan C.R., Zaroni M.V.B., Kajitvichyanukul P., Krishnan-Ayer R., *Heterogeneous photocatalytic treatment of organic dyes in air and aqueous media*. J Photochem Photobiol C Photochem Rev 9 (2008) 171-192.
- [C24] Panniello A., Curri M.L., Diso D., Licciulli L., Locaputo V., Agostiano A., Comparelli R., Mascolo G. *Nanocrystalline TiO₂ based films onto fibers for photocatalytic degradation of organic dye in aqueous solution*. Appl Catal B Environ 121-122 (2012) 190-197.
- [C25] Chen H., Nanayakkara C.E., Grassian V.H., *Titanium Dioxide Photocatalysis in Atmospheric Chemistry* Chem Rev 112 (2012) 5919–5948.
- [C26] Kapridaki C., Maravelaki-Kalaitzaki P., *TiO₂-SiO₂ - PDMS nano-composite hydrophobic coating with self-cleaning properties for marble protection*. Prog Org Coat 76 (2013) 400-410.
- [C27] Quagliarini E, Bondioli F, Goffredo G, Cordonì C, Munafò P *Self-cleaning and de-polluting stone surfaces: TiO₂ nanoparticles for limestone* Constr Build Mater 37 (2012) 51-57. DOI: 10.1016/j.conbuildmat.2012.07.006

- [C28] Bergamonti L., Alfieri I., Franzò M., Lorenzi A., Montenero A., Predieri G., Raganato M., Calia A., Lazzarini L., Bersani D., Lottici P.P., *Synthesis and characterization of nanocrystalline TiO₂ with application as photoactive coating on stones*. Environ Sci Pollut R 21 (2014) 13264-13277.
- [C29] Fonseca A.J., Pina F., Macedo M.F., Leal N., Romanowska-Deskins A., Laiz L., Gómez-Bolea A., Saiz-Jimenez C., *Anatase as an alternative application for preventing biodeterioration of mortars: Evaluation and comparison with other biocides*. Int Biodeter Biodegr 64 (2010) 388-396.
- [C30] Graziani L., Quagliarini E., Osimani A., Aquilanti L., Clementi F., Yéprémian C., Lariccia V., Amoroso S., D'Orazio M., *Evaluation of inhibitory effect of TiO₂ nanocoatings against microalgal growth on clay brick façades under weak UV exposure conditions*. Build Environ 64 (2013) 38-45.
- [C31] Bergamonti L., Alfieri I., Lorenzi L., Montenero A., Predieri G., Barone G., Mazzoleni P., Pasquale S., Lottici P.P. *Nanocrystalline TiO₂ by sol-gel: Characterisation and photocatalytic activity on Modica and Comiso stones* Appl Surf Sci 282 (2013) 165-173.
- [C32] Testino A., Bellobono I.R., Buscaglia V., Canevali C., D'Arienzo M., Polizzi S., Scotti R., Morazzoni F., *Optimizing the Photocatalytic Properties of Hydrothermal TiO₂ by the Control of Phase Composition and Particle Morphology. A Systematic Approach*. J Am Chem Soc 129 (2007) 3564-3575.
- [C33] Tian G., Fu H., Jing L., Xin B., Pan K., *Preparation and Characterization of Stable Biphasic TiO₂ Photocatalyst with High Crystallinity, Large Surface Area, and Enhanced Photoactivity*. J Phys Chem C 112 (2008) 3083-3089.
- [C34] Zhang J., Xu Q., Feng Z., Li M., Li C., *Importance of the Relationship between Surface Phases and Photocatalytic Activity of TiO₂*. Angew Chem Int Ed 47: (2008) 1766 -1769.
- [C35] Neppolian B., Yamashita H., Okada Y., Nishijima H., Anpo M., *Preparation of unique TiO₂ nano-particle photocatalysis by a multi-gelation method for control of the physicochemical parameters and reactivity* Catalysis Lett 105 (2005) 111-117.
- [C36] Sakatani Y., Grosso D., Nicole L., Boissière C., Soler-Illia G.J., Sanchez C., *Optimised photocatalytic activity of grid-like mesoporous TiO₂ films: effect of crystallinity, pore size distribution, and pore accessibility*. J Mater Chem 16 (2006) 77-82
- [C37] Zhang Z., Wang C.C., Zakaria R., Ying J.Y., *Role of particle size in nanocrystalline TiO₂-based photocatalysts*. J Phys Chem B 102 (1998)10871-10878
- [C38] Chae S.Y., Park M.K., Lee S.K., Kim T.Y., Kim S.K., Lee W.I., *Preparation of size-controlled TiO₂ nanoparticles and derivation of optically transparent photocatalytic films*. Chem Mater 15 (2003) 3326-3331.
- [C39] Zumeta I., Díaz D., Santiago P., *Synthesis of TiO₂ Nanoparticles with Narrow Size Distribution and Their Evaluation in the Photocatalytic Oxidative Degradation of Bis(4-nitrophenyl) Phosphate*. J Phys Chem C 114 (2010) 11381-11389.

- [C40] Kim S.J., Lee E.G., Park S.D., Jeon C.J., Cho Y.H., Rhee C.K., Kim W.W., *Photocatalytic effects of rutile phase TiO₂ ultrafine powder with high specific surface area obtained by a homogeneous precipitation process at low temperatures*. J Sol-Gel Sci Technol 22 (2001) 63-74.
- [C41] Addamo M, Bellardita M, Di Paola A, Palmisano L *Preparation and photoactivity of nanostructured anatase, rutile and brookite TiO₂ thin films* Chem Commun (2006) 4943-4945. DOI: 10.1039/b612172a
- [C42] Roy HG *Comparison of Photocatalytic Activities of Anatase and Rutile Titania Nanostructures Synthesized by Microwave Irradiation* Research and Application of Material 1 (2013) 65-72. DOI: 10.12966/ram.09.02.2013
- [C43] Yu JC, Yu J, Ho W, Jiang Z, Zhang L *Effects of F - Doping on the Photocatalytic Activity and Microstructures of Nanocrystalline TiO₂* Chem Mater 14 (2002) 3808-3816
- [C44] Sung-Suh HM, Choi JR, Hah JH, Bae YC, Koo SM, Chan BY *Comparison of Ag deposition effects on the photocatalytic activity of nanoparticulate TiO₂ under visible and UV light irradiation* J Photoch Photobiol A 163 (2004) 37-44. DOI: 10.1016/S1010-6030(03)00428-3
- [C45] Park JH, Kim S, Bard AJ *Novel carbon-doped TiO₂ nanotube arrays with high aspect ratios for efficient solar water splitting* Nano Lett 6 (2006) 24-28
- [C46] Sathish M, Viswanathan B, Viswanath RP, Gopinath CS *Synthesis, characterization, electronic structure, and photocatalytic activity of nitrogen-doped TiO₂ nanocatalyst* Chem Mater 17 (2005) 6349-6353
- [C47] Zaleska A *Doped-TiO₂ : A Review* Recent Patents on Engineering 2 (2008) 157-164
- [C48] Akpan UG, Hameed BH *The advancements in sol-gel method of doped-TiO₂ photocatalysts* Appl Catal A-Gen 375 (2010) 1-11. DOI: 10.1016/j.apcata.2009.12.023
- [C49] Dozzi MV, Prati L, Canton P, Selli E *Effects of gold nanoparticles deposition on the photocatalytic activity of titanium dioxide under visible light* Phys Chem Phys 11 (2009) 7171-7180. DOI: 10.1039/b907317e
- [C50] Smitha VS, Manjumol KA, Baiju KV, Ghosh S, Perumal P, Warriar KGK *Sol-gel route to synthesize titania-silica nano precursors for photoactive particulates and coatings* J Sol-Gel Sci Technol 54 (2010) 203-211
- [C51] Primo A, Corma A, García H *Titania supported gold nanoparticles as photocatalyst*. Phys Chem Phys 13 (2011):886-910. DOI: 10.1039/c0cp00917b
- [C52] Yogi C, Kojima K, Hashishin T, Wada N, Inada Y, Della Gaspera E, Bersani M, Martucci A, Liu L, Sham TK *Size Effect of Au Nanoparticles on TiO₂ Crystalline Phase of Nanocomposite Thin Films and Their Photocatalytic Properties* J Phys Chem C 115 (2011) 6554-6560. DOI: 10.1021/jp110581J
- [C53] Djaoued Y, Brüning R, Bersani D, Lottici PP, Badilescu S *Sol-gel nanocrystalline brookite-rich titania film*. Mater Lett 58 (2004) 2618- 2622. DOI: 10.1016/j.matlet.2004.03.034

- [C54] Chen X, Mao SS (2007) *Titanium dioxide nanomaterials: synthesis, properties, modifications, and applications* Chem Rev 107:2891-2959
- [C55] Kawahara T, Konishi Y, Tada H, Tohge N, Nishi J, Ito S *A patterned TiO₂ (Anatase)/TiO₂ (Rutile) bilayer-type photocatalyst: Effect of the Anatase/Rutile Junction on the Photocatalytic activity* Angew Chem Int Edit 41 (2002) 2811-2813. DOI: 10.1002/1521-3773(20020802)41:15<2811::AID-ANIE2811>3.0.CO;2-#.
- [C56] Alapi A, Sipas P, Ilisz I, Wittmann G, Ambrus Z, Kiricsi I, Mogyorósi K, Dombi A *Synthesis and characterization of titania photocatalysts: the influence of pretreatment on the activity* Appl Catal A-Gen 303 (2006) 1-8. DOI: 10.1016/j.apcata.2006.01.026
- [C57] Zhang H, Banfield JF *Understanding Polymorphic Phase Transformation Behavior during Growth of Nanocrystalline Aggregates : Insights from TiO₂* J Phys Chem B 104 (2000) 3481-3487
- [C58] Ozawa T, Iwasaki M, Tada H, Akita T, Tanaka K, Ito S *Low-temperature synthesis of anatase - brookite composite nanocrystals : the junction effect on photocatalytic activity* J Colloid Interf Sci 281 (2005) 510-513
- [C59] Ardizzone S, Bianchi CL, Cappelletti G, Gialanella S, Pirola C, Ragaini V *Tailored anatase/brookite nanocrystalline TiO₂. The optimal particle features for liquid-and gas-phase photocatalytic reactions* J Phys Chem C 111 (2007) 13222-13231
- [C60] Li JG, Ishigaki T, Sun X *Anatase, Brookite and Rutile Nanocrystals via Redox Reactions under Mild Hydrothermal Conditions: Phase-Selective Synthesis and Physicochemical Properties* J Phys Chem C 111 (2007) 4969-4976
- [C61] Henderson M A, Lyubinetsky I *Molecular-Level Insights into Photocatalysis from Scanning Probe Microscopy Studies on TiO 2 (110)* Chem Rev 113 (2013) 4428-4455
- [C62] Di Paola A, Bellardita M, Palmisano L *Brookite, the Least Known TiO₂ Photocatalyst.* Catalysts 3 (2013) 36-73
- [C63] Kandiel TA, Robben L, Alkaim A, Bahnemann D *Brookite versus anatase TiO₂ photocatalysts: phase transformations and photocatalytic activities* Photochem Photobiol Sci 12 (2013) 602-609
- [C64] Sabbah, H. *Amorphous titanium dioxide ultra-thin films for self-cleaning surfaces* Mater Express 3 (2013) 171-1753, 171-175. DOI: 10.1166/mex.2013.1106
- [C65] Guettaï, N, Amar HA *Photocatalytic oxidation of methyl orange in presence of titanium dioxide in aqueous suspension. Part I: Parametric study.* Desalination 185 (2005) 427-437. DOI: 10.1016/j.desal.2005.04.048
- [C66] Coutinho CA, Gupta VK *Photocatalytic degradation of methyl orange using polymer-titania microcomposites,* J Colloid Interf Sci 333 (2009) 457-464. DOI: 10.1016/j.jcis.2009.02.016
- [C67] Chang H, Su C, Lo CH, Chen LC, Tsung TT, Jwo CS *Photodecomposition and Surface Adsorption of Methylene Blue on TiO₂ Nanofluid Prepared by ASNSS* Mater Trans 45 (2004) 3334-3337

- [C68] Ding Z, Lu GQ, Greenfield PF *Role of the Crystallite Phase of TiO₂ in Heterogeneous Photocatalysis for Phenol Oxidation in Water* J Phys Chem B 104 (2000) 4815-4820
- [C69] Kapinus EI, Viktorova TI *Kinetics of the photocatalytic degradation of methylene blue on titanium dioxide* Theor Exp Chem 46 (2010) 163-167
- [C70] Kapinus EI, Viktorova TI, Khalyavka TA *Dependence of the rate of photocatalytic decomposition of safranin on the catalyst concentration* Theor Exp Chem 45 (2009) 114-117. DOI:10.1007/s11237-009-9071-z
- [C71] Khalyavka TA, Shimanovskaya VV, Strelko VV, Kapinus EI *Photocatalytic activity of titanium dioxide in the degradation of methylene blue and tetrachlorofluorescein in aqueous solutions* Theor Exp Chem 37 (2001). 58-62. DOI: 10.1023/A:1010474025193
- [C72] Smitha V.S., Manjumol K.A., Baiju K.V., Ghosh S., Perumal P., Warriar K.G.K., *Sol-gel route to synthesize titania-silica nano precursors for photoactive particulates and coatings* J. Sol-Gel Sci. Technol. 54 (2010) 203-211. DOI: 10.1007/s10971-010-2178-9.
- [C73] Watson S., Beydoun D., Scott J., Amal R., *Preparation of nanosized crystalline TiO₂ particles at low temperature for photocatalysis*, J. Nanopart. Res. 6 (2004) 193-207. DOI: 10.1023/B:NANO.0000034623.33083.71.
- [C74] Anania L., Badalà A., Barone G., Belfiore C., Calabrò C., Mazzoleni P., Pezzino A., *The stones in monumental masonry buildings of the “Val di Noto” area: New data on the relationships between petrographic characters and physical-mechanical properties*, Constr. Build. Mater. 33 (2012) 122 -132.
- [C75] Barone G., La Russa M.F., Lo Giudice A., Mazzoleni P., Pezzino A., *The Cathedral of S. Giorgio in Ragusa Ibla (Italy): characterization of construction materials and their chromatic alteration*, Environ. Geol. 55 (2008) 499-504
- [C76] Barone G., Campani E., Casoli A., La Russa M.F., Lo Giudice A., Mazzoleni P., Pezzino A., *The Cathedral of St. Giorgio in Ragusa Ibla (Italy): a case study of the use of protective products*, Environ. Geol. 54 (2008) 1501-1506.
- [C77] Carbone S., Grasso M., Lentini F., *Considerazioni sull'evoluzione della Sicilia sud-orientale dal Cretaceo al Quaternario*, Mem. Soc. Geol. It. 24 (1982) 367-386
- [C78] Carbone S., Grasso M., Lentini F., *Lineamenti geologici del plateau Ibleo (Sicilia S.E.): presentazione delle carte geologiche della Sicilia Sud-Orientale*, Mem. Soc. Geol. It., 38 (1987) 127-35.
- [C79] Mazzei R, Margiotta S, Foresi LM, Riforgiato F, Salvatorini G *Biostratigraphy and chronostratigraphy of the Miocene Pietra Leccese in the type area of Lecce (Apulia, southern Italy)*. Boll Soc Paleontol I 48 (2009) 129-145
- [C80] Balenzano F, Moresi M, Tria A *Significato paleogeografico della presenza di Glauconite nella “Pietra Leccese” (Calcarene Miocenica del Salento)*. Mineral Petrography Acta 37 (1994) 437-450.

- [C81] Bossio A, Foresi LM, Margiotta S, Mazzei R, Salvatorini G, Donia F *Stratigrafia neogenico-quaternaria del settore nord - orientale della provincia di Lecce (con rilevamento geologico alla scala 1:25.000)*. Geol Rom 39 (2006) 63-87.
- [C82] Vasanelli E, Sileo M, Calia A, Aiello MA *Non-destructive techniques to assess mechanical and physical properties of soft calcarenitic stones*. Procedia Chemistry 8 (2013) 35 - 44. DOI: 10.1016/j.proche.2013.03.006
- [C83] UNI EN 10921:2001- Beni culturali - Materiali lapidei naturali ed artificiali - Prodotti idrorepellenti - Applicazione su provini e determinazione in laboratorio delle loro caratteristiche, UNI Ente Nazionale Italiano di Unificazione, 2001
- [C84] Hiemenz PC, Rajagopalan R (1997) In: Principles of Colloid and Surface Chemistry, 3rd edn. Marcel Dekker, New York
- [C85] Jiang J, Oberdörster G, Biswas P *Characterization of size, surface charge, and agglomeration state of nanoparticle dispersions for toxicological studies* J Nanopart Res 1 (2009) 77-89
- [C86] Nam W, Kim J, Han G *Photocatalytic oxidation of methyl orange in a three-phase fluidized bed reactor* Chemosphere 47 (2002) 1019-1024
- [C87] Kodom T., Amouzou E., Djaneye-Boundjou G., Moctar B.L. *Photocatalytic Discoloration of Methyl Orange and Indigo Carmine on TiO₂ (P25) Deposited on Conducting Substrates: Effect of H₂O₂ and S₂O₈²⁻* Int J Chem Technol 4 (2012) 45-56
- [C88] Oakes J, Gratton P *Kinetic investigations of the oxidation of Methyl Orange and substituted arylazonaphthol dyes by peracids in aqueous solution* J Chem Soc Perkin Trans 2 (1998). 2563-2568
- [C89] Al-Qaradawi S., Salman SR *Photocatalytic degradation of methyl orange as a model compound* J Photoch Photobio A 148 (2002) 161-168
- [C90] Antonioli G., Fermi F., Oleari C., Reverberi R., *Spectrophotometric scanner for imaging of paintings and other works of art*, in: Proceedings Second European Conference on Color in Graphics, Imaging and Vision (2004) pp. 219 - 224.
- [C91] UNI EN 15866:2010 - Conservation of cultural property - test methods - colour measurement of surfaces, UNI Ente Nazionale Italiano di Unificazione, 2010
- [C92] UNI 11259:2008 - Determination of the photocatalytic activity of hydraulic binders - Rhodamine B test method. UNI Ente Nazionale Italiano di Unificazione; 2008.
- [C93] Ohta N., Robertson A.R., *Colorimetry: Fundamentals and applications*. (2005) Wiley & Sons, New York.
- [C94] UNI EN 15801:2010: Conservation of cultural property - test methods - Determination of water absorption by capillarity. UNI Ente Nazionale Italiano di Unificazione, 2010
- [C95] Washburn E. W., *The dynamics of capillary flow*, Phys. Rev. 17 (1921) 273-283.

- [C96] Peruzzi R., Poli T., Toniolo L. *The experimental test for the evaluation of protective treatments: a critical survey of the "capillary absorption index"*. J Cult Her 4 (2003) 251-254. DOI: 10.1016/S1296-2074.
- [C97] UNI EN 12370:2001 - Natural stone test methods - Determination of resistance to salt crystallization UNI Ente Nazionale Italiano di Unificazione, Milano.
- [C98] Di Maggio R., Fedrizzi L., Rossi S., *Effect of the chemical modification of the precursor of ZrO₂ films on the adhesion of organic coatings* J Adhes Sci Technol 15 (2001) 793-808
- [C99] Rahal R., Wankhade A., Cha D., Fihri A., Ould-Chikh S., Patil U., Polshettiwar V., *Synthesis of hierarchical anatase TiO₂ nanostructures with tunable morphology and enhanced photocatalytic activity* RSC Adv 2 (2012) 7048-7052. DOI: 10.1039/c2ra21104a
- [C100] Zhang H., Banfield J. F., *Understanding Polymorphic Phase Transformation Behavior during Growth of Nanocrystalline Aggregates: Insights from TiO₂*. J. Phys. Chem. B 104 (2000) 3481-3487.
- [C101] Lutterotti L, Matthies S, Wenk HR, Goodwin M *Combined Texture and structure analysis of deformed limestone from time-of-flight neutron diffraction spectra* J Appl Phys 81 (1997) 594-600
- [C102] Bersani D., Antonioli G., Lottici P.P., Lopez T., Raman study of nanosized titania prepared by sol-gel route. *Journal of Non-Crystalline Solids*, 232-234 (1998) 175-181. DOI: 10.1016/S0022-3093(98)00489-X
- [C103] Lottici PP, Bersani D, Braghini M, Montenero A *Raman scattering characterization of gel-derived titania glass* J Mater Sci 28 (1993) 177-183
- [C104] Bersani D., Lottici P.P., Ding X.Z. *Phonon confinement effects in the Raman scattering by TiO₂ nanocrystals* Appl Phys Lett 72 (1998) 73-75
- [C105] Swamy V., Kuznetsov A., Dubrovinsky L., Caruso R., Shchukin D., Muddle B. *Finite-size and pressure effects on the Raman spectrum of nanocrystalline anatase TiO₂*. Physical Review B, 71 (2005) 184302. DOI: 10.1103/PhysRevB.71.184302
- [C106] Swamy V *Size-dependent modifications of the first-order Raman spectra of nanostructured rutile TiO₂* Phys Rev B 77 (2008) 195414
- [C107] Golubović A., Šćepanović M., Kremenović A., Aškračić S., Berec V., Dohčević-Mitrović Z., Popović Z.V., *Raman study of the variation in anatase structure of TiO₂ nanopowders due to the changes of sol - gel synthesis conditions* J Sol-Gel Sci Technol 49 (2009) 311-319. DOI: 10.1007/s10971-008-1872-3
- [C108] Kosmulski M. *The significance of the difference in the point of zero charge between rutile and anatase* Adv Colloid Interfac 99 (2002) 255-264
- [C109] Kosmulski M. *pH-dependent surface charging and points of zero charge. IV. Update and new approach* Colloid Interf Sci 337 (2009) 439-448. DOI: 10.1016/j.jcis.2009.04.072.

- [C110] Strataki N., Bekiari V., Stathatos E., & Lianos P. *Effect of aggregation of dyes adsorbed on nanocrystalline titania films on the efficiency of photodegradation*, J Photoch Photobio A 191 (2007). 13-18. DOI: 10.1016/j.jphotochem.2007.03.023
- [C111] Nishikiori H, Nagaya S, Tanaka N, Katsuki A, Fuji T *Acid-Base and Monomer-Dimer Equilibria of Methylene Blue in Dip-Coated Bull Chem Soc Jpn* 72 (1999) 915-921
- [C112] Liu B., Wen L., Nakata K., Zhao X., Liu S., Ochiai T., Murakami T., Fujishima A., *Polymeric adsorption of methylene blue in TiO₂ colloids-highly sensitive thermochromism and selective photocatalysis* Chem-Eur J 18 (2012) 12705-12711.
- [C113] Zhao Z., Malinowski E.R. *Determination of the Hydration of Methylene Blue Aggregates and Their Dissociation Constants Using Visible Spectroscopy*. Appl Spectrosc 53 (1999) 1567-1574
- [C114] Braswell E. *Evidence for trimerization in aqueous solutions of methylene blue* J Phys Chem 72 (1968) 2477-2483
- [C115] Georges J. *Deviations from Beer's law due to dimerization equilibria: theoretical comparison of absorbance, fluorescence and thermal lens measurements*. Spectrochim Acta A 51 (1995) 985-994
- [C116] Heger D., Jirkovský J., Klán P. *Aggregation of Methylene Blue in Frozen Aqueous Solutions Studied by Absorption Spectroscopy*. J Phys Chem A 109 (2005) 6702-6709
- [C117] Ghanadzadeh Gilani A., Moghadam M., Hosseini S.E., Zakerhamidi M.S., *A comparative study on the aggregate formation of two oxazine dyes in aqueous and aqueous urea solutions* Spectrochim Acta A 83 (2011) 100-105.
- [C118] Antonov L., Gergov G., Petrov V., Kubista M., Nygren J., *UV-Vis spectroscopic and chemometric study on the aggregation of ionic dyes in water*. Talanta 49 (1999) 99-106.
- [C119] Houas A., Lachheb H. Ksibi M., Elaloui E., Guillard C., Herrmann J.M. *Photocatalytic degradation pathway of methylene blue in water*. Appl Catal B-Environ 31 (2001) 145-157.
- [C120] Li H., Li J., Huo Y., *Highly active TiO₂-N photocatalysts prepared by treating TiO₂ precursors in NH₃/ethanol fluid under supercritical conditions*. J Phys Chem B 110 (2006) 1559-1565.
- [C121] Tahiri H., Ichou Y.A., Herrmann J.M., *Photocatalytic degradation of chlorobenzoic isomers in aqueous suspensions of neat and modified titania* J Photoch Photobio A 114 (1998) 219-226.
- [C122] Dunham R. J., *Classification of carbonate rocks according to depositional texture*, in: Ham We (Ed.), Classification of carbonate rocks: American Association of Petroleum Geologists Memoir, 1962, pp. 108-121.
- [C123] Kay G.M., *North American geosynclines*. Memoir no. 48. Boulder, Colorado, Geological Society of America (1951) 143 pp.

[C124] Djaoued Y., Badilescu S., Ashrit P.V., Bersani D., Lottici P.P., Robichaud J., *Study of anatase to rutile phase transition in nanocrystalline titania films*. J. Sol-Gel Sci. Technol. 24 (2002) 255-264.

[C125] Miliani C., Velo-Simpson M.L., Scherer G.W., *Particle-modified consolidants: A study on the effect of particles on sol-gel properties and consolidation effectiveness*. J Cult Herit 8 (2007) 1-6.

[C126] Folk R. L., *Spectral subdivision of limestone types*. in Ham, W.E., ed., *Classification of Carbonate Rocks-A Symposium*, Am. Assoc. Petr. Geol. Memoir 1 (1962) 62-84.

CONCLUSIONS

The research has focused on the synthesis, characterization and application of inorganic and hybrid organic-inorganic systems for conservative treatments of wood (**Part A and B**) and stone (**Part C**). The wood preservatives synthesized and tested for biocidal activity are polyamidoamines functionalized with hydroxyl and siloxane groups, while the coatings applied on the stones are water based TiO₂ nanosols with photocatalytic and self-cleaning properties.

(Part A) Model monomeric amidoamines were synthesized by addition reaction between an α,β -unsaturated amide (2-propenamide or N,N'-methylenebisacrylamide) and an amine (ethanolamine or diethanolamine). Their synthesis is a simple system for the study of polyamidoamines. This allowed the study of the main parameters, mainly solvent (water) and temperature, that influence the reaction.

(Part B) Polyamidoamines in different reaction conditions were then synthesized. The polymers were functionalized with OH groups (PAAOH) and siloxane groups (SiPAA, SiPAAOH). The alkoxysilane function may undergo hydrolysis and condensation to form an inorganic network inside the wood. The various polymers were characterized by spectroscopic techniques (ESI-MS, NMR, FTIR, Raman), in order to study the structure and degree of polymerization, and with thermal analysis.

The hybrid polymers have been incorporated into the lignocellulosic structure of the wood and subjected to heat treatment in order to increase the crosslinking. The high degree of crosslinking (DOC Degree of Condensation) within the wood has been demonstrated by ²⁹Si-NMR spectra. The electron microscope (SEM) observations, demonstrate that the two treatment procedures, dip coating and vacuum impregnation, are effective and that all the solvents used are good carriers to vehicular the SiPAA solutions in the wood.

Three different preparations were applied as a protective coating on wood samples (sapwood of *Pinus sylvestris*) and tested for efficacy against biotic attack, both xilophagous insects and fungi, and resulted effective. After aging tests the polymers with siloxane functionality (SiPAA, SiPAAOH) are effective on wood-decay fungi. The treatments are effective against both fungi and insects. The polyamidoamine are harmless to human health and the environment. The synthesis of these new polymeric wood preservatives has the advantage that no molecular fragment is released as a by-product of the reaction; the reactions are conducted in water, alcohols or in low molecular weight solvent Augeo SL191.

The results obtained by biocidal effectiveness test are very promising and have been protected by an international patent application.

(Part C) Sol-gel TiO₂ based coatings for the photocatalytic self-cleaning of biocalcarene stones have been synthesized and characterized.

Nanocrystalline titania sols in acid and basic aqueous environments (TiAcAc, TiAcAu, TiAcN, TiAcNNa, TiMaA, TiMaAN) have been prepared by sol-gel, processing titanium isopropoxide with two complexing agents, acetic acid and malonic acid and different peptizers, i.e. acetic acid, nitric acid and triethylamine. XRD, Raman and TEM measurements on the corresponding titania powders have revealed nanocrystalline particles of anatase (5-6 nm) and of brookite in lesser amount.

The effectiveness of the photocatalytic sols was verified by evidence of degradation of dyes under UV-Vis irradiation. In accordance with the rules on cultural heritage, the harmlessness of coating towards the substrate has been investigated.

DLS and ELS-IEP analyses have indicated that preparations with acetic acid, acetic/nitric acids or malonic/triethylamine (basic) gives *stable* sols, namely TiAcAc, TiAcN and TiMaA.

Coatings at different pH were applied to biocalcarenes typical of southern Italy (Comiso, Modica, Noto and Lecce stones) used in the Baroque period of interest for cultural heritage.

Satisfactory results are obtained by photodegradation under UV irradiation of stones coated by TiAcN. The colour difference before and after the treatments is acceptable. The coatings do not alter the intrinsic properties of stones in the capillarity absorption of water, do not prevent the salts crystallization and leave unchanged the stone characteristics.

On *Pietra di Noto*, both acid (TiAcN) and basic (TiMaA) titanium coatings have been applied. Both nanosols are suitable for harmless protection of *Pietra di Noto*, but the basic one exhibits better performances in term of filmogenic properties, colour changes, water absorption, durability enhancement and photocatalytic degradation of organic dyes and then it should be preferred for calcarenite substrates.

The results highlight the compatibility of the treatments with respect to the properties of the calcarenite stones, showing no chromatic changes, no alteration of physical properties, an improvement of the resistance to salts crystallization and good photocatalytic activity on both dyes. In particular, TiMaA sol, thanks to its basic nature, is suited for the self-cleaning of carbonatic stones, widely employed in ancient and modern architecture. This opens perspectives for further applications in the cultural heritage field.

ACKNOWLEDGMENTS

This work has been partly financially supported by “Fondazione Cariparma” and Renner Italia spa, Minerbio (BO), Italy.

It has been completed with the collaboration of:

Claudia Graiff, Ilaria Alfieri, Andrea Lorenzi - Dipartimento di Chimica, Università di Parma, Italy

Valentina Selva Bonino, Beatrice Bonati, Monica Mattarozzi, Roberta Magnani, Ilaria Domenichelli, Clelia Isca, Marco Milioli and Giuseppe Foroni – Dipartimento di Chimica, Università di Parma, Italy

Lisa Elviri, Ruggero Bettini and Andrea Della Bella - Dipartimento di Farmacia, Università di Parma, Italy

Laura Lazzarini – IMEM-CNR, Parma, Italy

Domenico Acquotti – Centro Interdipartimentale Misure "Giuseppe Casnati" – Università di Parma, Italy

Emma Salvioli Mariani, Luca Barchi and Andrea Comelli – Dipartimento di Fisica e Scienze della Terra, Università di Parma, Italy

Sabrina Palanti and Elisabetta Feci, CNR-IVALSA, Istituto per la Valorizzazione del Legno e delle Specie Arboree, Sesto Fiorentino, Italy

Maistrello Lara – Dipartimento di Scienze della Vita, Università di Modena e Reggio Emilia, Italy

Rosa di Maggio, Fabrizio Girardi and Elisa Cappelletto – Dipartimento di Ingegneria dei Materiali e Tecnologie Industriali, Università di Trento, Italy

Elisabetta Chiappini and Alessia Berzolla – Università Cattolica del Sacro Cuore (UCSC) - Centro per la Protezione dei Beni Culturali dagli Organismi dannosi “CPBC”. Piacenza, Italy

Ludovic Bellot-Gurlet, Philippe Colombar, Céline Paris and Gwenael Gouadec, MONARIS – UPMC, Paris VI, Place Jussieu, Paris, France

and of all the coauthors of the papers listed below, in particular the students of “Sciences for Cultural Heritage”, University of Parma.

PUBLICATIONS

Parts of this work have already been published, accepted or sent for publication:

1. L. Bergamonti, I. Alfieri, A. Lorenzi, G. Predieri, G. Barone, G. Gemelli, P. Mazzoleni, S. Raneri, D. Bersani, P.P. Lottici, *Photocatalytic activity of nanocrystalline TiO₂ coatings by sol-gel on Pietra di Noto biocalcarenite*, J Sol-Gel Science & Technology – sent for publication on January 2015
2. C. Graiff, D. Pontiroli, L. Bergamonti, C. Cavallari, P.P. Lottici, G. Predieri, *Structural Investigation of N,N'-methylenebisacrylamide via X-ray Diffraction Assisted by Crystal Structure Prediction*, Journal of Applied Crystallography, 2015 – in press
3. L. Bergamonti, I. Alfieri, A. Lorenzi, A. Montenero, G. Predieri, R. Di Maggio, F. Girardi, L. Lazzarini, P.P. Lottici, *Characterization and photocatalytic activity of TiO₂ by sol-gel in acid and basic environments*, J. Sol Gel Science & Technol 73, 91-102 (2015) – DOI: 10.1007/s10971-014-3498-y
4. L. Bergamonti, I. Alfieri, M. Franzò, A. Lorenzi, A. Montenero, G. Predieri, M. Raganato, A. Calia, L. Lazzarini, D. Bersani, P.P. Lottici, *Synthesis and characterization of nanocrystalline TiO₂ with application as photoactive coating on stones*, Environmental Science & Pollution Research 21, 13264-13277 (2014) - DOI: 10.1007/s11356-013-2136-5
5. L. Bergamonti, I. Alfieri, A. Lorenzi, A. Montenero, G. Predieri, G. Barone, P. Mazzoleni, S. Pasquale, P.P. Lottici, *Characterization and photocatalytic activity of TiO₂ nanoparticles on Modica and Comiso stones*, Applied Surface Science 282, 165-173 (2013) - ISSN 0169-4332 – DOI: 10.1016/j.apsusc.2013.05.95
6. L. Bergamonti, D. Bersani, S. Mantovan, P.P. Lottici, *Micro-Raman investigation of pigments and carbonate phases in corals and molluscan shells*, Europ. Journal of Mineralogy **25**, 845-853 (2013) - ISSN 0935-1221 - DOI: 10.1127/0935-1221/2013/0025-2318

Patent

L. Bergamonti, E. Chiappini, G. Predieri, S. Palanti, L. Maistrello, “*Wood preservative composition*” Int. Patent application WO 2015/004590 A1